A. Yücel Odabaşı Colloquium Series

3rd International Meeting

Progress in Propeller Cavitation and its Consequences -

Experimental and Computational Methods for Predictions

15 - 16 NOVEMBER 2018
ISTANBUL TECHNICAL UNIVERSITY
www.ayocol.itu.edu.tr

Edited by

Devrim B. Danışman
Burcu Erbaş
Çağatay Sabri Köksal

Faculty of Naval Architecture and Ocean Engineering

A Yücel Odabaşı Colloquium Series

3rd International Meeting

Progress in Propeller Cavitation and its Consequences -

Experimental and Computational Methods for Predictions

15 - 16 November 2018
ISTANBUL TECHNICAL UNIVERSITY
www.ayocol.itu.edu.tr

Edited by

Devrim B. Danışman
Burcu Erbaş
Çağatay Sabri Köksal

Faculty of Naval Architecture and Ocean Engineering

TABLE OF CONTENTS

Keynote Addresses

Keynote Address 1: Investigation of Scale Effects on Propeller Sheet and Tip Vortex Cavitation Based on Hybrid Simulation Methods

M. Abdel-Maksoud

Keynote Address 2: Developments in Experimental Modelling of Two-Phase Flows in Naval Hydrodynamics

P. Brandner

Keynote Address 3: Multi-functional Marine Structures: New Frontiers for Cavitating and Ventilating Flows

Y. L. Young

PAPERS

SPONSORS

Anadolu Shipyard

The Chamber of Turkish Naval Architects and Marine Engineers

Turkish Lloyd

Med Marine

Ship and Yacht Exporters Association

Presidency of the Republic of Turkey
Presidency of Defence Industries

Gürdesan Ship Machinery Corp.

Turkish Shipbuilders' Association

Turkish Chamber of Shipping

Istanbul Technical University

PREFACE

As a tribute to the late Professor A. Yücel Odabaşı's (1945 – 2009) life-long endeavors in promoting the science of Naval Architecture and in particular Naval Hydrodynamics, a biennial international colloquium aiming to focus on a different theme on each occasion, gathering specialists from around the world, was organized. First of these colloquiums was held in 2014 at Istanbul Technical University and concentrated on the subject of propeller noise and vibrations. The second colloquium was on maneuvering of ships and submarines. The theme of the third colloquium in the series is selected as "Progress in Propeller Cavitation and its Consequences – Experimental and Computational Methods for Predictions". In this colloquium, the recent developments in experimental and computational methods for predicting propeller cavitation performance of surface vessels and submarines will be discussed and new opportunities for collaborative research will be sought. The progress of the construction of a new large scale cavitation tunnel, ITU-CAT, will be presented during the colloquium. The ITU-CAT project is sponsored by the Presidency of Defence Industries, SSB.

The Proceedings contain the papers presented at A Yücel Odabaşı Colloquium Series; 3rd International Meeting - Progress in Propeller Cavitation and its Consequences: Experimental and Computational Methods for Predictions, which took place at Faculty of Naval Architecture and Ocean Engineering of Istanbul Technical University (ITU), Ayazaga Campus, Maslak, Istanbul, Turkey, on 15-16 November 2018. The Proceedings can be downloaded from the colloquium webpage at http://www.ayocol.itu.edu.tr/.

We wish to acknowledge the Sponsors of the Colloquium for their generosity. We would like to thank the authors and presenters for their valuable contributions. We would especially like to thank the keynote speakers of this year's event, Prof.Moustafa Abdel-Maksoud , Prof. Paul Brandner and Prof.Yin Lu Young for sharing their knowledge and expertise in Propeller Cavitation and its Consequences. We would also like to acknowledge the tremendous help and efforts of the members of the local organizing committee in the preparation of the colloquium. We hope that, while commemorating Prof. Odabaşı, this colloquium will offer a fruitful platform for domestic and international specialists together with the key-note lecturers on this thematic subject "Propeller Cavitation and its Consequences".

Ismail Hakkı Helvacıoğlu Emin Korkut

COLLOQUIUM COMMITTEES

Standing Committee

Dr. Mehmet Atlar, *University of Strathclyde, UK*
Dr. Sander Çalışal, *University of British Columbia, Canada / Piri Reis University, Turkey*
Dr. Atilla İncecik, *University of Strathclyde, UK*
Dr.Ömer Gören, *Istanbul Technical University, Turkey*
Dr. Barbaros Okan, *Istanbul Technical University, Turkey*
Dr. Öner Şaylan, *Istanbul Technical University (Retired), Turkey*

Technical Committee

Prof. Moustafa Abdel-Maksoud, *Hamburg University of Technology, TUHH, Germany*
Prof. Paul Brandner, *University of Tasmania, Australia*
Prof. Steven Cecio, *University of Michigan, USA*
Prof. (vis.) Patrick Fitzsimmons, *University of Strathclyde, UK*
Prof. Emin Korkut *Istanbul Technical University, Turkey*
Prof. (vis.) Noriyuki Sasaki, *University of Strathclyde, UK*
Prof. Tom van Terwisga, *MARIN & TU Delft, Nederlands*

Local Organizing Committee

Dr. Devrim B. Danışman (Secretary), *Istanbul Technical University, Turkey*
Dr. Burcu Erbaş, *Istanbul Technical University, Turkey*
Mr. Emre Kemal Gürtunca*, Presidency of the Republic of Turkey Presidency of Defence Industries*
Dr. Ismail H. Helvacıoğlu (Chair), *Istanbul Technical University, Turkey*
Mr. Çağatay Sabri Köksal, *Istanbul Technical University, Turkey*
Dr. U. Oral Ünal, *Istanbul Technical University, Turkey*

PROF. A. YÜCEL ODABAŞI

(1945 – 2009)

Professor Odabaşı, a graduate of ITU (1967), earned his Ph.D. degree from the same university in 1971. Following his Ph.D., he joined Strathclyde University where his work on the application of Lyapunov's theory to ship stability gained him a well-deserved international reputation which was acknowledged by STAB Award in 2012 post mortem. In 1974 he joined BSRA where he worked on every field of ship hydrodynamics and made significant contributions, in particular in the field of wake scaling. In 1988 he moved to USA to set up BMT International as its first director and CEO. He returned to ITU-Turkey in 1991 where he inspired a generation of young academics while at the same time succeeding to lead Turkish Lloyd to worldwide recognition. He was awarded the gold medal of NECIES-UK and numerous awards from NAVSEA, SNAME, BSRA.

A. Yücel Odabaşı Colloquium Series
3^{rd} International Meeting - Progress in Propeller Cavitation and its Consequences:
Experimental and Computational Methods for Predictions
15^{th} – 16^{th} November 2018, Istanbul, Turkey

Numerical Study on Characteristics of Cloud Cavitation on a Ship Propeller

Keun Woo Shin[1*], Poul Andersen[2]
[1]Propeller & Aftship R&D Department, MAN Energy Solutions, Frederikshavn, Denmark
[2]Department of Mechanical Engineering (MEK), Technical University of Denmark (DTU), Kgs. Lyngby, Denmark

Abstract: Cavitating flows on a ship propeller, showing extensive sheet and cloud cavitation in a cavitation tunnel test, are simulated by DES in the behind-hull condition and the cavitation simulations are validated against the experimental results. It is attempted to resolve microbubble structures and dynamic bubble collapses of cloud cavitation by refining temporal and spatial discretizations from 58 μs to 14.5 μs and from 0.34 mm to 0.09 mm, respectively. Turbulent eddies leading to a re-entrant jet at the rear part of the sheet cavity are better resolved on the refined grid, hence the sheet cavity detachment is reproduced more dynamically with an abrupt pressure recovery and cloud cavitation is simulated as scattered patches resembling densely distributed microbubbles. The minimum pressure at the blade position of the maximum angle-of-attack is better resolved by the smaller time-step and the growing and collapsing rates of the sheet cavity are better predicted with less numerical delays. The simulation results imply a possibility to predict micro-scale behaviors and violent collapses of cloud cavitation on ship propellers accurately by CFD with sufficient refinements of temporal and spatial discretizations.

Keywords: cloud cavitation, sheet cavitation, ship propeller, hull wake, DES

1 INTRODUCTION

The prevention of cloud cavitation is of major importance in ship propeller designs, because it is often associated with intense noise generation and blade surface erosion. Cloud cavitation on ship propellers is often generated by a mechanism by which extensively developed sheet cavitation is detached from the blade surface by a re-entrant jet. It has things in common with that of cavity shedding and unsteady cloud cavitation on static hydrofoils, which has been intensively studied by experimental and numerical approaches (Arndt et al 2000, Arndt 2010). Recent studies report that propagating shock waves can be another mechanism of cavity shedding, when the vapor fraction inside the cavity is radically increased (Ganesh et al 2017). Cloud cavitation can also be brought about by a periodic flow disturbance on an oscillating hydrofoil (Reisman et al 1994), which may represent cavitating flows on ship propellers, as the angle of attack on the blade varies periodically depending on non-uniform hull wake in a propeller revolution.

The increase in computational power enables practical use of CFD methods for simulating propeller cavitation. CFD made by turbulent viscous solvers like RANS, DES and LES for unsteady sheet cavitation on a propeller installed on a hull model or in a hull wake field have been validated against cavitation tunnel test results (Bensow & Bark 2010, Paik et al 2013, Vaz et al 2015). The lead time of the propeller design process can be significantly reduced by using easy-to-use and computationally efficient potential flow solvers such as boundary element method (BEM) for estimating sheet cavitation extents in design optimizations (Du & Kinnas 2018), but it has inherent limitations in accounting for cavitation detachment induced by turbulent eddies.

Sheet cavitation detachment from the blade surface in a form of cloud cavitation simulated by DES with a hull wake model has been validated against experimental results (Shin et al 2015), but only a large-scale structure of cloud cavity is simulated as a lump, and microbubble structures and dynamic bubble collapses are not reproduced well. In this work, it is attempted to resolve micro-scale behavior and violent collapse of cloud cavitation by refining the spatial and temporal discretization.

2 PROPELLER MODEL

A 4-blade propeller with a model-scale diameter of D = 0.25 m and an expanded area ratio of A_E/A_O = 0.38 is considered in cavitation simulations. The propeller is designed for a single-screw 35,000 DWT handysize bulk carrier. It is a Kappel propeller characterized by a smoothly curved tip bending towards the suction side of the blade. The blade geometry and the design method of the tip-modified propeller are described in Shin & Andersen (2016) and Andersen (1996). A cavitation tunnel test has been conducted on the propeller with a complete hull model in SSPA. The hull model fitted with the propeller in the cavitation tunnel is shown in Figure 1(a). The tunnel flow speed of V_S = 4.5 m/s and the propeller speed of N = 24.0 rps in the experiment are applied to initial simulations and N is adjusted to reach the thrust coefficient of K_T = 0.213 from the experiment. The same case has been simulated in Shin et al (2015). In this work, the hull wake

---

** Corresponding author e-mail: keun.shin@man-es.com* model in the CFD setup is updated and the computational grid in cavitating regions and the time step are refined as described in the following sections.

3 CFD SETUP

Since separated flows leading to cavitation detachment is underestimated by unsteady RANS (Shin 2014), the DES solver of the commercial CFD software StarCCM+ is adopted for the following simulations. Cavitating flows are modelled by an Eulerian multiphase approach of the volume-of-fluid (VOF) method and a vapor transport equation with an interphase mass transfer model based on the asymptotic Rayleigh-Plesset equation.

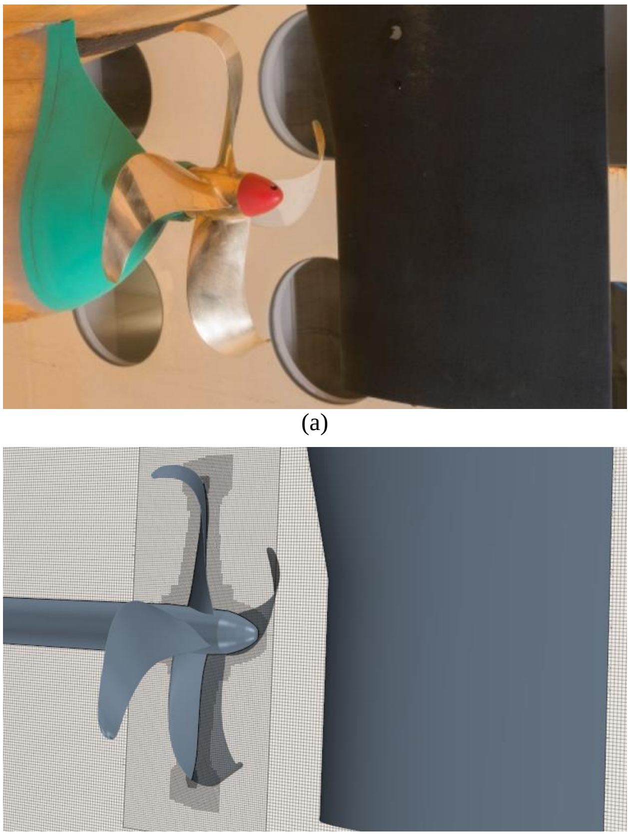
(a)

(b)

Figure 1 (a) Propeller model installed on the hull in the cavitation tunnel test, (b) computational model in the cavitation simulations

A trimmed hexahedral grid is prepared around a rudder and a propeller with a shaft extending to the inlet in a cylindrical fluid domain extending 3·*D* from the propeller plane to the inlet and 6·*D* to the outlet with a radial extent of 4·*D*. A cylindrical subdomain is defined around the propeller for propeller rotations, which are modelled by the rigid body motion and the sliding grid. The rotating domain is shown on the vertical cross section along the centerline in Figure 1(b). The surface grid size is set to $\Delta x = 0.5 - 1.0$ mm on the blade and hub and it is refined to 0.25 – 0.5 mm along the blade edges. The tip regions surrounded by cylinders at $0.8{\cdot}R$ – $1.0{\cdot}R$ in Figure 2 is set to have a consistent volumetric grid size of $\Delta x_{Tip} = 0.34$ mm for resolving cavity shedding. Boundary-layer flows are resolved by the prism-layer grid leading to non-dimensional wall distances of $y^+ \leq 2$.

For considering propeller flows in the behind-hull condition, hull wake is modelled as a propeller inflow instead of including a hull model (Shin et al 2011). Although the nominal hull wake measurements from towing tank tests are available, the hull wake field from a bare-hull simulation is applied to the wake modelling, because towing tank tests are made at a low Reynolds number, compared to cavitation tunnel tests, and so hull wake differs depending on Reynolds number. Axial wake is applied directly by an inlet boundary condition and transverse wake consisting of radial and tangential components is modelled by momentum sources applied 0.6·*D* upstream from the propeller plane. It has an advantage to save computational cost by excluding the hull model, but iterative numerical tests without the propeller model are necessary for achieving the nominal wake field on the propeller plane by adjusting momentum source strengths. In Figure 3, the velocity field on the propeller plane from the final wake model test is compared with the nominal wake from the bare-hull simulation.

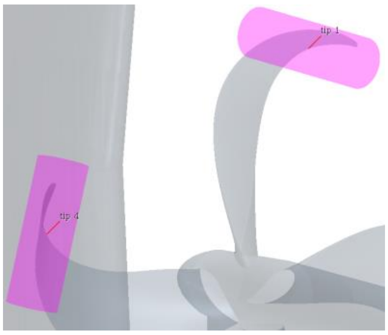

Figure 2 Volumetric grid refinement in regions surrounded by cylinders for resolving cavity shedding

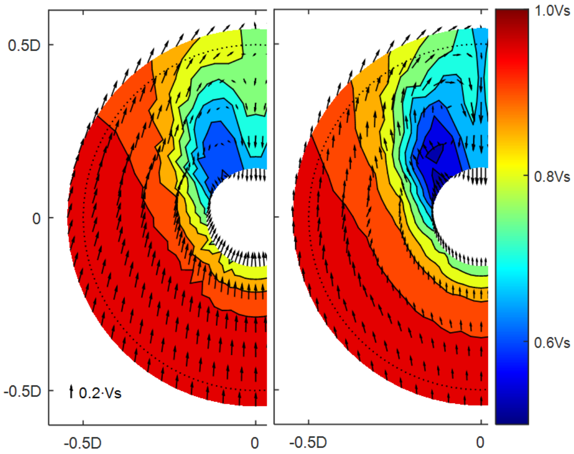

(a) (b)

Figure 3 Hull wake from (a) bare-hull simulation and (b) wake modelling

4 CAVITATION SIMULATION

A cavitation simulation is made by using the initial grid setup described in the previous section. After starting it with a relatively large time-step and running for a few revolutions, Δt is gradually reduced to 0.5° rotation per Δt and it is run for two more revolutions. A 2nd-order implicit time-stepping scheme is used. N is 3.6% increased to reach K_T from the experiment with 0.1% deviation. In Table 1, propeller performance is compared between the cavitation tunnel test and CFD. The deviations in K_Q and η_B are as small as around 1.0%, where η_B is the behind-hull propeller efficiency.

Table 1 Comparison of propeller performance between the cavitation tunnel test and CFD ($\Delta\phi = \phi_{CFD}/\phi_{Exp} - 1$)

	N [rps]	K_T	$10 \cdot K_Q$	η_B	ΔN [%]	ΔK_T [%]	ΔK_Q [%]	$\Delta\eta_B$ [%]
Exp	24.0	0.213	0.313	0.634				
CFD	24.9	0.213	0.310	0.640	3.6	-0.1	-1.1	0.9

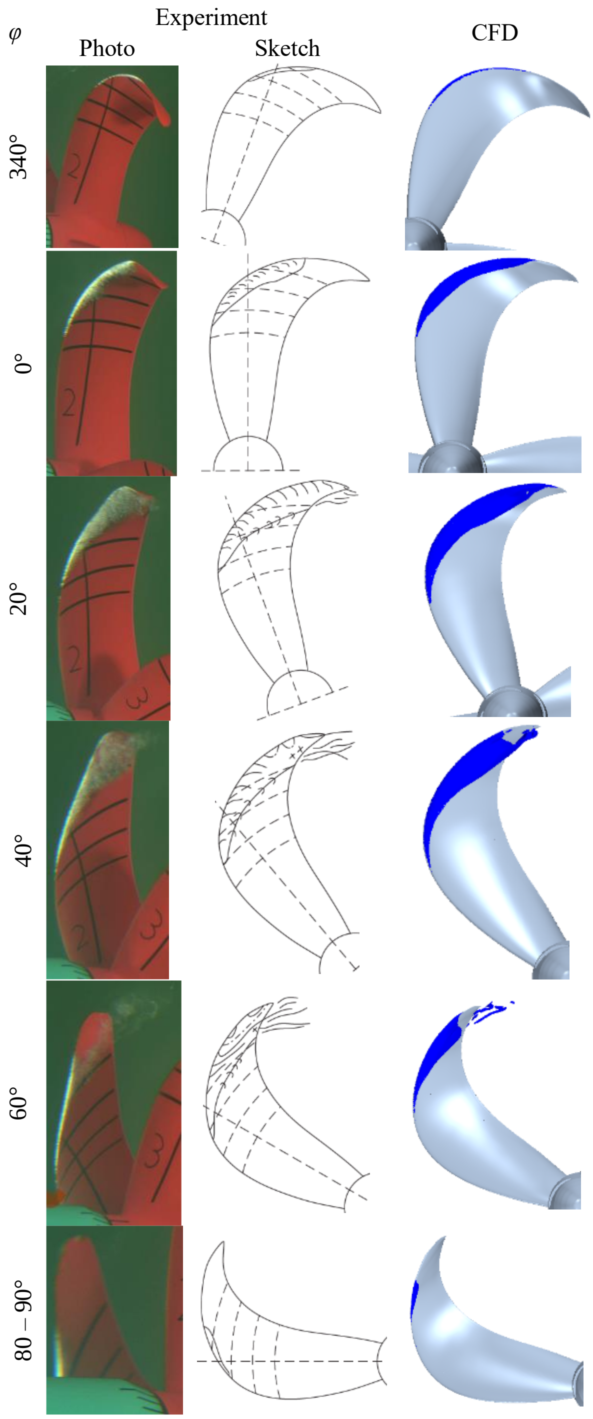

Figure 4 Unsteady cavitation on the suction side of the blade in the experiment and CFD

In Figure 4, unsteady cavitation on the suction side of the blade is compared between the experiment and CFD at several blade positions. The cavity interface in CFD is defined by the iso-surface of 10% vapor volume fraction. As the blade enters the region of high axial wake, the leading-edge sheet cavitation starts at $\varphi \approx 340°$ in both the experiment and CFD, where φ is the blade angle and $\varphi = 0°$ indicates 12 o'clock position. The sheet cavitation is extended at $\varphi = 340° - 20°$ and CFD shows reasonable agreements with the experiment in the radial and chordwise extents of the attached sheet cavitation.

The sheet cavity becomes a bit cloudy and unstable at the trailing edge of $0.9 \cdot R - 1.0 \cdot R$ at $\varphi = 20°$ in the experiment, whereas the sheet cavity is not extended to the trailing edge in CFD. At $\varphi = 40° - 60°$, the sheet cavity is detached in a form of cloud cavitation in both the experiment and CFD, but the seemingly core part of the cloud cavitation is simulated as lumps without resolving microbubbles. At $\varphi = 60°$, the cloud cavitation seems to be separated along the constant-radius chord line of $0.9 \cdot R$ and a bit radially outwards in the experiment and the bifurcation is also simulated by CFD. The sheet cavitation disappears from the blade surface at $\varphi = 80°$ earlier in CFD than at $\varphi = 90°$ in the experiment.

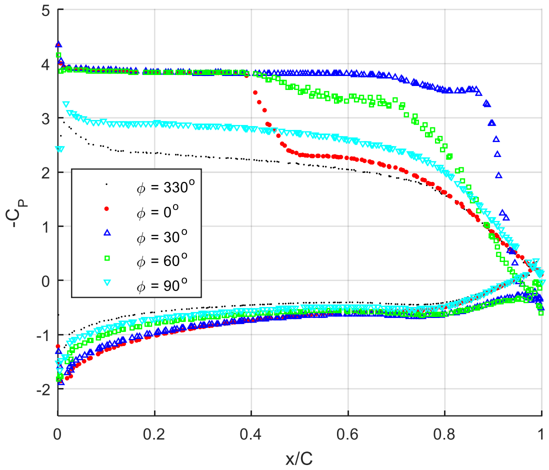

Figure 5 C_P on the section of $0.9 \cdot R$ in CFD

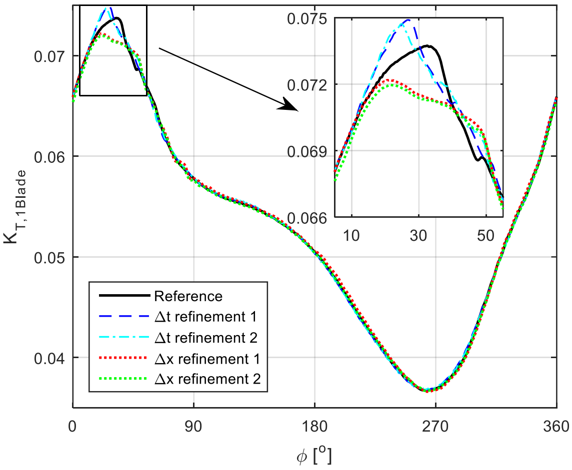

Figure 6 Variation of single-blade thrust over a propeller revolution in CFD with the refinements of temporal and spatial discretizations

In Figure 5, the pressure coefficient C_P on the section of $0.9 \cdot R$ in CFD is presented with respect to the chordwise position x/C, where $C_P = (P - P_\infty)/(0.5 \cdot \rho \cdot N^2 \cdot D^2)$ and C is the chord length. At $\varphi = 340° – 0°$, the leading-edge suction is increased to lead to the suction-side sheet cavitation and the region under the cavity has constant pressure equal to the saturated vapor pressure P_V, that is, $|-C_P| = \sigma_N$, where σ_N is the cavitation number, $\sigma_N = (P_\infty - P_V)/(0.5 \cdot \rho \cdot N^2 \cdot D^2)$. At $\varphi = 0° – 40°$, the constant-pressure region is lengthened according to the extension of the sheet cavity. The suction-side pressure distribution aft of the mid-chord does not have a smooth curve at $\varphi = 40° – 60°$, as the rear part of the sheet cavity is detached. The sheet cavitation disappears after $\varphi = 90°$, as the minimum pressure is higher than P_V.

5 REFINEMENT OF DISCRETIZATION

The simulation in the previous section is made with a time step of $\Delta t_0 = 58.0$ μs corresponding to 0.5° rotation per Δt and a grid size $\Delta x_{Tip0} = 0.34$ mm in the region with extensive sheet cavitation and detachment. Four simulations are made again with refining the temporal and spatial discretizations, as listed in Table 2.The prism-layer grid thicknesses of 0.02 – 0.05 mm are not affected by the refinements of the tip-region grid.

Figure 7 Unsteady cavitation in CFD with the refinements of temporal and spatial discretizations

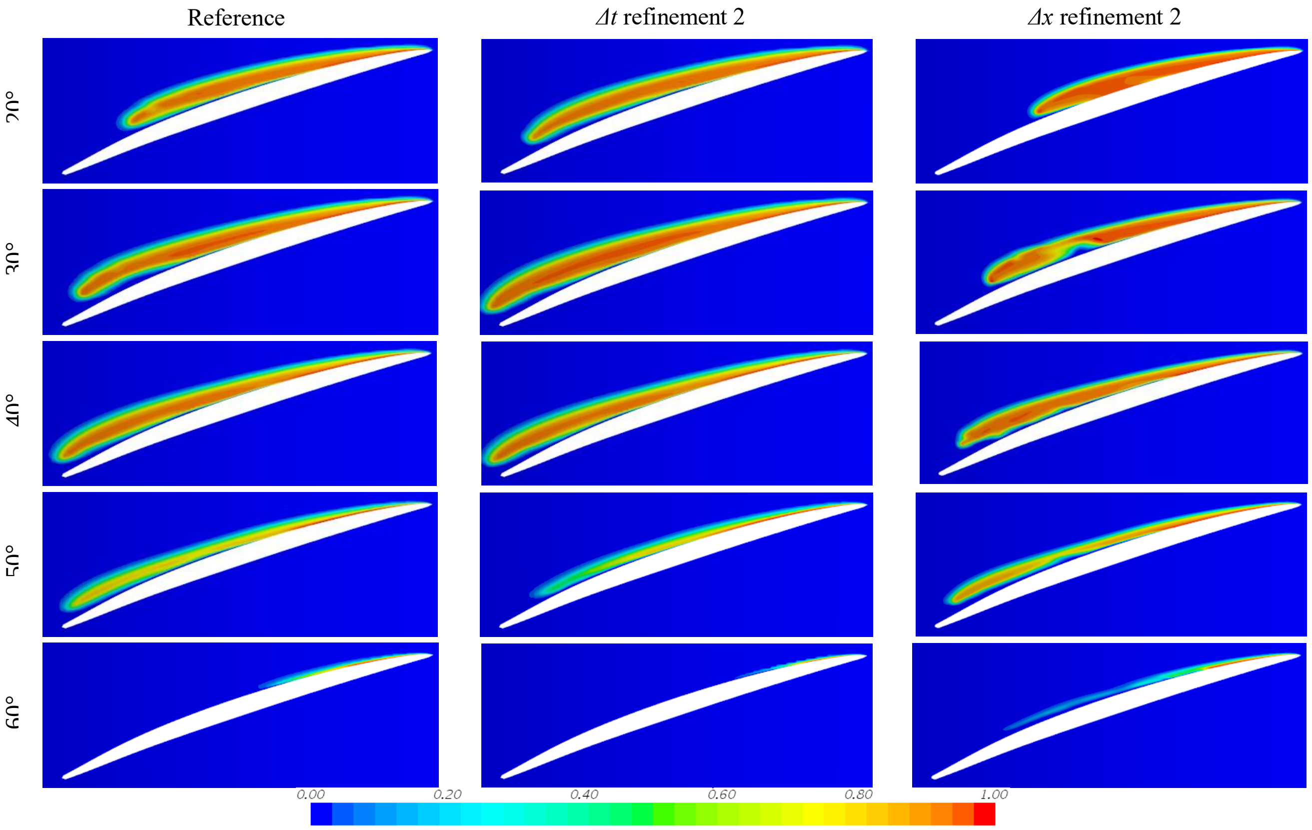

Figure 8 Vapor volume fraction on 0.9·*R* section in CFD with the refinements of temporal and spatial discretizations

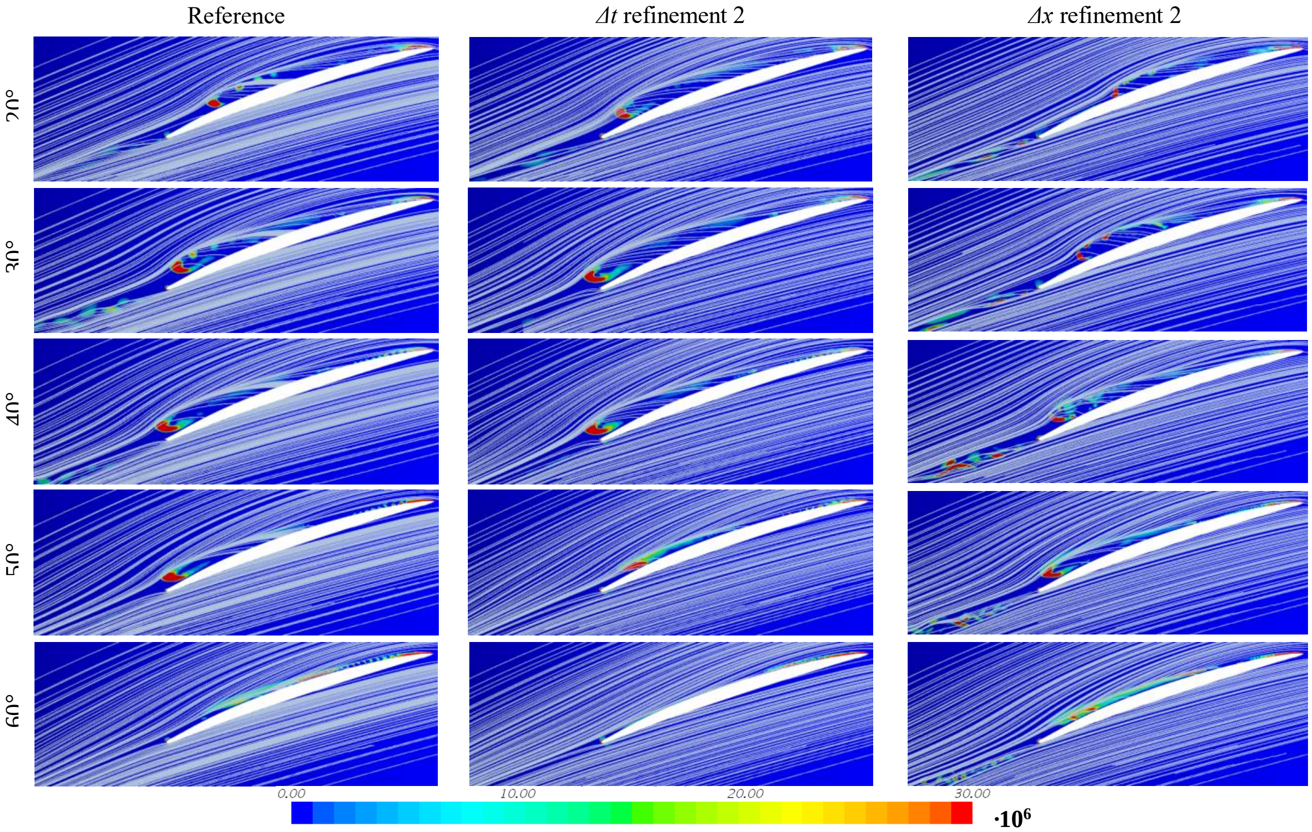

Figure 9 Q-criterion and streamlines on 0.9·*R* section in CFD with the refinements of temporal and spatial discretizations

The changes in K_T are within 0.1% for the temporal refinements and K_T is 0.5 – 0.6% lowered for the grid refinements. In Figure 6, the variation of single-blade thrust coefficient $K_{T,1Blade}$ is presented with respect to φ. The thrust is increased in the upper propeller disk, where high axial hull wake is formed. $K_{T,1Blade}$ is not symmetric with respect to the centerline, that is, vertically straight blade positions of $\varphi = 0°$ & 180° because of the outer-radii blade skewed back to the trailing edge and the effect of the tangential hull wake. The thrust peak is shown at $\varphi = 25° – 35°$ corresponding to the maximum extent of the sheet cavitation and $K_{T,1Blade}$ is the lowest at $\varphi \approx 270°$.

Table 2 Simulation list with refinements of discretization

	Reference	Δt Refine 1	Δt Refine 2	Δx Refine 1	Δx Refine 2
Δt	Δt_0	$0.5 \cdot \Delta t_0$	$0.25 \cdot \Delta t_0$	Δt_0	Δt_0
Δx_{Tip}	Δx_{Tip0}	Δx_{Tip0}	Δx_{Tip0}	$0.5 \cdot \Delta x_{Tip0}$	$0.25 \cdot \Delta x_{Tip0}$

$K_{T,1Blade}$ differs at $\varphi = 10° – 55°$ in the simulations with the refinements of Δt and Δx. The thrust peak is higher in the Δt refinements, because the instantaneous minimum pressure at the blade position of the largest angle-of-attack is better resolved by the smaller time-steps. As the growth and decay of the sheet cavitation are accelerated by the Δt refinements, $K_{T,1Blade}$ has steeper slopes around the peak and so the peak is shown earlier than the reference. The peak is lower and it is shown earlier on the refined grids, because the sheet cavitation is detached earlier by the re-entrant jet better resolved on the smaller grids. As the sparsely distributed sheet cavitation aft of the mid-chord at $0.9 \cdot R – 1.0 \cdot R$ is better resolved on the refined grids, $K_{T,1Blade}$ declines more gradually than the reference.

In Figure 7, unsteady cavitation on the suction side of the blade is compared in the simulations with the refinements of Δt and Δx. As the differences in $K_{T,1Blade}$ are insignificant before $\varphi = 20°$, the sheet cavitation extent does not differ noticeably and hence the comparison is presented from $\varphi = 20°$.

The sheet cavity aft of the mid-chord at $0.9 \cdot R – 1.0 \cdot R$ is destabilized earlier for the smaller time-steps. It agrees better with the experimental result showing the destabilized sheet cavity from $\varphi \approx 20°$. The detachment of the sheet cavity also occurs earlier and the detached cavity is more extended at $\varphi = 50° – 60°$ for the smaller time-steps. It implies that the growth and collapse of the sheet cavity are delayed by the larger time-step in the reference simulation.

The sheet cavity is destabilized later on the refined grids than at $\varphi = 30°$ on the reference grid. The sheet cavity destabilized at $\varphi = 40°$ still covers a large area of the blade surface at $0.9 \cdot R – 1.0 \cdot R$ on the refined grids unlike the sparsely distributed cavity aft of the mid-chord on the reference grid. The most of the unstable sheet cavity is still connected to the fore part at $\varphi = 50°$ and the rear part is detached at $\varphi = 60°$. The sheet cavity detachment occurs later on the refined grids than on the reference grid. The later destabilization and detachment of the sheet cavity on the refined grids may be because the growth and collapse of the sheet cavitation are delayed due to the increase of $\Delta t / \Delta x$. The scattering of the detached cavity to small patches is more pronounced on the refined grids at $\varphi = 70° – 80°$ and it resembles densely distributed microbubbles of cloud cavitation.

In Figure 8, the distribution of vapor volume fraction α on the cylindrical section of $0.9 \cdot R$ is compared between the simulations with the refinements of Δt and Δx. α is over 90% in the most part of the sheet cavity in the growing phase of $\varphi = 20° – 40°$. The sheet cavity is extended all over the suction side of the blade at $\varphi = 30° – 40°$. The sheet cavity aft of the mid-chord is detached from the blade surface, but it is still connected to the fore part of the sheet cavity.

The growth and decay of the sheet cavity are faster and the sheet cavity extent at $\varphi = 30° – 40°$ is larger for the smaller time-step than for the reference. The growth and decay of the sheet cavity are slower and α in the fore part of the sheet cavity is higher on the smaller grid. The lower side of the sheet cavity aft of the mid-chord is unstable at $\varphi = 30° – 50°$, because turbulent eddies at the rear part of the sheet cavity are better reproduced on the refined grid.

In Figure 9, Q-criterion and streamlines on the $0.9 \cdot R$ section are compared for investigating differences in vortex flows. Strong vortices are formed at the fore and rear ends of the sheet cavity. Strong vortices have high Q-criterion values above $3.0 \cdot 10^7$ and streamlines just go around the high Q-criterion region without capturing vortex flows.

While there are smaller vortices in front of the strong vortex at the rear end of the sheet cavity at $\varphi = 20° – 30°$ and vortices behind the trailing edge of the blade oscillate like the von Karman vortices in the reference simulation, a strong vortex at the rear end is formed without other small vortices for the smaller time-step. As the maximum angle-of-attack is resolved and the cavitation is intensified by the smaller time-step, the rear part of the sheet cavity may be stabilized. As smaller irregular vortices at the rear part of the sheet cavity are developed on the refined grid especially at $\varphi = 40°$, the sheet cavity is extended less than the reference. The vortex shedding behind the trailing edge is also intensified on the refined grid.

The surface pressure on the $0.9 \cdot R$ section in Figure 10 shows that the constant low pressure on the suction side is extended to about $0.8 \cdot C$ at $\varphi = 30° – 50°$, but $-C_P$ has a slight decrease from $0.5 \cdot C$, as the sheet cavity is detached from the blade surface. The suction is recovered with a high gradient at $0.8 \cdot C – 1.0 \cdot C$.

As the sheet cavity is more extended for the smaller time-step, the high-suction region is more extended at $\varphi = 30° – 40°$. The extent of the high-suction region is less at $\varphi = 50°$ than the reference, because the cavity collapse is accelerated by the smaller time-step. While $-C_P$ has a gradual decline at 0.8·*C* – 0.9·*C* and afterwards the suction recovery occurs with a steep slope at $\varphi = 30° – 40°$ in the simulations without the grid refinement, the suction is recovered without a gradual decline at 0.8·*C* – 0.9·*C* and the slope is steeper on the refined grid. The pressure is reversed at 0.9·*C* – 1.0·*C* of $\varphi = 40°$ due to the fluctuation after the pressure recovery on the refined grid.

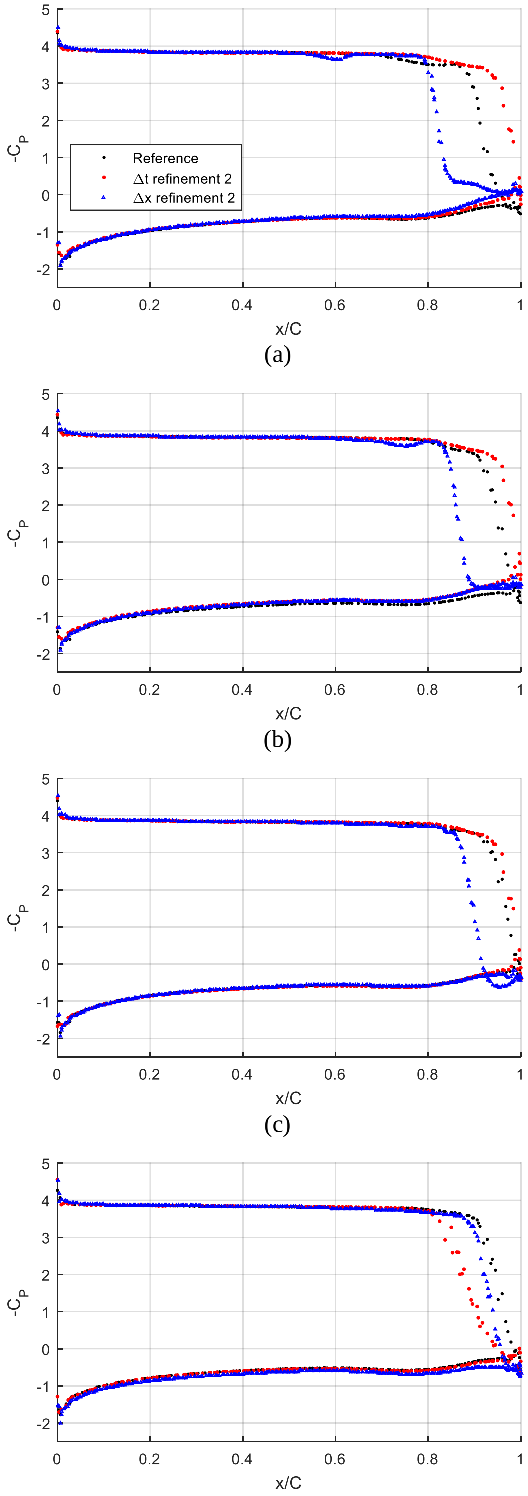

(a)

(b)

(c)

(d)

Figure 10 C_P on the section of 0.9·*R* in CFD with the refinements of temporal and spatial discretizations: (a) $\varphi = 30°$, (b) $\varphi = 35°$, (c) $\varphi = 40°$, (d) $\varphi = 50°$

6 CONCLUSION

Cavitating flows on a ship propeller are simulated by DES in the behind-hull condition. The temporal and spatial discretizations of the CFD model are refined for resolving sheet cavity detachment and cloud cavitation. Turbulent eddies forming a re-entrant jet at the rear part of the sheet cavity are better resolved on the refined grid, hence the cavity detachment is reproduced more dynamically with an abrupt pressure recovery and cloud cavitation is simulated as scattered patches resembling densely distributed microbubbles.

Since the minimum pressure at the blade position of the maximum angle-of-attack is better resolved by the smaller time-step, the sheet cavity is more extended. When the time-step is not small enough, the growth and collapse of the sheet cavity can be numerically delayed.

The CFD results imply a possibility to predict micro-scale behaviors and violent collapses of cloud cavitation on conventional and innovative ship propellers accurately by using CFD with sufficient refinements of temporal and spatial discretizations.

REFERENCES

Andersen, A. (1996). ‘A comparative study of conventional and tip-fin propeller performance’. Proceedings of 21st Symposium on Naval Hydrodynamics, Trondheim, Norway.

Arndt, R. E. A., Song, C. C. S., Kjeldsen, M. & Keller, A. (2000). ‘Instability of partial cavitation: a numerical/experimental approach’. Proceedings of 23rd Symposium on Naval Hydrodynamics, Val de Reuil, France.

Arndt, R. E. A. (2010). ‘Sheet/Cloud cavitation revisited’. Proceedings of 13th International Symposium on Transport Phenomena and Dynamics of Rotating Machinery, Honolulu, HI, USA.

Bensow, R. E. & Bark, G. (2010). ‘Simulating cavitating flows with LES in Openfoam’. Proceedings of 5th European Conference on Computational Fluid Dynamics, Lisbon, Portugal.

Du, W. & Kinnas S. (2018). ‘Coupling a numerical optimization technique with a panel method or a vortex lattice method to design cavitating propellers in non-uniform inflows’. Proceedings of 10th International Symposium on Cavitation, Baltimore, MD, USA.

Ganesh, H., Makiharju, S. A. & Ceccio, S. L. (2017). ‘Bubbly shock propagation as a mechanism of shedding in separated cavitating flows’. Journal of Hydrodynamics **29**(6), pp.907-916.

Paik, K., Park, H. & Seo, J. (2013). ‘URANS simulations of cavitation and hull pressure fluctuation for marine propeller with hull interaction’. Proceedings of 3rd International Symposium on Marine Propulsors, Tasmania, Australia.

Reisman, G. E., McKenney, E. A. & Brennen, C. E. (1994). ‘Cloud cavitation on an oscillating hydrofoil’. Proceedings of 20th Symposium on Naval Hydrodynamics, Santa Barbara, CA, USA.

Shin, K. W., Andersen, P. & Mikkelsen, R. (2011). ‘Cavitation simulation on conventional and highly-skewed propellers in the behind-hull condition’. Proceedings of 2nd International Symposium on Marine Propulsors, Hamburg, Germany.

Shin, K. W. (2014). ‘Cavitation simulation on Kappel propeller with a hull wake field’. Proceedings of 16th Numerical Towing Tank Symposium, Marstrand, Sweden.

Shin, K. W., Regener, P. B. & Andersen, P. (2015). ‘Methods for cavitation prediction on tip-modified propellers in ship wake fields’. Proceedings of 4th International Symposium on Marine Propulsors, Austin, TX, USA.

Shin, K. W. & Andersen, P. (2015). ‘CFD analysis of cloud cavitation on three tip-modified propellers with systematically varied tip geometry’. Proceedings of 9th International Symposium on Cavitation, Lausanne, Switzerland.

Shin, K. W. & Andersen, P. (2016). ‘CFD study on effective wake of conventional and tip-modified propellers’. Proceedings of 31st Symposium on Naval Hydrodynamics, Monterey, CA, USA.

Vaz, G., Hally, D., Huuva, T., Bulten, N., Muller, P., Becchi, P., Herrer, J. L. R., Whitworth, S., Mace, R. & Korsstrom, A. (2015). ‘Cavitating flow calculations for the E779A propeller in open water and behind conditions: code comparison and solution validation’. Proceedings of 4th International Symposium on Marine Propulsors, Austin, TX, USA.

Tip Vortex Cavitation Simulation of a Propeller in a Gate Rudder® System

Naz Yilmaz[1*], Serkan Turkmen[2], Batuhan Aktas[1],
Patrick Fitzsimmons[1], Noriyuki Sasaki[1], Mehmet Atlar[1]
[1]Department of Naval Architecture, Ocean and Marine Engineering, University of Strathclyde, Glasgow G4 0LZ, UK
[2]School of Marine Science and Technology, University of Newcastle, Newcastle upon Tyne NE1 7RU, UK

Abstract: The GATE RUDDER® system is a novel propulsion arrangement or Energy Saving Device (ESD) inspired by the new concept of elementary propulsive efficiency and its optimization in a ship's wake to recover more energy. The performance of a GATE RUDDER® system in the hull wake, therefore, is important not only for the efficiency but also from the cavitation, noise and vibration point of view. The World's first gate rudder was installed on a 2,400 GT container ship in 2017 in Japan. By using the data associated with this vessel and other model test data with different ships, this paper explores the differences on the efficiency and cavitation performance of a conventional rudder and propeller system with the GATE RUDDER® system using Experimental and Computational Fluid Dynamics (EFD and CFD) approaches. There is specific emphasis on the accurate simulation of the tip vortex cavitation of the propeller in both rudder systems which has been modelled by using Yilmaz's recently developed advanced adaptive mesh refinement approach. The results of the CFD simulations are compared with the results of the model tests conducted in the Emerson Cavitation Tunnel and the full-scale experiences with the above-mentioned container vessel as discussed in the paper.

Keywords: Gate Rudder, Propeller Cavitation, Cavitation Tunnel Tests, Tip Vortex Cavitation, CFD, Adaptive Mesh Refinement

1 INTRODUCTION

In order to improve the energy efficiency of ships, and hence to achieve targeted carbon emission (e.g. EEDI regulations by IMO), various technological and operational solutions have been studied by the maritime industry. These solutions recently included the developments of various novel Energy Saving Devices (ESD) applied on the underwater hull and renewable energy saving devices onboard, using alternative fuel sources and sophisticatedly optimized hull forms. Such ESD solutions still, developed at model scale have their challenges to prove their effectiveness on full-scale ships. Although many ESDs already exist and some new types are still being introduced, their effectiveness, especially in full-scale, need to be investigated and proven further by using preferably Computational Fluid Dynamics (CFD) and Experimental Fluid Dynamics (EFD) methods under operational conditions. This is not only at the development stage of these devices but also at the selection stage for a particular ship type.

The selection of an effective ESD technology for a ship amongst the wide range of solutions may be made based on the personal preference of the so-called experts of the company, often due to a bias against a particular type of technology, rather than using a sophisticated tool. However, the selection of such devices must be carried out using scientifically proven methods, preferably by using the CFD and supporting EFD approaches as well as by conducting a techno-economic feasibility assessment of the selected technology on a particular marine system, taking into consideration the payback time, maintenance requirements and expenses, retrofitting, etc., for a given operational profile.

Within the framework of a newly introduced ESD system, the main purpose of this study is to utilize the EFD and CFD methods to demonstrate the effectiveness of a novel ESD, which is called the "GATE RUDDER®" system, with a specific emphasis on the cavitation and noise performance of this ESD in comparison to a conventional rudder-propeller system.

The GATE RUDDER® system is a new and innovative ESD technology for ships to propel and steer them more efficiently. As opposed to a conventional rudder, which is behind a propeller, the GATE RUDDER® has two rudder blades with asymmetric sections which are located alongside the propeller, and each blade can be controlled independently. The two rudder blades, encircling the propeller at the top and sides, provide a duct effect and hence produce additional thrust as opposed to the additional drag of a conventional rudder behind the propeller. See Figure 1 for comparison of the conventional rudder and the GATE RUDDER® system on two sister vessels. The independent control of the two rudder blades also provide effective control of the propeller slipstream and hence steering, Sasaki et al (2015). Thus the GATE RUDDER® system presents not only more propulsive

---

* *Corresponding author e-mail: naz.gorener@strath.ac.uk*

efficiency but also higher maneuverability. In addition to these two major advantages of the GATE RUDDER® system, there are other claimed performance superiorities of this system, including reduced vibrations, as reported through full-scale performance trials (Sasaki et al., 2018), and which may be associated with the reduced cavity volume on the blades as well as the tip vortex in the propeller slipstream. These effects require investigations.

In order to cast light on the cavitation performance of the GATE RUDDER® system, this paper investigated the cavitation performance of the GATE RUDDER® system in comparison with that of a conventional rudder-propeller system, for the first time, by using the CFD and EFD approaches. The rudder systems used in this investigation for the conventional and GATE RUDDER® arrangements are based on the two sister vessels recently built in Japan and have been in service since 2016 (conventional rudder-propeller system) and 2017 (GATE RUDDER® system). The cavitation tunnel tests for the EFD investigations were conducted in the Emerson Cavitation Tunnel at the University of Newcastle upon Tyne.

Following this introductory section, the paper begins with the background to the GATE RUDDER® concept and details of the rudder and propeller arrangements of the two sister ships as presented in §2. The details of the rudder and propeller models, cavitation tunnel test set-up, and test conditions and procedures, which formed the basis for the EFD investigations, are presented in §3. The details of the CFD simulations of the propeller with the conventional and GATE RUDDER® in the cavitating conditions are presented in §4 to form a basis for the EFD investigations. This is followed by the presentation and discussion of the comparative results for the cavitation simulations based on the CFD and EFD approaches for the Conventional and GATE RUDDER® system in §5. Finally, the concluding remarks with future work are presented in §6.

2 GATE RUDDER ® CONCEPT

The rudder is one of the resistance components of the ship. The main purpose of the GATE RUDDER® propulsion system is to replace the resistance source (of a conventional rudder system) with a thrust source (like a duct) to achieve higher propulsive efficiency. With this idea, the rudder may become an ESD placed alongside the propeller instead of behind the propeller to simulate the duct effect of a ducted propeller but with additional maneuverability capability by independently moving the two rudder blades to control the propeller slipstream in contrast to the nozzle of a fixed ducted propeller. The GATE RUDDER® arrangement also reduces the viscous energy loses created by the hull boundary layer and the wake flow more effectively than the traditional rudder-propeller arrangement, Sasaki et al (2018).

In a similar way, although many ideas and applications exist to combine a rudder and a propeller, such as podded propulsion systems, steerable ducted propellers and so on (e.g. Carlton, 2012), these propulsion systems generally work with limited applications in the full scale without high propulsive performances and maneuverability abilities. Whereas the GATE RUDDER® propulsion system has a flexibility that can be applied to a new design as well as a retrofit system to almost many types of conventional vessel where the conventional rudder-propeller system is used.

As reported in Sasaki et al (2018) the GATE RUDDER® propulsion system originated in Japan and has been further developed in the UK through CFD and EFD studies since 2014. Based on these developments, the first GATE RUDDER® propulsion system was applied on a 2400 GT container ship and the full-scale sea trials were carried out on November 2017 in Japan. The performance gain expected from the application of this novel ESD was demonstrated by the comparison of these trial results with of the results of her sister container vessel of the similar size and characteristics but fitted with a conventional flap rudder-propeller system that was delivered one year before. Both vessels currently operate in the same route in Japan between Hokkaido and Yokohama. Figure 1 shows the propeller and rudder arrangement of these two sister vessels, which are indicated as Ship A (with the conventional rudder-propeller system) and Ship B (with the GATE RUDDER® propulsion system), respectively while Table 1 presents their main particulars.

The analyses of the sea trials data conducted in the same geographic region of Japan with the two vessels within a year interval and those of the voyage data on the same service routes indicated that the container vessel with the GATE RUDDER® system can save abt. %14 more fuel over the vessel with the conventional rudder-propeller system. It was noticed that 8-10% of this attractive energy saving was confirmed by the CFD and EFD studies while the remaining saving can be attributed to the scale-effect associated with the powering estimation with the GATE RUDDER® system as demonstrated in recent studies, (Sasaki et al., 2018).

Based on the experiences during the sea trials and following onboard experiences of the both vessels' captains during service, it was noticed that the vessel with the GATE RUDDER® experienced less propeller excited vibrations with quieter aft end characteristics compared to those of the vessel with the conventional rudder-propulsion system. Based on these findings, as the main objective of this paper, it was decided to explore the cavitation and noise characteristics of the two propulsion systems using the detailed CFD and EFD investigations based on the aft end arrangement and operating conditions of these two sister vessels and by using a state-of-the-art commercial CFD tool and model tests conducted in a medium-size cavitation tunnel with simulated wakes.

Table 1. Main Particulars of two sister ships.

Vessel particulars	Ship A (Conventional Rudder)	Ship B (GATE RUDDER®)
Loa (m)	111.4	111.4
Lpp (m)	101.9	101.9
B (m)	17.8	17.8
D (m)	8.5	8.5
d (m)	5.24	5.25
Main Engine	3309kW/220rpm	3309kW/220rpm
Prop. Dia (m)	3.48 (CPP)	3.30 (CPP)
Draft of Sea Trial (m)	4.30	4.30

Figure 1. Conventional Flap-Rudder (Top) vs. GATE RUDDER® (Bottom).

3 CAVITATION TUNNEL TESTS

3.1 Cavitation Tunnel and test set-up

Although comprehensive experimental tests were conducted with a 2m model during the GATE RUDDER® developments in towing tanks and circulation channels, which involved powering, maneuvering and seakeeping, no cavitation tunnel tests were conducted until this study explored the comparative cavitation and underwater radiated noise (URN) characteristics of the GATE RUDDER® propulsion system.

The aft end and propeller arrangements of the conventional rudder (without the flap) and GATE RUDDER® systems were represented with the model rudders and propellers of the two vessels with a scale ratio of 13.2 and fitted downstream of the H33 K&R dynamometer of the Emerson Cavitation Tunnel (ECT) of Newcastle University. ECT is a medium-size facility with a measuring section of 3.1m x 1.21m x 0.8m (L x B x H) with other details as shown in Figure 2 and reported in (Atlar, 2011).

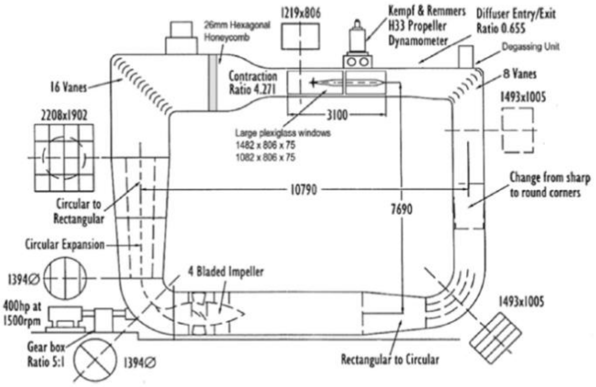

Figure 2. Emerson Cavitation Tunnel.

While the measuring section of the ECT usually allows a reasonable size dummy hull with a properly scaled aft end arrangement, in this investigation, a simple wake simulation arrangement was used due to time restrictions. In this arrangement, the wake of the H33 dynamometer was combined with the wake of a vertical plate of 0.85m length and 0.02m thickness which was placed between the trailing edge of the dynamometer strut and the model propellers with a diameter of 250mm, as shown in Figure 3. The wake plate was also covered with a sand paper of grit P36 to trip the wake flow in turbulent regime.

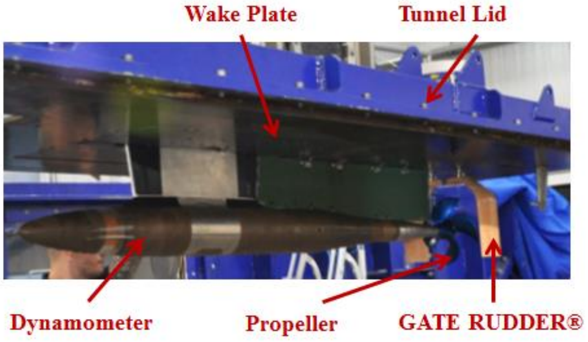

Figure 3. Test set-up with GATE RUDDER® at ECT including wake plate.

During the tests, propeller thrust and torque as well as the shaft rpm were recorded a data collection rate of 100Hz. The URN characteristics were recorded by using a B&K 8103 miniature hydrophone located inside the tunnel in a streamlined strut aligned with the tunnel flow. The cavitation observations were recorded by using moving and still cameras from the side and bottom windows of the ECT for each test condition as well as the oxygen content and temperature of the tunnel water.

3.2 Propeller and Rudder Geometries

The model propeller and rudder geometries for the conventional rudder and GATE RUDDER® propulsion systems were provided by KAMOME Propeller Co, LTD. The same Controllable Pitch Propeller (CPP) model of 250mm diameter with four-blades and high skew was used behind the conventional rudder and GATE RUDDER® systems as shown in Figure 4.

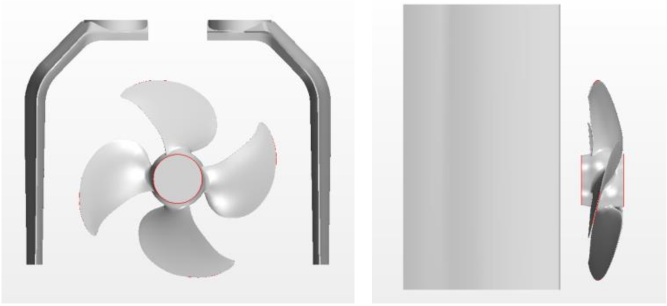

Figure 4. GATE RUDDER® arrangement (Left) and Conventional Rudder arrangement (Right)

3.3 Test Conditions

The cavitation tunnel tests were conducted at 5 different test conditions that represented the equivalent full-scale operational conditions of the container ships. Table 2 presents the test conditions with advance velocity ratio (*J*), tunnel speed (*V*), revolution speed (*n*), tunnel (P_{tun}) and vacuum pressure (P_{vac}) and tunnel temperature (*T*) parameters that have been set during the tests.

Table 2. Test Conditions.

Test Conds'	***J***	***V***	***n***	***Ptun***	***Pvac***	***T***
		m/s	rpm	mmHg	mmHg	°C
Cond' 1	0.000	0.000	1200	830.7	-200	17.1
Cond' 2	0.154	0.925	1438	830.7	-200	17.1
Cond' 3	0.260	1.560	1438	830.7	-200	17.1
Cond' 4	0.501	3.000	1438	830.7	-200	17.1
Cond' 5	0.494	3.970	1925	830.7	-400	17.1

The tests were first conducted with the conventional rudder-propeller system arrangement for the above stated conditions and this was followed with the GATE RUDDER® propulsion set-up for the same conditions. During the tests the associated test data for the propeller performances, cavitation observations and URN were collected with each test set-up and analyzed for the comparisons of the data between the conventional rudder propeller and GATE RUDDER® propulsion system as well as to support the CFD studies.

4 COMPUTATIONAL FLUID DYNAMICS (CFD) INVESTIGATIONS

Although 5 different operating conditions were simulated during the cavitation tunnel tests, only one cavitating condition, which produced the strongest tip vortex cavitation (Condition 5), has been presented in the CFD simulations as given in Table 3.

Table 3. EFD and CFD Conditions.

Conditions	J	V	n	σ_n
	[-]	[m/s]	[rpm]	[-]
EFD Condition 5	0.494	3.970	1925	1.714
CFD Condition 5	0.500	3.000	1440	1.730

In Table 3 J is the advance velocity ratio (or coefficient) of the propeller given by Equation 3, V is the tunnel in-flow speed, n is the propeller shaft rotational speed and σ_n is the propeller cavitation number based on the shaft speed as described in Equation 2.

4.1 Numerical Method

The CFD simulations for the two propulsion arrangements and for the above described test condition were carried out by using in the well-known commercial CFD software, STAR-CCM+ for marine applications. For the cavitation simulation, two fluids (water and vapour) medium, which are described in the software, and the Volume of Fluid (VOF) method was used for multiphase modelling.

Based on the experience with the rotational fluid domains, for describing the effect of the propeller rotation, the overset mesh method was preferred instead of the sliding mesh approach to be able to simulate the tip vortex cavitation in combination with the rudder and hence to eliminate the data transfer problems between the rotating and stationary domain.

For turbulence modelling, Large Eddy Simulation (LES) turbulence models were preferred for cavitation simulations. In contrast to the Reynolds Average Navier-Stokes (RANS) model, scale-resolving simulations are able to solve the large scales of turbulence and model small-scale motions. For scale-resolving simulations, there are two approaches involving Detached Eddy Simulation (DES) and LES which are available in STAR-CCM+ (STAR-CCM+ User Guide, 2018). LES turbulence model has been preferred more commonly for simulating complex flows such as cavitation, especially for the tip vortex type of cavitation.

The Schnerr-Sauer cavitation model, which is based on Rayleigh-Plesset equation, was also used for this study to simulate the cavitation. The bubble growth rate in the Schnerr-Sauer model (Schnerr & Sauer, 2001) was estimated by using Equation 1 as follows,

$$(\frac{dR}{dt})^2 = \frac{2}{3}(\frac{p_{sat} - p_\infty}{\rho_l}) \qquad (1)$$

The cavitation number based on the rotational speed of the propeller shaft is defined as follows.

$$\Sigma_n = \frac{p - p_{sat}}{0.5\rho_l (nD)^2} \qquad (2)$$

where p is the tunnel pressure, p_{sat} is the saturation pressure of water, ρ_l is the density of the fluid, n is the shaft speed and D is the diameter of the propeller.

The advance velocity ratio can be calculated using Equation 3.

$$J = \frac{V_A}{nD} \qquad (3)$$

where V_A is the advance velocity of fluid. Thrust and torque coefficient of the propeller is calculated as follows.

$$K_T = \frac{T}{\rho n^2 D^4} \qquad (4)$$

$$K_Q = \frac{Q}{\rho n^2 D^5} \qquad (5)$$

where T and Q are thrust and torque values of the propeller respectively and ρ is the density of water. Using K_T and K_Q, the propeller open water efficiency is calculated using Equation 6.

$$H_0 = \frac{J}{2\pi}\frac{K_T}{K_Q} \qquad (6)$$

4.2 Computational Domain Preparation

As stated earlier, for modelling of the rotation effect, the overset mesh method was used to eliminate the data transfer problems of the sliding mesh approach that may occur between the rotating and stationary domains during the stretching tip vortices from the tip of the propeller blades through the rudder geometry. Within the scope of this study, two different flow domains were prepared for the cavitation simulations, which are associated with the conventional rudder and the GATE RUDDER® configurations. Accordingly, two regions were prepared as the background and overset regions for the simulations of both propulsion systems.

Figure 5 presents the flow domain has been prepared for cavitation simulations of the GATE RUDDER® system including the background and overset mesh regions.

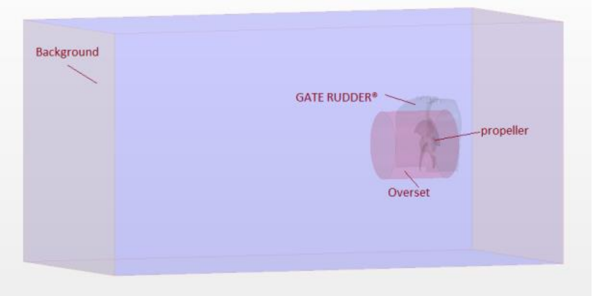

Figure 5. Computational Flow Domain for GATE RUDDER® system.

4.3 Mesh Generation

4.3.1 Sheet Cavitation

A suitable mesh arrangement was generated for each computational case for the sheet cavitation simulations on the propeller blades. While a 0.006D surface size for the mesh generation was applied on the propeller surfaces in general, smaller surface size with a 0.004D was preferred for a volumetric control around the propeller tip regions with a cylinder geometry.

Figure 6 presents the generated mesh for sheet cavitation simulations for the conventional rudder-propeller and GATE RUDDER® propulsion systems, respectively.

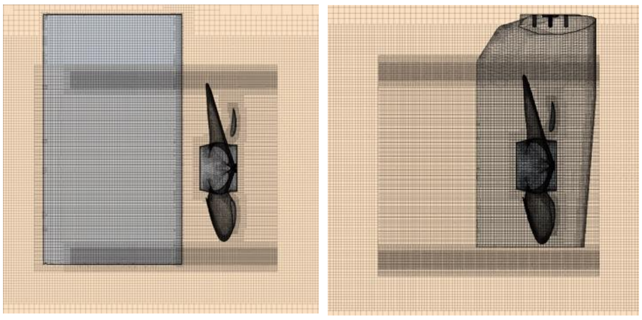

Figure 6. Generated mesh for sheet cavitation Conventional Rudder-propeller system (Left); GATE RUDDER® Propulsion system (Right).

4.3.2 Tip Vortex Cavitation

Although the sheet cavitation could have been simulated successfully using the mesh arrangement, which is shown in Figure 6, it was expected that the existing mesh and analysis methods were not sufficient to capture the tip vortex cavitation, and to predict the propeller performance accurately, as reported in the open literature [e.g. Viitanen & Siikonen, 2017, Lloyd et al., 2017, Shin & Anderson, 2018]

For capturing a sudden pressure drop and cavity bubbles in a propeller slipstream, an adaptive mesh refinement approach has been developed by the leading author of the present paper. The new mesh refinement approach, which is called MARCS (Mesh Adaption Refinement for

Cavitation Simulations), has been presented using various standard test propellers such as INSEAN E779A, PPTC and the Princess Royal propellers in the past (e.g. Yilmaz et al, 2018). This method was also applied in this study to simulate the tip vortex cavitation for the both propulsion systems.

In the MARCS procedure, the mesh was refined only in the region where the tip vortex cavitation may occur in propeller slipstream. Before the application of this procedure, the simulation was run and sheet cavitation was simulated using the coarse mesh arrangement as shown in Figure 6. At the end of this simulation, using the existing solution, the q-criterion limit was determined by creating a threshold region in the STAR-CCM+ software as shown in Figure 7 (on Left).

In the cavitation simulations, the volume fraction of the vapour indicates the regions of the cavity volume where the absolute pressure drops below the saturated vapour pressure of the water, thus demonstrates the cavitating volume. In the meantime, a region was prepared by using the q-criterion to define the zone where the vortices have been developed, thus generating the blue region as shown in Figure 7 (Left). The combination of the both regions provides a specification of the volumetric trajectory on which an adaptive mesh generation mechanism for capturing the sudden pressure drop region and tracking the tip vortices in the propeller slipstream rather effectively and accurately.

Within the framework of the MARCS approach, a field function was created to generate finer meshes where the q-criterion was above 20000s^{-2}. Having generated the finer meshes, a mesh refinement table, which included the coordinates of each cell needed to be refined and their surface sizes, was prepared automatically by STAR-CCM+ using the suitable field functions to generate meshes. Figure 7 presents the isosurface of the q-criterion above 20000s^{-2} (Left) and generated mesh (Right) using the refinement table that was prepared by using the q-criterion trajectory.

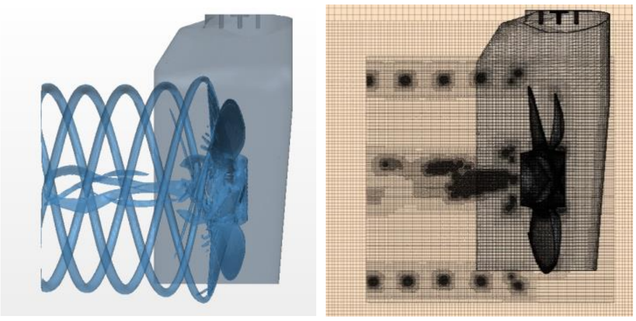

Figure 7. Generated Mesh for Tip Vortex Cavitation (Left; Q-Criterion > 20000s^{-2}, Right; Mesh).

In order to familiarize the reader with the further details of the applied MARCS approach, a flowchart is provided in Figure 8 to demonstrate the sequential steps of this approach.

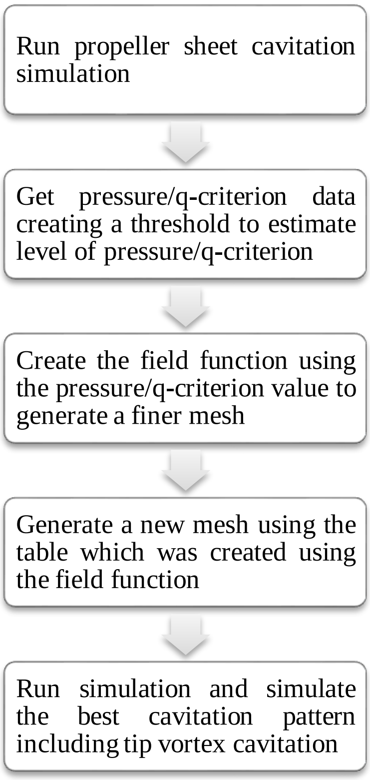

Run propeller sheet cavitation simulation

Get pressure/q-criterion data creating a threshold to estimate level of pressure/q-criterion

Create the field function using the pressure/q-criterion value to generate a finer mesh

Generate a new mesh using the table which was created using the field function

Run simulation and simulate the best cavitation pattern including tip vortex cavitation

Figure 8. Flow chart summarizing MARCS approach.

5 RESULTS AND DISCUSSION

As stated earlier, although 5 different operating conditions were simulated during the cavitation tunnel tests, which are shown in Table 2, only one cavitating condition, which produced the strongest tip vortex cavitation (Condition 5), was simulated in the CFD simulations as given in Table 3, for the both propulsion systems.

Table 4 shows the comparative propeller performance characteristics (*ie* K_T, K_Q *and* η_o) of the both propulsion systems based on the CFD simulations (analysis) and cavitation tunnel test measurements (i.e. EFD analysis).

Table 4. EFD and CFD Results Comparisons between conventional and GATE RUDDER®.

Conditions		K_T	$10K_Q$	η_0
		[-]	[m/s]	[rpm]
Conventional Rudder	EFD	0.2156	0.2910	0.5835
	CFD	0.2071	0.2717	0.6067
	Deviation	3.9%	6.6%	-4.0%
GATE RUDDER®	EFD	0.1716	0.2497	0.5415
	CFD	0.1712	0.2374	0.5741
	Deviation	0.2%	4.9%	-6.0%

As shown in Table 4, although the CFD predictions for the performance of the propeller shows a good agreement with the experiments (EFD), especially for the GATE RUDDER® system simulations in terms of K_T, for which the deviation is less than 1%, K_Q could only be predicted within a %5 and %6.6 deviation for the GATE RUDDER® and the conventional rudder system, respectively. The deviation in the K_Q predictions can be related to the geometrical differences, the presence of the wake plate and the similar (but not exact) conditions between the EFD and CFD predictions due to the time restrictions of this study that requires further fine tuning and investigations.

As far as the CFD predicted cavitation patterns are concerned, Figure 9a and Figure 9b shows the sheet cavitation and tip vortex cavitation, respectively, in comparison for the conventional rudder-propeller system (Left) and GATE RUDDER® propulsion system (Right).

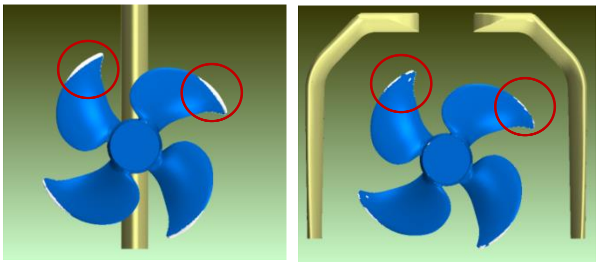

Figure 9a. Sheet Cavitation Comparisons (CFD) Conventional Rudder (Left); GATE RUDDER® (Right).

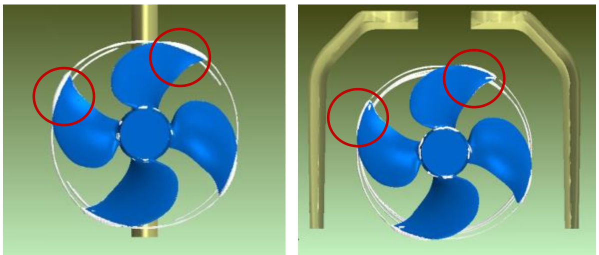

Figure 9b. Tip Vortex Cavitation Comparisons (CFD) Conventional Rudder (Left); GATE RUDDER® (Right).

As clearly shown in Figure 9a and 9b, not only the sheet vortex extent and volume on the blades but also the tip vortex volume and strength was reduced on the GATE RUDDER® system (Right) compared to the conventional rudder-propeller system (Left). The reduction on the cavitation volumes associated with the GATE RUDDER® arrangement is also the indication for the reduced propeller induced vibrations and URN levels compared to the conventional rudder-propeller system.

The comparative cavitation patterns for the conventional rudder-propeller system and GATE RUDDER® propulsion system, as observed from the cavitation tunnel tests (Left) and from the CFD simulations (Right), are presented in Figure 10a and 10b, respectively.

As observed during the cavitation tests with the conventional rudder-propeller system, a strong sheet cavity was covering almost a 20% of each blade surface and more accentuated at the top dead center (i.e. wake shadow region), as shown in Figure 10a (Left). Due to the effect of the wake plate, the deformation of the tip vortices at the same region was also observed and this deformation was combined with the effect of the rudder in downstream resulting in the bifurcation of the tip vortex at the rudder leading edge. In spite of the accentuated sheet cavity dynamics at the wake shadow and deformation of the tip vortex at the rudder leading edge, the tip vortex cavitation was transported in downstream through the propeller slipstream and the rudder without losing its strength.

The above described cavitation pattern and part of the cavity dynamics can be also observed in the CFD simulations when once compares the left and right illustrations in Figure 10. The dynamics resulting from the wake plate will not be reflected on the results due to the time restrictions.

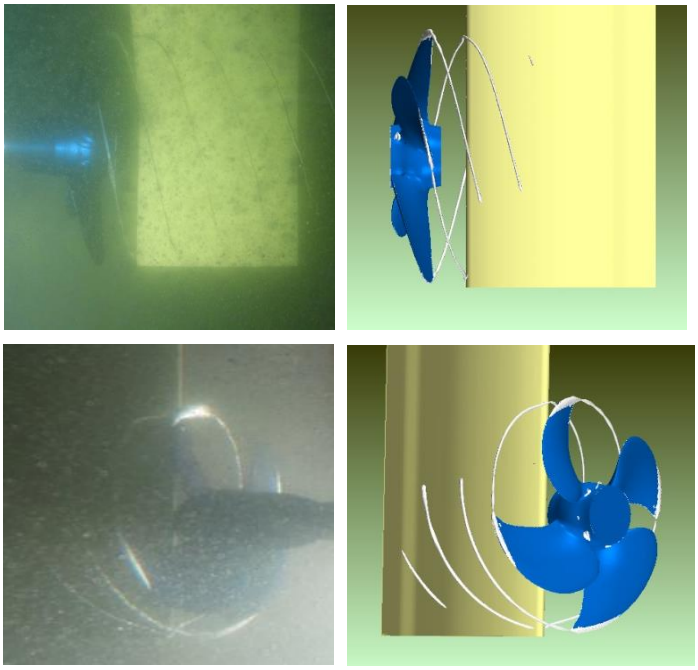

Figure 10a. Cavitation Comparisons for Conventional Rudder-propeller system

(Left: EFD from tunnel tests; Right; CFD predictions).

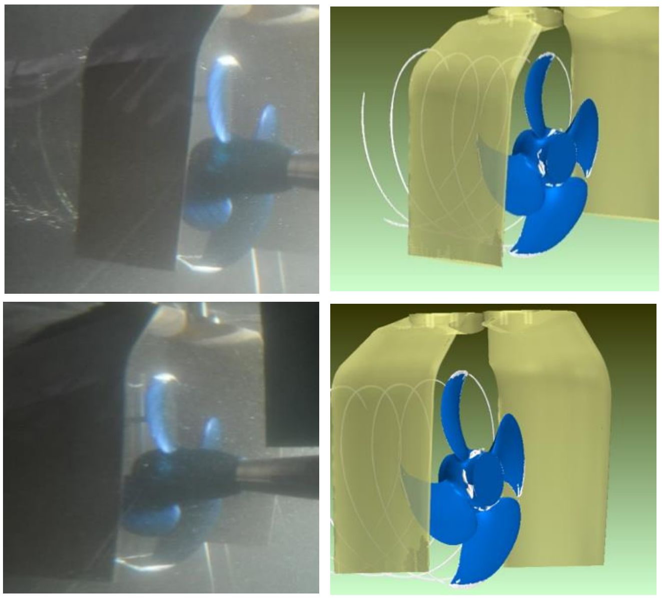

Figure 10b. Cavitation Comparisons for GATE RUDDER® Propulsion system (Left: EFD from tunnel tests; Right; CFD predictions).

On the other hand, the cavitation observations with the GATE RUDDER® arrangement in the tunnel indicated that the sheet cavitation on the blades was developed at a lesser extent, about 15% of each blade, in comparison to the conventional rudder case, and it was combined with a reduced strength of the tip vortex cavitation as shown in Figure 10b. In contrast to the observations with the conventional rudder-propeller arrangement, the tip vortex cavitation developed on the GATE RUDDER® propeller had no deformation or bifurcation, as expected, extending smoothly in the downstream at a reduced strength. These patterns and cavity dynamics were also captured well with the CFD simulations, thanks to recently developed MARCS procedure.

6 CONCLUDING REMARKS

The investigations on the cavitation performance of a newly introduced novel ESD, the GATE RUDDER®, was conducted by using the CFD and EFD approaches in comparison with the cavitation performance of a conventional rudder-propeller system. The investigation aimed to shed a light on the reduced hull vibrations and quieter aft end performance experienced with the world’s first GATE RUDDER® system fitted on a container vessel compared to its sister ship with the conventional rudder-propeller system. The investigation also aimed to explore the cavitation performance of this novel ESD by using a state-of-the-art CFD tool and associated MARCS procedure validated by the cavitation tunnel tests for the first time. The investigations conducted so far have indicated that:

- The model test data and supporting CFD predictions are the first information reported to on the cavitation performance of the GATE RUDDER® system in comparison with that of a conventional rudder-propeller system.
- Yilmaz’s recently developed new adaptive mesh refinement technique (MARCS) successfully captured the cavitation performance characteristics of the GATE RUDDER® as well as the conventional-rudder, especially with the interaction of the tip vortices with the rudder arrangements, based on the comparison with the EFD results.
- Based on the EFD and CFD investigations conducted in the model-scale with a relatively simple hull wake simulation arrangement, the GATE RUDDER® propulsion system can display reduced sheet and tip vortex volumes and variations compared to those of the conventional rudder-propeller arrangement. No observation was made with the GATE RUDDER® for the deformed and hence bifurcated tip vortex at the rudder leading edge of the conventional rudder and hence lesser cavity dynamics.
- Although the above findings are based on the model-scale investigations with relatively simple hull wake arrangements, they may strongly support the lesser vibrations and quieter aft end characteristics of the GATE RUDDER® experienced onboard by the ship crew.

There is no doubt that the results in this paper presents only the preliminary GATE RUDDER® investigations and hence require further work regarding: i) More detailed CFD modelling of the current test case; ii) More sophisticated or representative modeling of the model ship arrangements, preferably using a full hull model in a larger test facility; iii) Further CFD simulations at the full-scale. Regarding further work (i) we will be improving our CFD model in terms of the propeller hydrodynamic performance and cavitation patterns by using the exact tunnel details by including the wake plate arrangement that could not be included due to the time restrictions of this paper, as shown in Figure 11.

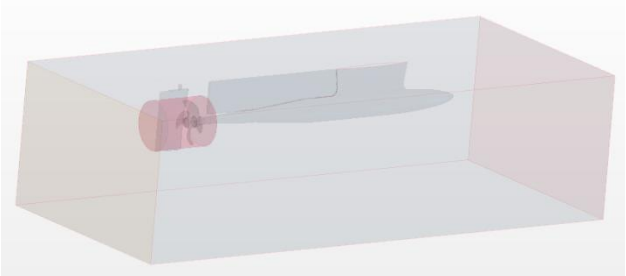

Figure 11. Flow domain for the new CFD simulations including dynamometer and wake plate geometries.

ACKNOWLEDGEMENTS

The principal author of this paper is sponsored by the Turkish Ministry of Education during this study. The access provided to High Performance Computing for the West of Scotland (Archie-West) thorough EPSRC grant no. EP/K000586/1 is gratefully acknowledged. The authors are also grateful to KAMOME Propeller Co, Ltd. for providing the model propeller and rudders as well as supporting the tunnel experiments at ECT.

REFERENCES

Atlar, M. (2011). “Recent upgrading of marine testing facilities at Newcastle University”. In: Proceedings of the 2nd International Conference on Advanced Model Measurement Technologies for the Maritime Industry (AMT’11). Newcastle upon Tyne, UK.

Carlton, J. (2012). “Marine propellers and propulsion” 3rd Edition, 2012.

Lloyd, T., Vaz, G., Rijpkema, D., Reverberi, A., (2017), Computational fluid dynamics prediction of marine propeller cavitation including solution verification, Fifth International Symposium on Marine Propulsors smp’17, Espoo, June 2017.

Sasaki, N., Atlar, M., and Kuribayashi, S. (2015) “Advantage of twin rudder system with asymmetric wing section aside a propeller” Journal of Marine Science and Technology.

Sasaki, N., Kuribayashi, S., Atlar, M. (2018). “GATE RUDDER ®”, 3rd International Symposium on Naval Architecture and Maritime, 24-25 April, Istanbul, Turkey.

Schnerr, G. H., Sauer, J. (2001). “Physical and Numerical Modeling of Unsteady Cavitation Dynamics”, ICMF-2001, 4th International Conference on Multiphase Flow, New Orleans, USA, May 27-June 1, 2001

Shin, W. K., Andersen, P., (2018), “CFD Analysis of Propeller Tip Vortex Cavitation in Ship Wake Fields”, The 10th International Symposium on Cavitation (CAV2018), Baltimore, Maryland, USA, 14-16 May 2018.

STAR-CCM+ User Guide, 2018

Viitanen, V, M, Siikonen, T., (2017), Numerical Simulation of Cavitating Marine Propeller Flows, 9th National Conference on Computational Mechanics, MekIT’17.

Yilmaz, N., Atlar, M., Fitzsimmons, A., P. (2018). “An Improved Tip Vortex Cavitation Model for Propeller-Rudder Interaction”, The 10th International Symposium on Cavitation (CAV2018), Baltimore, Maryland, USA, 14-16 May 2018.

A. Yücel Odabaşı Colloquium Series
3^{rd} International Meeting - Progress in Propeller Cavitation and its Consequences:
Experimental and Computational Methods for Predictions
15^{th} – 16^{th} November 2018, Istanbul, Turkey

A Study on Cavitation Erosion Resistance of Marine Propeller Materials, Using a Water Jet Test Rig

Onur Usta[1*], Cagatay Sabri Koksal[1], Emin Korkut[1]
[1]Istanbul Technical University, Faculty of Naval Architecture and Ocean Engineering, 34469 Maslak-Istanbul, Turkey

Abstract: This paper presents an experimental study to investigate the damage caused by cavitation erosion for different propeller materials in various conditions. In order to make accurate and reliable evaluation of the cavitation erosion resistance of materials, the effect of cavitation number on the erosion rate in different test durations was studied using a water jet test rig, which was set-up at Istanbul Technical University (ITU).

Cavitation erosion tests were conducted according to ASTM G-134 standards, to evaluate the cavitation erosion resistance of three propeller materials, such as Cu1 (manganese-bronze), Cu3 (nickel-aluminium-bronze) and Cu4 (manganese-aluminium-bronze) alloys. The erosion tests were performed for three different cavitation numbers by the time durations of 30, 60 and 90 minutes. The erosion rate, which is a function of mass loss per time, was used as an indicator for damage behaviour on the material. Moreover, the maximum pitting depths on the damaged surfaces over time, the erosion intensity values, were obtained by a 3D optical profilometer system.

According to the mechanical properties of investigated samples, such as yield strain, tensile strength, Brinell hardness and Rockwell B hardness; the study showed excellent erosion resisting performance of Cu3 compared to that of Cu4, contrary to expectations. Moreover, according to the test results, the erosion becomes more pronounced with increasing testing duration as well as decreasing cavitation numbers independently of the material.

The ultimate aim of the study carried out is try to explore the similarity of the cavitation erosion formation between the erosion tests in water jet test rig and cavitation tunnels for propellers. This will enable the replication of the propeller material and cavitation characteristics as an erosive indicator in a simpler setup with more number of samples tested.

Keywords: Water jet rig; cavitation erosion test; ASTM G-134 standards; ship propeller materials.

1 INTRODUCTION

Cavitation erosion is perhaps the most detrimental result of the cavitation on propellers, which results in an increase in noise and vibration characteristics, loss of propeller performance as well as high maintenance costs. Many researchers have been investigated this problem to clarify the incipient condition to understand the erosion mechanism or develop a new material which is stronger for resisting to the cavitation erosion.

The cavitation erosion may severely damage propeller blade/s by removing some material from the surface. Therefore it may be very useful to predict erosion in design stage of the propeller to take action against. Then, the prediction of cavitation erosion depends on both fluid flow conditions and material properties. On the fluid side, the key issues are flow aggressiveness and cavitation intensity. On the material side, it depends upon the mechanical properties of the material (Choi et al., 2012).

Evaluation of new materials for their resistance to cavitation erosion needs an extensive effort including both the intensity of the cavitation field and the resistance of the material. In the absence of historical information on the performance of a new material in the target cavitating flow fields, experimental studies in the laboratory offer a convenient means of assessing the cavitation erosion performance (Kim et al., 2014).

The work of estimating the cavitation erosion of different materials began in the 1930's, and then comprehensive studies were carried out using water or different fluids (Sreedhar et al., 2017). The laboratory experimental studies for marine applications aim at obtaining within the required short time periods an evaluation of the cavitation resistance of the new material, whereas in the real field cavitation erosion may occur after a long duration of exposure. For this purposes, several types of cavitation erosion testing methods have been developed. Such accelerated erosion test techniques include: i- the utilization of ultrasonic vibration to generate the cavitation erosion (Zhou and Hammitt, 1983; Hattori et al., 2009; Laguna-Camacho et al., 2013; Dular, 2016; Taillon et al., 2016), ii- cavitation flow loops with strong flow separation or venturi effects (Hammitt, 1966; Baker, 1994; Escaler et al., 2001) and iii- cavitating (water) jets (March, 1987;

* *Corresponding author e-mail: onurusta@itu.edu.tr*

Momma, 1991; Momma and Lichtarowicz, 1995; Soyama and Asahara, 1999; Soyama and Kumano, 2002; Soyama, 2005; Choi et al., 2012; Franc et al., 2012; Soyama, 2013; Kim et al., 2014; Hutli et al., 2016; Li et al., 2017; Hutli et al., 2018; Peng et al., 2018). There are also attempts to test model propellers in water tunnels (Pfitsch et al., 2009; Mantzaris, 2015). Some of these techniques are standardized and follow the American Society for Testing and Materials (ASTM) Standards (ASTM Standard G134-95; 2010; Kim et al., 2014).

Cavitation erosion tests should be carried out according to certain standards in order to have scientific validity and to be reproducible. The ASTM established standard methods using specific conditions under the G134 and G32 (ASTM G32, 2010; ASTM G134-95, 2010; Kim et al., 2014).The ultrasonic technique (ASTM, G32, 2010) and the water jet technique (ASTM G134-95, 2010) are the two most popular laboratory techniques for testing cavitation erosion characteristics of materials.

In ultrasonic cavitation testing, the cavitation is generated by a vibratory device employing a magnetostrictive ultrasonic horn. The high frequency oscillations of the horn, typically tens of kilohertz, induce cyclic formation of very high and very low pressures, which generate high negative tension in the liquid (Kim et al, 2014). The water jet rigs have been used extensively for material testing due to the flexibility these jets provide to control and dial the cavitation intensity. The great advantage of cavitation erosion testing by use of water jet test rig is that the cavitating jet apparatus can simulate different cavitating conditions.

Within the above context, this paper is structured to contain six sections. Following this introduction, section 2 presents a literature review on water jet technique – ASTM G134. Section 3 presents the description of the cavitation erosion test technique, using a water jet rig. Cavitation erosion investigation on aluminium samples (Al-6063) and cavitation erosion tests on three different propeller materials are given in Section 4 and Section 5, respectively. Finally section 6 presents the main conclusions obtained from the study.

2 WATER JET TECHNIQUE – ASTM G134

The idea of using a water jet for an erosion test was first proposed and implemented by Lichtarowicz (1972). Lichtarowicz noted in his study that much more severe erosion would be achieved by water jetting compared to air jet system (Lichtarowicz, 1972; Lichtarowicz, 1979). Yamaguchi and Shimizu (1987) and later Lichtarowicz's Ph.D. student Momma (Momma, 1991) have contributed to the method's involvement in the literature with their successful studies of testing mechanisms and applications. Later, many researchers have used the water jet technique to study the resistance of various materials to the cavitation erosion (Momma and Lichtarowicz, 1995; Soyama and Asahara, 1999; Soyama and Kumano, 2002; Choi et al, 2012; Franc et al, 2012; Soyama, 2013; Hutli et al, 2016; Li et al, 2017; Hutli et al., 2018).

Compared to the ultrasonic horn technique, the cavitation generated by a water jet provides more realistic cavitation bubble clouds than that by ultrasonic horn, with distribution of various size micro bubbles, shear flows with vortices, and dense bubble clouds, which collapse on the sample. By the control of the operating pressure, the jet angle, the stand-off distance and the testing time, either quick erosion for an initial screening or accelerated erosion relevant to the real flows may be obtained (Kim et al., 2014).

Cavitation intensity produced by cavitating jets can be varied in a wide range through the adjustment of the jet velocity, jet diameter, the jet angle, the stand-off distance (Figure 4), and the ambient pressure in which they are discharged (Kim et al, 2014). This flexibility makes a cavitating jet a useful research and testing tool to study parametrically the effect of these variables on the material behaviour. To briefly describe the method, cavitation erosion is formed on the sample by spraying high pressure water from the nozzle to the sample where the nozzle and the sample are placed in a cavitation chamber filled with liquid. Tests are carried out under specified pressure and temperature conditions, using generally tap water.

3 CAVITATION EROSION TESTS WITH WATER JET TECHNIQUE

This section contains the cavitation erosion tests carried out with the high pressure water jet (cavitating jet) system, which has been established in accordance with ASTM G134 standards in Ata Nutku Ship Model Testing Laboratory at Istanbul Technical University.

The test set-up used in this study was inspired by the work of Lichtarowicz and Momma (Lichtarowicz, 1972; Lichtarowicz, 1978; Momma, 1991; Momma and Lichtarowicz, 1995). The three main parameters investigated by the water jet tests were the type of material, cavitation number and exposure time.

The basic test procedure, which was followed, is given below:

(a) Sample was prepared suitably for the sample holder geometry and sample surface was polished up to mirror like surface.

(b) Weight of the sample was measured by an electronic balance and recorded before and after the tests.

(c) Sample surface was scanned using an optical profilometer before and after the tests.

(d) Sample was exposed to the cavitating jet for a predetermined period of time.

(e) The sample was taken out from its holder and carefully dried in a dry environment.

3.1 General Testing Procedure and Test Rig Properties

The test rig satisfies the following requirements to carry out the cavitation erosion experiments:

- To supply a steady flow of liquid at sufficiently high pressure and flow rate to produce a cavitating jet with a wide range of pressure levels.
- To control and measure both the upstream and the downstream pressures.
- To vary and measure the nozzle size.
- To control and measure the temperature.
- To vary and measure the stand-off distance from the nozzle to the target.
- To control exposure time of a cavitating jet even for a few seconds.
- To take the photographs and videos of cavitating jet from a wide range of angles.

A high-pressure plunger pump which can provide 344 bars (5000 psi) pressure with 20 lt/min of water pumping capacity was used to pump the water to the inside of the cavitation chamber. This pump is called as P1. Because the P1 is a one directional pump, an auxiliary pump (P2) that delivers water to the P1 at a flow rate of 20 lt/min was also used.

The cavitation chamber (test chamber) in which the tests were carried out is a cylindrical chamber with a diameter of 225 mm and a length of 260 mm covered with two plexi-glass with thickness of 30 mm. There is a nozzle at which water is sprayed at different speeds, a nozzle holder and the sample holder for holding the sample inside the chamber. The other elements of the water jet tests assembly are the pressure relief valve for adjusting the pressure inside the cavitation chamber, the pressure gauge for monitoring the pressure, the thermometer to control temperature, the barrier functioning as a barrier between the nozzle and the sample named shutter. In addition, the test system consists of a water tank with a capacity of 200 lt. The test rig is presented on the right hand side and the cavitation chamber, which was used for cavitation erosion tests, is presented on the left hand side of Figure 1.

Figure 1 The water jet test rig and the cavitation chamber

Figure **15**2 below shows the water jet test rig scheme.

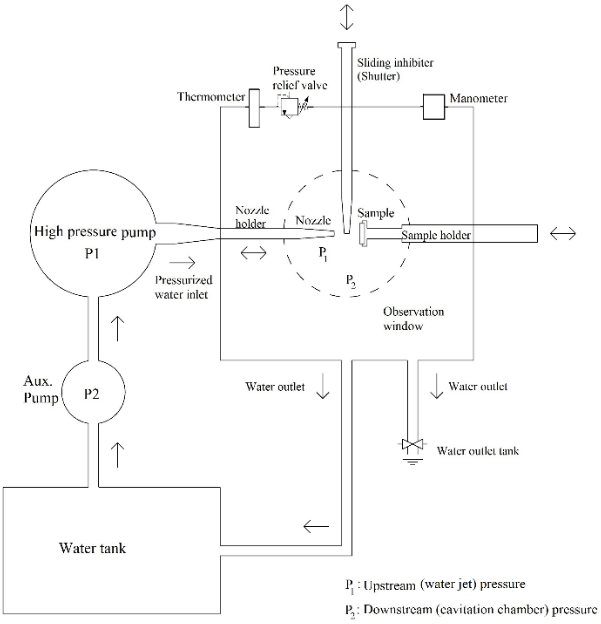

Figure 2 Water jet test rig scheme

During the cavitation erosion tests, the upstream pressure (water jet pressure) P1, and the downstream pressure (the pressure inside the chamber) P2 were measured and varied separately by adjusting a valve at each side. The stand-off distance (S_{off}), which is shown in Figure 1, is defined as the distance from the inlet edge of the nozzle to the target surface. The position of the high pressure inlet pipe with a nozzle at its end and the target holder tube were both adjustable along their common axis. This enabled to change their locations inside the chamber as well as to change the stand-off distance between the nozzle and the sample surface. A photograph from the tests is presented in Figure 1.

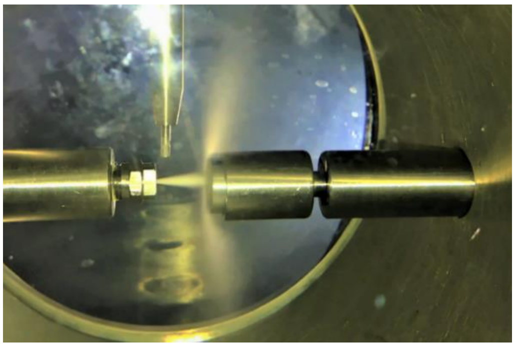

Figure 2 A photograph from cavitation erosion tests (S_{off}=18 mm)

Time duration of the tests was precisely controlled by a shutter mechanism. Before starting the timepiece, the shutter was off positioned. When all the conditions were stable, in other words when the water jet pressure and the pressure inside the chamber are stable, shutter was opened and timepiece was started. The mass of each sample were measured before and after each erosion test, and mass loss, Δm, was defined as the difference between the two values. The samples were measured on an electronic balance

(Model: A&D HR-202 HR-202) with a precision of ±0.01 mg.

3.2 Cavitation Number Definition

A typical cavitation number (σ) given in (1) was modified and introduced for the first time by Lichtarowicz (1979) for cavitating water jet tests as follows:

The cavitation number is a dimensionless parameter derived from the ratio of static and dynamic pressures. If the ratio between the static pressure suppressing the vaporization, cavitation, and the stagnation pressure of water jet generating a vortex as a core of cavitation is defined as the cavitation number (σ), it can be expressed as:

$$\sigma = \frac{P - P_v}{\frac{1}{2}\rho U^2} \tag{1}$$

Where P is the static ambient pressure based on the reference point definition, P_V is the vapour pressure, ρ is the density of water and U is the flow velocity.

In the cavitating jet method, velocity is increased by reducing the pressure using a nozzle. Thus the cavitation number is: (Lichtarowicz 1979; Momma 1995):

$$\sigma = \frac{P_2 - P_v}{P_1 - P_2} \tag{2}$$

Since the long orifice nozzle is used here, the jet is already cavitating from the inlet edge inside the nozzle and the flow velocity is controlled by vapour pressure P_v; not by the downstream pressure P_2.

$$\sigma = \frac{P_2 - P_v}{P_1 - P_2} = \frac{P_2 - P_v}{P_1 - P_v} \tag{3}$$

Then vapour pressure P_V, of water is negligibly small compared to P_1 and P_2 in most cases and so the cavitation number becomes a form of simple pressure ratio;

$$P_v << P_1 \text{ and } P_v << P_2; \quad \sigma = \frac{P_{downstream}}{P_{upstream}} = \frac{P_{chamber}}{P_{water\ jet}} = \frac{P_2}{P_1} \tag{5}$$

3.3 The Stand-Off Distance (S_{off})

The stand-off distance (S_{off}), is defined as the measured distance from the exit of the nozzle to the target surface of the test sample. It is a major parameter in the cavitation erosion tests. Because it determines the extent of cavitation damage on the test material depending on the given parameters (ASTM, 2010).

The optimum stand-off distance was defined as the stand-off distance for which the erosion rate had reached its maximum value. Stand-off distance is shown in Figure 4.

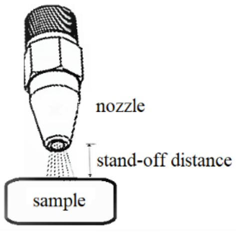

Figure 3 The stand-off distance

4 CAVITATION EROSION INVESTIGATION ON ALUMINIUM SAMPLES

The validation of the established test system was carried out by comparing the results of tests conducted by Momma (Momma, 1991). In Momma's study, cavitation erosion tests of Al-6063 material were carried out using a unit that is very similar to the water jet test rig established within the scope of this paper. In the validation study, the effect of stand-off distance to the cavitation erosion was investigated.

The reason for choosing a weak material such as Al-6063 for cavitation erosion investigation was to shorten the test time for erosion. Using the results obtained from the 30-minute tests in the study, a correlation was established between the stand-off distance and the erosion rate. The principal conditions of the high-pressure water jet tests are given in Table 1.

Table 1 Main conditions of Al-6063 testing with high pressure water jet

Material	Al-6063
t (min)	30
P_2 (bar)	3.6
P_1 (bar)	120
Cavitation number, σ	0.03
S_{off} distance (mm)	5, 8, 10, 12, 18, 15, 20, 25
D_{nozzle} (mm)	1.4

In the validation tests, the effect of 8 different stand-off distance on the cavitation erosion rate was studied. The tests were carried out for 30 minutes each with a water jet pressure of 120 bar and the chamber pressure of 3.6 bar (cavitation number of 0.03). 1.4 mm diameter nozzle was used and the water temperature was 27 (± 3) ° C.

4.1 Cavitation Erosion Rate and Erosion Intensity Prediction Methods

The erosion rate can be used to compare the resistances of different materials to cavitation erosion. The erosion rate is a characteristic value of the resistance of a material to erosion and the erosion rate of each material will be different (Soyama and Kumano, 2002). Momma and Lichtarowicz (1995) defined the erosion rate as;

$$\text{Erosion rate (ER)} = \frac{\text{weight loss (gr)}}{\text{test duration (min)}} = \frac{\Delta m}{\Delta t} \tag{6}$$

where Δm and Δt are the total (cumulative) mass loss and the total cavitation exposure time, respectively. Therefore using the weight loss method (Momma, 1991; Momma and Lichtarowicz, 1995), the erosion rates were calculated in the study.

The second method to compare different materials with regards to resistance to cavitation erosion is erosion intensity. Mottyll and Skoda (2016) used the highest erosion depth on the tested sample by the time as the erosion intensity, given as below:

$$\text{Erosion intencity (EI)} = \frac{\text{highest erosion depth} (\mu\text{m})}{\text{test duration} (\text{min})} = \frac{h_{\max}}{\Delta t}$$

(7)

In this study, the highest erosion depth on the tested sample surface was determined by the optical profilometer. As the test duration were 30 minutes in all tests, the highest erosion depths occurred on the surface was taken as the erosion rate in this study.

4.2 Test results of the Al-6063 samples

The test results of the Al-6063 samples are presented below:

Table 2 Al-6063 cavitation erosion test results

S_{off} *(mm)*	Δm *(gr)*	*ER* x 10^{-4} *(gr/min)*	$h_{\max}$ (μm)	*EI* *(µm/min)*
5	0.0113	3.766	130	4.333
8	0.0091	3.033	106	3.533
10	0.0062	2.066	99	3.300
12	0.0020	0.666	92	3.066
15	0.0014	0.466	86	2.866
18	0.0004	0.133	29	0.966
20	0.0001	0.033	23	0.766
25	0	0.000	17	0.566

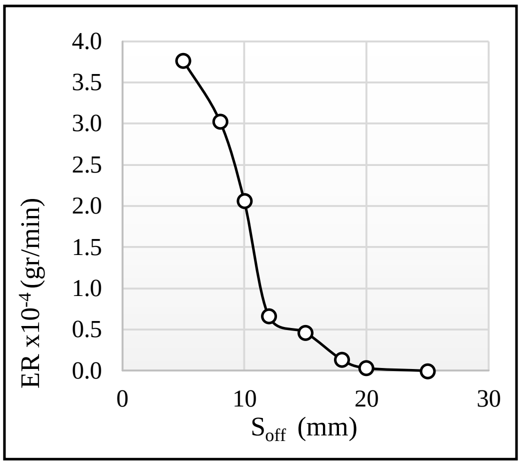

Figure 4 S_{off} (mm) – erosion rate graph

As far as the S_{off} distance is concerned, the erosion rate is inversely proportional to the distance between nozzle and sample.

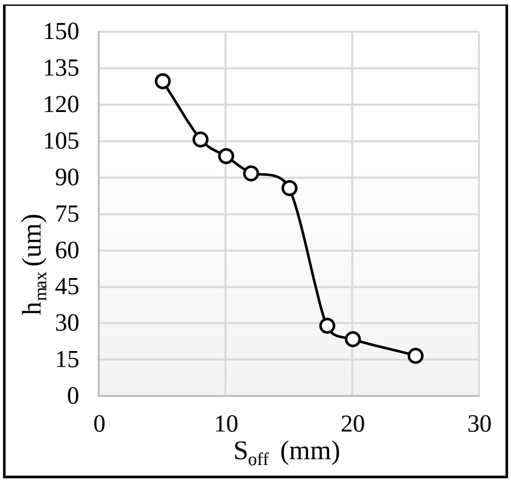

Figure 6 S_{off} (mm) – highest erosion depth (pit) on the tested sample surface

S_{off} distance is inversely proportional to the maximum pit depth (erosion intensity) that is formed on the sample surface. In other words, as S_{off} distance increases the erosion decreases.

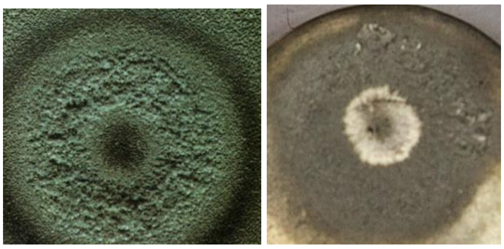

(a) **(b)**

Figure 5 Cavitation erosion test results of Al-6063 sample (S_{off}= 18 mm and t=30 min). (a) Momma (1991); (b) the results from this study

Figure 7 (a) and (b) show the results of Momma (1991) and the results of this study, respectively. It should be noted that in Momma's study, the nozzle diameter was 4 mm and the sample diameter was also 4 mm. However, the tests performed within this study were conducted with 2 mm diameter samples using a nozzle with a 1.4 mm diameter.

Based on the comparison of the figures one may deduce that the erosion characteristic is similar and there was a ring-shaped erosion around the middle region where the effect of pressurized water can be seen in both study. Momma (1991) stated that there were two erosion rings and erosion at the outer ring (the second ring) was much less severe than that at the inner ring (the first ring). The same result was also observed in this study. The size of the rings formed were also similar in both studies. According to the Figure 8, when S_{off} distance increases, cavitation erosion decreases. The samples used in the tests are in gold colour whereas the eroded region is black.

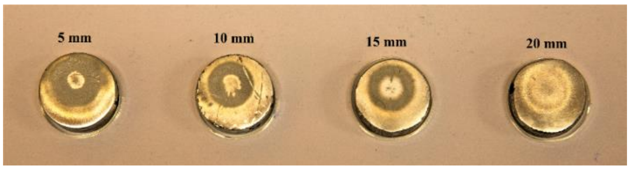

Figure 6 Effect of S_{off} distance to the cavitation erosion

When the cavitating water jet striked the target sample surface, the flow was directed radially outwards and a stagnation region was formed at the centre of the sample. Then ring shape erosion was produced with uneroded area at the centre (Momma, 1991). The same result was also obtained in this study. Thus, the results of the experimental setup are consistent with the test results of Momma (1991). Moreover, according to the results of the water jet tests carried out with copper samples (for nozzle distances between 3 mm and 15 mm), Hutli et al. (2018) have found that as the nozzle distance increases, the weight loss decreases. The same result was also obtained from this study.

Figure 9 below shows the 3-D optical profilometer analysis images of the Al-6063 surfaces showing the highest pitting depth on the surfaces. The Figure 9 (a) shows the optical profilometer analysis of the sample before the cavitation erosion test. Figure 9 (b) and Figure 9 (c) show the S_{off}=20 mm and S_{off}=10 mm test results, respectively.

The Figure 10 (a) show the 2-D optical profilometer analysis of the sample before the cavitation erosion test. Figure 10 (b) and Figure 10 (c) show the S_{off}=20 mm and S_{off}=10 mm test results, respectively.

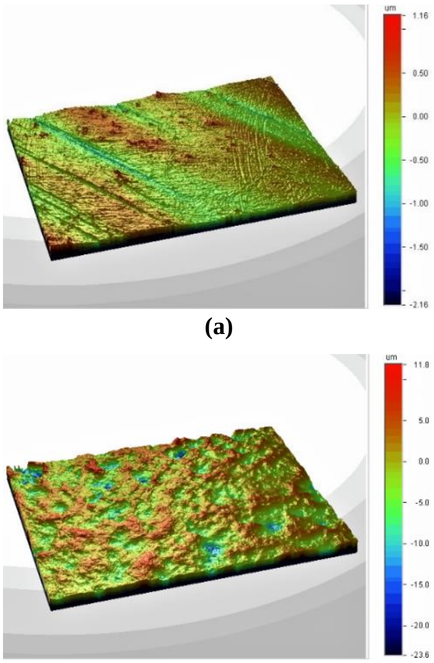

(a)

(b)

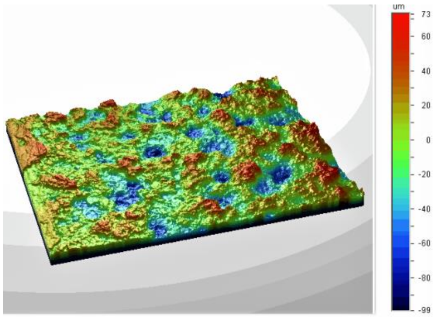

(c)

Figure 7 Optical profilometer analysis of the Al-6063 surfaces showing the highest pitting depth on the surfaces (a) untested surface, (b) S_{off}=20 mm and (c) S_{off}=10 mm (3-D)

It is clearly seen from the Figure 9 above, cavitation erosion on the surface increases as the S_{off} decreases.

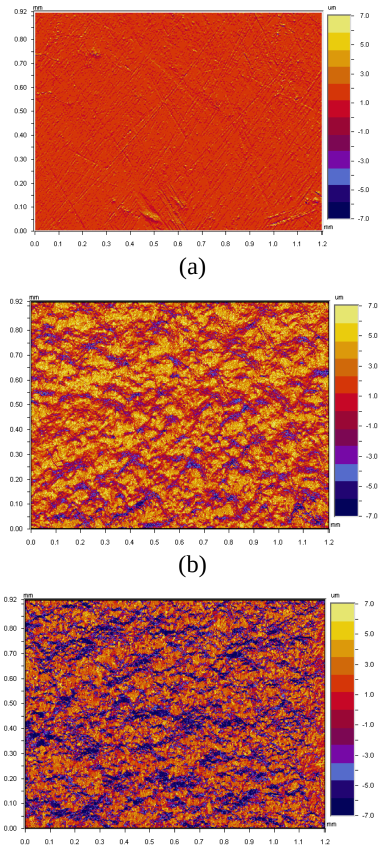

(a)

(b)

(c)

Figure 10 Optical profilometer analysis of the Al-6063 surfaces in the same scales. (a) untested sample, (b) Soff=20 mm and (c) Soff=10 mm (2-D)

5 CAVITATION EROSION TESTS OF PROPELLER MATERIALS

5.1 Determination of the Test Conditions

When the studies of the four different research groups (Momma, 1991; Soyama and Asahara, 1999 and 2002; Choi et al, 2012; Hutli et al, 2018) and the ASTM G-134 standards (ASTM, 2010) were reviewed, it was decided that the water jet pressure in the tests should be in the range of 200-300 bar.

The downstream pressure (P2), in the tests can be adjusted between 1-15 bar with the pressure relief valve placed on the cavitation chamber. Considering the strength and durability of the chamber, it was decided that the pressure inside of the chamber would be maximum 10 bars. When the minimum value of the P2 was determined to be 2.5 bar, the water jet pressure for the desired cavitation numbers that the pump should deliver was chosen as 250 bar and kept constant. In this matter, cavitation erosion tests were conducted with the following three cavitation numbers of 0.01, 0.02 and 0.03.

Cavitation erosion test conditions are given in Table 3.

Table 3 Conditions of high pressure water jet tests

Materials	Cu1, Cu3, Cu4
t (min)	30, 60, 90
P_2 (bar)	2.5, 5, 7.5
P_1 (bar)	250
Cavitation number, σ	0.01, 0.02, 0.03
S_{off} distance (mm)	5
D_{nozzle} (mm)	1.4

To give a brief summary of the conditions given in Table 3, a 1.4 mm diameter steel nozzle sprayed high pressure water to the Cu1, Cu3 and Cu4 propeller materials at 250 bar inlet pressure during 30, 60 and 90 minutes. The chamber pressure were 2.5, 5 and 7.5 bar (σ = 0.01, 0.02 and 0.03). Thus, 27 cavitation erosion tests were carried out (3 different propeller materials, 3 different test periods and 3 different cavitation numbers; 3^3=27).

Water temperature during the tests was 27(±3) °C. The samples tested in each test were stored in a desiccator in a non-humid environment with no moisture. Thus, it was ensured that no condition affected the surfaces of the samples until the surface analysis with the optical profilometer.

5.2 Materials Used in the Tests

The test samples used in cavitation erosion tests were made of Cu1 (manganese-bronze), Cu3 (nickel-aluminium-bronze) and Cu4 (manganese-aluminium-bronze) alloys. They had 20 mm diameter and 10 mm cylinder height.

Figure 11 Tested samples of the Cu1, Cu3 and Cu4 materials

The samples were manufactured and polished, respectively, and finally mechanically polished to mirror like surface before the cavitation erosion tests. Mechanical properties of the samples used in tests are given in Table 4.

Table 4 Mechanical properties of the samples used in tests

Alloy type	Yield strain $R_{p0.2}$ [N/mm^2]	Tensile strength R_m [N/mm^2]	Brinell hardness (3000 kg force)	Rockwell B hardness
Cu1	175	440	130	65-70
Cu3	245	590	159	84-89
Cu4	275	630	180	85-90

When Table 4 is examined, it is noted that among the samples used in this study, Cu4 is the one with the highest mechanical properties. Thus, it was expected that the most resistant material for cavitation erosion would be Cu4 before testing.

5.3 Test Results of the Propeller Materials

Cavitation erosion test results for three different cavitation number conditions using the Cu1, Cu3 and Cu4 materials for 30, 60 and 90 minutes are given below.

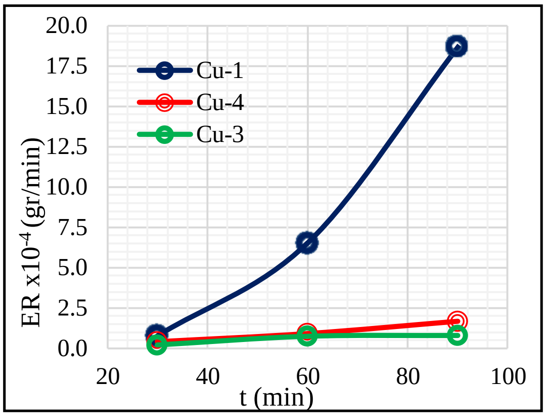

Figure 12 Test results of erosion rate change with time (σ =0.01)

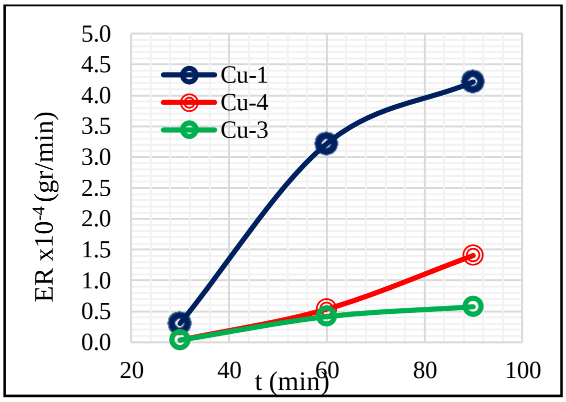

Figure 13 Test results of erosion rate change with time (σ =0.02)

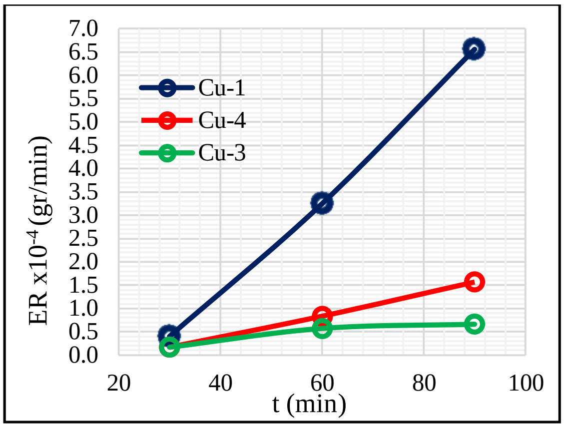

Figure 14 Test results of erosion rate change with time (σ =0.03)

The above figures show the erosion rate by test duration of 30, 60 and 90 minutes for the Cu1, Cu3 and Cu4 materials corresponding to different cavitation numbers. When the results of different materials are compared, Cu1 indicated the biggest erosion rate and Cu4 and Cu3 followed, respectively. Besides, the erosion rate and intensity are the highest when the cavitation number is the smallest (σ =0.01).

Figures 15, 16 and 17 show the results of the erosion test for the Cu1, Cu3 and Cu4 samples in three different cavitation numbers and three different test periods, respectively. In these figures, the first line represents the results at σ =0.01, the second line represents the results at σ = 0.02 and the third line represents the results at σ =0.03. The first column represents Cu1, the second column represents Cu2, and the third column represents the results of the Cu3 material. The samples used in the tests are in gold colour. The eroded region is black.

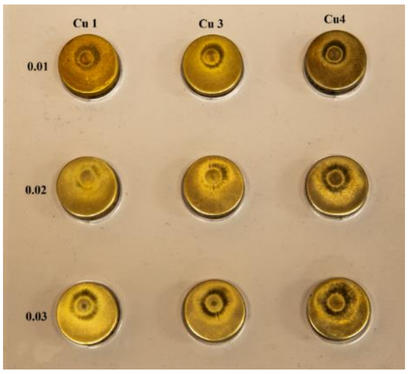

Figure 15 Cavitation erosion test results of 30 minutes test duration

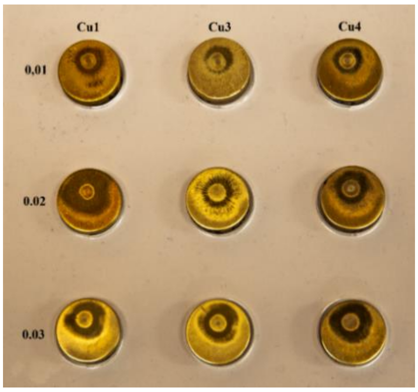

Figure 16 Cavitation erosion test results of 60 minutes test duration

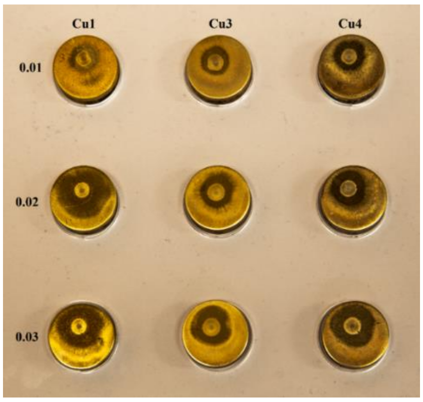

Figure 16 Cavitation erosion test results of 90 minutes test duration

When the figures are examined, it can be said that the samples of Cu1 had the most eroded area on the surface compared to those of Cu3 and Cu4. Additionally as the erosion test duration increases, erosion formation on the surface also increases.

6 CONCLUSIONS

The general conclusions below are drawn from the cavitation erosion tests using a water jet test rig;

- In general, the results obtained in this work are in good agreement with previously published results.

- Performing cavitating jet test is a simpler and cheaper way to investigate the resistance of different materials to cavitation erosion comparing the cavitation tunnel tests.
- Cavitation erosion occurrence for tested materials depends on the cavitation number.
- The stand-off distance is a crucial parameter for bubble collapse effect on the sample surfaces. As the stand-off distance decreases, cavitation erosion on the sample surface increases.
- As the cavitation number decreases, the mass loss, the erosion rate, and the eroded area increase. The cavitation number has a strong influence on the cavitation intensity and on the distribution and strength of the bubbles in the cavitation chamber.
- As the erosion test time increases, erosion formation on the surface also increases.
- Although Cu4 has the superior mechanical properties, such as yield stress, tensile strength, Brinell hardness and Rockwell B hardness; the study showed excellent erosion resisting performance of Cu3 compared to that of Cu4, contrary to the expectations. In addition to that, it was found that the erosion becomes more pronounced with increasing testing duration as well as decreasing cavitation numbers independently of the material. On the other hand, in some conditions erosion rate increases as the cavitation number increases.

REFERENCES

ASTM Standard, Standard No: G134-95. (2010). Standard Test Method for Erosion of Solid Materials by a Cavitating Liquid Jet, Annual Book of ASTM Standards, Vol. 03.02, West Conshohocken, pp 558–571.

ASTM Standard, Standard No: G32-10. (2010). Standard Test Method for Erosion for Cavitation Erosion Using Vibratory Apparatus.Annual Book of ASTM Standards, Vol. 03.02.

Annual Book of ASTM Standards, ASTM, (2010). Section 3 Material Test Methods and Analytical Procedures, vol. 03.02, American Society for Testing and Materials (ASTM).

Baker, J.S. (1994). Cavitation Resistant Properties of Coating Systems Tested on a Venturi Cavitation Testing Machine, Bureau of Reclamation, Research Laboratory and Services Division, Denver, CO.

Choi, J. K., Jayaprakash, A. Chahine, G. L. (2012). Scaling of cavitation erosion progression with cavitation intensity and cavitation source, Wear, Vol. 278–279, pp. 53–61.

Dular, M. (2016). Hydrodynamic cavitation damage in water at elevated temperatures, Wear, Vol. 346, 347 pp. 78-86.

Escaler, X. Avellan, F. Egusquiza, E. (2001). Cavitation Erosion Prediction from Inferred Forces Using Material Resistance Data, 4th Int. Symposium on Cavitation, CAV2001, Pasadena, CA.

Franc, J. P., Riondet, M., Karimi, A., Chahine, G. L. (2012). Material and velocity effects on cavitation erosion pitting, Wear 274– 275 (2012) 248– 259.

Hammitt, F.G. (1963). Observations on cavitation damage in a flowing system, Transactions of the ASME, Journal of Basic Engineering, Vol. 85, pp. 347–356.

Hattori, S., Hirose, T. and Sugiyama, K. (2009). Prediction method for cavitation erosion based on measurement of bubble collapse impact loads, J. Phys. Conf. Ser. Vol. 147.

Hutli, E., Nedeljkovic, M. S. & Bonyár, A. (2018). Cavitating flow characteristics, cavity potential and kinetic energy, void fraction and geometrical parameters-analytical and theoretical study validated by experimental investigations, Internatıonal Journal of Heat and Mass Transfer, Vol. 117: pp. 873-886.

Hutli, E. A. F., Nedeljkovic, M. S., Radovic, N. A., & Bonyár, A. (2016). The Relation between the High Speed Submerged Cavitating Jet Behavior and the Cavitation Erosion Process, International Journal of Multiphase Flow, Vol. 83. pp. 27-38.

Kim, K., Chahine, G.L., Franc, J., Karimi, A. (2014). Advanced Experimental and Numerical Techniques for Cavitation Erosion Prediction, Chapter 2 Laboratory Testing Methods of Cavitation Erosion. https://doi.org/10.1007/978-94-017-8539-6.

Laguna-Camachoa, J. R., Lewis, R.,Vite-Torres, M. and Mendez-Mendez, J. V. (2013). A study of cavitation erosion on engineering materials, Wear, Vol. 301, pp. 467–476.

Li, D., Kang, Y., Ding, X., Wang, X., Fang, Z. (2017). Effects of Nozzle Inner Surface Roughness on the Performance of Self-Resonating Cavitating Waterjets under Different Ambient Pressures, Journal of Mechanical Engineering, Vol. 63(2017)2, pp. 92-102.

Mantzaris, A. 2015. “Establishment and verification of reproducible method for coating propeller blades such that the erosive cavitation can be detected”, Ms.C. Thesis, University of Newcastle Upon Tyne.

March, P. A. (1987). Evaluating the Relative Resistance of Materials to Cavitation Erosion: a Comparison of Cavitating Jet Results and Vibratory Results, Proc. Cavitation and Multiphase Flow Forum, ASME, Cincinnati.

Momma, T. (1991), Cavitation loading and erosion produced by a cavitating jet, Ph.D. Thesis, University of Nottingham.

Momma, T. and Lichtarowicz, A. (1995). A study of pressures and erosion produced by collapsing cavitation, Wear, Vol. 186-187, pp. 425-436.

Mottyll, S. and Skoda R. (2016). Numerical 3D flow simulation of ultrasonic horns with attached, cavitation structures and assessment of flow aggressiveness and cavitation erosion sensitive wall zones, Ultrasonics Sonochemistry, Vol. 31, pp. 570–589.

Peng, C., Tian, S. & Li, G. (2018). Joint experiments of cavitation jet: High-speed visualization and erosion test, Ocean Engineering, Vol. 149, pp. 1-13.

Pfitsch, W., Gowing, S., Fry, D., Donnelly, M., Jessup, S. (2009). Development of measurement techniques for studying propeller erosion damage in severe wake fields. Paper presented at the 7th international symposium on cavitation (CAV2009), Ann Arbour, Michigan.

Soyama, H., Lichtarowicz, A., Momma, T. and Williams, E. J. (1988). A new calibration method for dynamically loaded transducers and ıts application to cavitation ımpact measurement, Journal of Fluids Engineering, Vol. 120.

Soyama, H. and Asahara, M. (1999). Improvement of the corrosion resistance of a carbon steel surface by a cavitating jet, Journal of Materials Science Letters, Vol. 18 (23), pp. 1953-1955.

Soyama, H., Kumano, H., Saka, M. (2001). A New Parameter to Predict Cavitation Erosion, Fourth International Symposium on Cavitation, CAV2001:sessionA3.002, Pasadena, Ca. USA.

Soyama, H., Kumano, H. (2002). The Fundamental Threshold Level—a New Parameter for Predicting Cavitation Erosion Resistance, Journal of Testing and Evaluation, JTEVA, Vol. 30, No. 5.

Soyama, H. (2005). High-speed observation of a cavitating jet in air, Journal of Fluids Engineering, Vol. 127.

Soyama, H. (2013). Effect of nozzle geometry on a standard cavitation erosion test using a cavitating jet, Wear, Vol. 297, pp. 895-902.

Shimizu, S. and Yamaguchi, A. (1988). Erosion due to impingement of cavitating jet, (Japanese) J.Japan Hydraulics and Pneumatics Soc. V. 19, pp. 68.

Taillon, G., Pougoum, F., Lavigne, S., Ton-That, L., Schulz, R., Bousser, E., Savoie, S., Martinu, L. and Sapieha, J. E. K. (2016). Cavitation erosion mechanisms in stainless steels and incomposite metal–ceramic HVOF coatings, Wear, Vol. 364-365, pp. 201–210.

Turkish Lloyd. (2017). Section 2, Material Rules, (http:/www.turkloydu.org).

Zhou, Y. K. and Hammitt, F. G. (1963). Cavitation erosion incubation period, Wear, Vol. 86 (2), pp. 299-313.

Cavitation Tunnel Tests and Full-Scale Review of the First GATE RUDDER® System Installed on the 400TEU Container Ship

Serkan Turkmen[1], Masaki Fukazawa[2], Noriyuki Sasaki[3], Mehmet Atlar[3]
[1]Newcastle University, Newcastle Upon Tyne, UK
[2]Kamome Propeller Ltd., Japan
[3]Department of Naval Architecture, Ocean and Marine Engineering, University of Strathclyde, Glasgow G4 0LZ, UK

Abstract:
Following the successful installation of the world's first GATE RUDDER® system on a 400TEU container ship (see Figure 1), superior fuel saving and manoeuvring performances have been recorded with this vessel over her sister ship fitted with a conventional rudder. Also, noticeable reductions in the aft end vibrations and noise have been reported by the captains and crew of these vessels in service. This paper describes and discusses the results on the recent cavitation tunnel tests conducted in the Emerson Cavitation Tunnel with the same geometry of the full-scale rudders and propellers for the above-mentioned vessels except for the same wake distribution due to the current limitation of the test facility used. The results presented in the paper may help to shed a light on the full-scale cavitation and noise performances of the two sister ships currently operating between the North and South of Japan by following the same route.

Keywords: Gate Rudder, Cavitation, Noise

1 INTRODUCTION

"GATE RUDDER®" is a novel twin rudder arrangement which has blades with the asymmetric cross-sections enveloping the propeller at the upper part and aside the propeller as shown in Figure 1. This concept was originated in Japan (Sasaki, 2013) and has been further developing with joint activities in the UK and Japan, Sasaki et al (2018). Advanced energy saving and steering capability of the GATE RUDDER® have been demonstrated through both experimental and numerical studies (Sasaki et al 2015, Turkmen et al 2015) and recently this propulsion system was installed on a 400TEU domestic container ship in Japan for the first time.

Advanced energy-saving feature originates in the rudder thrust induced by the cambered twin rudder blades and the propeller, acting as an efficient accelerating ducted propulsor. The remarkable flap effect of the GATE RUDDER® increases the lateral forces and the yaw moment leading to improved steering and course keeping capabilities as reported in (Carchen et al, 2016, Turkmen et al 2016). Moreover, the recent sea trials confirmed that the GATE RUDDER® system has provided more than expected based on the previous studies, Sasaki et al (2018).

Recently, a pioneering experimental study on the cavitation and noise characteritics of the GATE RUDDER® has been completed in the Emerson cavitation tunnel for the first time invloving a GATE RUDDER® system. These tests were conducted in comparative manner, and involved with a GATE RUDDER® and its counterpart conventional single rudder combined with the same propeller.

Figure 1 First full-scale GATE RUDDER® system

This paper presents the details of these tests and results of the cavitation and noise performance of the both rudder arrangements and discusses the results. Following this introductory part, the remaining sections of the paper describe the test set-up & conditions in Section 2, the results and discussion in Section 3 and concluding remarks drawn from the study in Section 4.

2 TEST SET-UP & CONDITIONS

The experiments were carried out in the Emerson Cavitation Tunnel (ECT) of Newcastle University, which has a measuring section of 3.1m x 1.21m x 0.8m (LxBxH),

* *Corresponding author e-mail: Serkan.turkmen@ncl.ac.uk*

as shown in Figure 2 and described in details in (Atlar, 2011).

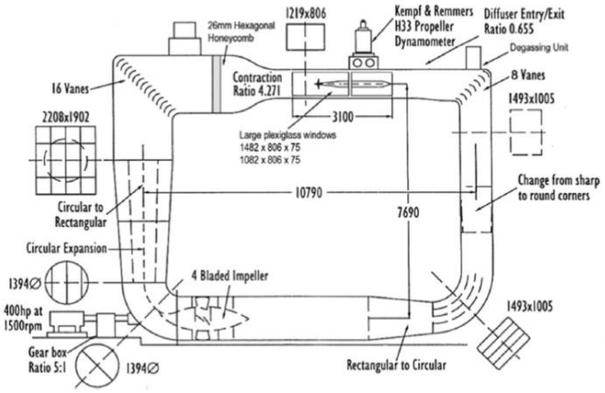

Figure 2 Emerson Cavitation Tunnel

The aft end and propeller arrangements of the conventional rudder (without the flap) and GATE RUDDER® systems were represented with the model rudders and propellers of the two vessels with a scale ratio of 21 and fitted in the downstream of the K&R H33 dynamometer of the ECT as shown in Figure 3.

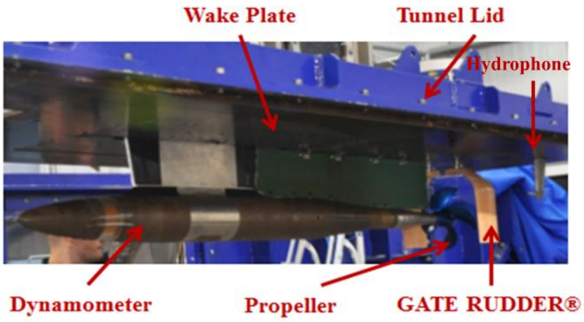

Figure 3 Test set-up with GATE RUDDER® at ECT

The model propeller and rudder geometries for the conventional rudder and GATE RUDDER® systems were provided by KAMOME Propeller Co, LTD. The same Controllable Pitch Propeller (CPP) model of a 250mm diameter with four-blades and high skew was used behind the conventional rudder and GATE RUDDER® systems as shown in Figure 4. The model propeller designed for the conventional propeller was used for both rudder systems in order to investigate the cavitation and noise characteristics in comparative manner.

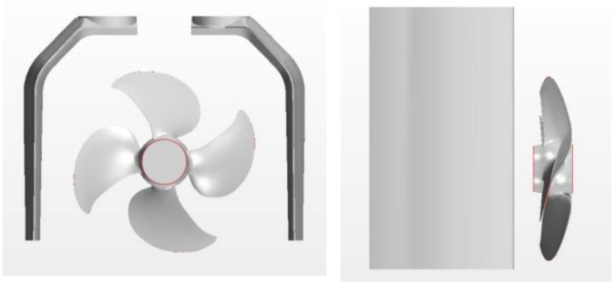

Figure 4 GATE RUDDER® system (Left) and Conventional Rudder system (Right)

While the measuring section of the ECT usually allows a reasonable size dummy hull with a properly scaled aft end arrangements, in this investigation, a very crude wake simulation arrangement was used due to the time limitation for the facility. In this arrangement, the wake of the H33 dynamometer was combined with the wake of a vertical plate of 0.85m length and 0.02m thickness which was placed between the trailing edge of the dynamometer strut and the model propellers with a diameter of 250mm, as shown in Figure 3. The wake plate was also covered with a sand paper of grit P36 to trip the wake flow in turbulent regime.

During the experiments following performance characteristics and associated parameters were monitored and recorded:

- *Propeller performance* (tunnel and shaft speed by encoder, torque and thrust by K&R H33 dynamometer)
- *Cavitation dynamics* (Extend and severity of cavitation recorded by high speed cameras)
- *Underwater noise levels* (Frequency and Sound Pressure Levels by B&K Type 8103 miniature Hydrophone)

During the tests, the propeller thrust and torque as well as the shaft rpm were recorded by a data collection rate of 100Hz. The URN characteristics were recorded by using a B&K 8103 Hydrophone located inside the tunnel in a streamlined strut aligned with the tunnel main flow. The distance between the hydrophone and propeller plane centre was longitudinally 170mm, transversally 235mm and vertically 80mm. The cavitation observations were recorded by using moving and still cameras from the side and bottom windows of the ECT for each test condition. As well as the oxygen and temperature of the tunnel water. Also, during the tests the background noise level, water temperature and dissolved air content were checked and kept similar for each test.

Test were conducted at 5 different operational conditions of these ships that varied from a bollard condition e.g. experienced in harbour manoeuvring (Test 1) to service (MCR) condition at 16.1 knots (Test 5). Table 1 presents these test conditions.

Table 4 Test conditions

Parameters	Test1	Test2	Test3	Test4	Test5
V_a (m/s)	0	0.925	1.56	3.00	3.97
n (rpm)	1200	1438	1438	1438	1925
P_v (mmHg)	-200	-200	-200	-200	-400

where V_a is advance speed; n is propeller shaft speed, P_v is the vacuum level applied during the tests.

3 RESULTS AND DISCUSSIONS

In the following the propeller performances and cavitation observations are given in separate sections i.e. for the

GATE RUDDER® (in Section 3.1) and Conventional Rudder arrangements (in Section 3.2) while the noise measurement results are presented in a common section (Section 3.3).

3.1 GATE RUDDER® test results

The initial conditions for the tests are given in **Table 5** while the performance data for the propeller of the GATE RUDDER®, set-up corresponding to the test conditions of Table 1, are presented in Table 6.

Table 5 Initial conditions for the GATE RUDDER® system tests

GATE RUDDER® test conditions	*Value*
Tunnel water density (kg/m^3)	1006
Vacuum applied (mmHg)	849
Atmospheric pressure (mmHg)	758
Tunnel Temperature (deg)	20.2

Table 6 Propeller performance data with the GATE RUDDER® system

	V	N	J	K_t	σ_n
Test1	0	20.0	0	0.37	4.31
Test2	0.925	24.1	0.15	0.33	4.31
Test3	1.56	24.0	0.26	0.29	4.31
Test4	3	24.1	0.50	0.18	4.31
Test5	3.97	32.1	0.50	0.18	1.66

Figure 5 shows the cavitation patterns experienced with the GATE RUDDER® system corresponding to Test1 (i.e. bollard condition). All propeller blades displayed moderate strength of tip vortex cavitation emanating from the leading edge of the blades, and not exactly from the tip but from a smaller radius due to the high skew of this propeller. The cavitating vortices appeared to be larger in thickness and stronger in strength at the upper part of the propeller plane than those at the lower part. The cavitating tip vortices twisted like ribbons leaving at the blade edges and continued in the downstream. While the traces of the tip vortices could not be detected by eye beyond the rudder trailing edges a well-develop hub vortex cavitation was observed in downstream as perturbed by transient distortions.

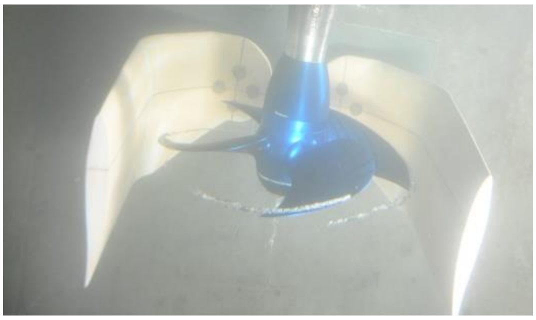

Figure 5 Cavitation pattern observed in Test 1 condition

Sample views of the cavitation patterns observed in the Test 2 condition is shown in Figure 6. A well-developed steady leading-edge sheet cavitation combined with the earlier mentioned tip vortex cavitation was covering about 10% of the suction side of the blade surfaces. This was accompanied by the dominant hub vortex cavitation extending to the downstream. Similar to the previous test condition, the cavitating tip vortices were leaving the blade leading edges almost half-way in a twisted ribbon form and extending in the downstream of each blade. These vortices were visible up to two full revolutions of the propeller's slipstream and after which becoming unsteady and desinent.

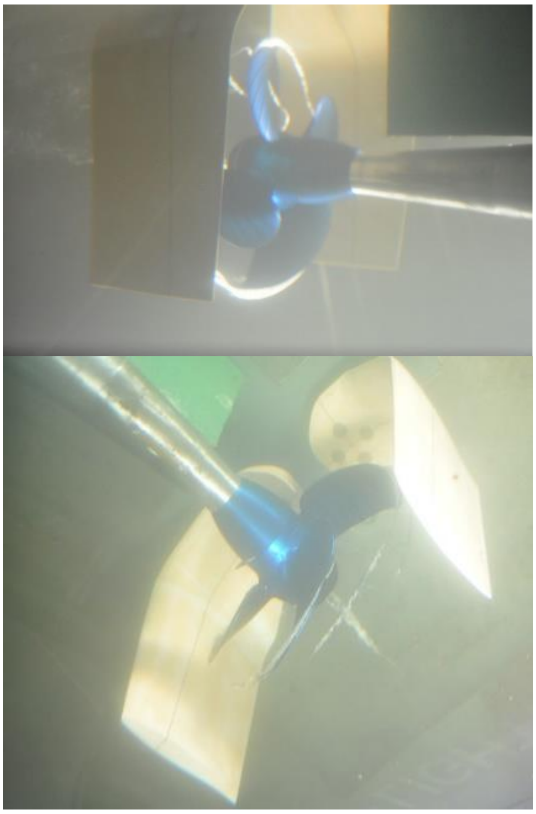

Figure 6 Cavitation pattern observed in Test 2 condition

Figure 7 shows the cavitation patterns observed in Test 3 condition. The pattern and cavitation dynamics observed in this condition were similar to Test 2 with reduced strength due to less loading on the propeller. However, the twisted cavitating vortex was still visible with the unsteady appearance after the rudder blades as well as the persistent cavitating hub vortex in the downstream.

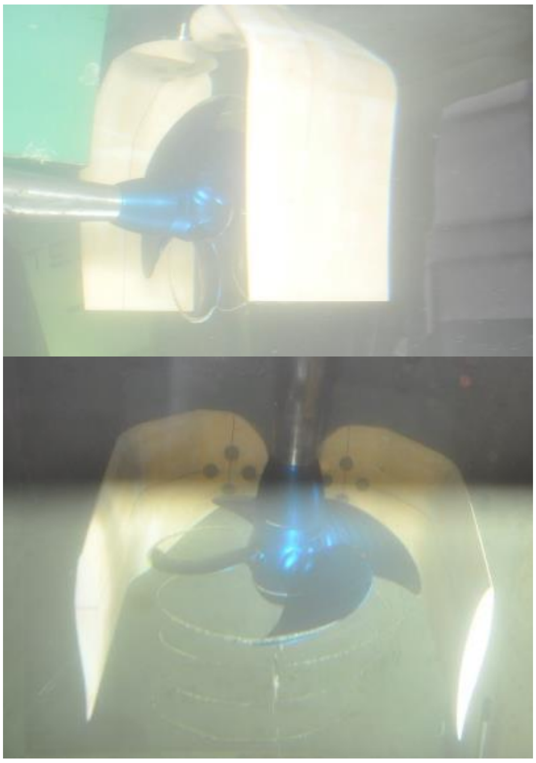

Figure 7 Cavitation pattern observed in Test 3 condition.

The sample views of the cavitation pattern observed in Test 4 condition are shown in Figure 8. The tip vortex cavitation still occurred but much weaker and intermittent. The strength of the cavitation reduced greatly and after one full revolution. The tip vortex cavitation became almost invisible as well as the hub vortex cavitation. This condition is corresponding to 10kts in full scale.

Figure 8 Cavitation pattern observed in Test 4 condition

Figure 9 displays the cavitation pattern observed during the Test 5 condition which corresponds to the MCR condition of the full-scale vessel at 16.1 knots. In spite of the relatively low propeller loading, the reduced cavitation number corresponding to this operating condition imposed the strongest tip vortex combined with the largest extent of sheet cavitation at the leading edge which covered about 15% of each blade. The cavitating tip vortex extended well beyond the GATE RUDDER® blades and this was also accompanied by the strong hub vortex cavitation in the downstream of the hub.

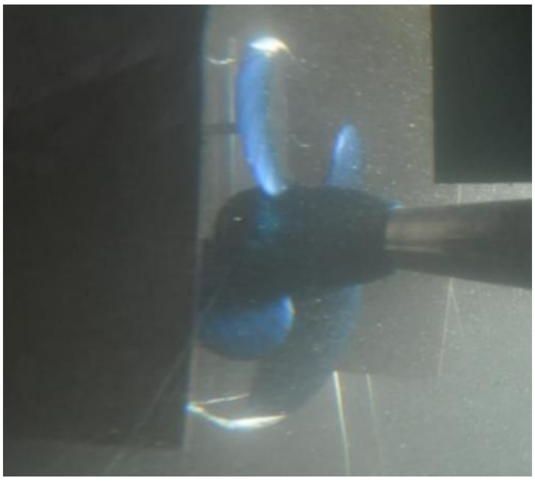

Figure 9 Cavitation pattern observed in Test 5 condition

3.2 Conventional rudder test results

The initial conditions of the cavitation tunnel are given in Table 4. The general performance characteristics of the propeller with the conventional rudder are presented in Table 5.

Table 4 Initial conditions for the Conventional Rudder system tests

Conventional rudder test condition	*Value*
Tunnel water density (kg/m3)	1006
Vacuum applied (mmHg)	846
Atmospheric pressure (mmHg)	765
Tunnel Temperature (deg)	17.8-18.0

Table 5 Propeller performance data with the Conventional Rudder system

	V	N	J	K_t	σ_n
Test1	0	20.1	0	0.42	4.31
Test2	0.925	23.9	0.15	0.38	4.31
Test3	1.56	23.9	0.26	0.33	4.31
Test4	3	23.9	0.50	0.22	4.31
Test5	3.97	32.19	0.49	0.22	1.66

Figure 10 shows the cavitation pattern experienced with the conventional rudder system corresponding to Test 1. All propeller blades displayed strong tip vortex cavitation emanating from the leading edge of the blades and combined with a narrow leading edge sheet cavitation. Because of the relatively high skew of the propeller blades, the cavitating vortices were leaving the blade leading-edges before the tips twisted like ribbons extending in the downstream.

Due to the effect of the wake plate, there were deformations of the tip vortices at the TDC and these deformations were combined with the effect of the rudder in downstream resulting in the bifurcation of the tip vortex at the rudder leading edge. In spite of the accentuated sheet cavity dynamics at the wake shadow and deformation of the tip vortex at the rudder leading edge, the tip vortex cavitation was transported in downstream through the propeller slipstream by interacting with the rudder and visible by eye for 3 to 4 revolutions of the propeller slipstream and disappearing afterward. No hub cavitation could be observed in this condition.

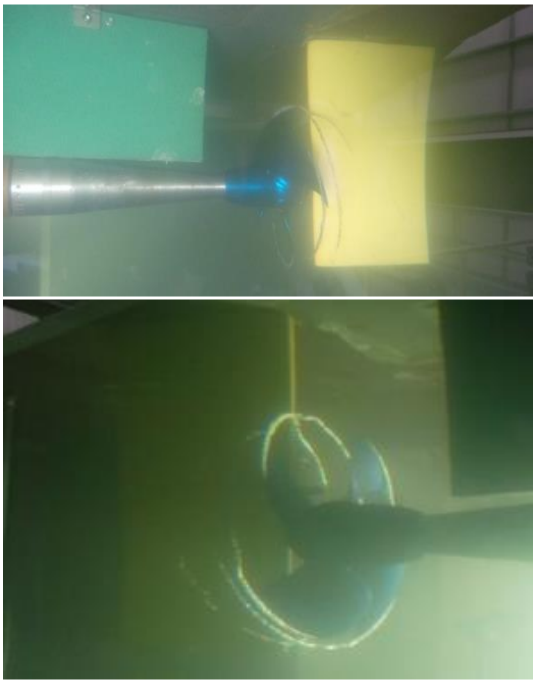

Figure 10 Cavitation pattern observed in Test 1 condition

Typical cavitation patterns observed in the Test 2 condition are shown in Figure 11. A strong tip vortex cavitation combined with the well-developed leading-edge sheet cavitation, which covered almost 15% of each blade surface, was observed. The extent and strength of the cavitation observed were increased around the TDC due to the effect of the wake plate as well as the dynamometer’s strut.

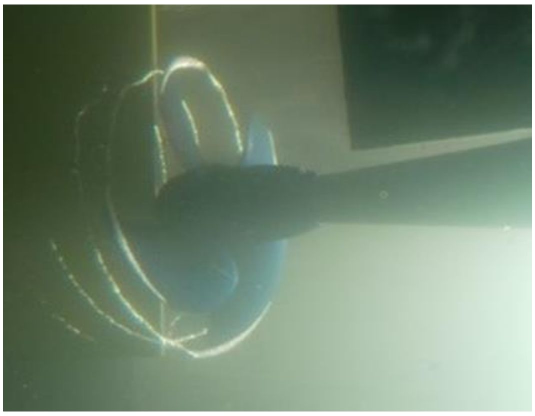

Figure 11 Cavitation pattern observed at Test 2 condition

The cavitating vortices emanating from all blades extended to the rudder and were deformed by the presence of the rudder before reaching at the leading edge of the rudder especially at the TDC and its vicinity. This deformation was combined with the effect of the rudder in downstream resulting in the bifurcation of the tip vortex at the leading edge. In spite of the accentuated sheet cavity dynamics at the wake shadow, first deformation of the tip vortex at the rudder leading edge, and then interacting with the rudder, the persistent tip vortex cavitation was transported in downstream through the propeller slipstream and the rudder without losing its strength. No hub vortex was visible for this test condition.

Figure 12 shows the cavitation patterns observed in Test 3 condition. The pattern and cavitation dynamics observed in this condition were similar to Test 2 with reduced extent and strength of the cavitation patterns due to less loading on the propeller.

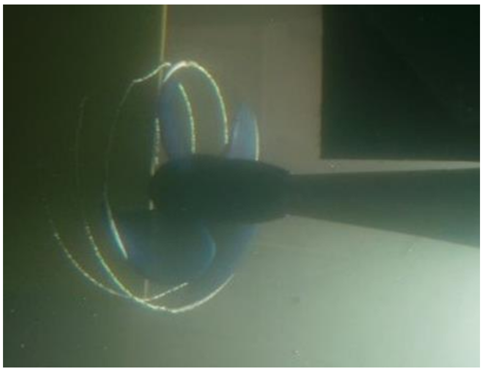

Figure 12 Cavitation pattern observed at Test 3 condition

However, the twisted cavitating tip vortex was still visible while the well-develop leading edge cavitation covered about 10% of the propeller tip. The cavitating tip vortex was steady and less perturbed by the wake effect and still interacting persistently with the rudder. No hub vortex was observed.

The cavitation patterns observed in Test 4 condition are shown in Figure 13. Intermittently flushing tip vortex cavitation could be observed only at the TDC and its vicinity due low propeller loading for this condition. Also no hub vortex was observed.

Figure 13 Cavitation pattern observed at Test 4 condition

As shown in Figure 14, much reduced cavitation number corresponding to the Test 5 condition displayed strongest tip vortex cavitation combined with the largest extent of the sheet cavitation at the leading-edge of the blades covering almost 20% of their suction sides. The deformation and bifurcation of the tip vortices at the leading edge of the rudder around the TDC were accentuated while the strong cavitating vortices were still interacting with the rudder without losing their strength and extending along the chord of the rudder and its downstream. However, no hub vortex cavitation was observed.

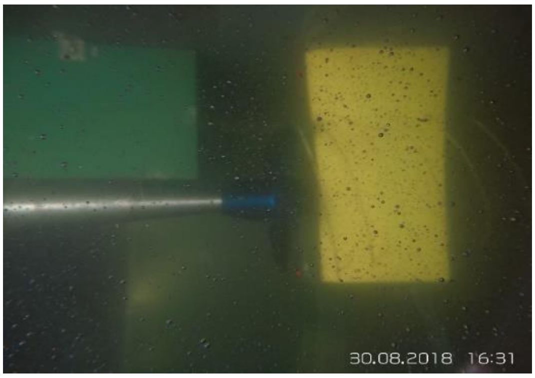

Figure 14 Cavitation pattern observed at Test 5 condition

3.3 Comparison of cavitation patterns

Based upon the observations of the cavitation patterns with the two rudder systems it can be concluded that both rudder arrangements presented similar cavitation patterns on their blades, which mainly involved the tip vortex cavitation combined with the leading edge sheet cavitation at the suction side of the blades. However, it was noticed that the strength and extent of the tip vortex and leading edge cavitation were reduced for the GATE RUDDER® system compared to those observed with the conventional rudder arrangement.

It was also noticed that the cavity dynamics at the TDC and BDC of the conventional rudder were rather different due to the presence of the rudder and its direct interaction with the propeller's slipstream. The deformation of the cavitating tip vortices at approach to the conventional rudder and their bifurcation at the leading edge displayed rather complex cavity dynamics as opposed to almost regular and steady appearance of the cavitating vortex trajectories of the propeller inside the GATE RUDDER® blades. It was also noticed that there was a slight difference in the thickness of the cavitating vortices at the upper and lower part of the propeller plane with the GATE RUDDER®.

However, the GATE RUDDER® system displayed continuous hub vortex cavitation for almost all the test conditions while the conventional rudder system did not due to the weakening effect of the rudder behind the propeller.

3.4 Comparison of noise measurement results

The comparative SPL (dB) measurements are presented for both rudder systems in the same graphs at narrow frequency band as shown from Figure 15 to 19 corresponding to earlier stated five test conditions.

Since the differences between measured sound pressure level and background noise level was greater than 10dB, no adjustments were necessary (ITTC 2014). The first five blade passing frequencies (BPF) are shown in these graphs by the dashed vertical lines. Half BPFs are also appearing in these graphs. This might be caused by different noise sources e.g. it may be associated with the grub screw at propeller hub. Apart from that, it can be clearly seen that the noise level mostly contributed by the cavitating vortex from the leading-edge in the frequency range between the first and third blade passing frequency (BPF) where the tonal noise is appearing. The cavitating hub vortex contributes the noise level at the middle-frequency range.

By investigating the comparative noise levels and patterns for all the test cases, the noise generated by the propeller appeared to be developing in the same way for both rudder systems. Overall, there is an indication that the GATE RUDDER® seemed to be quieter than the conventional rudder arrangement apart from the results in the Test 1 condition (Figure 16). In the rest of the test conditions, the GATE RUDDER® system presented reduced noise levels at the first few BPFs while the differences between the two rudder systems can be hardly seen in the middle and high-frequency ranges. The reason can be attributed to both the strong hub vortex cavitation and the tip vortex cavitation contributing to the noise level at this frequency ranges.

One evidence of the strong hub vortex contribution in the noise level can be confirmed at the test 4 condition where the GATE RUDDER did not generate hub vortex cavitation, and hence only at this condition a noticeable reduction of the noise level can be seen at the frequency range from 600 to 1100Hz. Perhaps another reason for not being able to have a clear evidence with the reduction in the noise levels with the GATE RUDDER® system in these tests is the absence of the proper hull wake simulation due to the time restrictions. According to the vibration measurements and captains' comments on both vessels, the noise and vibration were considerably lower on board the vessel with the GATE RUDDER® system. The wake distribution, which was not simulated in this test campaign, seems to be important and needs to be investigated further to take into account the interaction between the GATE RUDDER® and the ship stern.

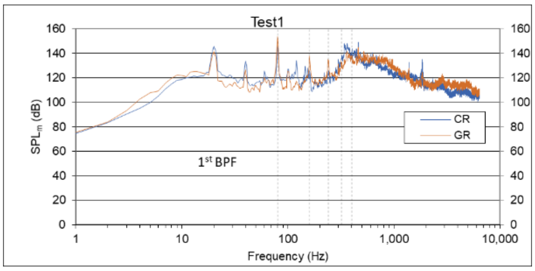

Figure 15 Comparison of the noise levels in the narrow band measured with the GATE RUDDER® and Conventional Rudder systems for Test 1 condition

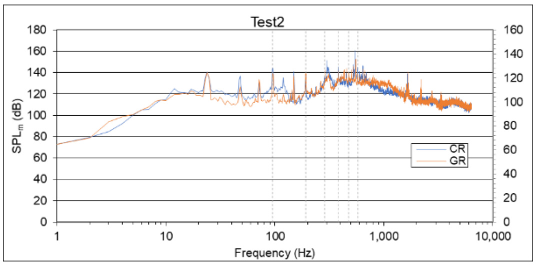

Figure 16 Comparison of the noise levels in the narrow band measured with the GATE RUDDER® and Conventional Rudder systems for Test2 condition

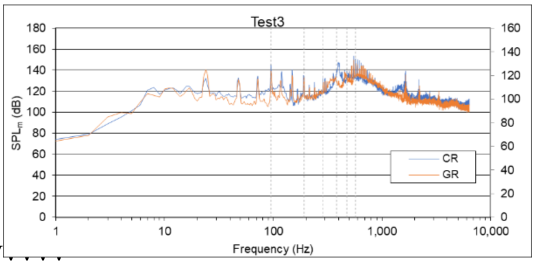

VV

Figure 17 Comparison of the noise levels in the narrow band measured with the GATE RUDDER® and Conventional Rudder systems for Test3 condition

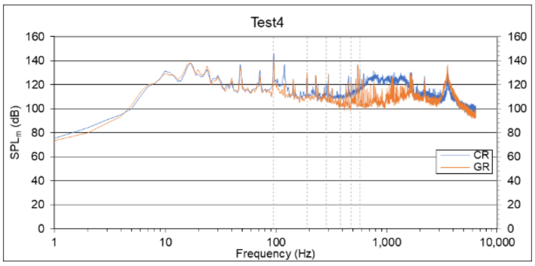

Figure 18 Comparison of the noise levels in the narrow band measured with the GATE RUDDER® and Conventional Rudder systems for Test 4 condition

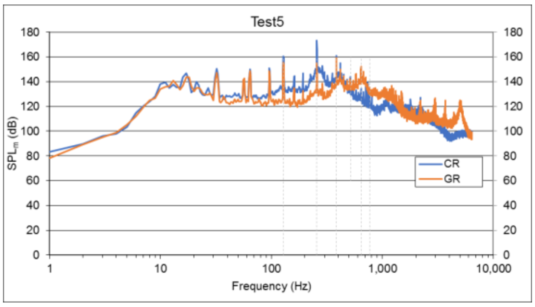

Figure 19 Comparison of the noise levels in the narrow band measured with the GATE RUDDER® and Conventional Rudder systems for Test 5 condition

3.5 Full Scale reporting

After the delivery of these vessels, the Authors were onboard the GATE RUDDER® driven ship to witness her performance monitoring, and at the same time, collecting invaluable information regarding the performance of the two vessels from the captain who had experience with the two vessels continuously. The information obtained from the captain is summarized in Table 5.

Table 5 Full Scale Ship Monitoring and on-board experience

(Data in the table are authorized by the ship owner)

	Sakura	Shigenobu
Rudder system	Flap Rudder	GATE RUDDER®
On board meas.	-	11-12 April 2018
Captain's experience	Aug.2016-Nov.2017	Dec.2017-Oct.2018
Fuel Saving	base	15-20% saving
Berthing	base	easier
Turning	base	better
Vibration	many trouble with navigation lights	No trouble
Noise	base	Quiter

Test 5 is the service condition that the ITTC recommended scaling procedure (ITTC, 2014) was applied. Although there might be uncertainty caused by factors (i.e. tunnel wall, viscous flow, dissolved gas content, reverberant environment, et.) the procedure provides good prediction (Atlar et.al, 2001). Results of one-third octave analyses for the model propeller was utilized. In Figure 20, measured noise level for the rudders in one-third band was used to predict full scale noise level.

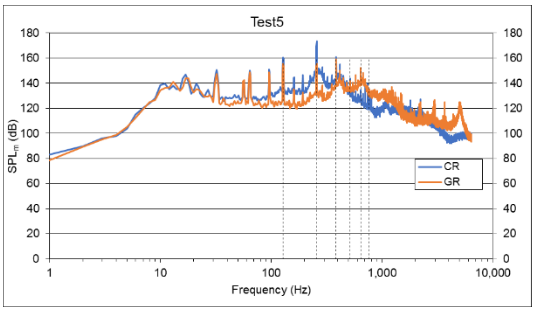

Figure 20 Comparison of the noise levels in the one-third octave band measured with the GATE RUDDER® and Conventional Rudder systems for Test 5 condition in model-scale

Noise result measurements were converted from one-third octave band to equivalent 1 Hz bandwidth (SPL_1) using the given equation:

$$SPL_1 = SPL_m - 10Log_{10}\,(0.23f_0) \tag{1}$$

where f_0 is the centre frequency. The noise level was corrected for the 1m reference distance by given equation below:

$$SPL = SPL_1 + 20Log_{10}\left[\frac{d}{d_{ref}}\right] \tag{2}$$

where d is the distance between hydrophone and $0.7R$ above the shaft line. R is the radius of the propeller. The formulas are given below to calculate the noise level differences (ΔL) and the frequency shift between model-scale and full-scale:

$$\begin{aligned}\Delta L_{(P)} &\\ = 20\,log_{10}&\left[\left(\frac{D_s}{D_m}\right)^z\left(\frac{r_m}{r_s}\right)^x\left(\frac{\sigma_s}{\sigma_m}\right)^{y/2}\right]\\ + 20\,log_{10}&\left[\left(\frac{n_sD_s}{n_mD_m}\right)^y\left(\frac{\rho_s}{\rho_m}\right)^{y/2}\right]\end{aligned} \tag{3}$$

$$\frac{f_s}{f_m} = \frac{n_s}{n_m}\sqrt{\frac{\sigma_s}{\sigma_m}} \tag{4}$$

where the subscripts s and m refer to full-scale and model scale, respectively. D is the diameter, r is the reference distance, σ is the cavitation number, ρ is the density (1025kg/m^3 for the sea water and 1006kg/m^3 for the tunnel water), n is the rotation speed (rps) and f is the frequency. z, x y are the constants defined by the test facility, Reynolds number, theoretical assumptions and the model test method. In the study, the values are chosen as y=2 and z=1 (Atlar et.al, 2001). It is not necessary to use the value of x as both full-scale and model-scale reference distances are 1m.

The frequencies are shifted with the ratio 0.11 and the noise levels are increased 31dB for the conventional rudder and 29dB for the GATE RUDDER® system. Predicted full-scale noise levels of both vessels are compared in Figure 21. Noise level change can be clearly observed around the first three BPF the noise spectra. The smaller propeller diameter and less load on the blades of the propeller with the GATE RUDDER® lead to a noise reduction.

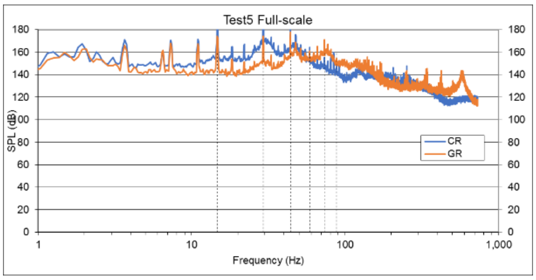

Figure 21 Comparison of the noise levels in the narrow band measured with the GATE RUDDER® and Conventional Rudder systems for Test 5 condition in full-scale prediction

4 CONCLUDING REMARKS

This paper presented the recently completed cavitation tunnel tests for the first time on a GATE RUDDER® system in comparison with a conventional rudder system based on the two full-scale sister ships fitted with these rudder systems. The crew of the two vessels experienced the noticeable differences in the vibration and noise characteristics at the aft end of these ships in service for the favour of the GATE RUDDER® fitted vessel. The tunnel tests, therefore, aimed to shed a light on this and to provide preliminary evidence for the crew's experience. The tests involved mainly the cavitation observations and noise measurements in the absence of a properly scaled hull wake due to the time restrictions. The tests results indicated that:

- Both rudder systems displayed similar cavitation patterns involving the tip vortex cavitation and leading-edge suction side cavitation. The GATE RUDDER® system also displayed additional hub vortex cavitation while the conventional rudder system did not. The extent and strength of the two former type cavitations with the GATE RUDDER® system were reduced compared to those of the cavitation observed with the conventional rudder system.
- The cavitation dynamics of the conventional rudder were different and complex especially at the TDC and BDC regions due to the interaction of the slipstream with the rudder while the GATE RUDDER® had much less activity with an almost regular slipstream trailing downstream in the envelop of the GATE RUDDER® blades.
- The measured noise levels were generally similar for both vessels although the GATE RUDDER® system appeared to be slightly quieter in spite of the strong hub vortex development with the GATE RUDDER® system when the conventional propeller design was used as in this test case. It is believed that the conduct of the tests with the proper wake simulation reflecting the interaction between the GATE RUDDER and ship stern, which is shown in Appendix A at Figure A.1, would help for much accurate assessment of the noise characteristics of the GATE RUDDER® as well as cavitation and vibrations that are due to be conducted in very near future.
- According to the ITTC recommended procedure, it is expected that the increased noise level (ΔL) of GATE RUDDER® fitted vessel is lower than the conventional rudder fitted vessel when the results were extrapolated to full-scale. Moreover, less power demand caused by the extra thrust originated from the GATE RUDDER® system should also lower the engine load which leads to the reduction of the structure-borne noise.

ACKNOWLEDGEMENT

The authors gratefully acknowledge Kamome Propeller Ltd. Japan for their support of this project.

REFERENCES

Atlar, M. (2011). "Recent upgrading of marine testing facilities at Newcastle University". In: Proceedings of the 2nd International Conference on Advanced Model Measurement Technologies for the Maritime Industry (AMT'11), Newcastle upon Tyne, UK.

Atlar, M., Takinaci, A.C., Korkut, E., Sasaki, N. & Aono, T. (2001). "Cavitation Tunnel Tests for Propeller Noise of a FRV and Comparisons with Full-Scale Measurement". CAV 2001: Fourth International Symposium on Cavitation, June 20-23, 2001, California Institute of Technology, Pasadena, CA USA.

Carchen, A., Shi, W, Sasaki, N. & Atlar, M. (2016). "A prediction program of manoeuvrability for a ship with a gate rudder system". A. Yücel Odabaşı Colloquium Series - 2nd International Meeting on Recent Advances in Prediction Techniques for Safe Manoeuvring of Ships and Submarines, Istanbul, Turkey. November 2016.

ITTC (2014). "ITTC- Recommended Procedures and Guidelines: Model scale noise measurements". 27th International Towing Tank Conference ITTC, Copenhagen, Denmark. Specialist Committee on Hydrodynamic Noise, Section 7.5- 02-01-05.

Sasaki, N. (2013). "ZEUS and NOAH projects of NMRI". 3rd International Symposium on Marine Propulsions (Smp'13), Tasmania, Australia, May 2013.

Sasaki, N., Atlar, M. & Kuribayashi, S. (2015). "Advantages of twin rudder system with asymmetric wing section aside a propeller". J Mar Sci Tecnol., 10.1007/s00773-015-0352-z

Sasaki, N., Atlar, M. & Kuribayashi, S. (2015)." Advantages of twin rudder system with asymmetric wing section aside a propeller". Journal of Marine Science and Technology, 1-12.

Turkmen, S., Carchen, A., Sasaki, N. & Atlar, M. (2015). "A New Energy Saving Twin Rudder System-Gate Rudder". SCC 2015, Intl Conference on Shipping in Changing Climate, Glasgow, 24-26 November

Turkmen, S., Sasaki, N., Atlar, M., Miles, A. & Takeda, T. (2016), "The Gate Rudder application to improve poor course keeping ability of ships". A. Yücel Odabaşı Colloquium Series - 2nd International Meeting on Recent Advances in Prediction Techniques for Safe Manoeuvring of Ships and Submarines, 17-18 November 2016, Istanbul, Turkey.

Appendix A – Comparative wake data

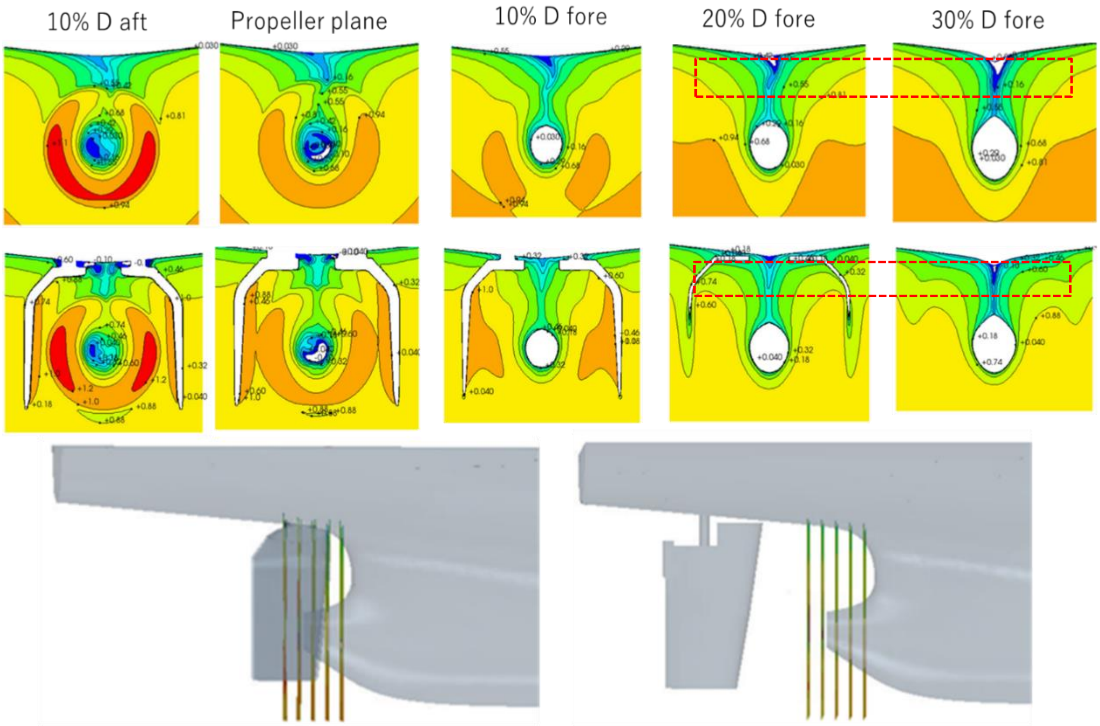

Figure A.1 CFD predictions of effective wake and propeller induced velocities at the aft end: Conventional rudder-propeller system (top figure); GATE RUDDER® system (bottom figure)

A. Yücel Odabaşı Colloquium Series
3rd International Meeting - Progress in Propeller Cavitation and its Consequences:
Experimental and Computational Methods for Predictions
15th – 16th November 2018, Istanbul, Turkey

Challenges in the Optical Design of a Cavitation Tunnel

Luca Savio[1,2], **Chittiappa Muthanna**[1,2] ,**Kourosh Koushan**[1,2]
[1]*Sintef Ocean, Department of Ship and Offshore Constructions, 7052 Trondheim, Norway*
[2]*NTNU, Department of Marine Technology, 7052 Trondheim, Norway*

Abstract: Cavitation is a phenomenon that has been studied since the very beginning of cavitation tunnels by means of visual observation as, in most cases, it easy to detect by the naked eye; for this reason, cavitation tunnels have always granted to a certain degree optical access to the test section. However, it was not until optical measurement techniques were introduced in cavitation tunnels that the optical design of the test section became an important design task. Many of the older tunnels grant visibility to the observer but suffer in general when optical measurement techniques such PIV and DIC are to be used.

When the project of replacing the test section of the cavitation tunnel operated by SINTEF Ocean (formerly MARINTEK) was established it was decided to focus on having a high-quality optical design for optical measurement techniques to be used on largest possible volume of the tunnel.

This paper describes what the design approach was and what are the challenges that have been encountered both during the design phase and during the construction. Besides the obvious compromises that every engineering endeavor must accept such as, for example, structural strength vs window area, some unexpected challenges were encountered during the production of the windows; this prompted a reflection on what is the quality level that is the right balance between manufacturing costs and optical properties.

We deem it to be appropriate and fitting to share our experience with the topic of optical design of cavitation tunnels on the occasion of the inauguration of the new large-scale cavitation tunnel ITU-CAT at Istanbul Technical University.

Keywords: Cavitation tunnel design, Optics

1 INTRODUCTION

The cavitation tunnel located in the Marine Technology Center in Tyholt, designed in the early 60s, was officially opened in 1967. As many of the designs of that time, the tunnel featured a round tests section with 5 circular windows, that allowed seeing the propeller that was located in the center of the test section. The main reason for having such limited optical access to the inside of the tunnel was that the tunnel could be pressurized to a maximum pressure of 6 bars absolute, aiming at studying super-cavitating propellers that would have required high pressurization to avoid cavitation. However, according to the operators of the tunnel throughout the years, the pressure inside the tunnel was seldom set over 1.5 bars, and with a maximum pressure of 2 bars reached just in a few occasions.

Because the high pressurization was never used, while due to the special windows that the tunnel featured optical measurement techniques could not be used, an application to funding to the Research Council of Norway was made to change the test section with a new one that would feature large optical windows and the possibility to insert the models from the top through a large opening, thus improving ease and safety of operations. Changing the test section required also changing the nozzle and diffuser as described in "(Savio 2017)".

The present paper gives an account of the strategy and the challenges that were encountered in the design and production of the optical windows of the new test section of the cavitation tunnel operated by SINTEF Ocean; moreover, it attempts at defining a strategy for modelling, at least in an approximate way, the optical distortion that are generated by the imperfections of the windows in a cavitation tunnel. The proposed model enables both studying the effects of pressure changes in the tunnel and assessing the impact of imperfection that are, for example, discovered during a survey of the optical quality of windows using standard techniques defined for example by ISO.

The first part of the paper deals with the problem of positioning the windows along the test section, while the second part tackles the problems related to the quality of the windows and modifications of the optical path during operation.

2 LAYOUT OF THE OPTICAL WINDOWS

The layout of the optical windows, i.e. their size and spacing, drew a considerable attention throughout the design of the new test section. As a result of the hydrodynamic design of the new nozzle and diffuser, the

---

* *Corresponding author e-mail: Luca.Savio@sintef.no*

total available length for the test section was 6 meters that was reduced to 5.99 meters because of limitations in the production, while the width and the height were 1.3 and 1.2 meters, respectively. Because the height and the width were very similar it was decided that the windows on the bottom and on the side should be interchangeable; after consulting with the company that performed the structural design the windows' longest side was set to 1100 millimeters.

In order to determine the width of the widows, taking into account the necessity of having structural reinforcements between the windows, a simplified approach, relying just on basic geometry, was used.

Figure 8 depicts a horizontal section of the cavitation tunnel that has a half-width equal to T, two set of windows, one that is W wide and one that is 2I wide, and the spacing between the windows equal to G. The reason for choosing this approach can be explained by considering a camera stereo system where the cameras would be ideally rotated 90 degrees apart one from the other, while the scene would be illuminated through the window that is 2I wide. In this simple approach to defining the optical system, all the possible combinations of camera positions that would meet the requirement of being 90 degrees rotated from each other define a region in the tunnel that is squared shaped, with a diagonal equal to W and centered at a distance D from the transversal center of the tunnel.

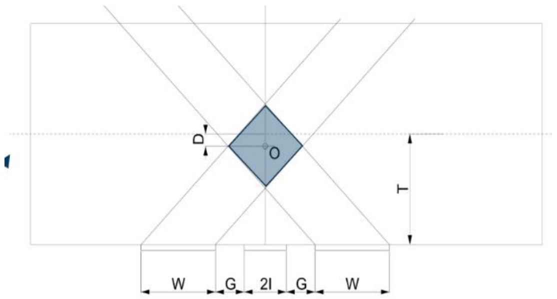

Figure 8 Horizontal cross section of the cavitation tunnel, showing a group of three windows

The distance D of the center O of the squared region can be found to be:

$$D = T - \left(I + G + \frac{W}{2}\right) = 0 \qquad (1)$$

It is of course of little use having an optical configuration in which D is not equal to zero, since that would result in a non symmetrical optical setup from the two sides of the tunnel and hence D must be equal to zero. By imposing D to be equal to zero it is possible to determine what is the allowed gap G in between the windows for the structural reinforcement of the tunnel, once the size W and 2I have been fixed.

Table 1 Possible values for the gap G, based on the windows sizes W and 2I

W/2I	**0.35**	**0.4**	**0.45**	**0.5**	**0.55**	**0.6**
0.35	0.3					
0.4	0.275	0.25				
0.45	0.25	0.225	0.2			
0.5	0.225	0.2	0.175	0.15		
0.55	0.2	0.175	0.15	0.125	0.1	
0.6	0.175	0.15	0.125	0.1	0.075	0.05
0.65	0.15	0.125	0.1	0.075	0.05	0.025
0.7	0.125	0.1	0.075	0.05	0.025	
0.75	0.1	0.075	0.05	0.025		

The table of the gaps that are allowed base on the configuration of the windows proved to be a very useful for narrowing down the problem of finding reasonable combinations of window sizes and gaps.

The final dimensions of the windows are 1.1 x 0.6 meters for the big ones, 1.1 x 0.4 for the small ones with a spacing equal to 0.15 meters between them; with this dimensions and neglecting the top surface of the tunnel, where the hatch for mounting the model is positioned, the new test section is made for 60% of its extent transparent.

3 OPTICAL QUALITY OF THE WINDOWS

The optical access to the inside of the test section is granted through large Polymethyl methacrylate (PMMA) windows or sometime through smaller optical glass windows.

PMMA windows are very robust and comparatively cheap, but as stated by "(Youngquist et al 2015)" the main concern for PMMA windows was that of providing protection from the environment while granting some optical access, so that, for example, pilot of jet fighter had to cope with rather significant optical distortions.

In the cavitation tunnel application, PMMA has proved to be able to withstand the cycles of pressurization and depressurization that are typical during operation and at the same time allowing observation of cavitation. However, if beside the use for observations the cavitation tunnel is also used for optical measurement techniques it is worth asking what the requirement for the quality of the windows are.

Further, PMMA has a rather small flexural rigidity, meaning that the variations of pressure inside the cavitation tunnel lead to large deformation of the windows, thus altering the optical path of any optical system that is placed outside the tunnel. Although currently this may not be considered a major issue, this may become an issue when techniques as PIV will be employed also in cavitating conditions.

Giving an, albeit very simplified, mathematical foundation to tackle the above-mentioned problems is the goal of this second part of the paper.

3.1 Production procedure of PMMA windows

PMMA windows are produced through cutting and routing of raw materials sheets. The sheets are obtained through cooling of the molten base component, though a process of polymerization that is typically confined between two polished flat surfaces. During polymerization PMMA produces significant heat and shrinks; without going to much into details, the combination of heat production with volume change during the production process makes the geometrical control of PMMA sheets difficult and leading ultimately to sheets that may present significant changes of thickness, in the order of magnitude up to 5% for the thicknesses that are relevant for the cavitation tunnel windows. However, the change in thickness is almost unnoticeable as it appears as a large scale waviness with wave length that are in the order of magnitude of the sheet size, while at the centimeter scale it is not possible to identify any sort of waviness. In principle, it possible to identify parts of a sheet that have the correct thickness and use just those parts or out of many sheets identify those that by chance are within the tolerances set for the project; however, such a procedure, although used in some demanding situations, is rather expensive. Commonly, in order to bring the sheets to the size that is needed for the specific application, the sheets are flattened by routing along with milling for the sides, if needed. The routing process introduces a much shorter waved inhomogeneity of the surface, which has been in the past disregarded due to primary function of PMMA windows as protection from the environment. The inhomogeneity may be both geometrical, meaning by that a physical un-evenness of the surface, or refractive, meaning that some areas seem to have a different refractive index; in any case in the framework of Snell's law that will be used in the following, the two can be interchanged as their net effect is to refract the light rays on a distorted path compared to the one they would have followed, were the surface free from any manufacturing defects.

3.2 The pinhole camera model and other simplifications

A widely mathematical model for an imaging device is the pinhole camera. The pinhole camera model arises from the simplest of the imaging devices that can be built as physical object: a small hole in a box. In the physical pinhole camera, the rays of light that enter through the small hole are focused by the small hole itself and projected on the opposite side of the box making an upside down image of the world outside the box; thus the pinhole has everything that is needed to model an imaging device: a focusing object, the small hole acts like a lens, and image plane, the side of the box opposite to the side with the hole in it. Due to its simplicity, but at the same time completeness the pinhole camera is well suited to be used as a mathematical model of real, more complex, imaging devices.

Moreover, since we are seeking a simplified approach to the problem, we consider a 2D model of the camera. In the 2D version the pinhole camera, the imaging plane is segment. **Figure 9** depicts a 2D pinhole camera system in its two variants: positive and negative. A negative system renders images that are upside-down, while a positive renders images with the same orientation as in the real world; however, both systems are equivalent in terms of mathematical modelling.

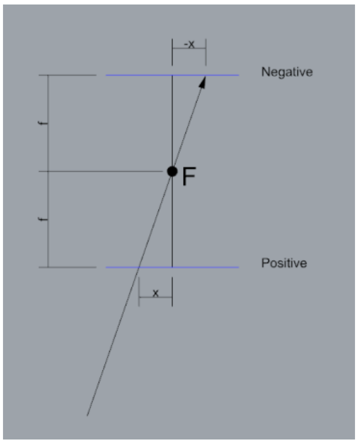

Figure 9 The pinhole camera model, positive and negative

By limiting the problem to the 2D case, we simplify greatly also the mathematics involved in the problem; in fact, the 3D Snell's law of refraction, which involves products 3D vectors, is simplified to the 2D counterpart: $n_1 sin(\theta_1)=n_2 sin(\theta_2)$.

Further we notice that the angles are involved are small and hence we apply the usual linearization of the trigonometric functions; hence Snell's law becomes $n_1\theta_1=n_2\theta_2$.

3.3 The equivalent refractive index for a cavitation tunnel

Although as we will show it is not a major concern for large facilities, the rays of lights travel through 3 different materials when the imaging cameras are placed outside the tunnel.

In **Figure 10** the imaging plane of a camera that has a focal length equal to f is depicted as a blue horizontal line. A ray departs from the camera focal point and travels through three layers of different materials: air with a refractive index $n=1$ and thickness equal to s, PMMA with a refractive index $n1 = 1.49$ and thickness equal to t and finally, a layer of water up to the distance D from the inside of the window that has refractive index $n_2 = 1.33$. The angle α represent the angle between the ray and the camera optical axis, while β_1 and β_2 the angles from the local normal after the ray has been refracted by PMMA and water, respectively. Finally, β_3 represents the refracted angle the ray would have traveled, if it were to propagate through a single medium that had a refractive index to be determined based on those of PMMA and water.

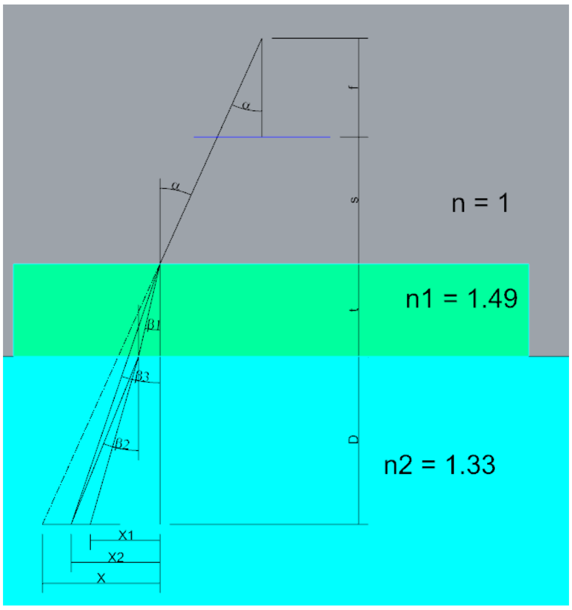

Figure 10 Actual and equivalent optical path when the ray of light propagates through three different media

In the following the approximation of small angle for trigonometric functions is made.

The length X_2 can be computed, with reference to **Figure 10**, as:

$$X_2 = t\beta_1 + D\beta_2 \tag{2}$$

With β_1 and β_2 expressed in terms of linearized Snell's law by:

$$\beta_1 = \frac{n}{n1}\alpha; \beta_2 = \frac{n1}{n2}\beta_1 = \frac{n}{n2}\alpha \tag{3}$$

The angle β_3 is:

$$\beta_3 = \frac{X_2}{D+t} = \frac{n}{n_x}\alpha \tag{4}$$

And the equivalent refractive index n_x is found to be:

$$\frac{n_x}{n} = \frac{D+t}{X_2}\alpha = \frac{D+t}{t\frac{n}{n1} + D\frac{n}{n2}} \tag{5}$$

In case the thickness of the window t can be neglected, Equation 5 leads to the usual assumption $n_x = n_2$. Equation (5) may be of some interest if the test object is close to the sides of the tunnel, while it is negligible farther inside the tunnel. Equation (5) allows simplifying the problem of computing the optical path inside the tunnel to a single interface rather than to a double interface. In the following a single interface will be used, with one of the media being air and the other one an hypothetical medium of refractive index $n = n_x$.

3.4 Optical distortions

There are several definitions of optical distortions that could be applied to the tunnel case, but because we are interested in the effects that distortions cause on images, we seek a more tailored approach to the specific case of an imaging device that is set to acquire images of an object inside the tunnel. More specifically, we would like to asses what is the effect of the optical distortions that can be assessed during an optical test in air or by other means as for example deformations during operation, once the same optical surface is placed on the water to air interface of the cavitation tunnel. In other word, we try to establish a procedure for setting realistic requirements on the quality of optical surfaces, in terms of quantities that can be measured before putting the windows in use.

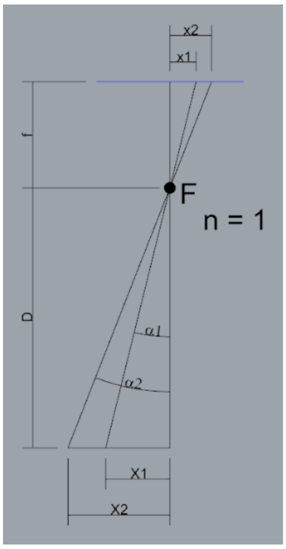

Figure 11 The projective mapping of a pinhole camera in the case of no distortions

To introduce the approach that we are proposing let us consider the projective mapping of the pinhole camera as depicted in ***Figure 11***, where the coordinates *X1* and *X2* are mapped through the focus **F** to the image plane on the coordinates x_1 and x_2 respectively. The device focal length is *f*, while the distance *D* defines where the segments X_1 and X_2 are measured. We are interested in finding what is the relation of the angles α_1 and α_2, the segments x_1 and x_2 and the focal length f in this case were no optical distortion are present. The relation that is sought is the usual projective relation for the pinhole camera:

$$\alpha_1 = \frac{X_1}{D} = \frac{x_1}{f}; \alpha_2 = \frac{X_2}{D} = \frac{x_2}{f} \tag{6}$$

By taking the difference of the two angles α_1 and α_2 we obtain:

$$\frac{\alpha_2 - \alpha_1}{x_2 - x_1} = \frac{X_2 - X_1}{x_2 - x_1}\frac{1}{D} = \frac{1}{f}; \tag{7}$$

Finally, by taking the limit of Equation (7) we can show that for a pinhole camera and zero optical distortion the following applies.

$$\lim_{(x2-x1)\to 0} \frac{\alpha_2 - \alpha_1}{x_2 - x_1} = \frac{d\alpha}{dx} = \frac{dX}{dx}\frac{1}{D} = \frac{1}{f} \Rightarrow \frac{d\alpha}{dx} = \frac{1}{f}$$

(8)

Equation (8) gives us also a rule to compute the derivative $d\alpha/dx$ starting from the knowledge of X; in fact, we can, by using the chain rule, write that:

$$\frac{d\alpha}{dx} = \frac{dX}{d\alpha}\frac{d\alpha}{dx}\frac{1}{D} = \frac{dX}{d\alpha}\frac{1}{f}\frac{1}{D} \tag{9}$$

Which will turn out very useful in the following.

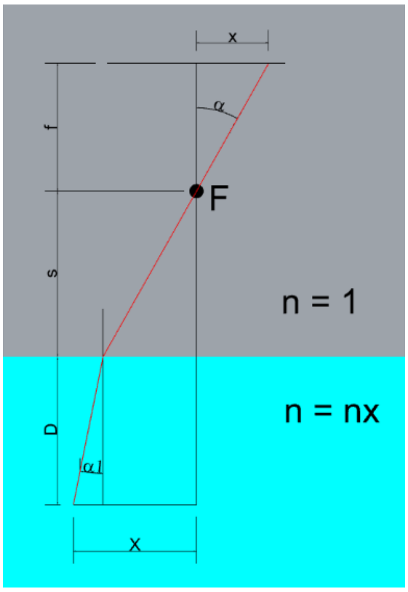

Figure 12 Optical path of a light ray in the two media with perfect interface case

The next step is to repeat the same exercise, but with the rays that are crossing a perfect interface between air and a medium with refractive index n_x. The camera is at a distance **s** from the interface and because of the different refractive indexes the ray propagating at an angle from the camera focus α is bent at the interface to α_1. By using the linearized Snell's law, we can see that

$$X = s\alpha + D\alpha_1 = s\alpha + D\frac{n}{n_x}\alpha \tag{10}$$

By applying the derivation rule expressed by Equation (9) we see that in this case:

$$\frac{d\alpha}{dx} = \frac{1}{fD}\left(s + D\frac{n}{n_x}\right) = \frac{1}{f}\left(\frac{s}{D} + \frac{n}{n_x}\right) \tag{11}$$

Which, as often is the case, for small **s** compared to D reduces to:

$$\frac{d\alpha}{dx} = \frac{1}{f}\frac{n}{n_x} \tag{12}$$

The result in Equation (12) was expected as it can be interpreted as an increase of focal length equal to n_x/n, which is the familiar magnification effect observed in object immersed, for example, in water.

We want now to introduce an imperfection at the interface between the two media. The imperfection can be interpreted either as a geometrical unevenness of the surface or as a variation of the refractive index, as it will be made clear in the following. However, we can start by thinking the imperfection being geometrical and being expressed by continuous function $\xi(\alpha)$ that can be derived at least twice as **Figure 13** shows.

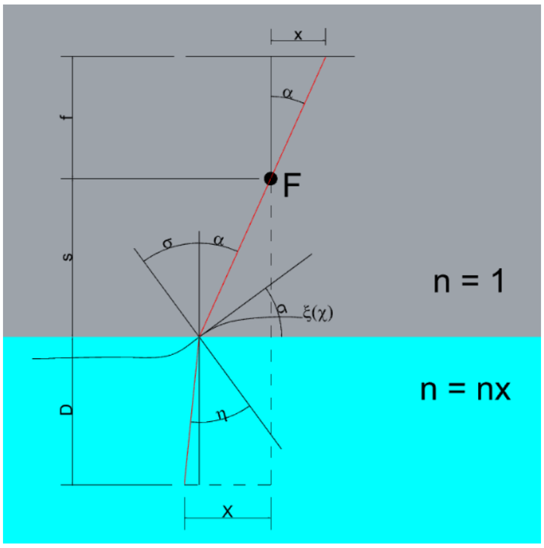

Figure 13 Optical path in the case of uneven interface

Further we introduce the variable $\sigma(\chi)$ as the local angle identified by the tangent of the curve $\xi(\chi)$ in $\chi = s\alpha$.

$$\sigma(\chi) = arctan(\frac{d\sigma}{d\chi}) \approx \frac{d\sigma}{d\chi} = \frac{d\xi}{d\alpha}\frac{d\alpha}{d\chi} = \frac{d\xi}{d\alpha}\frac{1}{s} \tag{13}$$

In analogy with what was done before, we find the distance X from the optical axis of the camera of the point that is imaged by the camera at an angle equal to α and at a depth D from the optical interface; we assume that the actual surface geometry change $\xi(\alpha)$ is negligible compared to D, keeping the latest constant. The angle to the vertical formed by a ray departing from the camera at an angle α is no longer α but $\alpha+\sigma$. After the refraction the angle to the local vertical defined by the surface $\xi(\alpha)$ is η, which can be once more computed through Snell's linearized law.

$$\eta = \frac{n}{nx}(\alpha + \sigma) \tag{14}$$

The distance X can be then computed as:

$$X = s\alpha + D\left[\frac{n}{n_x}(\alpha + \sigma) - \sigma\right] \tag{15}$$

Finally, recalling the derivation rule established by Equation (9) we can find:

$$\frac{d\alpha}{dx} = \frac{1}{f}\left[\frac{s}{D} + \frac{n}{n_x}\left(1 + \frac{d\sigma}{d\alpha}\right) - \frac{d\sigma}{d\alpha}\right] = \frac{1}{f}\left[\frac{s}{D} + \frac{n}{n_x}\left(1 + \frac{d^2\xi}{d\alpha^2}\frac{1}{s}\right) - \frac{d^2\xi}{d\alpha^2}\frac{1}{s}\right] \tag{16}$$

Equation (16) expresses the change in $d\alpha/dx$ in terms of difference in refractive index n/n_x and surface curvature $d\sigma/d\alpha$; in other words, it expresses the local change in focal length. There are several remarks to be made on Equation (16):

- No optical interface and homogeneous optical interface are as expected a special case of the equation
- Intuitively we were expecting curvature to play a role and $d\sigma/d\alpha = d^2\xi/d\alpha^2$ is the curvature of $\xi(\alpha)$

- no assumptions were made on the function $\xi(\alpha)$ that describes the surface imperfection; $\xi(\alpha)$ must be continuous and with at least to derivatives; $\xi(\alpha)$ could be expressed in terms of Fourier series allowing a large variety of reasonable surfaces to be represented. For example, the effect of window deflection due to depressurization can be studied using either FEM simulation or analytical solutions to compute the deformed shape of the window.
- The ratio n/n_x is to be considered as the average and not the local one. Local variations are covered by the term $d^2\xi/d\alpha^2$.
- The model is rather coarse; in fact, it fails to capture the fact that, for example, a flat surface induces a pincushion distortion. Although this may be considered a problem, it shall be noted that distortions of that kind can be eliminated with the existing calibration algorithms.

The two forms of Equation (16), i.e. the one in terms of $d\sigma/d\alpha$ and the one in $d^2\xi/d\alpha^2$, lead to two interpretations of the equation; the representation in terms of $d^2\xi/d\alpha^2$ is the most obvious, but the one in terms of $d\sigma/d\alpha$ leads to an interpretation in terms of optical distortion that is independent from the actual shape of $\xi(\alpha)$.

In fact, if we consider the following identity:

$$\frac{1}{f}\frac{d\sigma}{d\alpha} = \frac{s}{f}\frac{d\sigma}{d\chi} \tag{17}$$

We can see that $d\sigma/d\chi$ in Equation (17) has the dimensions of an angle divided by a length, which is consistent with the definition of optical distortion provided, for example, by ISO. In this latest interpretation of equation (16) the distortion may be of any kind, as would be measured for example during a specific test as those described by "(Youngquist et al 2015)".

3.5 An example of application

Equation 16 includes two terms: one arising from the change in refractive index at the interface of the ideal surface and one due to the imperfections of the surface. The first contribution is of little interest for determining the optical distortions induced by the window because, as already pointed out, the effect of this term is, in the model presented here, only to increase the focal length. Equation (16) can be rewritten in to Equation (18) where the two contributions are separated.

$$\frac{d\alpha}{dx} = \frac{1}{f}\left(\frac{s}{D}+\frac{n}{n_x}\right)+\frac{1}{f}\frac{d\sigma}{d\alpha}\left(\frac{n}{nx}-1\right) \tag{18}$$

Which can further rewritten, using Equation (17), as:

$$\frac{d\alpha}{dx} = \frac{1}{f}\left(\frac{s}{D}+\frac{n}{n_x}\right)+\frac{s}{f}\frac{d\sigma}{d\chi}\left(\frac{n}{nx}-1\right) \tag{19}$$

Where the term $d\sigma/d\chi$ is explicitly shown so that some order of magnitude considerations could be made. We can consider s to be in the order of magnitude of a few centimeters, while D may be considered to be around 1 meter, so that there is roughly a factor of 10 among them; if the first medium is air and the second can be approximated with water, then $n = 1$ and $n_x = 1.33$.

$$\frac{d\alpha}{dx} = \frac{1}{f}(0.1+0.75)+\frac{1}{f}\frac{d\sigma}{d\chi}(0.75-1) = \frac{0.85}{f} - \frac{0.025}{f}\frac{d\sigma}{d\chi} \tag{20}$$

Given these numbers it is possible to observe that the effect of the optical distortions is rather limited, unless the distortions are large, as Equation (20) shows. A procedure like the one shown in this example can be used to set an upper limit for the maximum distortion that is acceptable in a given optical system.

3.6 Extension to 3D

Extending the approach to 3D is not deemed necessary for two reasons: first, the 3D case can be approximated by considering singularly any of the planes of sheaf that is identified by the optical axes of the camera; secondly, if a full assessment of the effect of the distortions is to be performed in 3D, the approach presented here is too simplistic and, at the same time, programming the full 3D Snell's law is not a prohibitive task, although it may results being computationally demanding.

4 Conclusions and future work

In the present paper we have shown a strategy to tackle the effects of optical distortion in the cavitation tunnel case. It shall be noted that in literature there are several ways of dealing with the problem, but these are typically referring to simplified cases like flat or round surfaces; for this reason, we decided to seek a different approach and use the pinhole camera model. A different approach could have been to consider the thin lens model, which would have been able to capture finer details of the problem. Nevertheless, some aspects of the model are in agreement with the expectations, giving some confidence in to the model. The net result of the model is to predict a change in focal length due to the distortion. How to convert the change in optical length in to image quality is the next step; intuitively a local change in focal length leads to blur in the image, but at the moment we are not capable of quantify that effect.

REFERENCES

Youngquist, R. C.; Skow, M.; and Nurge, M. A.:(2015)'A Comparison of Three Methods for Measuring Distortion in Optical Windows', NASA TM 2015-218822.

ISO 1997 ‘Road Vehicles—Safety Glazing Materials—Test Methods for Optical Properties’, International Organization for Standardization, ISO 3538:1997(E).

G W C Kaye and T H Laby (1986) 'Tables of Physical and Chemical Constants',. Longman. 15th ed. 1986, 1993 reprint. ISBN 0-582-46354-8

Savio L., Sileo L., Muthanna C., Steen S., Spence S., Berget K., (2017) "The Upgrade of the Large Cavitation Tunnel of the Marine Technology Centre in Trondheim", Fifth International Symposium on Marine Propulsors smp’17, Espoo, Finland, June 2017

Propulsion Testing in the HYKAT Cavitation Tunnel

Christian Johannsen*

Hamburg Ship Model Basin (HSVA), D-22305 Hamburg, Germany

Abstract: The new cavitation tunnel ITU-CAT is a great facility that will enable the Istanbul Technical University to perform cavitation tests on a high technical level in future. Cavitation testing, however, is only one thing that can be done in a cavitation tunnel. Comparative propulsion testing is something else - as long as the tunnel is big enough to accommodate the whole ship model for wake generation. The paper presents a new testing technique that is available in HSVA's large cavitation tunnel HYKAT, meanwhile as a mature standard for our commercial customers. The new technique aims on the determination of small gains in a propulsor's efficiency, as it can be achieved for example by addition of fins to the propeller cap, by an asymmetric rudder, a costa bulb or whatever. The big advantage of performing those tests in HYKAT instead of a towing tank is that here the propulsor operates at high Reynolds numbers and in the ship model's wake field at the same time.

The paper describes the new technique, addresses its pros and cons and also presents results achieved by this new technique so far.

Keywords: Comparative Propulsion Testing, HYKAT Cavitation Tunnel, Testing at High Reynolds Number.

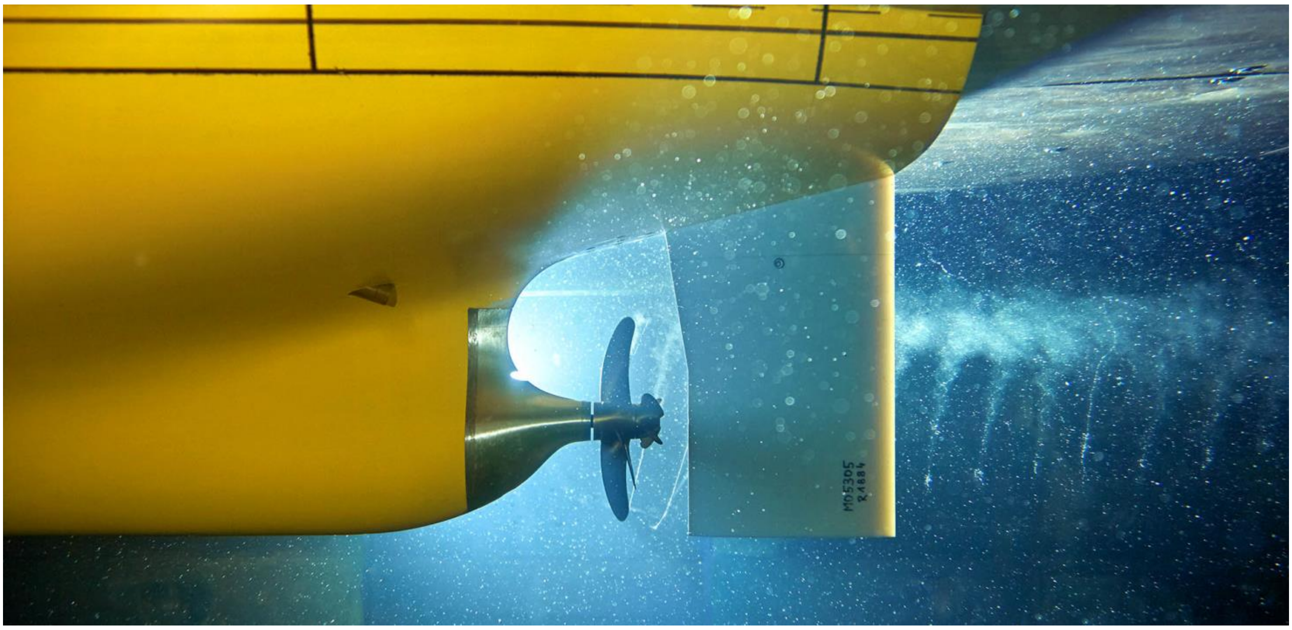

Figure 1 Propeller with Cap Fins in the Test Section of HYKAT Cavitation Tunnel

1 INTRODUCTION

Driven by the expectation of an ongoing oil price recovery, but more and more also by ecologic considerations, ship owners show much interest in retrofit measures to improve hydrodynamic efficiency of their ships.

Such measures, the so-called propulsion improving devices (PID), always come along with a certain investment at the beginning, combined with the vendor's promise of an energy saving potential over the following years. Serious calculation of the payback period, however, requires the reliable knowledge of the efficiency increase achievable by the PID in combination with the ship in question.

The prediction of such an efficiency gain is a classical task for a ship model basin such as the HSVA. However, the dimensions of these devices are typically quite small at model scale, so the measured influences are small as well and are prone to scale effects. The full scale prediction based on these model tests is therefore quite a challenge.

---

* *Corresponding author e-mail: johannsen@hsva.de*

To improve the situation, HSVA has developed a new testing procedure with increased accuracy and applicable for many types of PIDs on the market. This procedure is meanwhile a mature brick stone for the risk assessment prior to investing money into PIDs.

2 THE PROBLEM WITH THE SCALE EFFECTS

The scaling problem with investigation of PIDs at model scale shall be introduced here using the example of propeller caps equipped with fins. These small fins are mounted downstream of the propeller and rotating with it on its cap (Figure 1). As a result of the Helmholtz theorem of vorticity conservation a so-called hub vortex is induced into the ocean behind the propeller cap, representing the counterpart of the well-known tip vortices at the ends of the propeller blades. This hub vortex includes rotative energy, being lost in the ocean. It is the idea behind the hub cap fins to recover this energy. Different makers are on the market with fin caps of different size, shape, and fin number. A variety of caps tested at HSVA is shown in figure 2.

Figure 2 Different Maker’s Propeller Fin Caps

To understand the problem one has to introduce the Reynolds number *Rn*, which expresses the relation between inertial forces and friction forces and is a measure for the boundary layer characteristics in the flow around a body. A small Reynolds number stands for a small body moving slowly through a very viscid liquid. $Rn = \infty$ on the other hand characterizes the other extreme, i.e., an ideal frictionless flow condition.

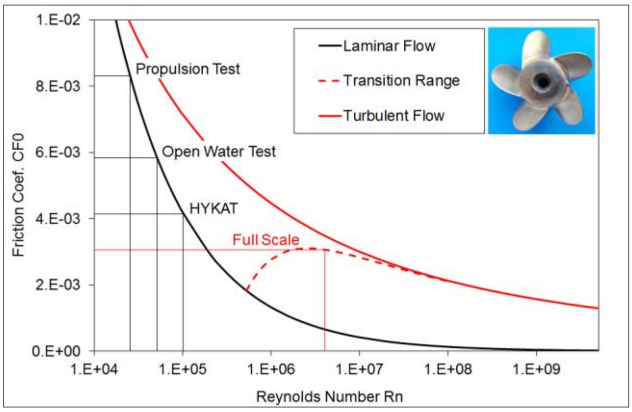

Figure 3 Flow Characteristics at Cap Fins of a 4,500 TEU CV

The flow characteristics around the propeller cap fins of a typical 4,500 TEU container vessel are shown in figure 3 for different scenarios. The non-dimensional friction coefficient C_{F0} (frictional resistance normalized with dynamic pressure and surface area) is plotted versus the Reynolds number (Prandtl-Schlichting friction line). In full scale the flow around the fins is almost fully turbulent, resulting in the lowest friction coefficient among the four scenarios indicated in figure 3. Modelling the same situation in a propulsion test carried out in a towing tank at scale 1 : 33, one gets the lowest Reynolds number among the four and as a result of that 2.7 times more friction.

Knowing about this massive friction exaggeration many model basins offer another test set-up for the comparative investigation of propeller cap fins, as it is shown in figure 4.

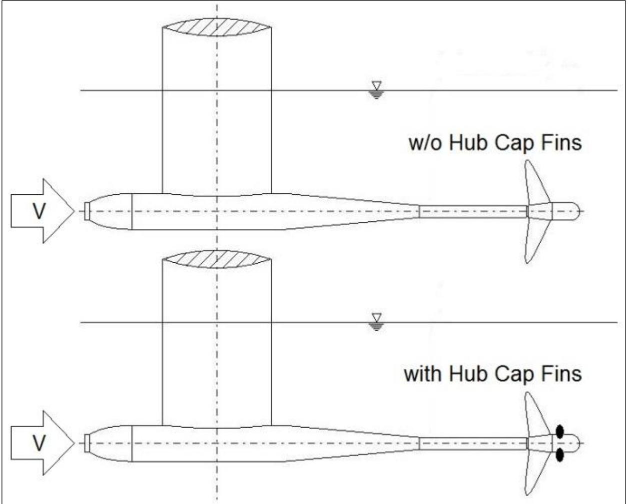

Figure 4 Open Water Set-Up for Comparative Testing

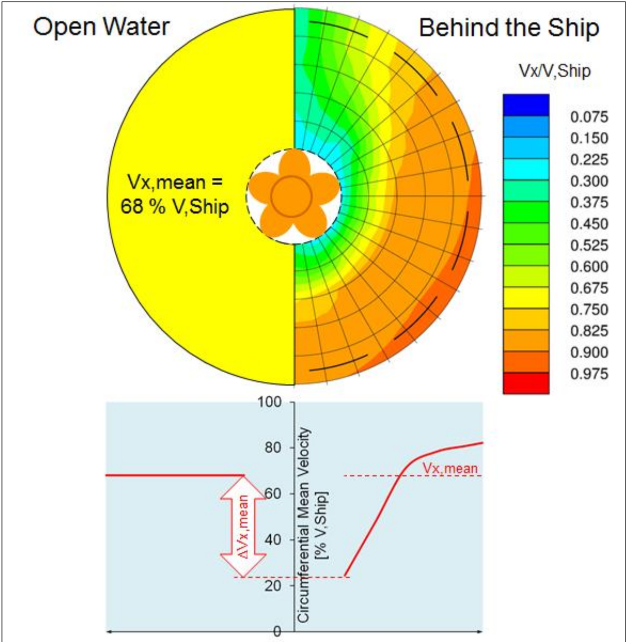

Figure 5 Axial Velocity Distribution and Circumferential Mean Velovity in Open Water and Behind a 4,500 TEU CV

This set-up, featuring a reversed standard propeller open water testing device, allows higher flow speed as no ship model is involved and Froude scaling has not to be fulfilled. According to figure 3 the friction forces get closer to full scale reality indeed, but are still exaggerated by a factor of 1.9. The bigger drawback of this set-up, however, is the fact that the propeller is operated in homogeneous inflow. On its upper right side figure 5 shows the axial velocity distribution in the propeller plane of the 4,500 TEU container vessel. The wake peak in the 12 o'clock position can be seen as well as the deceleration of the flow speed towards the inner propeller radii. On the left the corresponding situation in the open water set-up is shown. Here only the mean flow speed averaged over the whole propeller disc can be adjusted properly. The local velocity, however, is the same everywhere in open water conditions. This means that at the inner radii, where the propeller cap fins are located, the flow speed is significantly too fast. The lower part of figure 5, where the circumferential mean values on each radius are plotted versus the radius, may illustrate this in detail. Moreover, the whole radial load distribution of the propeller is altered and last but not least the variation of the angle of attack of the fins with their rotation is not existent at all in homogeneous inflow. The consequence is a significant falsification of the propulsion improving effect of the propeller cap fins in this set-up.

3 THE SOLUTION: COMPARATIVE TESTING IN THE HYKAT CAVITATION TUNNEL

The solution is the performance of comparative propulsion measurements in HSVA's large Hydrodynamics and Cavitation Tunnel HYKAT (Figure 6). The test section of this tunnel is 11 m x 2.8 m x 1.6 m big (L x B x H) and allows installation of the complete ship model as it was used in the corresponding towing tank tests. The tunnel is operated without a free surface so that Froude scaling has not to be fulfilled. In case of the example used in figures 3 and 5 the tunnel water speed reached 6 m/s and resulted in the HYKAT scenario shown in figure 3. There is still an exaggeration of the friction forces by 35 % but it is clearly visible that this test scenario comes closest to full scale reality in view of both modelling of friction effects (see Figure 3) and modelling of propeller inflow conditions (see Figure 5).

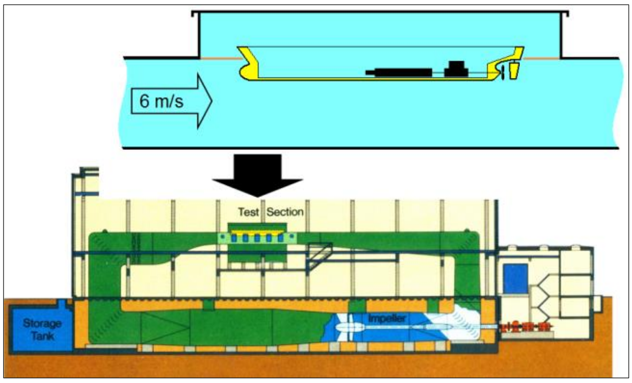

Figure 6 HSVA's Hydrodynamics and Cavitation Tunnel HYKAT

In HYKAT the ship model is fixed in the test section and its wave system is suppressed. Consequently the self-propulsion point of the model cannot be found in this set-up. The proposed testing procedure is therefore not a substitute for a regular self-propulsion test carried out in a towing tank. The effect of small propulsor modifications on its performance, however, can be investigated in HYKAT with high accuracy and at high Reynolds number. The basic assumption for this differential testing is illustrated in Figure 7. In the self-propulsion point of a ship the propeller has to equalize the ship's resistance R_{Hull} plus the resistance increase $\Delta R_{Prop.}$ that is caused by the propeller's action. As long as we talk about small propulsor modifications, such as addition of cap fins or small blade modifications, one can assume that $\Delta R_{Prop.}$ is not influenced by this. As long as the flow in front of the propeller is not changed by these modifications, also R_{Hull} will not change. As a consequence of this one can state that at constant tunnel water speed the propeller thrust $T = R_{Hull} + \Delta R_{Prop.}$ must be the same with and without cap fins as well.

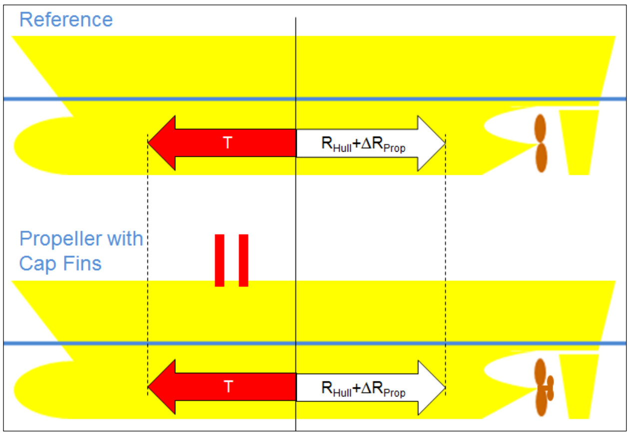

Figure 7 The Principle of Comparative Propulsion Testing in HYKAT

With this assumption the test procedure becomes quite easy and consists of the following steps visualized in figure 8 for the investigation of propeller cap fins:

1. For the ship model in its reference configuration (no cap fins) the propeller thrust T and torque Q are measured at a constant tunnel water speed for a number of different rotational propeller speeds N. Together with the resulting thrust coefficient $K_T = T / (\rho \cdot N^2 \cdot D^4)$ and the delivered power $P_D = 2 \cdot \pi \cdot N \cdot Q$ these values are plotted versus the propeller speed (Figure 8, black curves).
2. For a given K_T, representing the propulsion point of the vessel equipped with the reference propeller at a certain ship speed, the corresponding rotational propeller speed in HYKAT can be read off the above mentioned K_T-N-curve. At this propeller speed the corresponding thrust and torque can be found, this triple $(N, T, P_D)_{ref.}$ characterizing the reference arrangement in HYKAT.
3. For the propeller with cap fins the same set of measurements is then repeated at exactly the same

tunnel water speed as adjusted in step 1 (Figure 8, red curves).

4. For the alternative arrangement that rotational speed can then be determined, at which the same propeller thrust T is generated as the reference arrangement has revealed in its propulsion point in step 2.
5. The propeller speed found in step 4 defines the propulsion point of the alternative arrangement. It can be compared to the reference arrangement, indicating the influence of the arrangement change on the propeller shaft speed.
6. The major result, however, is the corresponding P_D value that can be related to the reference P_D to determine the propulsive gain ΔP_D that is achievable with the alternative arrangement.

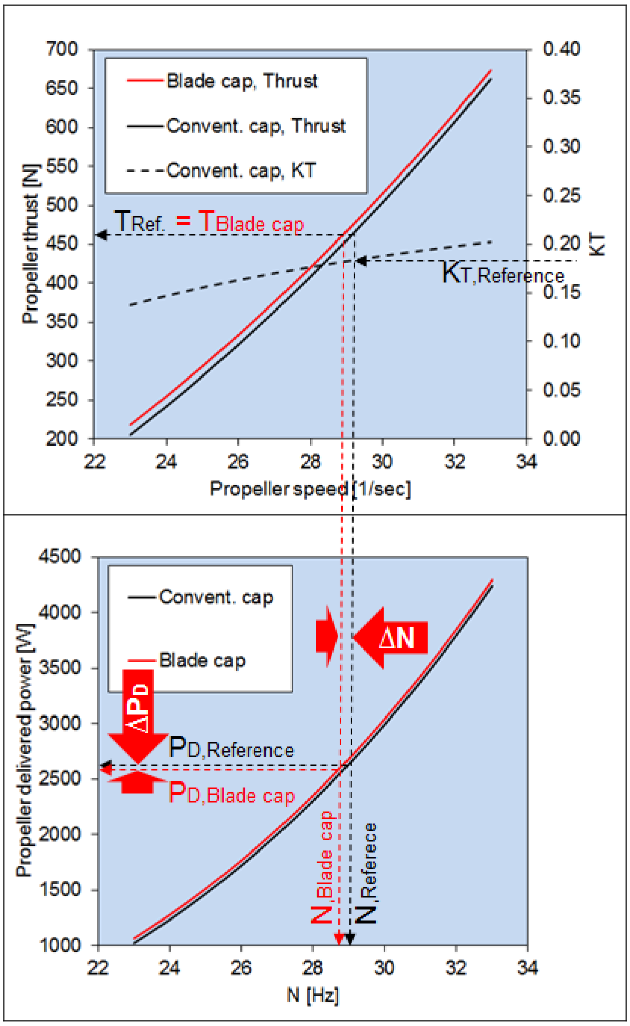

Figure 8 Procedure for Comparative Propulsion Testing in HYKAT Cavitation Tunnel

4 RESULTS

The above testing technique has meanwhile been applied manifold in HYKAT for a large variety of ship types. It has proven very high reliability as several repeat tests revealed constant results. It can be regarded as a mature brick stone for the assessment of propulsion improving re-arrangements.

Figure 9 gives a few examples from investigations of propeller cap fins. The propellers of five different projects were fitted with propeller fin caps as shown in figure 2. The propulsive gain was determined according to the procedure described in the foregoing section. This was done not only for one particular reference K_T, but over a larger range of thrust coefficients to figure out how the cap fin effect develops with increasing propeller load. Three different ship types of very different scale ration contributed to this investigation.

Quite consistently all tested luxury yachts revealed a remarkable efficiency increase in the range of 1 to 2 % power requirement. They all showed an increasing effect with increasing propeller load. This follows the theoretic expectations as with increasing load the rotative losses (and not only the *rotative* losses) increase. Consequently with higher load there is more energy loss to be regained.

In opposite to the yachts neither the container vessel nor the tanker showed a significant receptivity for the value of a propeller fin cap. Here the gains bobbed up and down around 0.5 %, being quite independent of the propeller load.

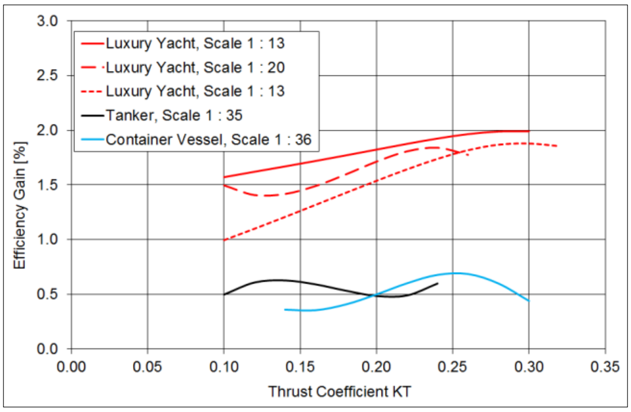

Figure 9 Efficiency Gains Achieved with Propeller Cap Fins

An explanation for this ship depending effectiveness can be found by a look into the differing propeller design philosophy for different ship types. Such luxury yacht propellers are optimized rather for high comfort than for highest possible efficiency. High comfort in this context means low propeller induced hull pressure pulses and resulting vibrations. This demand requires a radial load distribution along the propeller blades that features high blade loading on the inner radii but strong unloading close to the blade tips. This peculiarity ensures weak or even non-existing tip vortex cavitation but on the other hand causes strong hub vortex formation. The stronger the hub vortex the stronger the rotative losses and the higher the potential of the hub cap fins. As a confirmation of this theory it should be mentioned that those mega yacht propellers often show pronounce hub vortex cavitation in HYKAT, which disappears when a fin cap is mounted behind the propeller.

Merchant ship propellers in contrast are focused on high efficiency and almost never show hub vortex cavitation during the cavitation observations in HYKAT. For this reason it might not be surprising that the hub cap fins do not regain a lot.

The above findings, however, should not be generalized too quickly. Other influences like relative hub diameter, absolute propeller thrust load, blade number, or blade pitch adjustability may have an influence as well and need to be investigated in future. Reliable working equipment for these investigations is now on the market with HYKAT and the procedure described above.

More detailed descriptions of the method as well as further results can be found in the corresponding references given at the end of this paper (Müller 2017-1 and -2).

5 ENHANCEMENTS FOR UNCONVENTIONAL RUDDER INVESTIGATION

As explained above, the testing procedure so far presumes that the propeller thrust requirement is not dependent on the different arrangements to be compared. This assumption is justified for propeller cap fins for sure, it is probably reasonable for small blade modifications as well, but it is certainly inapplicable when the rudder geometry is changed significantly. This, however, is a pity because unconventional rudders are a well-known mean to improve propulsive efficiency. Asymmetric rudders as well as rudders with costa bulbs or even rudder fins are known in this regard.

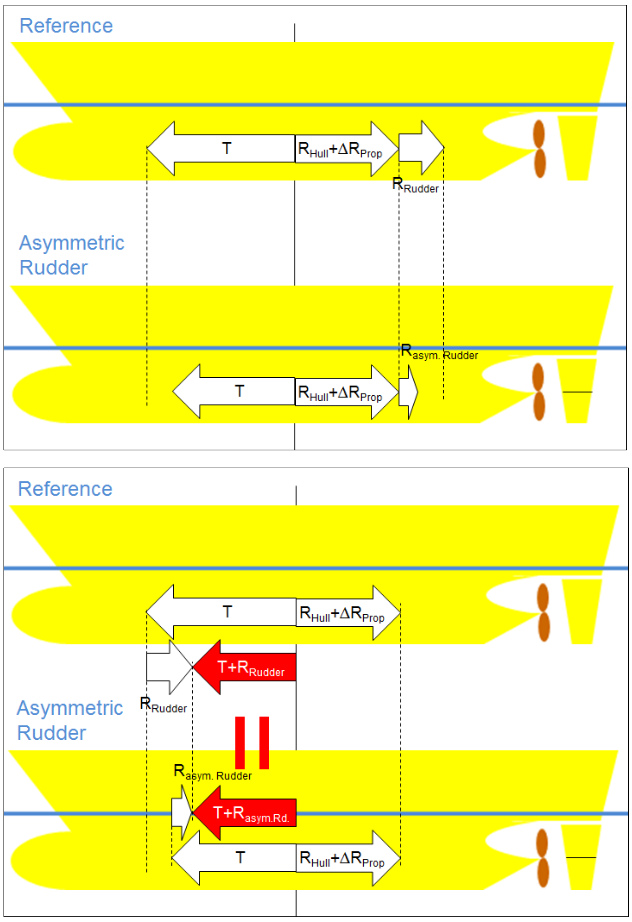

Figure 10 Enhancement of the Principal towards Investigation of Efficiency Improving Rudders

To include this group of devices in the scope of possible applications of the new procedure, just a small modification in the basic assumption is necessary. The upper half of figure 10 explains the idea. Taking the rudder into account as a separate part of the ship hull, the propeller thrust has to equalize the sum of hull resistance plus propeller-caused resistance increase plus – and this new term represents the enhancement of the method – the resistance of the rudder:

$$T = R_{Hull} + \Delta R_{Prop.} + R_{Rudder} \quad .$$

Even if R_{Hull} and $\Delta R_{Prop.}$ are not dependent on the actual propulsor arrangement, the change of the rudder does change the thrust requirement T as soon as the new rudder has a different resistance.

The lower part of figure 10 just represents a rearrangement of the force vectors shown in the upper part already. Here the rudder resistance vectors have been shifted to the left side of the balance so that the new basic assumption for the testing method becomes obvious. Instead of $T = const.$ one has to postulate $T + R_{Rudder} = const.$ Except for this little modification the whole procedure described in section 3 remains the same. For the test set-up this modification means that the rudder resistance needs to be measured. This, however, just requires installation of a one component load cell between hull and rudder blade. The photomontage in Figure 11 gives an idea how this is realized in HYKAT with a load cell located inside the rudder blade.

Figure 11 Montage Explaining the Concept for Rudder Resistance Measurement

HSVA is now about to gather experience with this enhanced set-up. First results were presented in HSVA’s latest newsletter already (Schmale 2018-1). Some more results will follow in November this year in Hamburg (Schmale 2018-2).

6 PROS AND CONS

The big advantage of the new testing method is that small modifications in a propeller/rudder arrangement can be investigated regarding their influence on the propulsive efficiency at high Reynolds number and in the ship model's wake field at the same time. With the enhancement described in the foregoing section the method is applicable for propeller fin caps, small propeller blade modifications, rudder modifications, rudder bulbs, or rudder fins.

The limitations are that the method does not allow determination of the vessels self-propulsion point. It always requires a thrust coefficient K_T for a reference condition as an input. Furthermore the method fails when the basic assumption $T + R_{Rudder} = const.$ doesn't apply. This is the case for propulsion improving devices that change the resistance of the hull itself or the resistance increase caused by the propeller. Consequently it doesn't work for ducts or fins or pre-swirl stators attached to the hull and it also doesn't work for bigger propeller changes like changes in diameter or blade number or radial load distribution.

Challenging propulsor arrangements are typically tested in a cavitation tunnel with respect to their cavitation behavior anyway. Once the model is installed in HYKAT, the additional effort for the comparative propulsion test is marginal. So, whenever applicable with respect to the aforementioned limitations, the new method represents a cost effective brick stone for reliable assessment of propulsion improving devices at HSVA.

7 SUMMARY

A new testing method is presented, featuring the large cavitation testing facility HYKAT for performance of comparative propulsion testing.

The new method allows assessment of the propulsion improving effect of a large variety of hydrodynamic devices at high Reynolds number and in the realistic three-dimensional wake at the same time.

Using this method the effectiveness of propeller fin caps was investigated for different ship types. The tests revealed that the effectiveness of this group of devices is dependent on the design philosophy behind the propeller in front of them.

The new method is available now as a mature brick stone for the risk assessment prior to investing money into propulsion improving devices.

REFERENCES

Müller, J. (2017-1). 'How much can a hub cap save?'. HSVA Newsletter NewsWave, Issue 1-17.

Müller, J. (2017-2). '"HYTES" – HYKAT Tested Energy Saving Devices'. 5th Int. Conf. on Advanced Model Measurement Technology for the Maritime Industrie (AMT'17), Glasgow, UK.

Schmale, J. (2018-1). 'Not only for hub caps – the enhanced procedure for propulsion tests in HYKAT'. HSVA Newsletter NewsWave, Issue 1-18.

Schmale, J. (2018-2). 'Propulsion Tests in HYKAT'. Annual Congress of the German Society for Maritime Technology (STG), Hamburg, Germany.

A. Yücel Odabaşı Colloquium Series
3rd International Meeting - Progress in Propeller Cavitation and its Consequences:
Experimental and Computational Methods for Predictions
15th – 16th November 2018, Istanbul, Turkey

An Experimental Investigation into PressurePores™ Technology to Mitigate Propeller Cavitation and Underwater Radiated Noise

Batuhan Aktas[1,*], Naz Yilmaz[1], Noriyuki Sasaki[1], Mehmet Atlar[1], Giorgio Tani[2], Fabiana Miglianti[2], Michele Viviani[2] and David Taylor[3]
[1]University of Strathclyde, Glasgow, UK
[2]University of Genova, Genova, ITALY
[3]OSCAR Propulsion, West Sussex, UK

Abstract: This paper presents a practical retrofitting technology, which is called "PressurePores™" technology, to reduce the cavitation induced noise from a marine propeller, and the results of an experimental investigation to show the merits of this technology for a more silent propeller. Strategically introduced PressurePores™ to the propeller blades, that may be producing limited thrust for the operating vessel due to the presence of cavitation, can reduce the overall cavitation volume, which would consequently result in a reduction of the radiated noise levels, while retaining the propeller's efficiency as much as possible.

To demonstrate this technology, in addition to the comprehensive CFD investigations, some cavitation tunnel tests and towing tank tests were conducted with the model propeller of a research catamaran for three different blade configurations. The first group of tests were conducted with the original propeller without any pore on its blades. The second group tests incorporated the PressurePores™ technology on the blades, while the third group was conducted with a reduced number of PressurePores™ on the blades. An overall finding from these tests indicated that a significant reduction in cavitation noise could be achieved (up to 17 dB) at design speed with a favourable PressurePores™ arrangement. Such reduction could be particularly effective in the frequency regions that are utmost important for marine mammals while this sub-cavitating propeller was losing only 2% of its efficiency. The extrapolation of the model scale noise measurements for the original propeller and its counterparts propeller blades with the PressurePores™ demonstrated that such an easy retrofit solution could significantly help the vessels to achieve, e.g. the industry-recognised DNV Silent notation, Environmental Transit noise levels.

Keywords: Pressure Relief Holes; PressurePores™; Cavitation Noise Mitigation; Experimental Hydrodynamics;

1 INTRODUCTION

The technological developments of the last half-century have revolutionised the world that we live in at the moment. One of the main driving factors for such swift advancement is the globalisation of the world. Commercial shipping has made globalisation possible by providing the most efficient means of transportation. With the ever-increasing world population and the fundamentals of economies of scale, the volume of commercial shipping has experienced an increasing trend over the last five decades. Unfortunately, this has also resulted in the elevation of emissions produced by the maritime industry IMO, (2013).

One of the most adverse by-products of the commercial shipping has been underwater radiated noise (URN) emission Ross, (1976). The extraordinary expansion of the world fleet has resulted in increased levels of the ambient noise in the world's seas, especially in the low-frequency domain Frisk, (2012). Unfortunately, this domain is also utilised by marine mammals for various fundamental living activities. Thus, exposing them to such an abrupt change in ambient noise levels may disorient them or disrupt their communication signals, leading to behavioural changes of these mammals or local extinction Richardson et al., (2013), White & Pace, (2010).

Within the framework described above, the recently conducted PressurePores™ Technology (Patent Application Number PCT/GB2016/051129) project aimed to explore the merits of implementing pressure relieving holes on marine propellers to mitigate the cavitation induced noise for a more silent propeller. This paper is associated with the presentation of the results from the experimental investigation of this project.

In order to achieve the aim of the project, first, a literature review was conducted in the related field. This revealed that in the late 90s, Sharma et al. from the Indian Institute

* *Corresponding author e-mail: batuhan.aktas@strath.ac.uk*

of Technology in Bombay conducted research involving cavitation noise on marine propellers Sharma et al., (1990). In that study, Sharma et al. tried to delay the onset of the tip vortex cavitation and to reduce the produced noise without influencing the propeller performance adversely. Based on this rationale, Sharma at al. modified propellers by drilling 300 holes of 0.3mm diameter in each blade. These holes were drilled at the tip and the leading edge areas of the blades. Sharma et al. tests indicated that the dominant cavitation type at inception was the tip vortex cavitation under any testing conditions. The modifications did not demonstrate any measurable influence on the performance characteristics of any of the propellers tested. But, as it was expected, it had a great influence on the Tip Vortex Cavitation (TVC).

Regarding the acoustic benefit, there was a great improvement by the complete attenuation of the low-frequency spectral peaks, e.g. as shown in **Figure 1**. The tests with the original (unmodified) propellers showed a consistent rise of spectrum levels throughout the frequency range as the advance coefficients were reduced, but this was not the case for the modified propellers. The advance coefficients had a weak effect on the noise levels. This was attributed to the consequences of the modification where the tips were unloaded, and the suction peak in the leading edge was reduced while the TVC strength was reduced due to the increase in the angle of incidence.

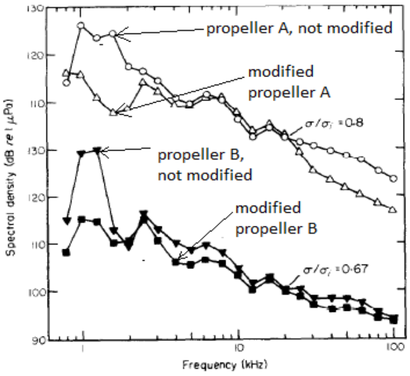

Figure 14 Influence of blade modification on cavitation noise for J=0.38. Sharma et al., (1990).

Figure 1 presents a comparison of the noise characteristics for the original and the modified propellers A and B at the advance coefficient of J=0.38. In such a low J value, the improvement was more significant. Particularly for low frequencies, between 1 and 2 kHz, a reduction of about 15 dB was observed in the noise levels of both propellers. In conclusion, “the modifications carried out had no measurable influence on the performance characteristics of the basic propellers”. However, they achieved a delay in the onset of the cavitation and significant noise reductions. One interesting point to note in Sharma et al. ’s work was that they tested all propellers in uniform flow conditions. This inherently disregards the presence of the ship hull in front of the propeller which is one of the most significant contributors to the cavitation and hence induced radiated noise.

To shed further light on this concept, and explore the effect of hull wake, an independent pilot experimental study was conducted in the Emerson Cavitation Tunnel of Newcastle University as part of an MSc study Xydis, (2015) by following Sharma et al., (1990). This pilot study was conducted using rather heuristic hole arrangements and limited test cases without any numerical optimization of these arrangements. While the study demonstrated some encouraging signs of the radiated noise reduction, the level of the reduction in cavitation extent to support this mitigation needed more sophisticated and detailed observations. Inspired from this MSc study, and based on the model propellers tested in the study, a comprehensive Computational Fluid Dynamics (CFD) based investigation was conducted by Aktas et al., (2018) to demonstrate the effectiveness of this mitigation method, which is later patented as the PressurePores^{TM} Technology by the sponsoring company. Based on the outcomes of this investigation, the best performing cases with the strategically selected PressurePores^{TM} were chosen to be tested at a towing tank for the efficiency measurements while at a cavitation tunnel for the cavitation and noise measurements to confirm the results of the CFD investigations. The results of the towing tank and Cavitation tunnel test have confirmed the findings of the high fidelity numerical simulation for the propeller efficiency and cavitation observations as well as confirming the significant reduction in the emitted cavitation noise levels (up to 17 dB). The reductions from the noise spectra are also found to be prominent in the frequency regions that can be important for some marine mammals while the propeller was loosing about 2% of its efficiency.

The detail of the experimental investigation summarized above is presented in this paper by the following layout; after this introductory section, Section 2 presents the description of the propeller model used as well as the experimental set-up and test conditions for the cavitation tunnel tests which were conducted in the University of Genova Cavitation Tunnel. Section 3 describes the details and results of the cavitation observations while Section 4 presents those of the radiated noise measurements. In Section 5 the details and results of the propeller performance tests, which were conducted in the CTO towing tank of Gdansk, and finally Section 6 presents the main conclusions obtained from the investigations.

2 PROPELLER MODEL, EXPERIMENTAL SET UP & TEST CONDITIONS

The experimental approach adopted in this study necessitated the use of several experimental artefacts. These included a propeller model that has two modified versions incorporating the PressurePores^{TM} technology, a cavitation tunnel and a towing tank described in the following. The adopted experimental test matrix is also provided.

2.1 Propeller Model

The propeller model used for both tests represented the port side propeller of the Newcastle University's research catamaran, *The Princess Royal* with a scale ratio of *3.409*, giving a *220mm* model propeller diameter. The reason was selecting this propeller as the test case two folds: firstly this vessel has become almost benchmark vessel worldwide for the URN and cavitation investigations; secondly, the Authors had extensive information and access to this vessel which can be used for validating the investigation in full-scale as part of the PressurePore^{TM} technology project.

The propeller model was manufactured with high accuracy by considering the cavitation testing as shown by the deviation contour plot given in Figure 15. The principal dimensions of the full-scale propeller are given in Table 1.

Table 7 Propeller main characteristics and particulars

Full Scale Diameter [m]	0.75
Pitch Ratio at 0.7R	0.8475
Expanded Blade Area Ratio	1.057
Number of blades	5
Rake angle	0°
Skew angle	0°

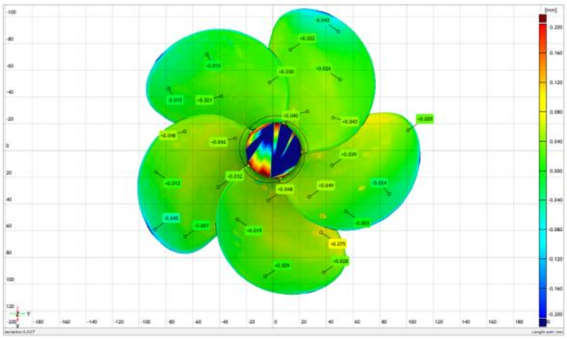

Figure 15 Manufacturing accuracy Image of the Princess Royal Propeller

The application of the PressurePore^{TM} technology to this benchmark test propeller utilised the knowledge and experience gained through the CFD investigations conducted with this propeller as well as another test case propeller, which belonged to a 95000 tonnes merchant tanker, and tested in the Emerson Cavitation Tunnel by Xydis, (2015). In these investigations, the pore configurations applied were simulated initially by using the earlier version of the TVC model developed, and later by using the state of the art adaptive mesh refinement technique of Yilmaz et al., (2017). Based on these investigations, two sets of PressurePores^{TM} configurations were selected to be tested at the CTO towing tank for accurate prediction of the propeller open water performance parameters and in the University of Genova cavitation tunnel for the cavitation observation and underwater noise measurements. The selected PressurePore^{TM} configurations are shown in Figure 3 and 4, as applied on the model propeller, and represented by the following legend: "Modified Propeller" and "Modified Propeller-2", respectively. The diameter of the pores is 1mm, and 33 pores were used for the Modified propeller while 17 pores for the Modified-2 propeller model.

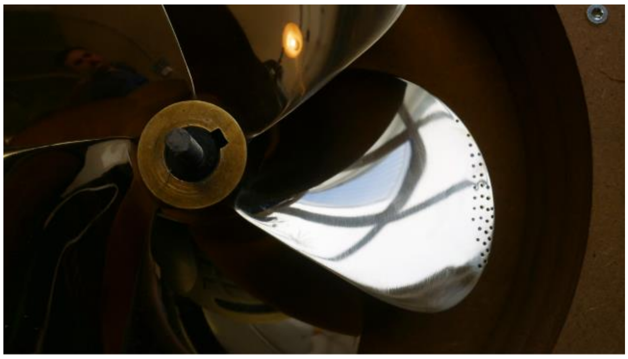

Figure 16 PressurePores^{TM} as applied on The Princess Royal propeller for Modified Propeller

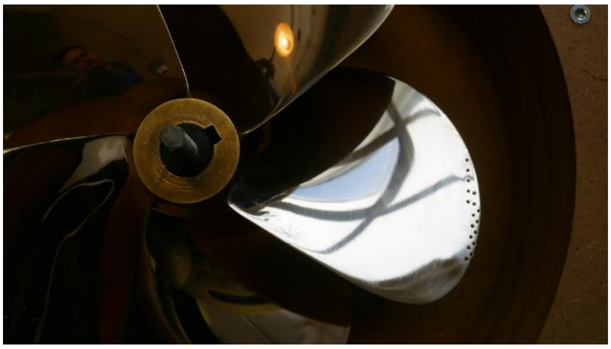

Figure 17 PressurePores^{TM} as applied on the Princess Royal propeller for Modified Propeller-2

2.2 Experimental testing facilities

As stated earlier, two testing facilities were used for the experimental investigations. These were the medium-size cavitation Tunnel of the University of Genoa (UNIGE) and the large towing tank of the Centrum Techniki Okrętowej S.A. (CTO) Model Basin in Gdansk.

The cavitation tunnel of the University of Genova (UNIGE) is a Kempf & Remmers closed water circuit tunnel, schematically represented in Figure 4. The tunnel has a square testing section of 0.57m×0.57m, having a total testing section length of 2m. The nozzle contraction ratio is 4.6:1, allowing to achieve the maximum speed in the test section of 8.5 m/s. The tunnel is equipped with a Kempf &

Remmers H39 dynamometer, which measures the propeller thrust, the torque and the rate of revolution.

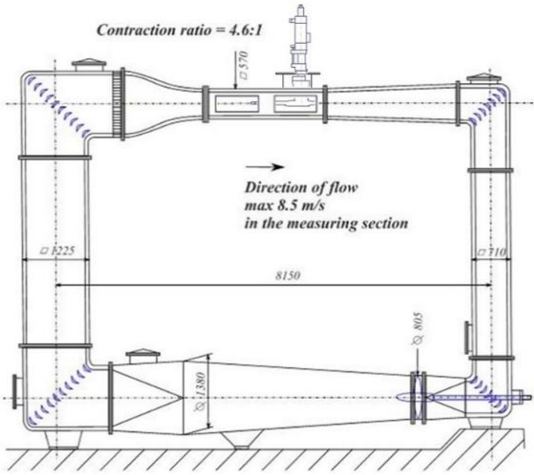

Figure 18 UNIGE cavitation tunnel

The CTO towing tank is approx. 270 m x 12 m x 6 m in length, breadth and depth respectively and is fitted out with a towing carriage of a maximum speed of 12 m/s. The performance of the propeller model before and after the application of the PressurePores^{TM} technology was measured by using the standard open water dynamometer as shown in Figure 6.

Figure 19 Towing tank open water test set-up

2.3 Test set-up and test matrix

The test set-up used for the cavitation tunnel tests is shown in Figure 7. In order to simulate the tests in realistic operational conditions, the cavitation tunnel tests were carried out behind a simulated (nominal) wake field which was produced based on the wake survey conducted at the Ata Nutku Towing tank of Istanbul Technical University, Korkut & Takinaci, (2013). For this purpose, a wire mesh wake screen was built in the cavitation tunnel test section and resulting wake filed was verified by using a 2D Laser Doppler Velocimetry (LDV) device. The cavitation tunnel setup is schematically presented in Figure 20.

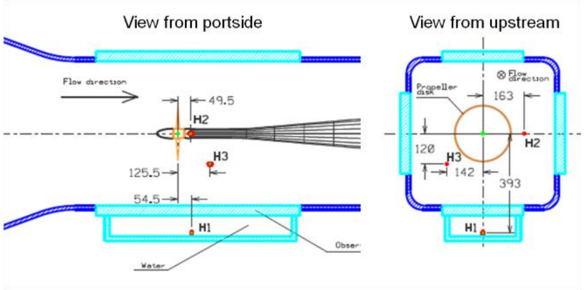

Figure 20 Cavitation tunnel setup, longitudinal view.

The comparative velocity distributions of the simulated wake in the UNIGE tunnel measured by the LDV, and that of the nominal wake measured in the ITU towing tank can be seen in Figure 8. As shown in the top section of Figure 8, a part of the wake data measured in the UNIGE tunnel is missing due to the limitation of the optical access for the LDV which was caused by the obstruction of the propeller shaft. The LDV measurements could be carried out by the probe that could approach to the measurement zone only from the starboard side of the test section.

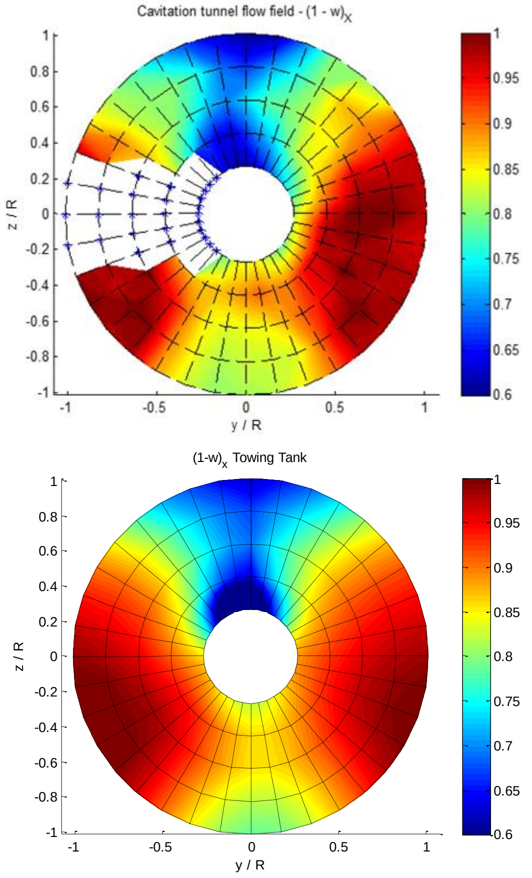

Figure 21 Nominal wake field: Simulated in cavitation tunnel (top); Measured at towing tank (bottom).

Based upon the typical in-service operational conditions of The Princess Royal, which correspond to 10.5kn and 15.1 kn vessel speeds, the cavitation tunnel test matrix is constructed as shown in Table 2.

Table 8 full-scale operational conditions during sea trials

Condition	Engine [RPM]	Shaft [rps]	STW (kn)	K_T	10KQ	σ_N (nD)
V1	1500	14.3	10.5	0.211	0.323	1.91
V2	2000	19.0	15.1	0.188	0.318	1.07

In Table 2 STW represents the vessel speed through the water. K_T and K_Q are the standard thrust and torque coefficient, respectively, while the cavitation number is defined based on the propeller shaft speed using Equation (1):

$$\sigma_n = \frac{P_a + \rho g h_s - P_v}{0.5\rho(nD)^2} \tag{1}$$

where P_a is the atmospheric pressure, g is the gravitational acceleration, ρ is the density of water, h_s is the shaft immersion of the propeller, P_v is the vapour pressure, n is the propeller shaft speed in rps, and finally D is the diameter of the propeller.

Table 9 Non-dimensional performance and operational parameters for propellers

Performance Characteristics	Symbol	Formula
Thrust coefficient	K_T	$\frac{T}{\rho n^2 D^4}$
Torque coefficient	K_Q	$\frac{Q}{\rho n^2 D^5}$
Advance coefficient	J	$\frac{V_a}{nD}$
Efficiency	η_0	$\frac{J \times K_T}{2\pi \times K_Q}$

where T is the thrust, V_a is the advance velocity, Q is the torque and η_0 is the propeller efficiency.

The model scale test conditions were specified according to the thrust coefficient identity. As shown in Table 2, while Condition V2 corresponded to the actual service speed of the research vessel, Condition V1 corresponded at 10.5kn speed condition.

The cavitation tunnel tests were completed in three stages: the first stage involved the tests with the original propeller model with no pore (Intact propeller). The second stage, the propeller model with 33-1mm pores on each blade (Modified propeller); and the third and final stage, with 17-1mm pores on each blade (Modified-2) which was achieved by closing a half of the pores on the Modified propeller with an adhesive material and smoothening them with care.

During the tests, the water quality was assessed based on the dissolved oxygen content of the tunnel which was monitored by using the ABB dissolved oxygen sensor, model 8012/170, coupled with an ABB analyser model AX400.

3 CAVITATION OBSERVATIONS

In order to make qualitative comparisons between the cavitation experienced by the intact and modified propeller cases, cavitation observations were carried out. For this purpose, a mobile stroboscopic system was utilised to visualize and record the cavitation phenomenon on and off the propeller blades. The cavitation recordings were made with three Allied Vision Tech Marlin F145B2 Firewire Cameras, with a resolution of 1392 x 1040 pixels and a frame rate up to 10 fps.

Table 10 Cavitation observations for V1 and V2 for Intact and Modified propeller

Condition	K_T	σ_N	Intact propeller observations	Modified propeller observations	Modified Propeller-2 observations
V1	0.211	1.91	TVC everywhere, starting from blade L.E.; S.S. sheet cavitation at 0°, from 0.8R to the tip, for 15% of the chord at 0.8R, 100% at 0.97R; S.S. sheet cavitation at 180°, from 0.85R to the tip, for 10% of the chord at 0.85R.	Pores cavitation everywhere; TVC at 0° and 180°, only cloudy vortex at other positions; S.S. sheet cavitation at 0°-45° from 0.8R for 10%of the chord, merging with holes cavitation at outer radii; S.S. sheet cavitation at 180°, from 0.85R for 5% of the chord, merging with holes cavitation at outer radii.	Pores cavitation everywhere; TVC everywhere, at 90° and 270° the cavitating core is at inception; S.S. sheet cavitation at 0°, from 0.8R, for 15% of the chord, at 180°, from 0.85R for 10% of the chord.
V2	0.188	1.07	TVC everywhere, starting from blade L.E.; double vortex at 0°-60°; S.S. sheet cavitation at 0°, from 0.8R to the tip, for 50% of the chord at 0.8R, 100% at 0.85R; S.S. sheet	Pores cavitation everywhere; TVC everywhere, with double vortex at 0°-60°; S.S. sheet cavitation at 0°-45° from 0.8R for 30%of the chord, merging with holes	Pores cavitation everywhere; TVC everywhere, the cavitating core is now well developed but still presents unstable

			cavitation at 90° and 270°, from 0.9R for 10% of the chord; S.S. sheet cavitation at 180°, from 0.83R to the tip, for 50% of the chord at 0.83R, 100% of the chord at 0.92R	cavitation at outer radii; S.S. sheet cavitation at 180°, from 0.83R for 20% of the chord, merging with holes cavitation at outer radii.	behaviour; double vortex at 0°; S.S. sheet cavitation at 0° from 0.8R for 40% of the chord, at 180° from 0.8R for 30% of the chord.

Condition V1

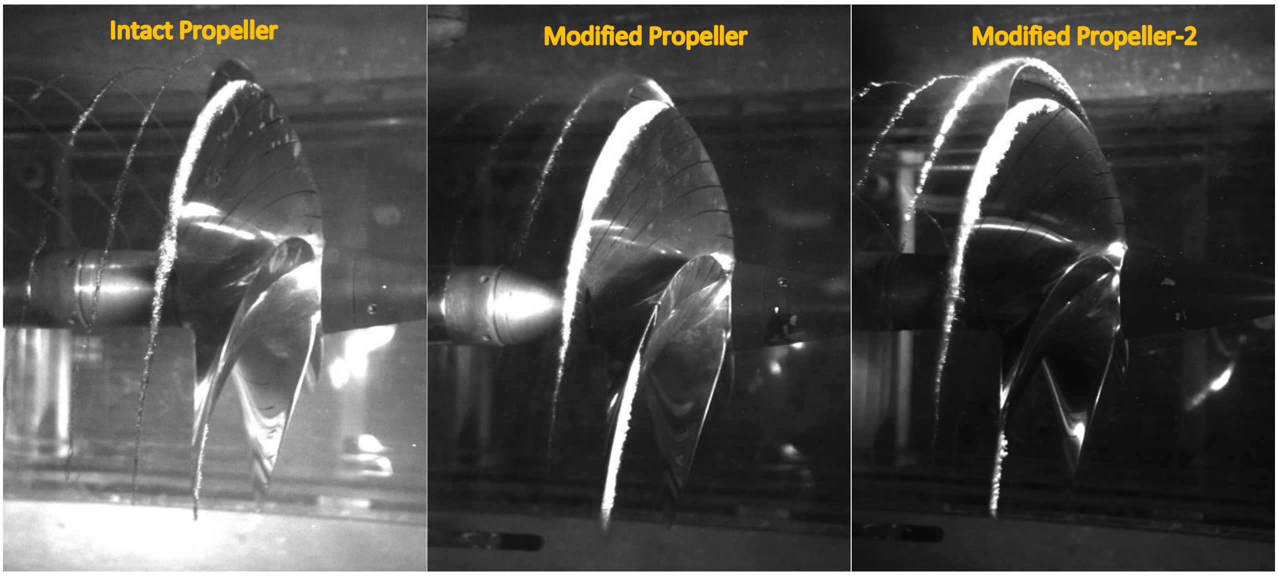

Figure 22 Intact vs Modified propeller and Modified Propeller-2, condition V1, viewed from starboard

Condition V2

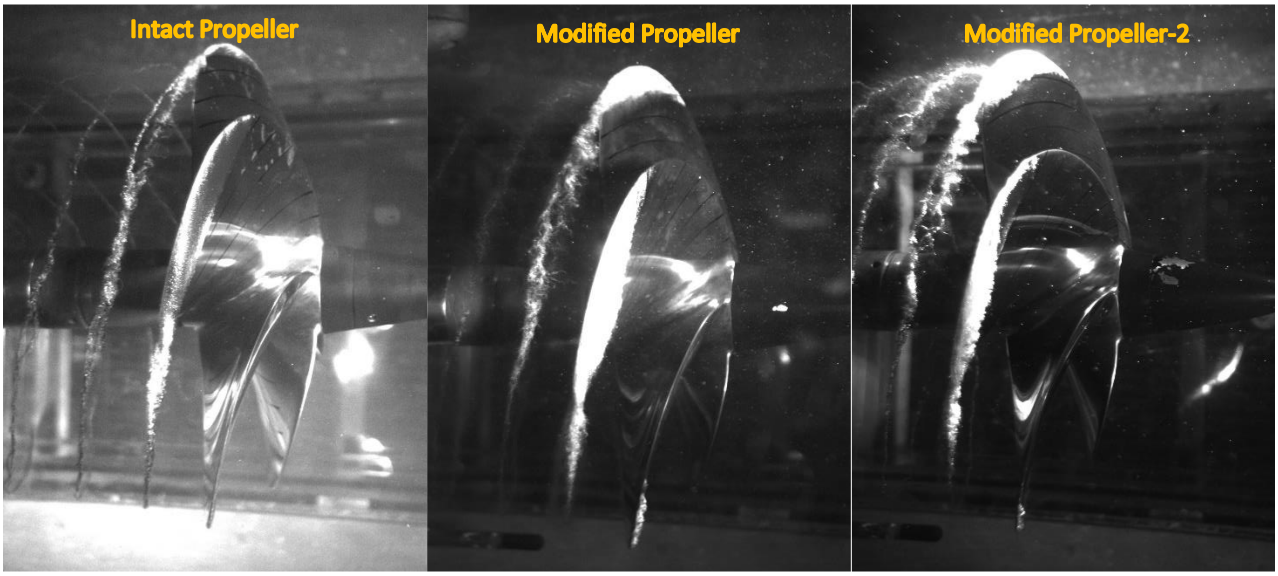

Figure 23 Intact vs Modified propeller and Modified Propeller-2, condition V2, viewed from starboard

4 RADIATED NOISE MEASUREMENTS

In this section the details of the test set-up for the noise measurements, the analyses and presentations of he these measurements and results are presented.

Figure 20 shows a scheme of the setup adopted during these tests including the positions of the three hydrophones utilized. In particular, two hydrophones were mounted on fins at the downstream of the propeller: one on the port side at the same vertical position with the propeller shaft (H2); the other (H3) on the starboard at a lower vertical position. The third hydrophone (H1) was mounted in an external plexiglass tank filled with water and mounted on the bottom window of the testing section. The measurements from H3 was used for the noise results presented throughout this manuscript.

Moreover, noise tests were also repeated at least three times. For the post-processing of the noise measured the ITTC, (2017) guidelines for the model scale noise measurements were followed.

The average Power Spectral Density, G(f) in Pa^2/Hz, was computed from each sound pressure signal p(t) using Welch's method of averaging modified spectrograms. The Sound Pressure Power Spectral Density Level Lp is then given by Equation (2):

$$L_p(f) = 10\log_{10}\left(\frac{G(f)}{p_{ref}^2}\right) \quad (\mathrm{dB\ re\ 1\ \mu Pa^2/Hz}) \qquad (2)$$

where p_{ref} = 1 µPa.

The background noise was measured reproducing the same condition for corresponding test conditions regarding the shaft revolution, flow speed and vacuum by replacing the propeller with a dummy hub. Only one series of the background noise measurements were carried out since the tunnel operational conditions do not vary significantly passing from the intact to the modified propeller cases.

Comparing the total noise measured with the background noise, the net sound pressure levels of the propeller were analysed as follows:

1. Signal to noise ratio higher than 10 dB: No correction made
2. Signal to noise ratio higher than 3 dB but lower than 10dB:

$$\mathrm{L_{PN}} = 10\mathrm{Log_{10}}\left[10^{(\mathrm{L_{Ptot}}/10)} - 10^{(\mathrm{L_{Pbg}}/10)}\right] \qquad (3)$$

3. Signal to noise ratio lower than 3 dB:

Results disregarded (4)

Also, the net sound pressure levels may be scaled to a reference distance of 1-meter exploiting measured transfer functions, or simply according to Equation (5):

$$\mathrm{L_{PN@1m}} = \mathrm{L_{PN}} + 20\mathrm{Log_{10}}(\mathrm{r}) \qquad (5)$$

where r is the distance between propeller (acoustical centre) and sensor.

The latter formulation has been used in present work.

The acoustical centre of the propeller has been defined with respect to the centre of the propeller disk.

Based upon the above-described post-processing, Figure 11 to Figure 14 present the measured noise levels for the Intact propeller, Modified propeller and Modified Propeller-2 in the narrow and Third-octave band for condition V1 and V2. In both cases, significant reductions regarding the radiated noise levels can be observed over a frequency range from 200Hz to 1kHz. For the service speed condition V2, the reductions are consistent almost throughout the entire frequency range tested. For condition V1, the application of the PressurePores^{TM} Technology observed to cause some elevation of the URN in the high-frequency region.

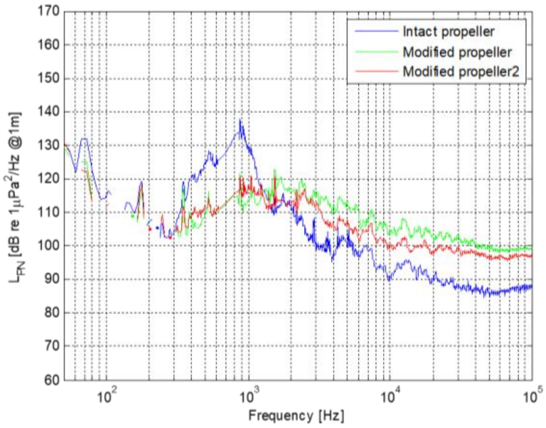

Figure 24 Comparison between Intact, Modified propeller and Modified Propeller-2 net noise levels at 1m (narrowband), condition V1, hydrophone H3

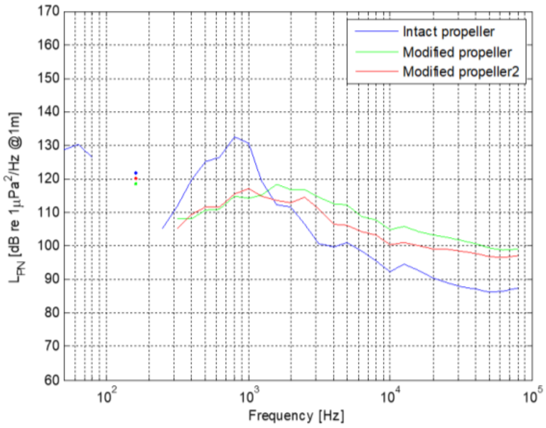

Figure 25 Comparison between Intact, Modified Propeller and Modified Propeller-2 net noise levels at 1m (one third octave band), condition V1, hydrophone H3

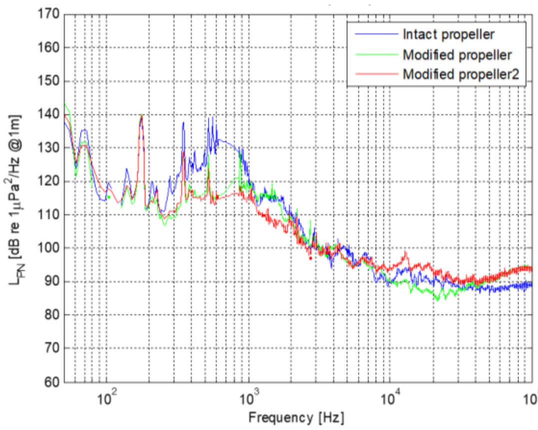

Figure 26 Comparison between Intact, Modified propeller and Modified Propeller-2 net noise levels at 1m (narrowband), condition V2, hydrophone H3

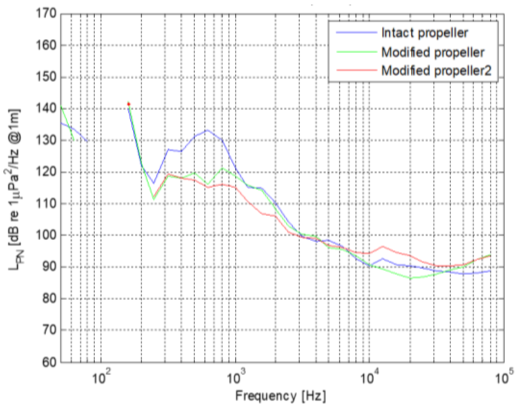

Figure 27 Comparison between Intact, Modified Propeller and Modified Propeller-2 net noise levels at 1m (one third octave band), condition V2, hydrophone H3

Figure 28 presents the net difference between the noise levels of the Intact propeller and both modified propellers for Condition V2 as measured by hydrophone H3 to demonstrate effectiveness of the PressurePore™ technology.

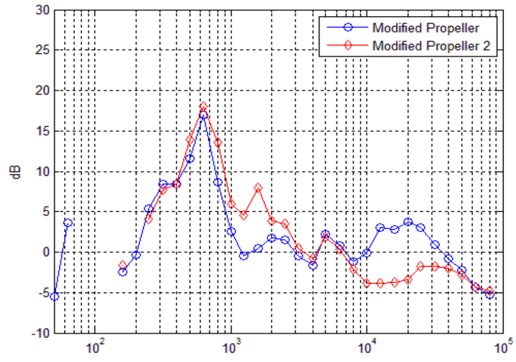

Figure 28 Noise reduction with application of pressure relief holes in Third Octave band for condition V2, measured at hydrophone H3

5 PROPELLER PERFORMANCE TESTS

This section presents the details and results of the propeller open water tests that were conducted at the CTO towing tank. The purpose of these tests was to determine performance characteristics of the propeller regarding thrust, torque and efficiency before and after the introduction of the PressurePores™ technology.

During these tests, the rate of the propeller shaft revolutions was set over a range to assure the Reynolds Numbers above the critical threshold of 500,000. Also, to confirm the typical convergence of the measurements, for single advance ratio of J = 0.6, the tests were repeated for three additional values of the Reynolds number. The test data analysed for the thrust, torque and efficiency were presented by the 4th-degree polynomials for the three propeller test cases as shown in Figure 16.

The operating condition of the Princess Royal propeller are very close to Advance Coefficient J=0.5. As shown in Figure 4, the open water tests indicated that there is a 2% loss of thrust and 4% gain in torque which consequently results in a propeller efficiency loss of 5.7% for Modified Propeller compared to the intact propeller. For Modified Propeller-2 case, with a half of the pores applied in the Modified propeller test case, the loss in thrust was about 0.1% while there was a 2.2% gain in torque which resulted in the efficiency loss of 2.3%.

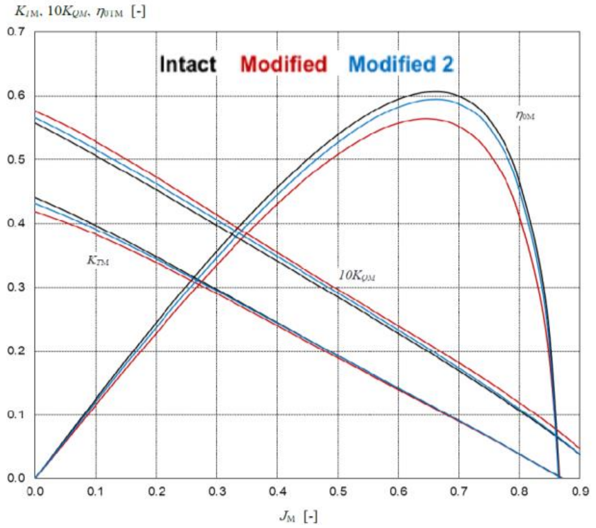

Figure 29 Open water characteristics of the PR propeller before and after the application of PressurePores™ (Modified propeller and Modified Propeller-2)

6 CONCLUSIONS

PressurePores™ Technology, which has been recent endorsed to reduce the cavitation induced noise of marine propeller, was validated by using model tests conducted in the University of Genova cavitation tunnel and CTO towing tank for the cavitation, noise and efficiency performances.

The test results conducted with the model propeller of a research vessel and for two different combinations of the PressurePores^{TM} technology indicated that significant reductions in the measured propeller noise levels can be achieved.

The comparative test results for the Modified Propeller test case indicated the noise reduction compared to the unmodified propeller can be as high as 17dB and particularly in the frequency region that are utmost important for some marine mammals. For the same configuration, the towing tank test data showed about a 2% loss in the propeller efficiency.

The test results for the Modified Propeller showed more superior underwater noise reduction in the high-frequency region but with a higher propeller efficiency loss, about 5.7%.

Acknowledegments

The authors would like to acknowledge the funding from Oscar Propulsion Ltd. that made this study possible.

REFERENCES

Aktas, B., Yilmaz, N., & Atlar, M. '*Pressure relieving holes to mitigate propeller cavitation and underwater radiated noise'*. Project Report, 2018 Department of Naval Architecture Ocean and Marine Engineering, Strathclyde University.

Frisk, G. V. 'Noiseonomics: The relationship between ambient noise levels in the sea and global economic trends'. Scientific Reports, 2(1), 2012, 2–5.

IMO. 'Noise from commercial shipping and its adverse impacts on marine life'. Marine Environment Protection Committee, 2013 International Maritime Organization (MEPC), 66th Session, Agenda item 17.

ITTC. 'Model-scale propeller cavitation noise measurements'. Recommended Procedures and Guidelines *7.5-02-01-05*, 2017, Retrieved from https://ittc.info/media/4052/75-02-01-05.pdf

Korkut, E., & Takinaci, A. C. '18M Research Vessel Wake Measurements' (p. 6). Project Report, 2013, Istanbul Technical University Faculty Of Naval Architecture And Ocean Engineering, İstanbul/Turkey.

Richardson, W. J. W., Greene, C. R., Jr., Malme, C. I. C., Thomson, D. H. D., Jr, C. G., … Thomson, D. H. D. Marine mammals and noise. Elsevier Science.

Ross, D. Mechanics of Underwater Noise. 1976, California, USA: Peninsula Publishing.

Sharma, S. D., Mani, K., & Arakeri, V. H. 'Cavitation noise studies on marine propellers'. Journal of Sound and Vibration, 138(2), 1990, 255–283.

White, P., & Pace, F. 'The Impact of Underwater Ship Noise on Marine Mammals'. 1st IMarEST Ship Noise and Vibration Conference, 2010.

Xydis, K. 'Investigation into Pressure Relieving Holes on Propeller Blades to Mitigate Cavitation and Noise'. 2015, MSc Thesis, School of Marine Science and Technology, Newcastle University.

Yilmaz, N., Khorasanchi, M., & Atlar, M. 'An Investigation into Computational Modelling of Cavitation in a Propeller's Slipstream'. Fifth International Symposium on Marine Propulsion SMP'17, Espoo, Espoo, Finland, 2017.

Propeller Effects on Maneuvering of a Submerged Body

Süleyman Duman[1]*, Savas Sezen[1] and Sakir Bal[2]
[1]Yildiz Technical University, Turkey,[2]Istanbul Technical University, Turkey

Abstract: In this study, the effects of propeller on maneuvering forces of a submerged body have been investigated by implementing body force method. The flow around a submerged body has been solved using a commercial RANS (Reynolds-averaged Navier-Stokes) solver based on finite volume method (FVM). For this purpose, a benchmark DARPA-Suboff bare hull form (AFF-1) has been chosen for the calculations. Oblique towing analyses have been carried out for two different drift angles at two different Reynolds number with and without propeller effects. The propeller-hull interaction has been modelled with an actuator disc coupled with experimental open water data based on body force method at self-propulsion points. Verification study has been carried out using Grid Convergence Index (GCI) method to determine the optimum grid number. Validation study has been done in terms of maneuvering forces and moment acting on the gravity center of submerged body with the available experimental data. The results have also been compared with those of other numerical results.

Keywords: Body force, CFD, DARPA Suboff, Oblique towing, Maneuvering, Propeller, RANS

NOMENCLATURE

CFD	Computational Fluid Dynamics
EFD	Experimental Fluid Dynamics
GCI	Grid Convergence Index
RANS	Reynolds-averaged Navier-Stokes
U_i	Velocity
P	Mean pressure
ρ	Fluid density
k	Turbulent kinetic energy
ε	Turbulent dissipation rate
$\varepsilon_{\text{-CFD}}$	Relative error between CFD and EFD results
$\varepsilon_{\text{-MNT}}$	Relative error between MNT and EFD results
L_{PP}	Length between perpendiculars
L_{OA}	Length overall
D_{max}	Maximum diameter
S	Wetted surface area
∇	Displacement volume
Re	Reynolds Number
β^o	Drift angle
F_x	Longitudinal force
F_y	Sway force
M_z	Yaw moment
Y_V,N_V	Sway maneuvering derivatives

1 INTRODUCTION

The maneuvering performance prediction of a fully submerged body is very crucial in naval hydrodynamic applications. There is a wide range of application area for fully submerged vehicles ranging from manned or unmanned military to industrial use. It is very important to know the 6-DOF (degrees of freedom) hydrodynamic maneuvering characteristics of the submerged body for stability and controllability.

Studies on predicting hydrodynamic characteristics of submerged bodies extend back to 1950s [1,2,3]. In 1967, Gertler and Hagen [4] presented the standard equations of motion for use in submarine simulation studies. After 12 years from this work, Feldman [5] revised these equations. Geometric characteristics and configurations of DARPA Suboff hull form were given by Grove et al. [6] in detail. Experiments of DARPA Suboff program were presented by Huang [7]. Roddy [8] performed horizontal and vertical Planar Motion Mechanism (PMM) experiments in order to provide validation data to be used in Computational Fluid Dynamics (CFD) works for future submarine advances. Park et al. [9] conducted an experimental study to determine the hydrodynamic coefficients of a submarine.

In recent years, the use of CFD method on predicting maneuvering performance of underwater vehicles and submarines has become a very popular research field. Toxopeus [10] performed CFD analyses for several drift angles. He calculated the hydrodynamic forces and moments and compared the results with the experiments. Vaz et al. [11] investigated the hydrodynamic forces and moments of DARPA Suboff for bare and appended forms using two different viscous solvers. They changed the drift

---

* *Corresponding author e-mail: sduman@yildiz.edu.tr*

angle from 0° to 90° by 2° increments. They found that numerical results are in a good agreement with those of experiments. Pan et al. [12] performed oblique towing and Planar Motion Mechanism (PMM) experiments to calculate the hydrodynamic maneuvering coefficients of the appended DARPA Suboff hull form with a ring wing supported by four struts in an "X" configuration. They have also carried out dynamic maneuvering simulations, e.g., pure heaving, pure swaying, pure pitching and pure yawing. Cao and Zhu [13] implemented RBF Neural Network technique with CFD-based calculations to obtain the hydrodynamic forces and moments of a submarine. The applicability of this technique has been discussed in their study. Duman and Bal [14] investigated the maneuvering performance of a surface combatant by performing unsteady RANS simulations. Duman et al. [15] simulated the pure sway dynamic maneuvers of a surface combatant by using overset grid technique. Sezen et al. [16] examined self-propulsion performance of DARPA Suboff bare and appended hull forms for a wide range of Reynolds numbers using body force method and original propeller. Delen et al. [17] have investigated self-propulsion characteristics of DARPA Suboff bare hull form with DTMB 4119 model propeller. Dogrul et al. [18] have also studied self-propulsion characteristics of DARPA Suboff bare hull form both modelling original propeller and actuator disc theory based on body force method. The differences of two approach have been presented.

In this study, the static drift simulations of DARPA Suboff bare hull form have been carried out to calculate the hydrodynamic forces and moment acting on the hull in the horizontal plane. First, a verification study has been conducted to evaluate the uncertainty in the computations. Then, the CFD method has been validated at several angle of attacks with the experimental data for bare hull form. After validation, computations have been repeated with a working propeller behind the vehicle where the propeller effects have been included into computations by an actuator disc model coupled with experimental open water data based on body force method at the self-propulsion points. Numerical maneuvering forces and moments have been used to calculate the maneuvering derivatives of the submerged body. The effects of the propeller on maneuvering forces have been discussed.

2 MATHEMATICAL BACKGROUND

2.1 URANS Approach

Reynolds-averaged Navier-Stokes equations are used for modeling of three dimensional, incompressible and turbulent flow around the submarine hull form. Governing equations given below are solved;

Continuity equation;

$$\frac{\partial U_i}{\partial x_i} = 0$$

Momentum equation;

$$\frac{\partial U_i}{\partial t} + \frac{\partial (U_i U_j)}{\partial x_j} = -\frac{1}{\rho}\frac{\partial P}{\partial x_i} + \frac{\partial}{\partial x_j}\left[\nu\left(\frac{\partial U_i}{\partial x_j} + \frac{\partial U_j}{\partial x_i}\right)\right] - \frac{\partial \overline{u_i' u_j'}}{\partial x_j}$$

The unknown parameters in the equations are the mean velocity, mean pressure and Reynolds stress, respectively. In this study, two equation k-ε turbulence model is used for modelling of Reynolds stress. Detailed information about the turbulence model can be found in Wilcox [19], Ferziger and Peric [20].

2.2 Uncertainty Assessment

Uncertainty study has been carried out using Grid Convergence Index (GCI) method which is based on Richardson extrapolation technique [21]. It was first proposed by Roache [22] to verify the numerical method. The method then has been improved by Celik et al. [23]. The significant parameter for uncertainty study is the refinement factor. It has been chosen as $\sqrt{2}$ as similar in [24], [25] and [24]. Detailed information about Grid Convergence Index (GCI) can be also found in [23].

3 GEOMETRY GRID RESOLUTION AND BOUNDARY CONDITIONS

DARPA Suboff bare hull form (AFF-1) has been selected to investigate the propeller effects on maneuvering forces and moments in oblique towing condition. Geometrical features and 3-D view of the submarine bare hull form have been given in Table 1 and Figure 1, respectively.

Table 1 Main particulars of DARPA Suboff AFF-1 [26]

L_{OA} (m)	4.356
L_{PP} (m)	4.261
D_{max} (m)	0.508
S (m^2)	5.989
∇ (m^3)	0.699

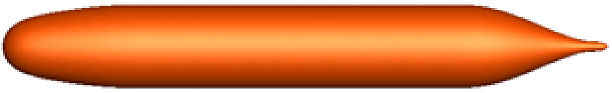

Figure 1 3-D view of DARPA Suboff (AFF-1)

In this study, the propeller effects have been included into computations via body force propeller method. The open water propeller data of E1619 original propeller have been used for actuator disc method. The actuator disc behind the bare hull submarine form is shown in Figure 2.

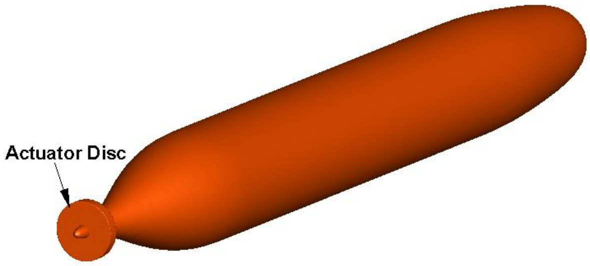

Figure 2 Actuator disc behind the submarine bare hull form

Trimmer mesh algorithm with unstructured fully hexahedral elements have been applied to discretize the computational domain. Mesh refinements have been done around the near field of submarine to capture the flow field precisely (Figure 3). Computational domain and domain dimensions have been shown in Figure 4 and Table 2 respectively. Here, the left side of the computational domain is defined as the pressure outlet while the right side is the velocity inlet. The rest of surfaces has been defined as the symmetry planes. The surface of DARPA Suboff has been identified as no-slip wall to satisfy the kinematic boundary condition.

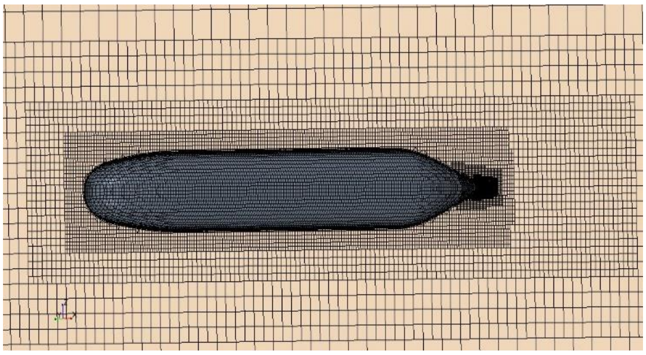

Figure 3 Unstructured grid on the DARPA Suboff bare hull form

An xyz-Cartesian coordinate system has been adopted where the upstream is in + x-direction. The total lateral clearance of the computational domain is given in Table 2.

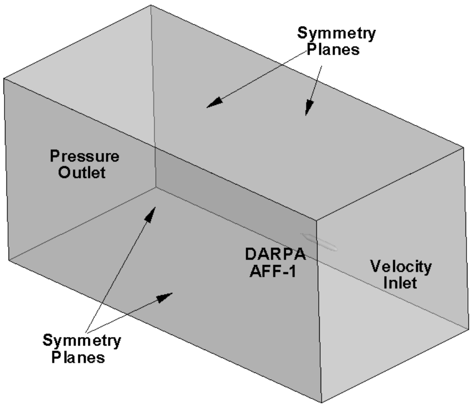

Figure 4 Computational domain and boundary conditions

Table 2 Computational domain dimensions.

Upstream	1.5*L_{PP}
Downstream	5*L_{PP}
Top	2*L_{PP}
Bottom	2*L_{PP}
Transverse	5*L_{PP}

4 COMPUTATIONAL RESULTS

Oblique towing simulations of DARPA Suboff for several drift angles have been performed using a RANS solver based on finite volume method. The numerical method has been verified by using Grid Convergence Index (GCI) method and validated with the available experimental data. Hydrodynamic analyses have been carried out at two different Reynolds numbers. The configurations of the numerical simulations are given in Table 3.

Table 3 Numerical simulation configurations of AFF-1.

Method	Drift angle (β^o)	Drift angle (β^o)
Re	$12*10^6$	$14*10^6$
w/o propeller	0, 4, 8, 12, 16, 18	0, 4, 8, 12, 16, 18
with propeller	0, 4, 8, 12, 16, 18	0, 4, 8, 12, 16, 18

4.1 Verification and Validation

Verification study for total resistance has been done for bare submarine form at the velocity of 3.046 m/s. The uncertainty value has been calculated as 0.58%. Detailed information about grid numbers can be found in Sezen et al. [24].

After finding the uncertainty value, the numerical method has been validated with the available experimental data. It has been found that the total resistance of DARPA Suboff bare hull form (AFF-1) is very close to the experimental result. Table 4 gives the comparison of numerical and experimental results for DARPA Suboff AFF-1 bare hull.

Table 4 Validation of the total resistance at V=3.051 m/s

	CFD	EFD	Relative difference (%)
R_T (N)	86.91	87.40	0.56

4.2 Hydrodynamic Results

The hydrodynamic analyses have been carried out with optimum grid number by GCI method. The forces and moments acting on the gravity center of AFF-1 have been computed at given drift angles for two different Re numbers. The numerical results have been compared with experiments as shown in Figures 5-7. The experimental results have been taken from Roddy [8].

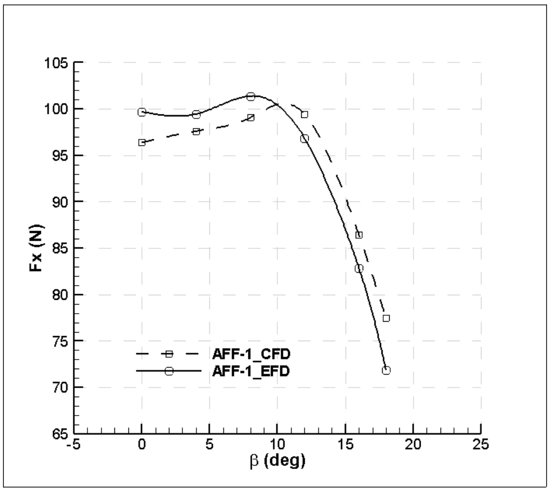

Figure 5 Comparison of longitudinal forces

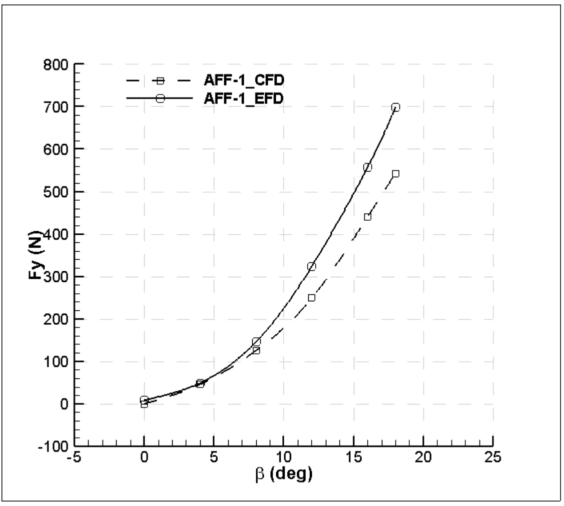

Figure 6 Comparison of sway forces

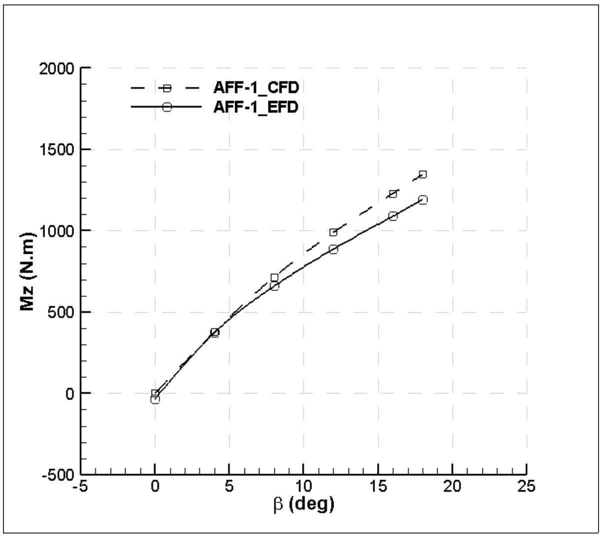

Figure 7 Comparison of yaw moments

The computational results are compatible with the experiments. However, the differences for sway forces and yaw moments deviate slightly after $\beta=8^o$. An offset almost the same in all drift angles is observed between the numerical and experimental longitudinal forces. It should be noted that the sign of this offset is reversed about $\beta=10^o$ (Figure 5).

In addition to the experiments, numerical results have also been compared with those of another numerical study [10]. The subindex "MNT" (see Tables 5-7) stand for the Menter's one-equation turbulence model as explained in Toxopeus (2008). The presented results are in a good agreement with both experimental and the numerical results (Tables 5-7). Additionally, the frictional resistance has been calculated for straight-ahead condition by using ITTC-1957 friction line to find out the capability of the present method for computing the shear forces (Table 5). It can be seen that the resistance where the viscosity predominates has been calculated with a high degree of accuracy.

The form factor of DARPA Suboff bare hull form has been computed with two different techniques. First the total resistance is divided into total shear force which is obtained by integrating the shear stresses along the submerged body, $(1+k)_{CFD}$. Later the total resistance obtained by experiments is divided into frictional resistance calculated from ITTC-1957 friction line and it is indicated as $(1+k)_{ITTC}$. Both results are in good agreement.

The sway forces and yaw moments are compared with the experiments and MNT method in Table 6 and Table 7, respectively. The results of the present method at $\beta=4^o$ are closer to the experiment then those of MNT results. However, the relative errors are higher when compared to the MNT method at $\beta=18^o$. These results lead us to think about that the present method may have deficiencies in modelling flow separations which occur at relatively higher drift angles.

Table 5 Comparison of surge forces with experiments and another numerical method

β°	X_{CFD}	X_{MNT}	X_{EFD}	$(1+k)_{CFD}$	$(1+k)_{ITTC}$	ε-$_{CFD}$ %	ε-$_{MNT}$ %	ε-$_{(1+k)}$ %
0	1.021	1.046	1.056	1.124	1.131	3.32	0.95	0.55
4	1.034	1.143	1.054	-	-	1.85	8.50	-
18	0.820	1.376	0.761	-	-	7.82	80.79	-

Table 6 Comparison of sway forces with experiments and another numerical method

β°	Y_{CFD}	Y_{MNT}	Y_{EFD}	ε-$_{CFD}$ %	ε-$_{MNT}$ %
4	0.485	0.410	0.520	6.77	21.21
18	5.744	6.322	7.397	22.34	14.53

Table 7 Comparison of yaw moments with experiments and another numerical method

β°	Mz_{CFD}	Mz_{MNT}	Mz_{EFD}	ε-$_{CFD}$ %	ε-$_{MNT}$ %
4	0.942	0.897	0.930	1.34	3.54
18	3.345	3.260	2.963	12.92	10.04

Table 8 CFD and EFD results for AFF-1 (multiplied by 10^3)

	β°	0	4	8	12	16	18
AFF-1 (CFD)	F_x	1.021	1.034	1.049	1.053	0.915	0.821
	F_y	0.000	0.485	1.331	2.643	4.669	5.744
	M_z	0.000	0.942	1.776	2.461	3.056	3.345
AFF-1 with propeller (CFD)	F_x	1.170	1.174	1.162	1.119	0.947	0.898
	F_y	0.000	0.481	1.338	2.765	4.710	5.797
	M_z	0.000	0.942	1.775	2.458	3.048	3.336
AFF-1 (EFD)	F_x	1.056	1.054	1.074	1.026	0.877	0.761
	F_y	0.090	0.520	1.545	3.437	5.911	7.397
	M_z	-0.083	0.930	1.640	2.208	2.709	2.963

4.3 Propeller Effects on Hydrodynamic Forces and Moments

The hydrodynamic forces and moment acting on the bare form of DARPA Suboff AFF-1 have been calculated for two different Reynolds numbers, $12x10^6$ and $14x10^6$ at self-propulsion point. Comparisons of hydrodynamic forces and moments between "with propeller" and "w/o propeller" cases at Re=$12x10^6$ are given in Figures 8-10.

As expected, an increase in longitudinal forces have been observed in the presence of propeller while lateral forces and yaw moments have been found almost identical in the case of bare hull (without propeller condition). It is also observed that the propeller effects on longitudinal forces decreases with increasing drift angles.

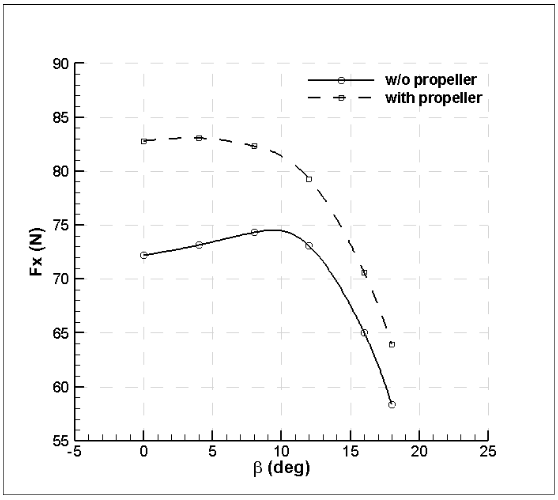

Figure 8 Comparison of longitudinal forces with and w/o propeller at different drift angles

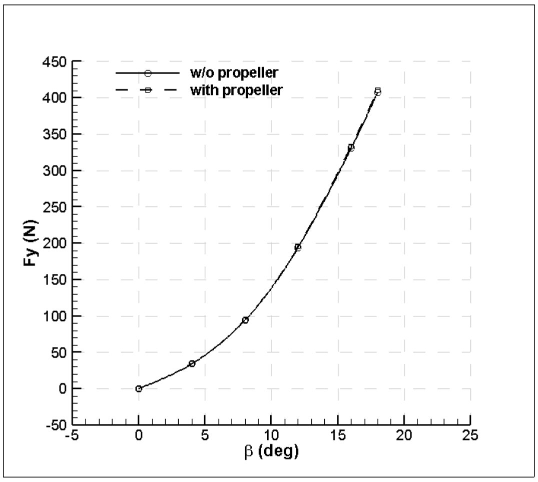

Figure 9 Comparison of sway forces with and w/o propeller at different drift angles

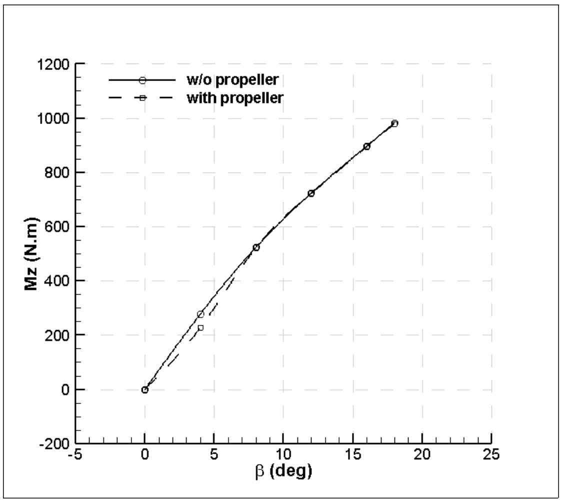

Figure 10 Comparison of yaw moments with and w/o propeller at different drift angles

The numerical and experimental results are given in Table 8 for Re=$14x10^6$ in nondimensional form. The towing speed (U) corresponding to the related Reynolds number and the characteristic length (L_{PP}) of the submarine have been used in nondimensionalization of longitudinal and lateral forces, yawing moments and maneuvering derivatives as described by Roddy (1990) [8].

4.4 Maneuvering Derivatives

The hydrodynamic maneuvering derivatives have been calculated by fitting a polynomial curve to the computational results. Detailed information about the calculation of static drift maneuvering coefficients can be found in [27]. The fitted curves for calculating the sway maneuvering derivatives are given in Figures 11-12.

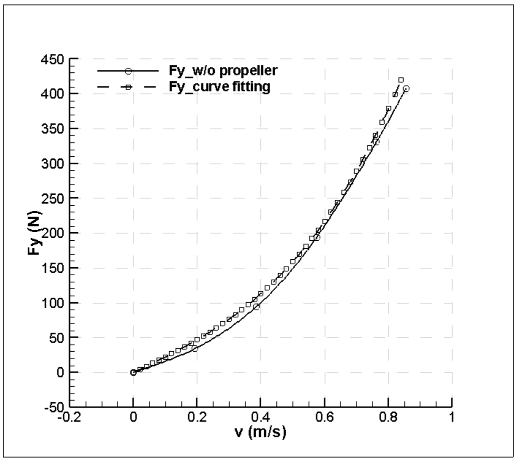

Figure 11 Calculation of sway maneuvering derivatives for AFF-1 w/o propeller

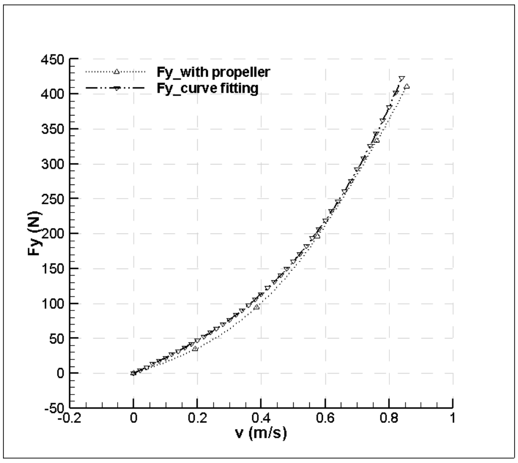

Figure 12 Calculation of sway maneuvering derivatives for AFF-1 with propeller

The sway maneuvering derivatives computed from cases of "with propeller" and "w/o propeller" analyses are given in Table 9. It can be seen that the effects of propeller on sway maneuvering derivatives at different Reynolds numbers are negligible. However, a wide range of velocity can provide a more accurate interpretation. Y_v terms are close to the experiment but there is almost 4 times difference in N_v derivatives. The possible reason of this is that a physical propeller working behind the submarine can model the flow much better than a modelled propeller with body force method.

Table 9 Maneuvering derivatives of DARPA Suboff bare hull form

	Re=12 x 10^6		Re=14 x 10^6		
Derivative	w/o propeller	with propeller	w/o propeller	with propeller	experimental
Y_v	-0.0087	-0.0087	-0.0087	-0.0086	-0.0059
N_v	-0.0543	-0.0543	-0.0545	-0.0545	-0.0127

5 CONCLUSIONS

The oblique towing simulations of DARPA Suboff bare hull form have been carried out at two different Reynolds numbers. The hydrodynamic forces and moments at six different drift angles have been computed. A verification study has been conducted to determine the uncertainty in the computations. The numerical results have been validated with the experimental data.

It is found that accurate results can be obtained by CFD method for hydrodynamic forces and moments. The integral values, e.g., longitudinal forces, sway forces and yaw moments, are in good agreement with the experiments. There is an increasing difference between sway forces and yaw moments after $\beta=8^o$. An offset almost the same in all drift angles is observed between the numerical and experimental longitudinal forces. It should be noted that the sign of this offset is reversed about $\beta=10^o$.

It is also found that propeller does not affect the sway forces and yaw moments while there is a considerable difference in longitudinal forces at relatively small drift angles. However, these effects decrease with increasing drift angles. Although the Y_v terms are close to the experiment, there is almost 4 times difference in N_v derivatives. An original propeller working behind the body may have different effects than the propeller modelled by body force method. This issue will be investigated in further studies.

REFERENCES

[1] M. R. Bottacini, "The Stability Coefficients of Standard Torpedos," U.S. Naval Ordnance Test Station Report NOTS 909, NAVORD Report 3346, Jul. 1954.

[2] J. D. Lambert, "The Effect of Changes in the Stability Derivatives on the Dynamic Behaviour of a Torpedo," Admiralty Research Laboratory, Technical Report ARL/R3/HY/13/0, 1960.

[3] A. Goodman, "Experimental Techniques and Methods of Analysis used in Submerged Body Research," presented at the Third Symposium on Naval Hydrodynamics, Office of Naval Research, 1960.

[4] M. Gertler and G. Hagen, "STANDARD EQUATIONS OF MOTION FOR SUBMARINE SIMULATION," Technical Report AD653861, Jun. 1967.

[5] J. Feldman, "STRAIGHTLINE AND ROTATING ARM CAPTIVE-MODEL EXPERIMENTS TO INVESTIGATE THE STABILITY AND CONTROL CHARACTERISTICS OF SUBMARINES," David W. Taylor Nval Ship Research and Development Center, Departmental Report DTRC/SHD-0393-20, Nov. 1987.

[6] N. C. Groves, T. T. Huang, and M. Chang, "GEOMETRIC CHARACTERISTICS OF DARPA SUBOFF MODELS," David Taylor Research Center, DTRC/SHD-1298-01, Mar. 1989.

[7] T. T. Huang, H.-L. Liu, and N. C. Groves, "EXPERIMENTS OF DARPA SUBOFF PROGRAM," David Taylor Research Center, Departmental Report DTRC/SHD-1298-02, Dec. 1989.

[8] R. F. Roddy, "INVESTIGATION OF THE STABILITY AND CONTROL CHARACTERISTICS OF SEVERAL CONFIGURATIONS OF THE DARPA SUBOFF MODEL (DTRC MODEL 5470) FROM CAPTIVE-MODEL EXPERIMENTS," David Taylor Research Center, Departmental Report DTRC/SHD-1298-08, Sep. 1990.

[9] J.-Y. Park, N. Kim, and Y.-K. Shin, "Experimental study on hydrodynamic coefficients for high-incidence-angle maneuver of a submarine," *Int. J. Nav. Archit. Ocean Eng.*, vol. 9, no. 1, pp. 100–113, Jan. 2017.

[10] S. Toxopeus, "Viscous-flow calculations for bare hull DARPA SUBOFF submarine at incidence," *Int. Shipbuild. Prog.*, no. 3, pp. 227–251, 2008.

[11] G. Vaz, S. Toxopeus, and S. Holmes, "Calculation of Manoeuvring Forces on Submarines Using Two

Viscous-Flow Solvers," presented at the OMAE2010, Shanghai, China, 2010.

[12] Y. Pan, H. Zhang, and Q. Zhou, "Numerical prediction of submarine hydrodynamic coefficients using CFD simulation," *J. Hydrodyn. Ser B*, vol. 24, no. 6, pp. 840–847, Dec. 2012.

[13] L. CAO and J. ZHU, "Prediction of Submarine Hydrodynamics using CFD-based Calculations and RBF Neural Network," *J. Ship Mech.*, vol. 18, no. 3, Mar. 2014.

[14] S. Duman and S. Bal, "Prediction of turning and zig-zag maneuvering performance of a surface combatant with URANS," *Ocean Syst. Eng.- Int. J.*, vol. 7, no. 4, pp. 435–460, Dec. 2017.

[15] S. Duman, F. Cakici, and S. Bal, "Numerical Simulation of Dynamic Maneuvering of a Surface Combatant Using Overset Grid Method," presented at the International Symposium on Naval Architecture and Marine Engineering, 2018, pp. 1–14.

[16] S. Sezen, A. Dogrul, C. Delen, and S. Bal, "Investigation of self-propulsion of DARPA Suboff by RANS method," *Ocean Eng.*, vol. 150, pp. 258–271, Feb. 2018.

[17] C. Delen, S. Sezen, and S. Bal, "Computational Investigation of The Self Propulsıon Performance of Darpa Suboff Vehicle," *TAMAP J. Eng.*, vol. 1, no. 1, 2017.

[18] A. Dogrul, S. Sezen, C. Delen, and S. Bal, "Self-Propulsion Simulation of DARPA Suboff," presented at the IMAM'2017, Lisbon, Portugal, 2017, pp. 503–511.

[19] D. C. Wilcox, *Turbulence Modeling for CFD*, 3rd edition. La Cãnada, Calif.: D C W Industries, 2006.

[20] J. H. Ferziger and M. Perić, *Computational methods for fluid dynamics*, 3., Ed. Berlin: Springer, 2002.

[21] L. F. Richardson, "The Approximate Arithmetical Solution by Finite Differences of Physical Problems Involving Differential Equations, with an Application to the Stresses in a Masonry Dam," *Philos. Trans. R. Soc. Lond. Ser. Contain. Pap. Math. Phys. Character*, vol. 210, pp. 307–357, 1911.

[22] P. J. Roache, "Verification of Codes and Calculations," *AIAA J.*, vol. 36, no. 5, pp. 696–702, 1998.

[23] I. B. Celik, U. Ghia, and P. J. Roache, "Procedure for estimation and reporting of uncertainty due to discretization in CFD applications," *J. Fluids Eng.-Trans. ASME*, vol. 130, no. 7, Jul. 2008.

[24] T. Tezdogan, Y. K. Demirel, P. Kellett, M. Khorasanchi, A. Incecik, and O. Turan, "Full-scale unsteady RANS CFD simulations of ship behaviour and performance in head seas due to slow steaming," *Ocean Eng.*, vol. 97, pp. 186–206, Mar. 2015.

[25] Y. H. Ozdemir, T. Cosgun, A. Dogrul, and B. Barlas, "A numerical application to predict the resistance and wave pattern of KRISO container ship," *Brodogradnja*, vol. 67, no. 2, pp. 47–65, Jun. 2016.

[26] N. C. Groves, T. T. Huang, and M. S. Chang, "Geometric characteristics of DARPA SUBOFF models (DTRC Model Nos. 5470 and 5471)," DTRC/SHD-1298-01, 1989.

[27] H. Yoon, "Phase-averaged stereo-PIV flow field and force/ moment/motion measurements for surface combatant in PMM maneuvers," PhD Thesis, University of Iowa, 2009.

A. Yücel Odabaşı Colloquium Series
3rd International Meeting - Progress in Propeller Cavitation and its Consequences:
Experimental and Computational Methods for Predictions
15th – 16th November 2018, Istanbul, Turkey

Full-Scale GATE RUDDER® Performance Obtained from Voyage Data

Masaki Fukazawa[1], Serkan Turkmen[2], A Marino[3], Noriyuki Sasaki[3]

[1]*Kamome Propeller Co.kamiyabe 690 Totsuka,Yokohama Japan zip 245-8542*
[2]School of Marine Science and Technology, University of Newcastle, Newcastle upon Tyne NE1 7RU, UK
[3]*Department of Naval Architecture, Ocean and Marine Engineering, University of Strathclyde, Glasgow G4 0LZ, UK*

Abstract: GATE RUDDER® system is a novel propulsion arrangement or Energy Saving Device (ESD) inspired by the new concept of elementary propulsive efficiency and its optimization in a ship’s wake to recover more energy. The performance of a GATE RUDDER® system in the hull wake, therefore, is important not only for the efficiency but also from the cavitation, noise and vibration point of view. The world’s first GATE RUDDER® was installed on a 2500GT container ship (Lpp=102m) built by Yamanaka Shipyard of Japan and delivered later in 2017. Excellent manoeuvring performance was reported with a significant fuel saving over her sister ship fitted with a conventional rudder. The comparative full-scale manoeuvring trials of the two sister ships with two different rudder configurations revealed that the resistance increase of the GATE RUDDER® during steering was extremely low compared to that of the conventional rudder. After some in-service experiences with both vessels, two important performance advantages with the GATE RUDDER® system have been observed. One of these advantages is the reduced sea margin requirement for the GATE RUDDER® fitted vessel while the other advantage is the improved speed-drop for the same vessel during manoeuvring in ports which makes the vessel’s berthing operations very easy and more efficient.

This paper investigates the reasons for the above-mentioned two important performance advantages of the vessel fitted with the GATE RUDDER® system, based on the performance data obtained not only from model tests, but also from the voyage data collected over the 7 months after the delivery of this vessel

1 INTRODUCTION

GATE RUDDER® system is a new and innovative ESD technology for ships to propel and steer them more efficiently. As opposed to a conventional rudder, which is usually behind a propeller, the GATE RUDDER® has two rudder blades with asymmetric sections, which are located aside the propeller, and each blade can be controlled independently. The two rudder blades, encircling the propeller at the top and sides, provide a duct effect and hence produce additional thrust, as opposed to the additional drag of a conventional rudder behind the propeller. See Figure 1 for comparison of the conventional rudder and GATE RUDDER® system on two sister vessels which are the subject of this paper. The independent control of the two rudder blades also provides effective control of the propeller slipstream and hence steering, Sasaki et al (2015). Thus the GATE RUDDER® system presents not only more propulsive efficiency but also higher manoeuvrability. In addition to these two major advantages of the GATE RUDDER® system, there are other performance superiorities, which are noticed based upon the further analysis of the voyage data, including reduced resistance during manoeuvring motion.

To shed a light on the further performance advantages of the GATE RUDDER® system, which are associated with the induced resistance during manoeuvring as well as the performance in waves, this paper investigates the details and sources of these performance improvements based on not only the model tests, but also the log book data obtained from the two sister container vessels shown in Figure 1 and detailed in Table 1. In the table Vessel A is fitted with a conventional flap rudder-propeller system while her sister Ship B is fitted with the GATE RUDDER® system.

Table 1 Principal dimensions of S Shigenobu & Sister Ship

	Ship A	Ship B
Loa (m)	111.4	
B (m)	17.8	
d (m)	5.24	
Main Engine	3309kW x 220rpm	
Rudder	Flap Rudder	GATE RUDDER
Delivery	August 2016	December 2017

---

* *Corresponding author e-mail: noriyuki.sasaki@strath.ac.uk*

2 GATE RUDDER CONCEPT

A ship's rudder is one of the sources in contributing to the ship's resistance. Within this context, the main purpose of the GATE RUDDER® system is to remove this source or rather replace with a thrust source (like a duct) to achieve higher thrust and hence improved propulsive efficiency. With this idea, the rudder may become an ESD by being placed aside the propeller, instead of behind the propeller, to simulate the duct effect of a ducted propeller, but with additional manoeuvring capability by independently moving the two rudder blades to control the propeller slipstream, in contrast to the fixed nozzle of the ducted propellers. The GATE RUDDER® arrangement also reduces the viscous energy losses created by the hull boundary layer and utilise the wake flow more effectively than the traditional rudder-propeller arrangement, Sasaki et al (2018).

In a similar way, although many ideas and applications exist to combine a rudder and a propeller, such as podded propulsion systems, steerable ducted propellers and so on (e.g. Carlton, 2012), these propulsion systems generally work with limited applications in the full scale without fully exploiting their propulsive performances and manoeuvring abilities. In contrast, the GATE RUDDER® propulsion system has a flexibility that can be applied to a new design as well as a retrofit system to many types of conventional vessels where the conventional rudder-propeller system can be used.

As reported in Sasaki et al (2018) the GATE RUDDER® propulsion system was originated in Japan and has been further developed in UK through CFD and EFD studies since 2014. Based on these developments, the first GATE RUDDER® system was applied to a 2400 GT container ship and the full-scale sea trials were carried out in November 2017 in Japan. The performance gain expected from the application of this novel ESD was demonstrated by the comparison of these trial results with those of her sister container vessel of the same design, except the rudder system, which is a conventional flap rudder-propeller system and this vessel was delivered one year before in 2016 as shown in Figure 1. Both vessels currently operate on the same route in Japan between Hokkaido and Yokohama.

The analysis of the sea trials data conducted in the same geographic region with the two vessels with about one year interval and those of the voyage data on the same service routes indicated that the container vessel with the GATE RUDDER® system can save abt. 14% more fuel over the vessel with the conventional rudder-propeller system.

Based on the experiences during the sea trials and following on-board experiences of both vessels' captains during service, it was noticed that the vessel with the GATE RUDDER® experienced less power demand (hence reduced sea margin) during the winter season when the wind and waves are relatively high compared with other seasons. Based on these observations, as the main objective of this paper, it has been decided to explore the resistance characteristics of both vessels associated with the manoeuvring motions during their navigations. However, these manoeuvring motions are not the motions imposed by large rudder helm angles but by rather small helm angles (within 20 degrees) which can be adopted by the auto pilot system in order to keep the same heading course in navigation

Figure 1 Conventional Flap-Rudder (Top) vs. GATE RUDDER® (Bottom)

3 MANOEVRING TESTS

3.1 Model test and test set-up

In order to investigate huge energy saving during her navigation period, test data obtained from the manoeuvring tests with 2.5 m wooden model equipped with GATE RUDDER® was reanalysed. This main particulars of this model, which represented a general cargo vessel, was slightly different from the container ship model since the latter has a superior manoeuvrability in course keeping compared to a cargo ship with larger fullness parameters such as C_B and L/B etc.

The main particulars of the vessel selected here are compared with the container ship as listed in Table 2. Figures 2 through 4 show the general view, aft end details with the conventional flap rudder and GATE RUDDER® arrangements as well as the measurement system arrangement during the tests.

Table 2 Ship Model for the Test

	Cargo	Container
L/B	5.717	5.725
B/d	2.892	3.397
CB	0.73	0.67
Vs (kts)	13	14.5

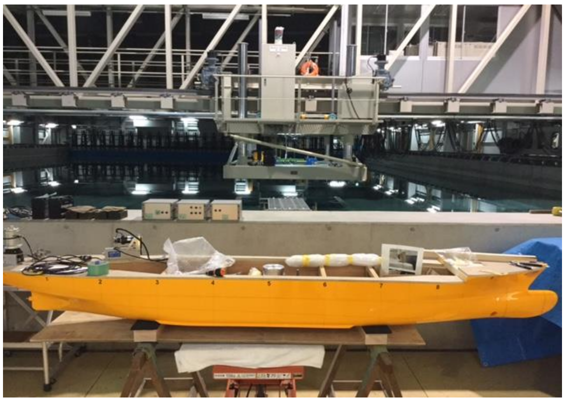

Figure 2 2.5 m Wooden Model

Figure 3 Fish Tail Rudder arrangement

3.2 Measurement system

Captive model tests and free running test were conducted in the Kyushu University model basin by following their standard procedures. During these tests, the forces and moments on the starboard rudder blade of the GATE RUDDER® were measured. These measurements were complemented by the propeller thrust and torque as well as the ship motions and hull hydrodynamic force/moments (only captive tests) measurements. Table 3 lists the measured parameters during the model test

Table 3 Conducted Manoeving Model Test

Kind of tests	Ship speed	Measured items
Speed trial	0 – max.	V, F, n, T, Q
Cartive Test	Design Vs	β,V, F, n, T, Q, F_X, F_Y N_Z, F_{RX}, F_{RY}, N_{RZ}
Free Runing	Design Vs	V, n, φ , φ ’, X,Y, X’,X’’,Y’,Y’’
Rudder Force Test	Design Vs Port Vs	β,V, F, n, T, Q, F_X, F_Y N_Z, F_{RX}, F_{RY}, N_{RZ}
Bollard Test	0	n. T, Q, F, F_{RX},F_{RY},N_{RZ}
V:model speed(m/s), F:towing force(N), n:rps, T: thrust(N), Q(N-m), Fx: ship X direction force(N), Fy: ship Y direction force(N), Nz: ship moment at Z axis(N-m), X: ship position X in thr tank, Y: ship position Y,F_{RX}: rudder x direction force (N), F_{RY}: rudder y direction force(N), N_{RZ}: rudder moment at z axis (N-m), φ: ship heading angle (deg.)β: shp oblique angle (deg.)		

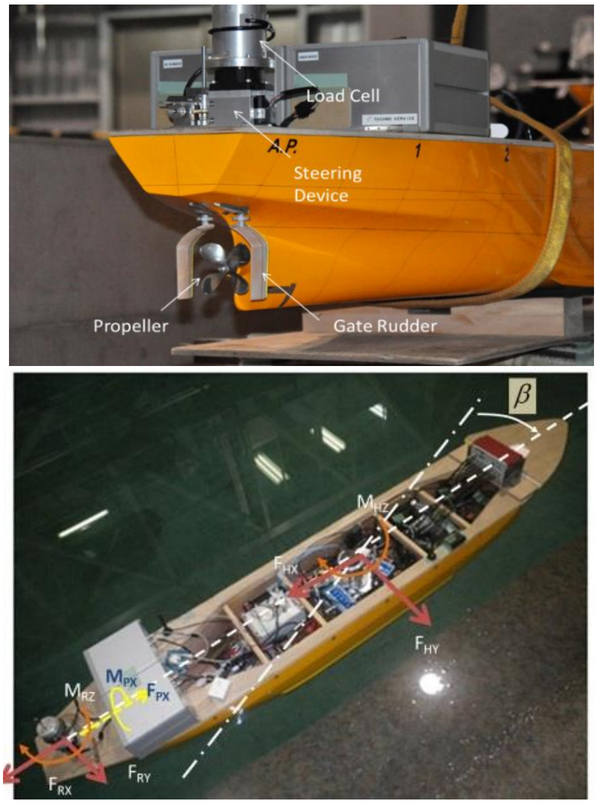

Figure 4 GATE RUDDER® arrangement and measurement System installed on the model

3.3 Test Conditions

The test conditions used for the captive and free running tests were decided from the speed trials prior to the

manoeuvring tests. The test conditions for the captive tests and rudder force measurements (during free running tests) are shown in Table 4 and Table 5, respectively.

Although comprehensive data collected during the manoeuvring test campaign, here in this study, only some parts of the captive tests and free running tests involving the measured rudder forces and moments are used.

It is also noted that the required thrust for the GATE RUDDER® case was much smaller than that of the conventional rudder case due to the additional thrust originated from the GATE RUDDER® blades.

Table 4 Test Conditions Captive Test

Kind of Rudder	***V***	***n***	***β***	***δ***	***T***
	m/s	rpm	deg.	deg	N
Fish Tail	0.5	11.22	0	0	156
			10	0	133
			-10	0	158
GATE RUDDER	0.5	11.46	0	0	146
			10	0	130
			-10	0	148

Table 5 Test Conditions Rudder Force Measurement

Kind of Rudder	***V***	***n***	***δ***	
	m/s	rpm	deg	
Fish Tail	0.5	11.22	-45,-30,-15, 0,15,30,45	
GATE RUDDER	0.5	11.46	port -30 -15 0 15 30 45 60	starboard -30 -15 0 15 30 45 60

3.4 Test results

Captive model tests and free running test were conducted in the Kyushu University model basin by following their standard procedures. During these tests, the forces and moments on the starboard rudder blade of the GATE RUDDER® were measured. These measurements were complemented by the propeller thrust and torque as well as the ship motions and hull hydrodynamic force/moments (only captive tests) measurements. Table 2 lists the measured parameters during the model test.

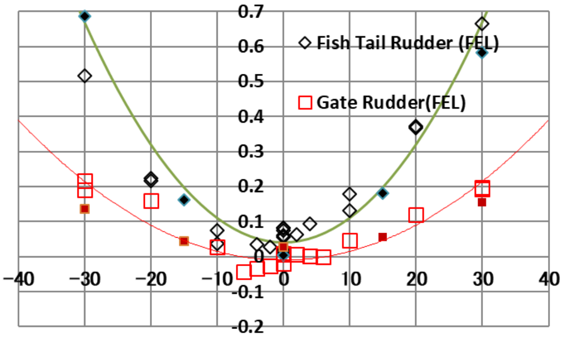

Figure 5 Resistance of rudder due to helm (fraction of ship resistance)

5 VOYAGE DATA AND DISCUSSION

From the model test, it is quite obvious that the resistance of the GATE RUDDER® is rather small compared with that of conventional rudders. This implies that the vessel equipped with the GATE RUDDER® should require a smaller sea margin than the vessel with the conventional rudder. In order to investigate this attractive feature, it has been decided to analyse the full-scale data collected with the two sister ships. This was because the owner of the both vessels routinely collects the data in their logbook as part of their strandard operation and management tasks.

After the delivery of the vessel with the GATE RUDDER®, 7 months of very interesting data were obtained from the logbook of the two ships. There was nothing special with these data but they were collected according to the owner's long term practice and experience. Also the data quality was the same as for other vessels , however it is very important and fortitious that two vesselas are running on the same route, almost the same day and in the same loading conditions (draught).

Apart form the logbook data, some special data collection were conducted by the onboard measuremets, e.g. accurate power monitoring by the newly fitted torque meter and conducting optimum rudder angle tests during voyage and recording the data. The full analysis results of these data and tests will be reported by the end of the ongoing GATE RUDDER® project which is supported by the Nippon Fundation.

Figure 6 presents the average wind speed data collected over the 7 months of onboard monitoring including the trend line. Year 2018, which covered the part of the onboard data monitoring and collection, was extraordinarily different from the last 10 years in Japan. Many typhoons attacked Japan and they might have affected the performance of the two vessels after August 2018.

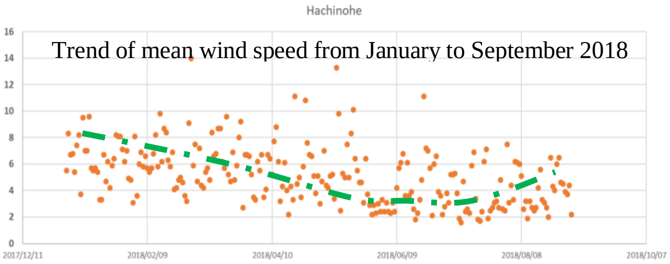

Figure 6 Trend of mean wind speeds (m/s) at Hachinohe from Jan. to Sept. 2018

Based upon the analysis of the two vessels' log book data, Figure 7 shows the comparison of the Admiralty Coefficients (C_{adm}) for both vessels over the 7 months of on board data collection campaign.

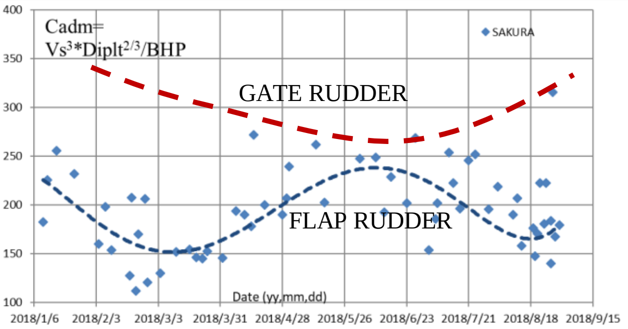

Figure 7. Trend of Admiralty coefficients based on logbook data of two sister ships (Jan. –Sept.2018)

As one can see from the trend lines plotted in Figure 7 the vessel with the GATE RUDDER® has clear powering performance superiority over her sister with the conventional rudder and this is particularly higher over the winter period.

The latter finding, i.e. better powering performance of the ship with the GATE RUDDER®, is most interesting and attractive that requires further investigation. In relation to this interesting finding, it is worthy to re-analyse the results of the seakeeping tests conducted with a container ship model with the GATE RUDDER® at the towing tank of the Newcastle University as part of an MSc study.

As shown in Figure 8, these tests involved the added wave resistance measurements with a 2.1m container model which was equipped with actively controlled GATE RUDDER® and its counter-part conventional rudder. These tests demonstrated the wave absorbing behaviour of the vessel under the effect of actively controlled GATE RUDDER® with small helm angles synchronized with the encounter wave frequency in head seas.

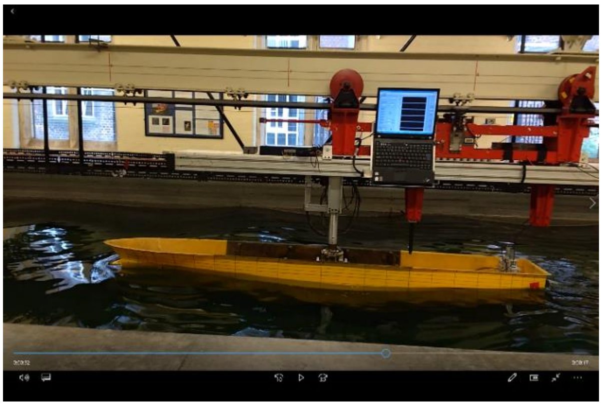

Figure 8 Active GATE RUDDER® Control Tests in waves

In order to investigate the rudder resistance further, the simulation program, which was developed by Newcastle University by Carchen et al. (2018), was used. The software was used to simulate the data collected during the model tests conducted at the Kyushu University manoeuvring basin, and presented in Figure 5.

Figure 9 shows the simulation results for the zig-zag tests from the same initial ship speed. In this figure time history of ship speed (m/s) and propeller thrust (kN) for the GATE RUDDER® and conventional rudder case, respectively. The rudder resistances were calculated according to the data measured during the model tests (Figure 5). The resistance curves of two data sets (for Fish Tail rudder and GATE RUDDER®) were interpolated with parabolic curves, which were implemented in the simulation programme developed by Carchen et.al.(2016).

For both Fish Tail and GATE RUDDER®, three points of the relative parabola were taken (at helm angle = -30°, 0°, 30°) and the resistance increment was measured. From these values, it was possible to obtain the coefficients of the curves to embed in the simulation programme.

According to the obtained measurements, and taking into account the ship motion effect, the two parabolas were embedded as follows:

Conventional rudder: $X_{Rud}/R = 2.261(0.6 \cdot \delta)^2 + 0.05$

GATE RUDDER®: $X_{Rud}/R = 0.776(0.6 \cdot \delta)^2 - 0.04$

where X_{Rud}/R is the resistance increment ratio to hull resistance due to the rudder, and δ is the helm angle.

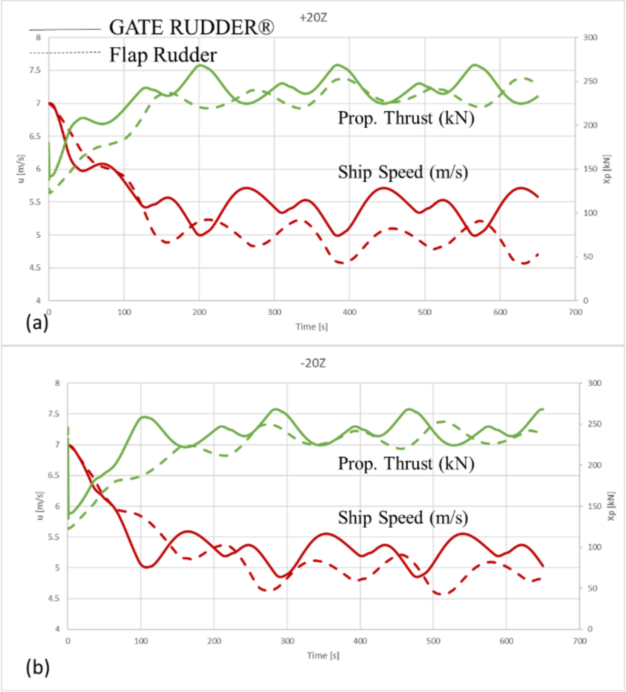

Figure 9 Propeller Thrust and Ship Speeds for two Ships

The rudder angle in the simulations shown in Figure 9 ranges from +20° and -20° (a), and from -20° and +20° (b), i.e. with the ship heading starboard and port at the beginning of the manoeuvre, respectively. The graphs show that, at the same propeller thrust, the GATE RUDDER® allows the ship to keep a higher speed. It is also visible that the velocity oscillations have a higher frequency when the GATE RUDDER® is used, which implies a higher manoeuvrability, compared to the conventional rudder (Figure 10). Another word the vessel with the GATE RUDDER® is more responsive to the helm actions. Based on these simulation results one can conclude that the rudder resistance has an important role for the power savings during the navigation and the GATE RUDDER® can save considerable energy during navigation. Since the power is proportional to V^3, the difference in ship speed indicated by Figure 9 corresponds 30% of power difference if we need to keep the same speed for both ships.

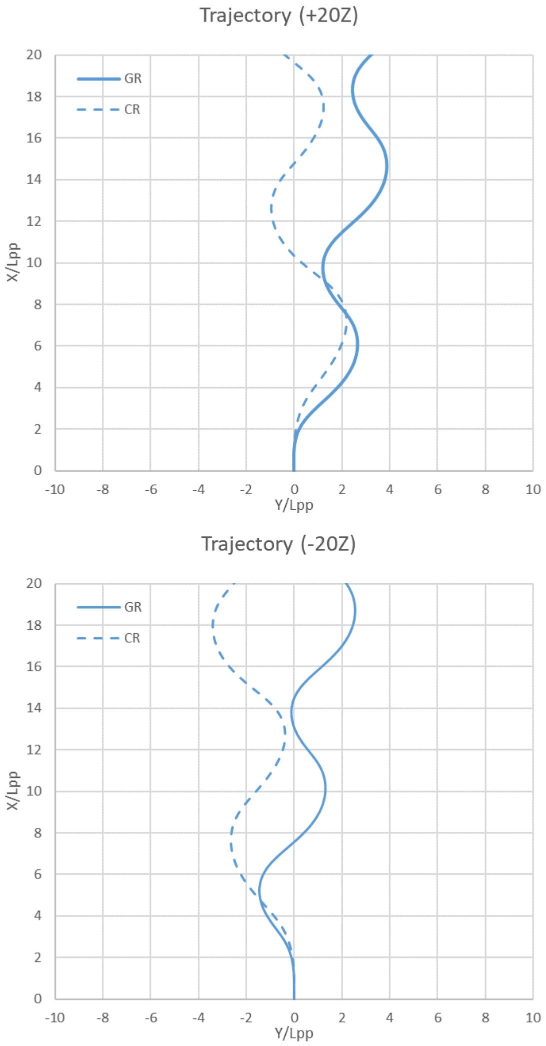

Figure 10 Trajectory during zig-zag test starboard (top) and portside (bottom)

6 CONCLUDING REMARKS

This paper investigated the reasons for the different tendencies in the energy saving performances of two sister ships (Figure 7), which are equipped with two different rudder systems, based on their voyage data.

The difference in the tendency was found during the winter season and typhoon season where the wind and wave was extremely high. Except these periods deviation of the powering performance of the two vessels is around 15% which is very close to the results obtained during the speed trials.

By investigating the model test manoeuvring data and conducting the simulation reflecting these data, it was concluded that the difference in rudder resistance during manoeuvring is the most likely reason for this.

The rudder resistance of the GATE RUDDER® is extremely low compared to that of a conventional rudder. This fact affects the voyage data for both ships in a different way.

It may require further study to conclude that the difference of the rudder resistance is the main cause. However, there is no doubt that the GATE RUDDER® has the big advantage of having smaller resistance during the manoeuvring motion.

REFERENCES

Carchen A., Shi W., Sasaki N, Atlar M, (2016) A Prediction of manoeuvrability. AYO2016, Istanbul Nov. 2016

Molland A.F., Turnock S.R., (2011). Marine Rudders and Control Surfaces,

Sasaki, N., Atlar, M. and Kuribayashi, S. (2016). The new hull form with twin rudders utilizing duct effects, J Mar Sci Technology (2016) 21: 297.

Sasaki N., Atlar, M. and Kuribayshi, S. (2015). Advantage of twin rudder system with asymmetric wing section aside a propeller. Journal of Marine Science and Technology

Sasaki N., Kuribayshi, S., Asaumi N., Fukazawa M., Nonaka T., Turkmen S., Atlar M., Measurement and calculation of gate rudder performance, AMT'17, 2017, Istanbul

Turkmen, S., Carchen, A., Sasaki, N. and Atlar M. (2015). Anew energy saving twin ruder system, International Conference on Shipping in Changing Climates, Nov. 2015, Glasgow.

A. Yücel Odabaşı Colloquium Series
3rd International Meeting - Progress in Propeller Cavitation and its Consequences:
Experimental and Computational Methods for Predictions
15th – 16th November 2018, Istanbul, Turkey

Effectiveness of Boundary Element Method Hydrodynamic Data for Propeller Hydroacoustics

Claudio Testa[1*], Federico Porcacchia[2], Luca Greco[1], Roberto Muscari[1]
[1]*CNR-INM Institute of Marine Engineering, Rome, Italy*
[2]*Roma Tre University - Department of Engineering, Rome, Italy*

Abstract: This work investigates capabilities and drawbacks of potential-based hydrodynamic data for the prediction of the noise signatures generated by marine propellers in open water. A fully-validated, three-dimensional, unsteady, free-wake panel method, along with the Bernoulli equation, are combined with the Ffowcs Williams and Hawkings Equation for permeable surfaces (FWH-P) to yield the sound signals at hydrophones located in the near-field. Outcomes of the proposed method are compared with the pressure disturbances coming directly from a Detached Eddy Simulation (DES) of the propeller and those predicted by a FWH-P/DES approach to shed light on the limits of applicability of Boundary Element Method (BEM) hydrodynamics for propeller hydroacoustics.

Keywords: BEM hydrodynamics, DES hydrodynamics, Acoustic analogy, Propeller hydroacoustics.

1 INTRODUCTION

High performance propellers and more powerful engines are widely used in marine applications, thus resulting in a general increase of the hydrodynamic noise radiated underwater. Due to the increasingly demanding constrains on propeller-induced noise in terms of certification rules, civil/military requirements and acoustic pollution, prediction and alleviation of noise footprints are crucial issues for international shipbuilding industry especially during the pre-design stage where hydroacoustic and hydrodynamic constrains guide the choice of the *optimal* propeller system. In this framework, the notable know-how gained through 30 years of research activities on Aeroacoustics proves that the Ffowcs Williams and Hawking Equation (FWH) is the most powerful approach to tackle the hydroacoustic analysis of rotary-wing devices since sound propagation is described by a rearrangement of the fundamental conservation laws for compressible flows into an inhomogeneous wave equation forced by three source terms identifying well-defined noise generation mechanisms (Ffowcs Williams & Hawkings 1969). It is worthy note how the results achieved within the European Project SILENV represent a sort of *breakpoint* for hydroacousticians respect to the analogue problems of noise generation and propagation in air, pointing out that non-cavitating propeller underwater acoustics is an inherently nonlinear problem, in that governed mainly by the hydrodynamic sources of sound in the flow field around the propeller. Specifically, sound from the FWH surface terms (namely, thickness and loading noise) appears significant only *close* to the propeller, decreasing rapidly respect to the volume terms contribution (namely, quadrupole noise) induced by the hydrodynamic sources of sound (*i.e.*, vortex released at the blade tip, vorticity, turbulence, etc..) which can be very intense and persisting around/downstream the propeller disk (28th ITTC).

Since such flow phenomena are at the origin of sound generation, their detection is mandatory for an accurate hydroacoustic prediction. To this aim, RANS (Reynolds Averaged Navier Stokes) simulations, widely and fruitfully used for the prediction of propeller performance, have proven to be not suited for hydroacoustic purposes because of the relevant numerical diffusion and intrinsic incapability to correctly model the vorticity and turbulence fields spreading downstream the propeller (Ianniello et al 2013). To overcome this limitation, the use of Detached Eddy Simulation (DES) approaches allows to combine the advantages of RANS computations (near solid boundaries) with those of Large Eddy Simulation (LES) calculations in fluid domains where the spatial discretization is fine enough. Although well suited for propeller hydroacoustics, the computational cost of the combined FWH/DES formulation is significant due to the demanding DES grid resolution. However, limiting our interest to the *near-field* (few diameters from the propeller hub) the tonal noise components may play an important role and a potential-based hydrodynamic theory for unsteady three-dimensional (3D) flows might be used, at reasonable computational costs, to detect the sources of sound inherently associated to the blades and vorticity convected downstream. Acoustic scattering problems in which hydroborne propeller sound interacts with the hull, being spread out into reflected and diffracted noise components, fall within this field of application (Testa & Greco 2018, Testa et al 2007).

In the attempt to define the effectiveness of Boundary Element Method (BEM) hydrodynamic data for propeller hydroacoustics, the present paper proposes a comparison

---

* *Corresponding author e-mail: claudio.testa@cnr.it*

between the noise signatures predicted by the FWH/DES and FWH/BEM approaches. The investigation is addressed both in the time and frequency domain to get a deep insight into the quality of the predicted signals in terms of waveform and harmonic content. The four-bladed propeller model INSEAN E779A (Di Felice et al 2004) extensively studied by the maritime community, is investigated in open water at an advancing ratio assuring comparable thrust and torque predictions between DES and BEM hydrodynamic simulations as well as coherent wake flow description. To avoid demanding 3D integrations for quadrupole noise detection, the porous FWH equation (Farassat & Myers 1988, Farassat 1996, Di Francescantonio 1997) is herein proposed, using a permeable acoustic surface of cylindrical shape, co-axial with the propeller shaft and rototranslating with the propeller blades.

2 ACOUSTIC MODEL

Let $f(\boldsymbol{x},t)$ (with $|\nabla f| = 1$) identify an arbitrary permeable surface S moving throughout the fluid domain with velocity $\mathbf{v}$. Under the assumption of negligible entropy changes, the acoustic pressure disturbance outside S, generated by the sources of sound inside and outside it, is governed by the Ffowcs Williams and Hawkings Equation (FWH-P) (Di Francescantonio 1997)

$$\begin{aligned}\overline{\boxdot}^2\, p' = {} & \frac{\bar{\partial}}{\bar{\partial} t}[\rho_0 \mathbf{v}\cdot\nabla f\ \delta(f)] + \frac{\bar{\partial}}{\bar{\partial} t}[\rho(\mathbf{u}-\mathbf{v})\cdot\nabla f\ \delta(f)] \\ & + \overline{\nabla}\cdot[\mathbf{P}\,\nabla f\ \delta(f)] - \overline{\nabla}\cdot[\rho\mathbf{u}\otimes(\mathbf{u}-\mathbf{v})\nabla f\ \delta(f)] \\ & + \overline{\nabla}\cdot\overline{\nabla}\cdot[\mathbf{T}\,H(f)] \qquad (1)\end{aligned}$$

where bars denote generalized differential operators, $\overline{\boxdot}^2 = (1/c_0^2)\left(\bar{\partial}^2/\bar{\partial}t^2\right) - \overline{\nabla}^2$ represents the wave operator

whereas $H(f)$ and $\delta(f)$ are the Heaviside and Dirac delta functions, respectively. In addition, $\mathbf{u}$ is the local fluid velocity, $\mathbf{P} = [(p-p_0)\mathbf{I}+\mathbf{V}]$ the compressive stress tensor, $\mathbf{V}$ is the viscous stress tensor whilst $\boldsymbol{T} = \rho(\mathbf{u}\otimes\mathbf{u}) + (p-p_0)\mathbf{I} - c_0^2(\rho-\rho_0)\mathbf{I}+\mathbf{V}$ represents the Lighthill tensor. Following the Green function approach presented in (Morino and Gennaretti 1992), in a space rigidly connected with the surface S the boundary-field integral solution of Equation (1) reads

$$\begin{aligned}p'(\mathbf{x},t) = & -\int_V \left[\hat{G}\,\nabla\cdot\nabla\cdot(\mathbf{T}\,H)\right]_\vartheta dV(\mathbf{y}) \\ & -\int_S \left[(\mathbf{Pn})\cdot\nabla\hat{G} - (\mathbf{Pn})^{\cdot}\cdot\nabla\vartheta\,\hat{G}\right]_\vartheta dS(\mathbf{y}) \\ & -\rho_0\int_S \left[\mathbf{v}\cdot\mathbf{n}\,\mathbf{v}\cdot\nabla\hat{G} + \left(\mathbf{v}\cdot\mathbf{n}(1-\mathbf{v}\cdot\nabla\vartheta)\right)^{\cdot}\hat{G}\right]_\vartheta dS(\mathbf{y}) \\ & -\int_S \left[\rho\mathbf{u}^-\cdot\mathbf{n}\,\mathbf{u}^+\cdot\nabla\hat{G}\right]_\vartheta dS(\mathbf{y}) \\ & -\int_S \left[\left(\rho\mathbf{u}^-\cdot\mathbf{n}(1-\mathbf{u}^+\cdot\nabla\vartheta)\right)^{\cdot}\hat{G}\right]_\vartheta dS(\mathbf{y}) \qquad (2)\end{aligned}$$

Here, V indicates the volume surrounding the porous surface S where the noise sources related to the Lighthill stress tensor are not negligible, $[\cdots]_\vartheta$ denotes that the kernel of the integral must be evaluated at the retarded emission time, $\tau = t - \vartheta$, being ϑ the time required by an acoustic disturbance released from a source in $\mathbf{y}$ to reach the observer point $\mathbf{x}$ at current time t. Furthermore, $\hat{G} = -1/[4\pi r(1-M_r)]_\vartheta$ indicates the retarded Green function, $r = |\mathbf{r}|$, $\mathbf{r} = \mathbf{x}(t) - \mathbf{y}(\tau)$ whilst $M_r = (\mathbf{v}\cdot\mathbf{r})/(c_0\, r)$ is the surface Mach number along the direction where radiation occurs. In addition, the symbol $(\ \ )^{\cdot}$ denotes time derivative computed in the space rigidly moving with V whereas $\mathbf{u}^- = \mathbf{u}-\mathbf{v}$, and $\mathbf{u}^+ = \mathbf{u}+\mathbf{v}$. Equation (2) states that the sources of sound enclosed by S affect the noise signature at $(\mathbf{x},t)$ through surface integral terms whereas the acoustic effect from those sources outside S comes from volume integral contribution. However, if S is such to include *all* the volume sources of sound, the contribution from the volume integral vanishes (namely the quadrupole term) and noise computation reduces to the solution of a boundary integral representation, here solved by a *zero-th* order BEM where S is divided into quadrilateral panels and p', $\mathbf{u}$ and their derivatives are assumed to be piecewise constant.

The input data set on the permeable surface (that is, pressure and velocity fields) are provided by a prior hydrodynamic analysis of the flowfield inside S. In this work, the turbulent flow past the propeller, is predicted by a DES (Muscari et al 2013) providing velocity and pressure data in the whole numerical domain to be used both as input for the hydroacoustic solver and validation purposes. Noise signals predicted by the FWH-P/DES combination are hereafter assumed as reference outcomes to address a comparison with those carried out through the solution of Eq. (2) (without the volume term) where the hydrodynamic data on S come from a steady-state simulation of the propeller in open water *via* a fully-validated free-wake three-dimensional (3D) panel code based on a BEM solution of the Laplace equation coupled with the Bernoulli equation (Greco et al 2007, 2014, 2018, Leone et al 2013). Obviously, the use of a potential hydrodynamic approach detects only the sources of noise due to the propeller motion, blades pressure distribution and trailed vorticity convected in the potential wake, losing any other kind of hydrodynamic phenomenology. Note that both DES and BEM hydrodynamic data on the porous surface are based on the assumption of incompressible flows that is fully adequate if the absence of compressibility effects represents a source of sound on its own and for low Mach rotational speed (Ianniello et al 2013).

3 NUMERICAL RESULTS

The hydroacoustics of INSEAN E779A (Di Felice et al 2004) in open water is investigated. The advance coefficient and shaft angular velocity are 0.88 and 25 rps, respectively. Propeller diameter is D = 0.22727 m. Figure 1 depicts the main features of CFD computational grid; it is composed by many patched and overlapped structured grid blocks, with those closer to the hub and blades assuring fine resolution of the wake portion closer to tip and root. Toroidal blocks embedding the hub and blades are used to resolve the downstream region where the wake is expected to evolve. A series of cylindrical blocks with increasing coarse grid define the background of the computational domain which is composed by a total of about 11 millions of cells. The acoustic observers are assumed to translate rigidly with the propeller hub. Their positions are shown in Figure1 whereas the XYZ coordinates respect to a frame of reference centered at the hub and co-moving with it, are listed in Table 1.

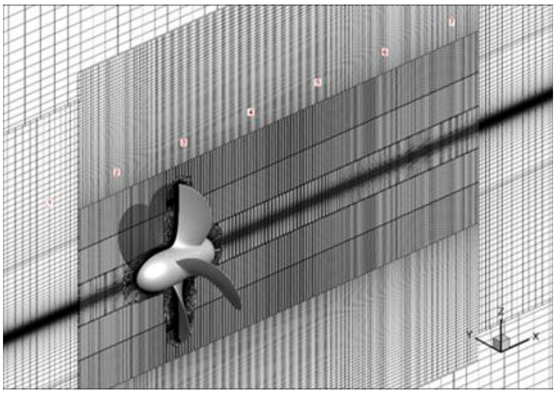

Figure 1 Sketch of CFD computational grid.

BEM computations are performed with 48 chordwise and spanwise panels for the propeller blades surface and about 900 total panels for the hub, whilst 180 panels per revolution discretize a wake length of about 3 diameters from the propeller disk (see Figure 2).

Table 1 Acoustic observers coordinates

Obs	[x/D]	[y/D]	[z/D]
1	-1	0	0.75
2	-0.5	0	0.75
3	0	0	0.75
4	0.5	0	0.75
5	1	0	0.75
6	1.5	0	0..75
7	2	0	0.75

The porous cylindrical surface S, immersed into the CFD domain, is shown in Figure 3. Radially, the radius size assures that, just outside the cylinder, the Lighthill stress tensor $\mathbf{T}$ is negligible at any time of DES simulation whereas longitudinally, the cylinder length guarantees that the end-closure is placed where the magnitude of $\mathbf{T}$ is bounded (in time) within the smallest values it assumes in the slipstream of the propeller. In fact, even though the limited size of the computational domain does not allow $\mathbf{T}$ to vanish behind the propeller, a well-posed CFD characterization of the volume sources of sound has to provide a smooth decay of $\mathbf{T}$ (at any time) in the regions where the mesh gets coarser, downstream in the freely evolving wake. Note that, the extension of the acoustic surface to the region where the vortices have dissipated, removes the spurious noise source nearly completely (Nitzkorski et al 2014).

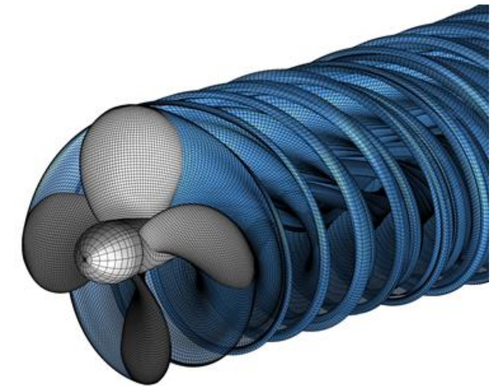

Figure 2 Sketch of BEM computational grid

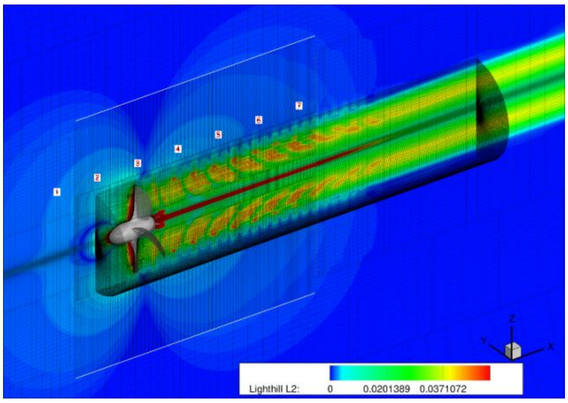

Figure 3 Sketch of FWH-P porous surface and averaged contour of the L2 norm of non-dimensional Lighthill stress tensor.

Figure 4 compares noise signals predicted by the FWH-P/DES and FWH-P/BEM approaches. For completeness, the pressure disturbances directly provided by DES simulations are shown, too. Here, DES input data over the acoustic surface come from a *running-averaged* solution of the collected data, that is, a phase-locked averaging process of the unsteady hydrodynamic flowfield, yielding a vortical flow filtered by any turbulence-induced effect. Such processing is adequate to investigate the *strength* of a BEM formulation in capturing the tonal noise hydrodynamic sources. To this aim, an analysis of the unsteady data set suggests to consider as statistically significant, those hydrodynamic samples ranging from the 6th to the 16th propeller revolution. As depicted, from Obs1 to Obs4, the agreement among predictions is excellent: the noise is dominated by vorticity phenomena, well captured by the BEM hydrodynamic solver, as confirmed also by the analysis in the frequency domain highlighted in Figure 5 where the frequency content of the signals shows only tones multiples of the shaft frequency f_0. At Obs5, the waveform and peak-to-peak comparison starts to get worse

(Figure 4). The frequency analysis in Figure 5 exhibits a contribution at f_0 that is the main responsible of the waveform distortion. This phenomenon is amplified at Obs6 where FWH-P/BEM and FWH-P/DES predictions are no more comparable. At this position, the FWH-P/DES signature is characterized by an important contribution from the first harmonic differently from the FWH-P/BEM outcome that remains purely dominated by the $4f_0$ frequency. Similar considerations hold at Obs7. The above results suggest that, within a longitudinal distance of 0.5÷1D from the hub, propeller hydroacoustics is dominated by potential wake vorticity effects. However, moving downstream, the DES averaged field detects important vorticity contributions that deeply modify the overall sound. Although averaged, these contributions are the results of complex interactions among vortices occurring during propeller revolution, that, locally, may give rise to stronger vortex structures inducing higher level of noise behind the disk. For instance, this happens at Obs7 where the noise magnitude is almost 5 times greater than at Obs6 located one radius upstream. For completeness, it is of interest to compare the vorticity field predicted by BEM and DES-averaged simulations. Making reference to the longitudinal XZ plane (see Figure 1), up to 2D downstream the propeller disk, Figure 6 compares the contour map of the vorticity component along the Y axis predicted by DES and the trailing wake location carried out by BEM (black lines). The overall propeller wake features, such as wake contraction, tip-vortices spacing/growth along X and mid-span trailed vorticity, are coherently described by the two solvers in the near wake region (up to 1D downstream). Further downstream, BEM predicted tip-vortex location shows a slight shift towards the propeller disk which is not present in DES simulation. This is confirmed also by the thrust coefficients values shown in Table 2 where BEM predictions are about 5% higher than DES outcomes. Nevertheless, the general shape of the trailed-wake is satisfactorily described. Finally, note that BEM-predicted wake tends to roll-up in the region close to the rotation axis similarly to what happens at the blade tip; such an unphysical solution is mainly due to the lack of a suitable hub-vortex model interacting with blades vorticity. In that flow region DES calculations correctly show the presence the hub-vortex.

Table 2 Thrust and torque numerical predictions

DES running averaged	**BEM**
KT = 0.1335	KT = 0.1407
10KQ = 0.2843	10KQ = 0.2971

Next, the comparison between FWH-P/BEM results and those carried out through the unsteady DES data set on the acoustic surface, is proposed. The FWH-P/DES computations in Figure 7, including here turbulence-induced noise effects, oscillate about the predictions provided by the FWH-P/BEM solver, at least up to Obs4. At Obs1 and Obs5, the low level of pressure fluctuations coming from the direct DES simulation emphasizes the effects caused by reflections of disturbances from the boundaries of the numerical domain. These disturbances persist despite the use of a stretched mesh towards the boundaries and, in turns, alter also the FWH-P/DES prediction. Such unphysical behavior is related to the way of modelling CFD boundary conditions, that should require the use of the characteristic method (Poinsot & Lele 1992). In the DES solver herein used, such issue is numerically controlled through a suitable varying mesh sizing (starting from the boundaries) able to filter the higher wavelengths frequency content of the reflected signals. To this aim, a devoted analysis, not shown here because well beyond the scope of this paper, highlights how these signals enter somehow into the acoustic surface, in that, for a porous cylinder such to encapsulate completely the quadrupole flow features, the noise at any observer inside S (due to surface terms) is not zero (as it should be). However, the mesh grid size from the boundaries to the acoustic surface makes these interior fictitious sources almost ineffective, as proven by the low levels of fictitious noise induced inside. Hence, the filtering effect of the acoustic surface makes FWH-P/DES results acoustically-consistent. Differently, DES pressure disturbances at the observer positions are much more prone to the issue of boundary reflections, especially where DES and FWH-P/DES outcomes do not match well. However, apart from Obs1 and Obs5, a satisfactory agreement is observed. At Obs2 and Obs3, turbulence-induced noise is almost negligible, since the waveforms, noise levels and frequency content of the overall sound, depicted in Figure 8, are very similar to those predicted by the running averaged technique. At Obs4, turbulence sources of sound determine a distortion of the signal; differently form Obs2 and Obs3, the spectrum highlights acoustic energy spread out over all the harmonics herein analyzed ($\leq 20 f_0$). Nevertheless, the FWH-P/BEM signal captures the main features of the noise and provides a sort of average signature about which the FWH-P/DES prediction oscillates. Akin to the running-averaged case previously discussed, from Obs5 on, the comparison between signals is no more reasonable; broadband noise due to flowfield vorticity and turbulence is exhibited and the $4 f_0$ harmonic is also not well captured by the FWH-P/BEM approach. As a matter of fact the characterization of the tonal hydrodynamic sources of sound by a potential-based theory is allowed only if the acoustic field concerns with the very near field, that, for this advancing ratio, is about one radius downstream. Differently, vorticity and/or turbulence effects have to be modeled for a reasonable hydroacoustic prediction. At lower advancing ratios, such effects are expected to become relevant because of the higher thrust delivered by the propeller blades; hence, the use of a BEM hydrodynamics might be not adequate for tonal noise predictions.

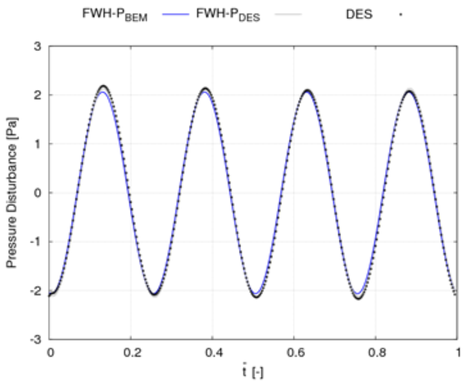

Obs1

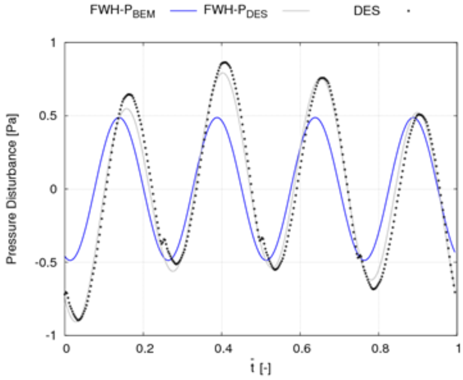

Obs5

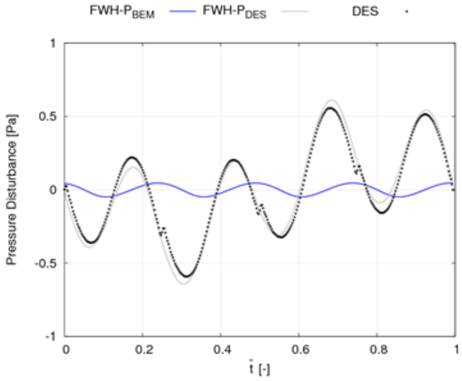

Obs6

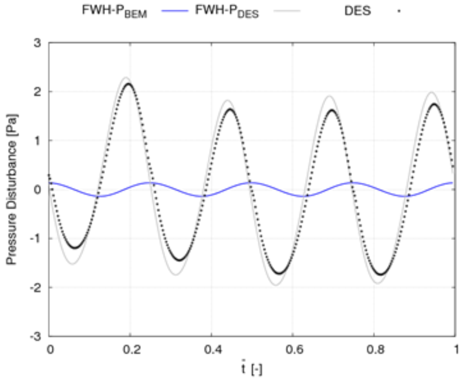

Obs7

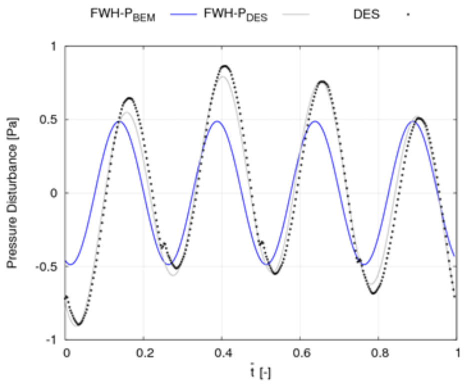

Obs5

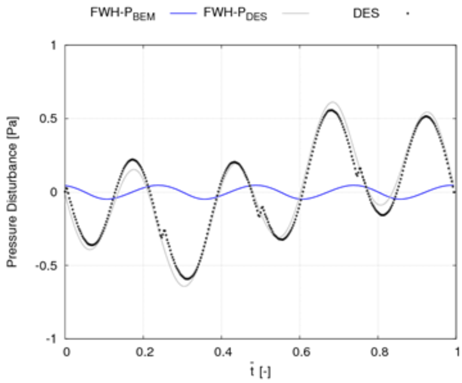

Obs6

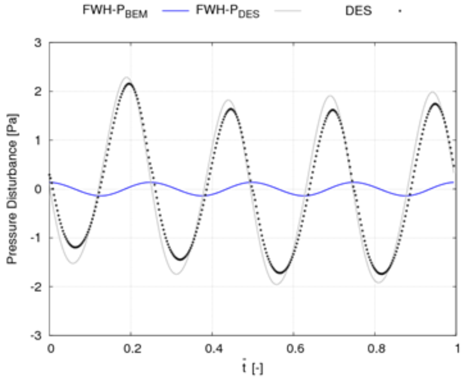

Obs7

Figure 4 Comparison among noise signals predicted by DES, FWH-P/BEM and FWH-P/DES computations during a propeller revolution. Running-averaged DES data are here considered

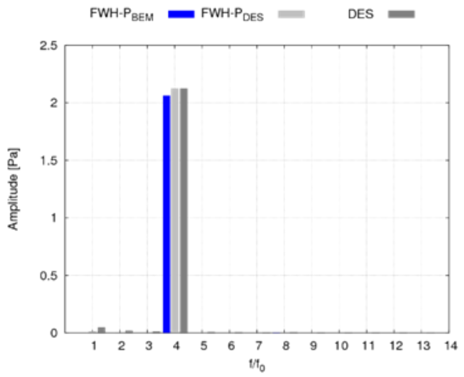

Obs1

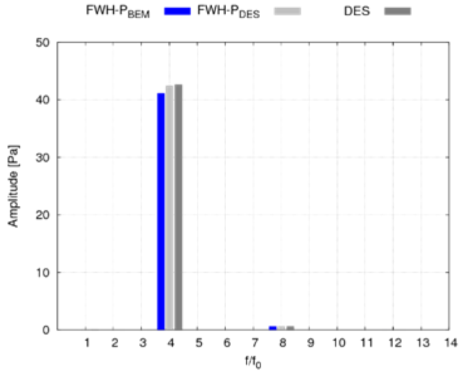

Obs2

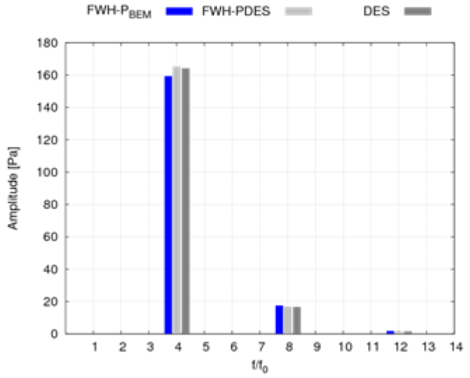

Obs3

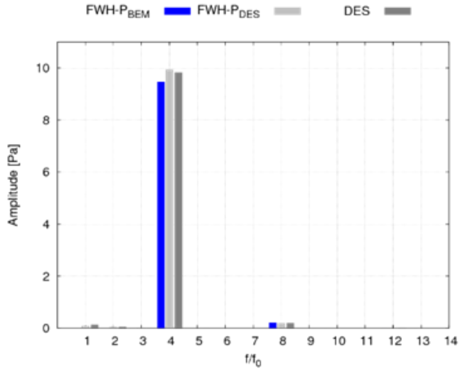

Obs4

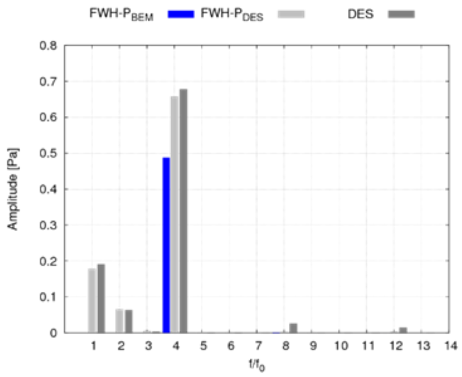

Obs5

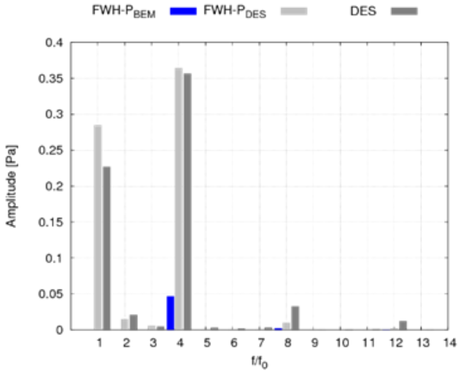

Obs6

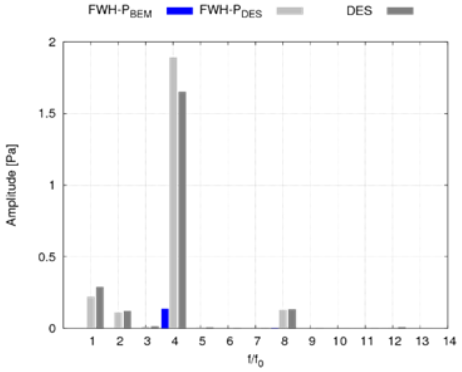

Obs7

Figure 5 Comparison among noise spectra predicted by DES, FWH-P/BEM and FWH-P/DES computations

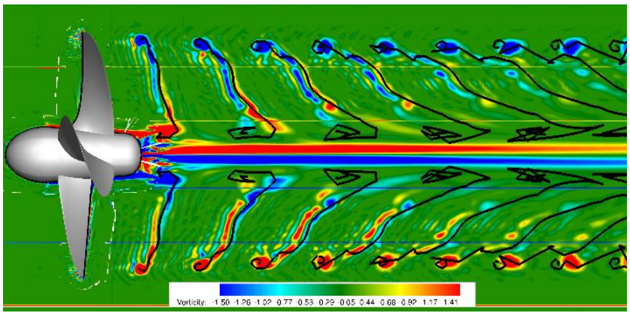

Figure 6 Vorticity field along the Y axis predicted by DES-averaged simulations compared to trailing wake location by BEM (black lines)

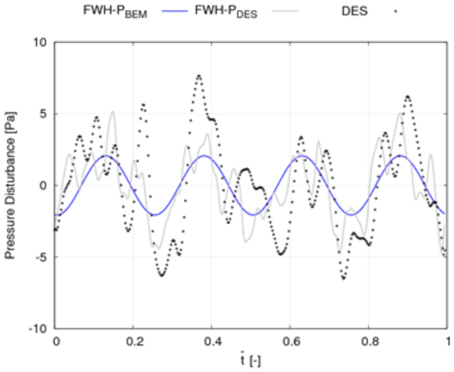

Obs1

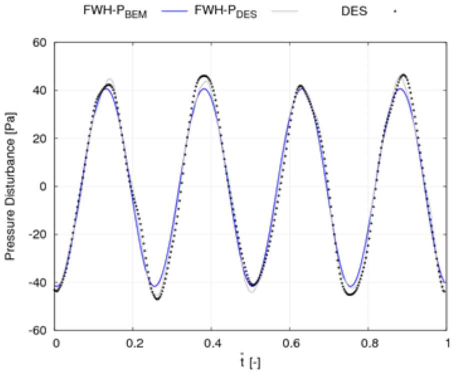

Obs2

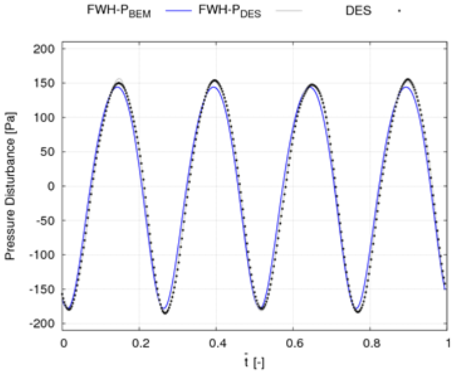

Obs3

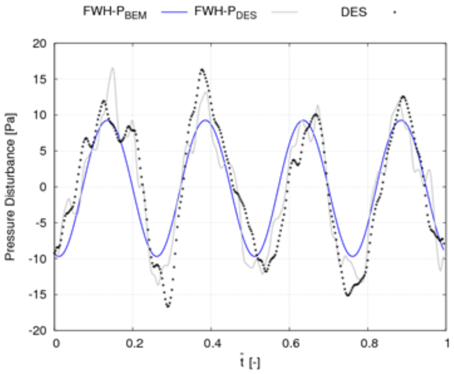

Obs4

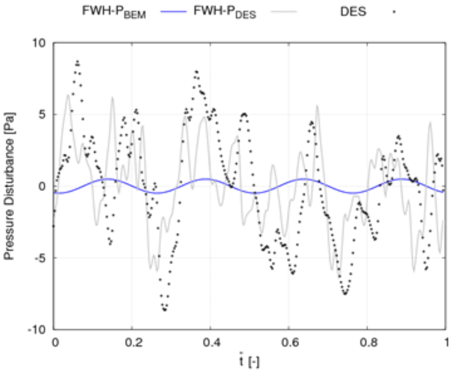

Obs5

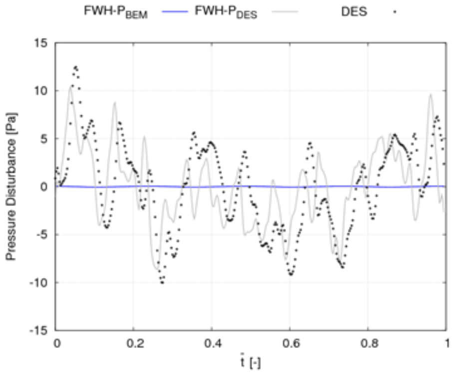

Obs6

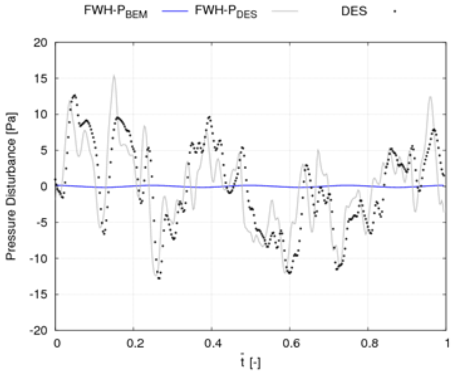

Obs7

Figure 7 Comparison among noise signals predicted by DES, FWH-P/BEM and FWH-P/DES computations during a propeller revolution. Unsteady DES data are here considered

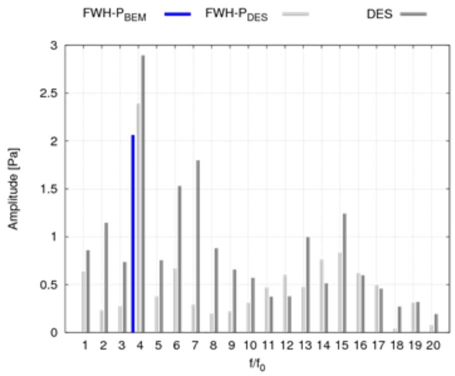

Obs1

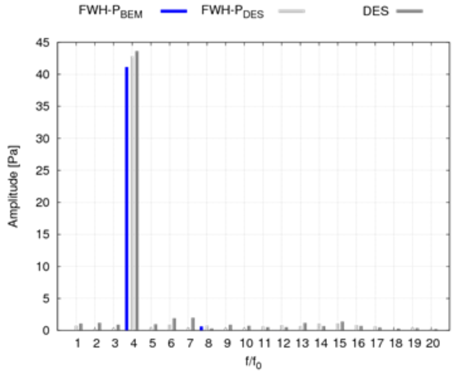

Obs2

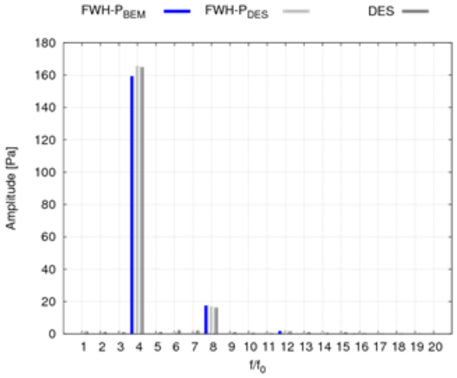

Obs3

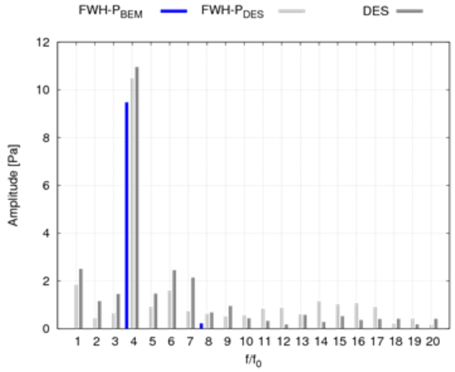

Obs4

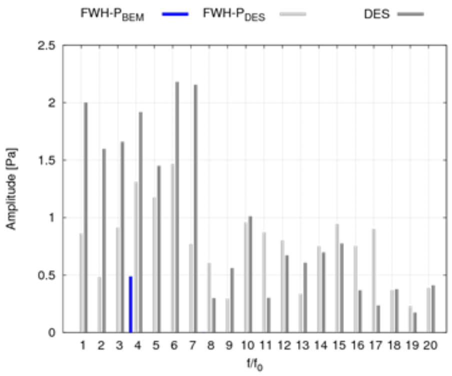

Obs5

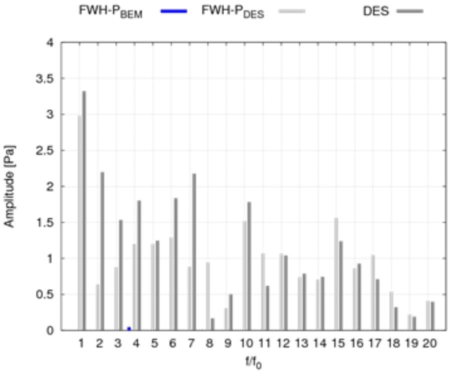

Obs6

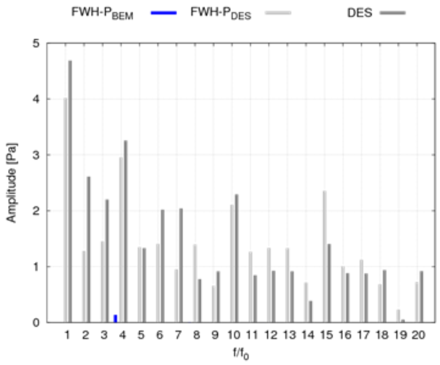

Obs7

Figure 8 Comparison among noise spectra predicted by DES, FWH-P/BEM and FWH-P/DES computations

CONCLUSIONS

The effectiveness for hydroacoustic purposes of a potential theory for incompressible flows is investigated. In view of acoustic applications in the near-field due to the wave sound hydrodynamically generated by skew propellers in open water, the FWH equation for permeable surfaces is combined with a BEM-based hydrodynamic formulation to predict the noise signals in the flow filed. Outcomes from the FWH-P/BEM technique are compared with those given by the combined use of the Acoustic Analogy and DES data. Although limited to a specific propeller and high advancing ratio, the main results of the investigations are:

- BEM hydrodynamics is adequate to capture the tonal sources of sound due to cyclic blade passages and trailing vortices convected downstream. Limiting to observers placed upstream and downstream up to 0.5÷1 diameter far from the disk, FWH-P/BEM signatures well match FWH-P/DES results obtained by a *running-average* post-processing of the DES solution. Since this technique inherently filters out any turbulence-induced effect by the definition of a mean-vorticity field, it is proven that propeller hydroacoustics is dominated by potential wake vorticity effects. However, moving downstream, DES averaged field detects important vorticity contributions that deeply modify the overall sound. These are completely lost by the BEM-based detection.
- Within the same range, similar conclusions hold for the comparison between FWH-P/BEM signatures and FWH-P/DES results obtained by an unsteady DES simulation. It is shown that, in presence of turbulence-induced noise effects, FWH-P/BEM predictions are in good agreement with FWH-P/DES outcomes or represent a sort of mean noise signal for FWH-P/DES predictions. However, moving downstream, the not modeled turbulent structures, evolving in the wake, make the use of BEM hydrodynamics data inadequate for any hydroacoustic investigation.
- The above results are preliminary. More advancing ratios should be investigated to define a sort of admissible distance from the hub where BEM hydrodynamics is able to detect the sources of tonal noise generated by a propeller. In view of the higher blade(s) load and more intense wake, it is expected a a crucial role of the turbulent structures and, in turns, a more limited range of BEM hydrodynamics data validity.

REFERENCES

Di Felice, F., Di Florio, D., Felli, M. (2004). ‘Experimental investigation of the propeller wake at different loading conditions by particle image velocimetry’. J. Ship Research, **48**(2), pp. 168-190.

Di Francescantonio, P. (1997). ‘A New Boundary Integral Formulation for the Prediction of Sound Radiation’. J. Sound Vib. **202**(4), pp. 491-509.

Di Mascio, A., Muscari, R., Dubbioso, G. (2014). ‘On the wake dynamics of a propeller operating in drift’. J. Fluid. Mech. **754**, pp. 263-307.

Farassat F. and Myers M.K. (1988). ‘Extension of Kirchhoff’s formula to radiation from moving surfaces’. J. Sound Vib., **123**(3), pp. 451–460.

Farassat F. (1996). ‘The Kirchhoff formulas for moving surfaces in aeroacoustics – The subsonic and supersonic cases’. NASA Technical Memorandum 110285.

Ffowcs Williams, J.E., and Hawkings, D.L. (1969). ‘Sound Generated by Turbulence and Surfaces in Arbitrary Motion’, Philosophical Transactions of the Royal Society, **A264**, pp. 321-342.

Greco, L., Testa, C., Salvatore, F. (2007). ‘Design oriented aerodynamic modelling of wind turbine performances’. J. Phys. (Conference Series), **75**.

Greco, L., Muscari, R., Testa, C., and Di Mascio, A. (2014). ‘Marine Propellers Performance and Flow-Field Features Prediction by a Free-Wake Panel Method’. J. Hydrod., Ser. B (English Ed.) **26**(5), pp. 780-795.

Greco, L., Testa, C., Campana, E.F. (2018). ‘Offshore Wind Turbine Unsteady Wake Modelling by Panel Method Aerodynamics’. Proc. of the 13th Conference on Sustainable Development of Energy, Water and Environment Systems (SDEWES), Palermo, Italy.

Ianniello, S., Muscari, R., Di Mascio, A. (2013). ‘Ship underwater noise through the acoustic analogy Part I: Nonlinear analysis of a marine propeller in a uniform flow", J. Mar. Sci. Tech., **18**, pp. 547-570.

Leone, S., Testa, C., Greco, L., Salvatore, F. (2013). ‘Computational analysis of self-pitching propellers performance in open water’. Ocean Engineering, **64**, pp. 122-134.

Morino, L., Gennaretti, M. (1992).‘Toward an integration of aerodynamics and aeroacoustics of rotors’, AIAA Paper, 92-02003, Proc. of the DGLR/AIAA 14th Aeroacoustic Conference, Aachen, Germany.

Muscari, R., Di Mascio, A., Verzicco, R. (2013). ‘Modeling of vortex dynamics in the wake of a marine propeller’. Computers & Fluids, **73**, pp. 65-79.

Nitzkorski, Z., Mahesh, K. (2014). ‘A dynamic end cap technique for sound computation using the Ffowcs Williams and Hawkings equations’. Phys. Of Fluids, **26**, 115101.

Poinsot, T.J., Lele, S.K. (1992). ‘Boundary Conditions for Direct Simulations of Compressible Viscous Flows’. J. Comp. Phys. **101**, pp. 104-129.

SILENV ‘Ships oriented innovative solutions to reduce noise and vibrations’. Project ID 234182, Funded under: FP7-TRANSPORT. https://cordis.europa.eu/project/rcn/92586_en.html

Testa C., Bernardini G., Gennaretti M., Ianniello S. (2007). ‘Sound Scattered by Helicopter Fuselages in Descent Flight Conditions’. AIAA-2007-3497, Proc. of the 13th AIAA/CEAS Aeroacoustics Conference, Rome, Italy.

Testa C., Greco L. (2018). ‘Prediction of Submarine Scattered Noise by the Acoustic Analogy’. J. of sound and Vibration, **426**(21), pp. 186-218.

28th ITTC. (2017) ‘Final Report and Recommendations of the Specialist Committee on Hydrodynamic Noise’. Proc. of the 28th Tank Conference, II, WUXI (China).

A. Yücel Odabaşı Colloquium Series
3rd International Meeting - Progress in Propeller Cavitation and its Consequences:
Experimental and Computational Methods for Predictions
15th – 16th November 2018, Istanbul, Turkey

Computational Investigation of Hydroacoustic Propeller Performances for Non-Cavitating Case

Samir E. Belhenniche[1*], Omar Imine[2], Omer Kemal Kinaci[3]

[1]*Naval Aero-Hydrodynamics Laboratory, Marine Engineering Department, Mechanical Engineering Faculty, USTO MB Oran, 31000 Algeria*

[2]*Aeronautics and Propulsive Systems Laboratory, Mechanical Engineering Department, Mechanical Engineering Faculty USTO MB Oran, 31000 Algeria*

[3]*Faculty of Naval Architecture and Ocean Engineering, Istanbul Technical University, 34469 Maslak-Istanbul, Turkey*

Abstract: As the propeller noise of a submarine in terms of its intensity and spectral content remains the main cause in its recognition by enemies, it has been a field of research for warship designers for many years. The aim of this study is to carry out a numerical simulation to assess the hydroacoustic performances of the Seiun Maru highly skewed marine propeller for non-cavitating case. As a preliminary study, the hydrodynamic performances are numerically tested and compared with the experimental and source and quasi-continuous method (SQCM) results, the obtained results have shown a good agreement with them. Using the time-dependent flow field data as an input, results of the simulation are used to solve the Ffowcs Williams and Hawkings (FWH) equation to extract the acoustic pressure and the sound pressure level for several hydrophones around highly skewed marine propeller operating in a non-uniform ship wake. The obtained results are presented and discussed.

Keywords: Seiun Maru; FWH; underwater noise; acoustic pressure

1 INTRODUCTION

Ships produce a significant level of noise, which ruins the marine habitat in the oceans. One of the most affected fish is the blue whale who communicates acoustically at low frequencies. Ship propellers also operate at low frequencies and they coincide with blue whale communication. Changes in blue whales' call level and rate were observed in seas where heavy marine traffic was found (McKenna, 2011).

Due to similar reasons, IMO plans to limit noise levels of ships but such attempts have reverted back due to insufficient knowledge on underwater acoustics (Ianniello, Muscari and Di Mascio, 2013). The adopted criteria are still based on basic empirical relations or numerical approximations. This lack of knowledge in state of the art of hydroacoustics can only be removed by developments in state-of-research.

However, literature in hydroacoustics; either experimental or numerical, is quite limited. This study aims to partially fill this gap by calculation of noise levels of Seiun Maru propeller at specific flow conditions. Mathematical background and numerical implementation were briefly explained first. Then the numerical approach was validated by experiments found in the literature both for open-water and behind-the hull cases before presenting the hydroacoustic results for the propeller.

2 PROPELLER GEOMETRY

The highly skewed Seiun Maru is a submerged five bladed marine propeller designed in Japan; it is a MAU type propeller characterized by a variable radial pitch distribution and a diameter of $D = 3.6m$. The propeller is widely used as a benchmark for numerical simulations of the flow around propellers. Propeller geometry is given in Figure 1. The offset data can be found in Table 1.

Table 1 The offset data of the Seiun Maru propeller

r/R	r	C	Skew	P/D	Rake
[-]	[mm]	[mm]	[mm]	[-]	[mm]
0.20	360	743.0	-2.4	0.945	-11.2
0.30	540	897.5	-53.6	0.987	50.2
0.40	720	1030.6	-47.3	1.010	65.1
0.50	900	1133.1	-1.2	1.015	59.4
0.60	1080	1191.9	91.9	0.993	39.5
0.70	1260	1185.3	265.7	0.944	1.7
0.80	1440	1076.8	533.5	0.871	-42.9
0.90	1620	820.8	893.2	0.780	-80.1
0.95	1710	587.6	1105.0	0.727	-91.2
1.00	1800	0.0	1336.7	0.668	-95.2

* *Corresponding author e-mail: samir.belhenniche@univ-usto.dz*

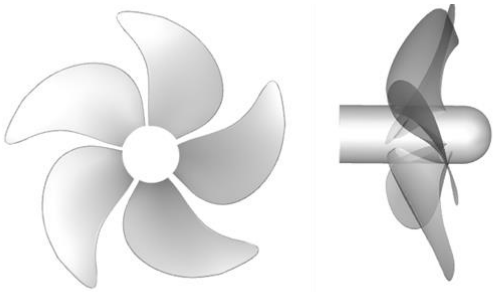

Figure 1 Seiun Maru propeller geometry

3 THE METHOD

Seiun Maru propeller was first validated with experiments for both open-water and behind-the-hull conditions. Then, hydroacoustic properties of the propeller was obtained by coupling the hydrodynamic solver with the hydroacoustic solver. In this section the mathematical background of the hydrodynamic solver along with the numerical implementation was briefly explained. The section ends with descriptions of fundamental propeller performance equations.

3.1 Mathematical background

In order to obtain the velocity and pressure fields, the conservation of mass and momentum equations were numerically solved. The equations are given as follows:

$$\frac{\partial u_i}{\partial x_i} = 0 \tag{1}$$

$$\frac{\partial(\rho u_i)}{\partial t} + \frac{\partial(\rho u_i u_j)}{\partial x_j} = -\frac{\partial P}{\partial x} + \frac{\partial}{\partial x_j}\left(\mu\frac{\partial u_i}{\partial x_j} - \overline{\rho u_i' u_j'}\right) \tag{2}$$

Where u_i is the averaged velocity, P is the averaged pressure, ρ is the density, μ is the dynamic viscosity and $-\overline{\rho u_i' u_j'}$ is the Reynolds stress. For an extensive explanation of the mathematical background, readers are referred to (Versteeg and Malalasekera, 2007).

The hydrodynamic solver is coupled with FWH equations (Ffowcs-Williams and Hawkings, 1969) implementing Farassat's (2007) impermeable formulation. Readers are referred to reference articles for further explanation of the mathematical background of numerical acoustics.

3.2 Numerical implementation

Navier-Stokes equations described in the previous subsection were solved by the finite volume method and $k-\varepsilon$ (Launder and Spalding, 1972) turbulence model was used for the open-water propeller case. For behind-the-hull condition, $k-\omega$ SST (Menter, 1994) turbulence model was selected to compute the transport of the turbulent shear stresses. $k-\omega$ SST is considered to be a more suitable option to represent the non-uniform ship wake. Figure 2 summarizes the computational domain for numerical simulations. The only difference in behind-the hull condition was at the inlet; where the axial velocities calculated from nominal ship wake were set (Belhenniche et al., 2017). The inlet, was set at a distance of $0.416D$ (Ji et al., 2012).

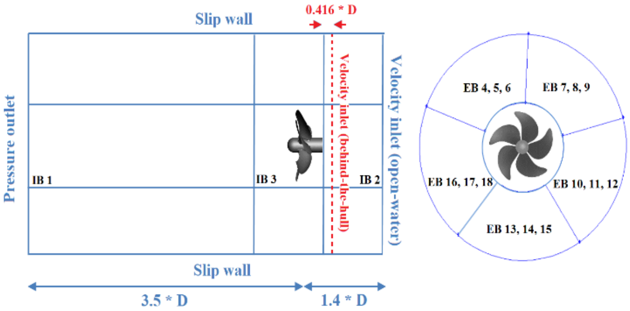

Figure 2 Computational domain for simulations

ANSYS Fluent 14.0 code based on the finite volume method was used for simulations. The uniform flow representing the open-water case was simulated by a steady solver in order to predict the propeller performance in open water. The unsteady solver was selected for behind-the-hull condition. For both steady and unsteady simulations, QUICK scheme was selected for the discretization of the momentum equations, while the Standard scheme was chosen for pressure discretization. For steady simulations, the moving reference frame (MRF) method was used. The pressure-velocity coupling was handled by the SIMPLE (Semi-Implicit Method for Pressure-Lined Equation) algorithm in the steady approach and the PISO algorithm in the unsteady case. The propeller rotation was numerically simulated by adopting the sliding mesh technique in unsteady simulations (Belhenniche et al., 2012). This meshing strategy allows a specific block to rotate inside stationary blocks. The time step size was set to $\Delta t = 0.00183756s$ which corresponds to a propeller rotation angle of 1^o.

To control the element sizes, the computational domain was divided into 18 blocks which consists of 3 inner and 15 outer blocks. One of the inner blocks covers the propeller. A hybrid mesh was adopted; tetra mesh was applied for the inner blocks and hexa mesh was used for the outer blocks using Gambit. The blades and the shaft were meshed using constant tetra cells with element sizes of $0.0056D$ and $0.011D$ respectively. Table 2 shows the grid structure for the open-water case. The specific positions of these blocks can be seen from Figure 3. The abbreviations IB and EB stand for inner and outer blocks respectively.

In order to resolve the turbulent boundary layer on the solid surfaces, ANSYS TGrid 14.0 was used, which is known to perform better in boundary layer generation. The propeller domain generated in Gambit was exported into TGrid. Then four layers of prismatic cells were attached to the blade surfaces. The first cell height off the solid surface was approximately $0.001065D$. Wall y+ range was within 1-120.

Table 2 Grid structure for the open-water case

Blocks	Mesh	Distribution	No. of elements
Inner block 3 (Propeller block)	Tetra	Start size : 0.0056*D* Max size : 0.0208D	1 246 228
Inner block 1 (Aft of propeller)	Tetra	Start size : 0.0208*D*	202 439
Inner block 2 (Forward of propeller)	Tetra	Start size : 0.0208D	58 287
Exterior blocks 4, 7, 10, 13 and 16 (Forward of propeller)	Hexa	Exponent distribution 12 x 25 x 25	37 500
Exterior blocks 5, 8, 11, 14 and 17	Hexa	Exponent distribution 12 x 25 x 33	49 500
Exterior blocks 6, 9, 12, 15 and 18 (Aft of propeller)	Hexa	Exponent distribution 12 x 25 x 45	67 500

3.3 Propeller performance equations

Although they are well known, non-dimensional equations used to assess open-water propeller performance are given below for the completeness of the study:

$$K_T = \frac{T}{\rho n^2 D^4} \tag{3}$$

$$K_Q = \frac{Q}{\rho n^2 D^5} \tag{4}$$

$$\eta_0 = \frac{J}{2\pi}\frac{K_T}{K_Q} \tag{5}$$

In these equations, n denotes propeller rotation rate, D refers to propeller diameter, T is the thrust, Q is the torque, and ρ is the density of water. K_T and K_Q are thrust and torque coefficients respectively and η_0 is the open-water propeller efficiency (Carlton, 2007).

4 UNCERTAINTY OF NUMERICAL SIMULATIONS

Numerical simulation uncertainty was carried out for a relatively low advance coefficient $J = 0.3$. Due to implementation of steady solver, time step size uncertainty was neglected. Iterative uncertainty was very low compared to the grid uncertainty; therefore it was assumed that $U_T \approx 0$. In this case, the total numerical uncertainty becomes $U_N \cong U_G$. Three different grids were used to calculate the thrust coefficient K_T which was taken as the integral variable. Simulation results are given in Table 3.

Table 3 Numerical results using different grids for $J = 0.3$

	Exp	Grid 1	Grid 2	Grid 3
No. of elem.	-	708k	1662k	3787k
K_T	0.357	0.347	0.352	0.353

Using these results, the total numerical uncertainty was found as $U_G = 0.0122 = 3.47\%S_{G_2}$. The error of grid 2 was $E = 0.005 = 1.4\%S_{G_2}$. So, $E < U_G$ and the numerical simulation is validated.

5 EXPERIMENTAL VALIDATIONS

Seiun Maru propeller was first validated with experiments for both open-water and behind-the-hull conditions. Comparisons were made using the experimental results presented in the literature.

5.1 Open-water condition

To match the condition in the experiments, the open water simulation was performed for Seiun Maru model scale with a diameter of $D = 0.4m$ and a propeller revolution of $n = 3.63rps$. The computational results were compared with the experimental data obtained by Ukon et al. (1989; 1990) for an advance coefficient range of $0.1 \leq J \leq 1$. Comparison of results are presented in Table 4.

Table 4 Seiun Maru open-water propeller performance

J	K_T Exp	K_T RANS	$10K_Q$ Exp	$10K_Q$ RANS
0.1	0.440	0.420	0.596	0.588
0.2	0.401	0.391	0.553	0.553
0.3	0.357	0.352	0.504	0.509
0.4	0.308	0.308	0.454	0.459
0.5	0.258	0.262	0.396	0.408
0.6	0.210	0.216	0.336	0.357
0.7	0.160	0.167	0.276	0.301
0.8	0.106	0.115	0.214	0.238
0.9	0.051	0.056	0.140	0.164
1	-	-	0.064	0.079

Open-water propeller results presented in a graph in Figure 3 show a comparison of the computed thrust and torque curves given for a wide range of advance ratio against experimental values. The open-water propeller performance predicted numerically were generally better for lower J. The discrepancy in results were higher as the advance ratio increased.

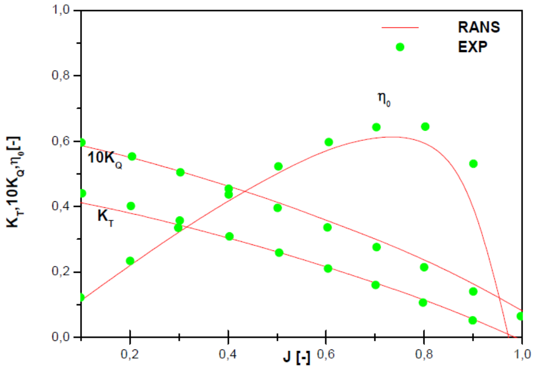

Figure 3 Seiun Maru open-water performance curves

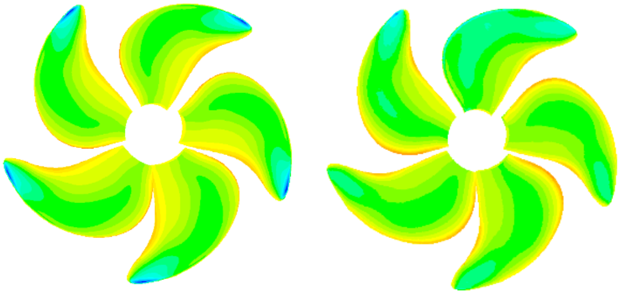

Figure 4 Pressure coefficients at the suction side for J=0.5 (left) and J=0.7 (right)

Figure 4 shows the C_P contours at the suction side for $J = 0.5$ and $J = 0.7$. Pressure coefficients in this figure lie between $-1.9 < C_P < 0.846$. There was a dramatic pressure decrease at the tips of the blades in low advance coefficients. This is accounted to higher propeller rotation rates which resulted in higher flow velocities; decreasing the pressure especially in these regions.

5.2 Behind-the-hull condition

Behind-the-hull propeller simulations were initialized by introducing the axial velocities calculated from the measured nominal wake by (Ukon et al., 1989; 1990) in towing tank. The wake distribution on the propeller disc is shown in Figure 5. Computational results were compared with the Source and Quasi-Continuous Method (SQCM) by (Nakatake et al., 2002). Parameters regarding propeller properties in numerical simulations are provided in Table 5. σ in that table denotes the cavitation number.

Table 5 Working conditions for behind-the-hull condition

	n (rpm)	σ (-)	J (-)
Simulation in non uniform ship wake (Non cavitating flow)	90.7	6.08	0.85

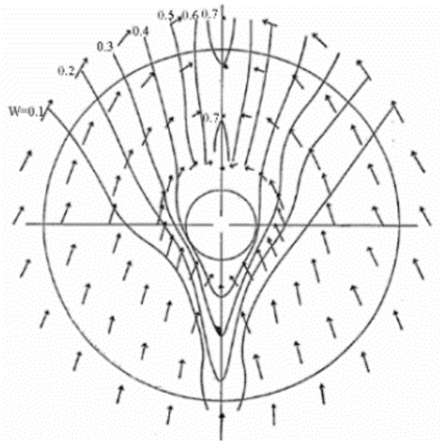

Figure 5 Wake distribution for flow simulation.

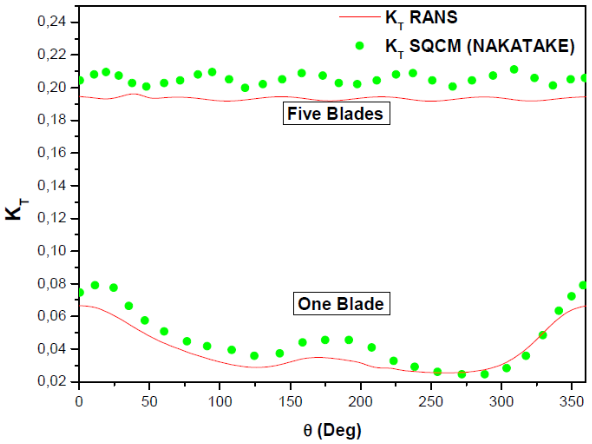

Figure 6 Thrust coefficient during propeller revolution

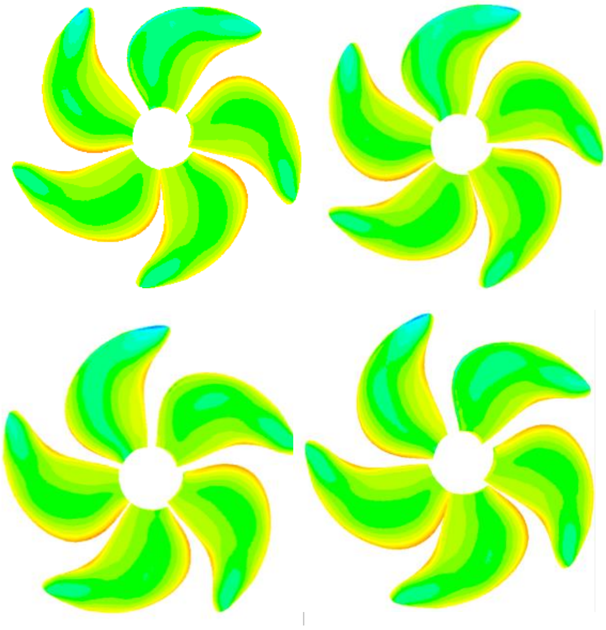

Figure 7 Pressure coefficients at different angles (suction) side. 0° (top left), 90° (top right), 180° (bottom left), 270° (bottom right)

Qualitatively, prediction of thrust agrees with (Nakatake et al., 2002) who used SQCM and taking viscous effects into account. Comparison is given in Figure 6; for one blade only and for the whole propeller. It is found worthy to mention that the thrust coefficient per blade in “five blades” case is actually lower than “one blade” case. This is due to:

- Each blade is at a different position producing a different thrust coefficient.
- The interactions between blades lower the total thrust.

Figure 7 shows the contours of pressure coefficients on blade suction side for different angle positions. The legend lies between $-1.95 < C_P < 1.03$. The angle of 0° corresponds to the top position. This figure notes the differences in pressure at each angle. This is due to the propeller being subjected to a non-uniform flow.

6 HYDROACOUSTIC RESULTS

Hydroacoustic calculations were performed for the propeller operating at $n = 90.7rpm$ in non-uniform ship wake (behind a ship hull). The reference pressure for Sound Pressure Level calculations was taken as $1\mu Pa$, The density was $\rho = 998.2kg/m^3$ and the velocity of sound in the undisturbed medium was $c = 1500m/s$. The hydrophones were located as given in Table 6 and they are schematically visualized in Figure 8.

Table 6. Hydrophone locations.

Hydrophones	*X*	*Y*	*Z*
1	0	0	3.3*R*
2	0	0	1.5*R*
3	0	-0.5*R*	*R*
4	0	10*R*	0

Simulations were conducted for 8 rounds of propeller rotations. Figure 9 presents acoustic pressure fluctuations in time at hydrophones 2 and 3 for the last rotation. 5 peaks in pressure graph correspond to 5 blades existing in Seiun Maru propeller. Acoustic pressures for hydrophones 1 and 4 were not presented because pressure peaks could not be identified at these locations. It is hypothesized that the underlying reason for this is the acoustic signal vanishing in the far field which is probably due to the insufficiency in grid resolution. However; further studies must be carried out to solidify this hypothesis.

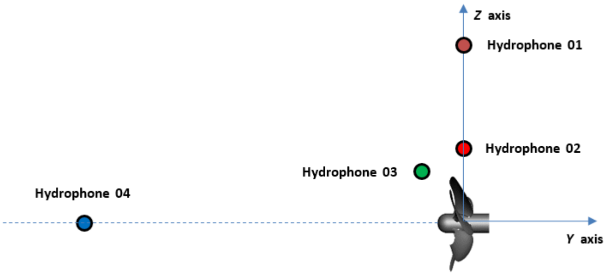

Figure 8. Schematic view of hydrophone locations given in Table 6.

Figure 10 shows the noise spectra in dB for hydrophones 2 and 3 up to 50 Hz. The sound pressure level (SPL) peaks of these graphs are in accordance with the blade passage frequency (BPF). Considering that BPF is given as;

$$BPF = n * Z \tag{6}$$

the first harmonic for the propeller must be at $7.558\,Hz$, while the second, third and the fourth would be at $15.116\,Hz$, $22.674\,Hz$ and $30.232\,Hz$. All the harmonics are clearly visible for hydrophone 3 while only the first two harmonics can be seen for hydrophone 2. A better grid refinement is needed around hydrophone 2 to better reflect the hydroacoustic properties of the propeller at that specific location.

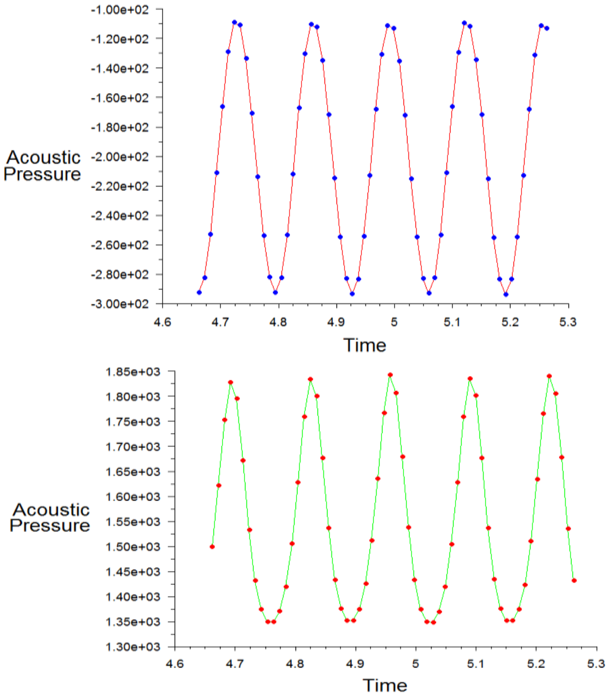

Figure 9 Computed acoustic pressures at hydrophone 2 (top) and hydrophone 3 (bottom)

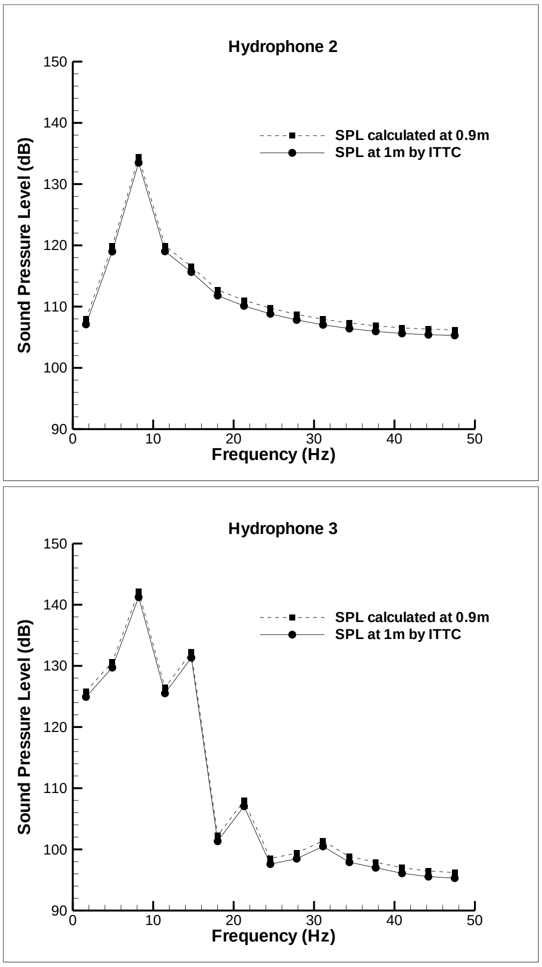

Figure 10 Noise spectra in dB for hydrophone 2 (top) and hydrophone 3 (bottom)

Figure 11 also exhibits the sound pressure levels carried to a reference distance of 1m, as recommended by the ITTC. As a distance normalization equation, ITTC proposes to use,

$$SPL = SPL_{ref} + 20\log_{10}\frac{d}{d_{ref}} \tag{7}$$

where the reference distance is taken as $d_{ref} = 1m$. Considering that the propeller diameter is $D = 3.6m$, the distance of hydrophone 2 is 2.7m away from the center and 0.9m from the tip of the propeller (in the z direction). The distance of hydrophone 3 is again 0.9m away from the tip (but this time in the y direction). Results derived from these two hydrophones were then carried by the ITTC distance normalization equation. As can be seen from the figure, there is not much deviation between the two due to sound pressure levels calculated for a distance very close to that recommended by the ITTC.

7 CONCLUSIONS

In this study, the benchmark Seiun Maru propeller was numerically solved to identify its hydroacoustic properties at selected locations in the fluid. The open-water and behind-the-hull conditions were previously studied experimentally and numerically by various other researchers in the field. Good accordance with other studies was found in terms of hydrodynamic properties of the propeller. After validation of the numerical approach, hydroacoustic results were presented. The intention was to present results for 4 hydrophones but the 2 hydrophones in the far field did not return very good results. The 2 hydrophones in the near field were comparably better.

The hydroacoustic properties of the propeller were reflected in the acoustic pressure and noise spectrum graphs. Deficiencies in hydroacoustic results point to the necessity of grid refinements in selected regions of the flow. Further studies are planned to address this issue.

REFERENCES

Belhenniche, S. E., Aounallah, O., Imine, O. & Celik, F. (2012). 'Application of CFD in analysis of steady and unsteady turbulent flow past a marine propeller'. International Conference of Heat and Mass Transfer, Palermo, Italy.

Belhenniche, S. E., Aounallah, O., Imine, O. & Celik, F. (2017). 'Effect of geometric configurations on hydrodynamic performance assessment of a marine propeller'. Brodogradnja **67**(4), pp.31-48.

Carlton, J. (2007). Marine Propeller and Propulsion. 2nd ed. Elsevier Ltd.

Farassat, F. (2007). 'Derivation of Formulations 1 and 1A of Farassat'. NASA Langley Research Center, Aeroacoustic Branch Report.

Ffowcs-Williams, J. E. & Hawkings, D. L. (1969). 'Sound generation by turbulence and surfaces in arbitrary motion'. Phil. Trans. R. Soc. Lond. A **264**(1151), pp.321-342.

Ianniello, S., Muscari, R. & Di Mascio, A. (2013). 'Ship underwater noise assessment by the acoustic analogy. Part I: nonlinear analysis of a marine propeller in uniform flow'. Journal of Marine Science and Technology, 18, pp.547-570.

Ji, B., Luo, X., Peng, X., Wu, Y. & Xu, H., (2012). 'Numerical analysis of cavitation evolution and excited pressure fluctuation around a propeller in non-uniform wake'. International Journal of Multiphase Flow, 43, pp.13-21.

Launder, B. E. & Spalding, D. B. (1972). 'Mathematical models of turbulence'. Academic Press.

McKenna, M. F. (2011). 'Blue whale response to underwater noise from commercial ships'. PhD. Thesis, University of California, San Diego.

Menter, F. R. (1994). 'Two-equation eddy-viscosity turbulence models for engineering applications'. AIAA Journal, **32**(8), pp.1598-1605.

Nakatake, K., Ando, J., Kataoka, K. & Yoshitake, A. (2002). 'A simple surface panel method SQCM for ship hydrodynamics'. International Association for Boundary Element Methods, UT Austin, TX, USA.

Ukon, Y., Kurobe, Y. & Kudo, T. (1989). 'Measurement of pressure distribution on a conventional and highly skewed propeller model – under non-cavitating condition'. Journal of the Society of Naval Architects of Japan 165, pp.83-94 (In Japanese).

Ukon, Y., Kurobe, Y. & Kudo, T. (1990). 'Measurement of pressure distribution on a full scale propeller'. Journal of the Society of Naval Architects of Japan 168, pp.65-15 (In Japanese).

Versteeg, H. K. & Malalasekera, W. (2007). An Introduction to Computational Fluid Dynamics. 2nd ed. Prentice Hall.

An Investigation of Underwater Ship Noise Utilizing Circulating Water Channel

Endang Widjiati[1] , Eko Budi Djatmiko[2], Wisnu Wardhana[2] and Wirawan Wirawan[2]*
[1]Indonesia Hydrodynamics Laboratory (IHL), Agency for the Assessment and Application of Technology
[2]Institut Teknologi Sepuluh Nopember (ITS)
Kampus ITS, Sukolilo, SURABAYA 60111, INDONESIA

Abstract: Measurement and investigation of two out of three main sources of ship noise, i.e. propeller noise and flow noise, conducted at the Indonesian Hydrodynamic Laboratory, Surabaya, Indonesia using the K16B-type cavitation tunnel are reported. The propeller noise experiment is conducted using a B-series four-blade bronze propeller (diameter 23cm) using a hydrophone placed in the tunnel at window section (60x90 cm2) of the measurement section (400x85x85 cm3). Moreover, the flow noise is conducted on a dummy model of the Virginia submarine of 1:80 scale placed at the measurement section and flowed with water at different velocities and pressures. With respect to propeller noise, preliminary process is accomplished to analyze the characteristics of measurement results in the frequency domain, with the objective being to detect when and which type of propeller noise occurs in any kind of condition. Flow noise measurement outcomes in the form of acoustic data signals are obtained in different conditions by varying the water pressure, flow velocity and propeller speed rotation. The frequency spectrum of the acoustic noise produced by the propeller and dummy, respectively, is compared with that of the system noise measured before the propeller and dummy is placed. Since different spectra are produced by different measurement conditions, it proves that this study is useful for determination of signal processing tools to investigate the characteristic of propeller and flow noise.

Keywords: Ship noise, propeller noise, flow noise, cavitation tunnel

1 INTRODUCTION

Measurement of acoustic signals has been an important subject in marine and ocean engineering due to the use of sonar on ships to detect and identify such objects as submarines. Performance of a submarine is determined, among others, by the performance of its sonar system in detecting the presence of ships or other objects in its surrounding. The detection mechanism exploits acoustic signals emitted by the object (passive sonar) or signals transmitted by the sonar system which are reflected back by the object being detected/identified (active sonar). For a passive sonar system, the received acoustic signals are those produced by the propeller, engine, as well as interaction between water and the body of the ship known respectively as propeller noise, machinery noise and hydrodynamic noise or it used to be called as flow noise.

Carlton (2007), Hodges (2010) and Ross (1987) show that the acoustic signal produced by a propeller is one of the greatest sources of noise from a vessel. Therefore, it is necessary to investigate the magnitudes and characteristics of acoustic signals of a propeller noise for various values of vessel velocity, propeller rotation speed and water pressure. For that purpose, previously reported research, e.g., Felli (2011), Park et.al. (2009), and Sharma et.al. (1990), studied the cavitation phenomenon on a propeller using a cavitation tunnel. In this study, a propeller of B-series with 4 blades is tested by using the cavitation tunnel located at Indonesian Hydrodynamic Laboratory (IHL) research facility in Surabaya, Indonesia (Widjiati et. al., 2012a)

Through a series of measurements, it can be observed that for a given combination of water velocity, propeller rotation speed and water pressure, a cavitation appears and vanishes. By synchronizing the acoustic signal measurement and video recording, the physical mechanism and characteristics of the measured acoustic signal can be studied in relation with the phenomenon that generates it, as illustrated by the image or video recordings.

Similar to study on propeller noise, the same cavitation tunnel is used to investigate the flow noise caused by a dummy model of the Virginia submarine with the scale of 1:80 (Widjiati et.al. 2012b). The measurements were successfully done in different conditions of water pressures, water pressures and water flow. Results of the measurements show that different frequency components occur. However, the spectrum of the acoustic signal recorded at different pressures with similar water speed gives quite similar pattern.

2 BACKGROUND THEORY

While a human voice is an acoustic signal propagating through the air, the signal received by a sonar system is an acoustic signal propagating underwater.

* *Corresponding author e-mail: ewidjiati@yahoo.com.au*

This underwater acoustic signal is commonly referred to as noise, which according to Ross (1987), is an unwanted sound that interferes with a system. Underwater acoustic signals, or underwater noise, might originate from a school of moving fish, water surface that interacts with wind producing waves, or moving vessels.

Acoustic noises originate from a moving vessel can be classified into 3 categories (Carlton, 2007 and Ross, 1987), namely machinery noise, flow noise and propeller noise. The machinery noise arises from vibration of an operating ship engine. The flow noise is caused by interaction between the moving ship hull with water. Two out of these three different noise investigated in the IHL's Cavitation Tunnel will be discussed in this paper.

2.1 Propeller Noise

Carlton (2007) states that propeller noise occurs as a result of water displacement around the propeller blades, pressure difference between suction and pressure surface of the rotating propeller blades, fluctuating cavitation resulting from varying wake field, and broken cavitation due to high pressure. Accordingly, propeller noise can be classified into one generated by cavitation and the other by non-cavitation. This research focus only on the cavitation noise since Carlton (2007) shows that above 25 knots, propeller cavitation noise is more dominant than any other components and tends to increase at higher velocities. However, at velocities under 25 knots, flow noise (boundary layer noise) dominates.

According to its physical appearance on the propeller, there are several types of cavitation, namely, tip and hub vortex cavitation, sheet cavitation, bubble cavitation, root cavitation, propeller-hull vortex cavitation and cloud cavitation. Main differences among these cavitations are the spot where these cavitations occur at the propeller. The hub and root cavitations arise close to the hub of the propeller, while other cavitations appear around to the blades of the propeller.

2.2 Flow Noise

As the second component of the vessel noise discussed, Howe (2007) explains how the theory of acoustics related to the aerodynamics with special reference to the generation of sound by interaction of water flow and rigid and elastic structures. The theory of how the Lighthill's acoustic analogy is discussed related to the theory of vortex sound. A few applications are described to exemplify the understanding of flow generated sound including the use of the acoustic Green function to estimate fluid-structure interaction noise when one or more sources are small compared to the acoustic wavelength.

This paper discusses the flow noise, i.e. the noise caused by the interaction between water flow and the hull of the dummy model of submarine based on the measurement in the cavitation tunnel. Some examples of how the flow noise measurement is performed in the cavitation tunnel belong to the HSVA (Hamburg Ship Model Basin), Germany and the University of Newcastle are reported in Felli (2011). Based on these, the flow noise is investigated using the IHL's Cavitation Tunnel.

2.3 Cavitation Tunnel

The cavitation tunnel at IHL is one of the experimental facilities used for investigating the hydrodynamics performance of a submerged object in the flowing water in the laboratory. The tunnel consists of impeller that runs the water of up to a certain velocity. The water flows in the vertical plane, within which propellers and other propulsion devices as well as the submarine model can be tested. Studies on the propeller cavitation and flow noise are examples of the object being investigated here.

The variety of water velocity in the tunnel means that the propeller and submarine model are tested at the different water flow. In term of the propeller, its rotation speed can also be varied, dependent on the capability of dynamometer on which the propeller is mounted in the tunnel. The pressure inside the tunnel can also be changed, simulating the condition where the propeller and submarine model are operating. The depth of the object position in the water is proportional to the pressure. Felli (2011) and Park et.al. (2009) are a few examples that describe how propeller cavitation and flow noise measurement is performed in the cavitation tunnel. The acoustic signal that results from the cavitation and flow noise, are recorded by a hydrophone positioned at a certain configuration in the tunnel.

3 METHODOLOGY

The experiment is conducted at the Indonesian Hydrodynamic Laboratory (IHL) using the K16B-type cavitation tunnel that is able to vary the speed of up to 12 m/s, rotate the propeller up to 80 rotations/s, and decrease and increase pressure until -1 bar absolute and +1 bar absolute, respectively. Figure 1 shows the cavitation tunnel scheme with the sizes given in mm. The tunnel is equipped with impeller the at the bottom right of Figure 1 which work to run the water in the tunnel, some sensors in the measurement section to adjust the water flow and pressure, and also the dynamometer that can rotate the propeller of up to 80 rotation/sec.

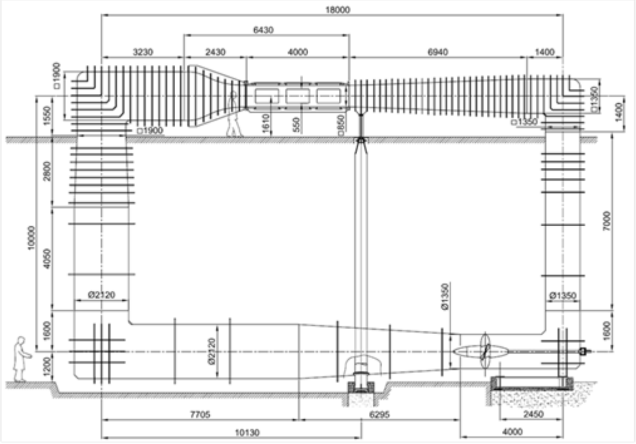

Figure 1 Schematic diagram of the IHL Cavitation Tunnel

The acoustic signal produced by the propeller cavitation and flow noise is recorded using the H2a-XLR Aquarian hydrophone with frequency range between 10-100kHz. The window where the hydrophone is placed is the part of window where the dynamometer sited, which is where the propeller positioned in the measurement section of the tunnel. Figure 2 shows the picture when the window with the dynamometer is placed at the measurement section with the model propeller attached to it.

Figure 2 The model propeller is attached to dynamometer is placed at the lid of the measurement section window

The dummy model of the Virginia submarine and how it is placed in the cavitation tunnel are shown in Figure 3. It is understood that a dummy holder has to be mounted in the dummy model to allow it to be placed at the lid of the measurement section window illustrated in Figure 3. The water flow in the tunnel is then set to be run at different velocities and the pressure inside the tunnel is adjusted at different values as given Section 4.

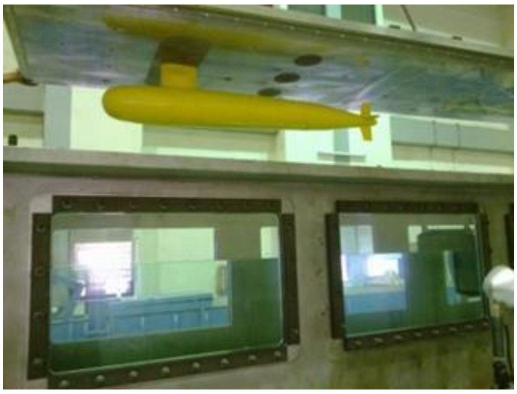

Figure 3 The dummy model of submarine is placed at the lid of the measurement section window

The configuration of the acoustic signal measurement as given in Figure 4, shows that the hydrophone is placed on one of the window lids, about 100 cm from the dummy model of submarine. This hydrophone is connected to the Rolls MP13 Mini Mic Preamplifier that operates to activate the phantom power. Furthermore, the output of the preamplifier is the input for the NI PCI 6143 DAQ Card by the use of the connector block. The recorded signal is displayed at the monitor using the Labview. The video recorder is also used to see the occurrence of the acoustic signal during the experiment.

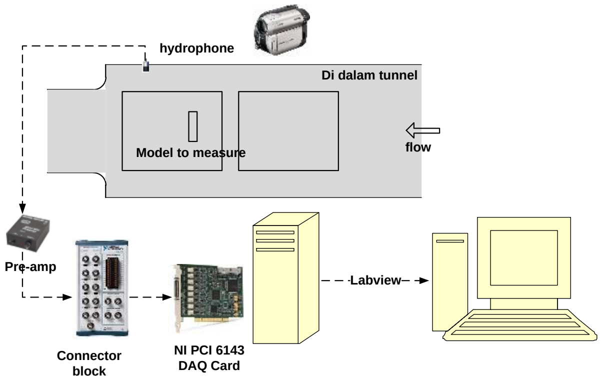

Figure 4 Measurement scheme

4 RESULTS

The recording process begins with the calibration using the underwater speaker. The sinusoidal signals with different frequencies are generated and activated using the Matlab program and is recorded by the hydrophone. This condition is conducted while there is no water flow. The objective of this process is to characterize the effect of the wall to the signal generated at the position where the dummy model of submarine will be placed. This process is followed by the acoustic signal generated by the impeller when the water flow is present with a particular speed. The purpose of this step is to identify the acoustic noise produced by the mechanical system of the cavitation tunnel.

4.1 Propeller Noise

Figure 5 (a) shows the signal spectrum received by the underwater speaker in the tunnel, which the known sinusoidal signal with sampling frequency F is generated. This illustrates that the received signal experienced a few reflections caused by the walls of the tunnel. Figure 5 (b) illustrates the spectrum of the acoustic signal where the propeller is in stationary condition, and the water flows with the speed of 3 m/s. In this condition, the water pressure is varied from 1 bar absolute to 1.8 bar absolute and the dynamometer fan that placed above the measurement section is on at the highest state. Since the sampling frequency is 50 kHz, means that the fan and the impeller attained at the frequency around 12 kHz and 20 kHz.

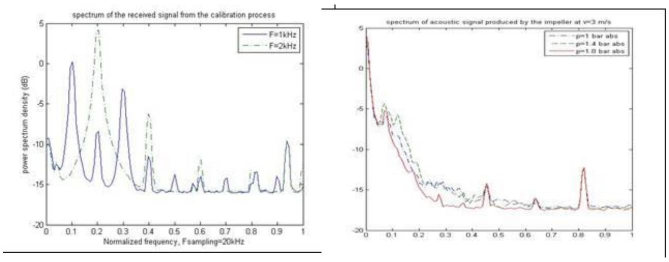

(a) (b)

Figure 5 Spectrum of the received signal

By varying the propeller velocity, the speed of water flow and the pressure in the tunnel, the propeller cavitation occurs and the acoustic signal induced can be evaluated. Table 1 shows the visual observation of the propeller cavitation where ‘n’ correspond to ‘no cavitation’ and ‘y’ contains ‘there is cavitation’. The frequency spectra of several signals are exemplified in Figure 6 (a) and (b).

Table 1 Visual observation of propeller cavitation

V_{prop}	p = 1 bar abs		p = 1.4 bar abs		p = 1.8 bar abs	
(rot/sec)	1 m/s	3 m/s	1 m/s	3 m/s	1 m/s	3 m/s
5-7	n	n	n	n	n	n
7-11	n	n	n	n	n	n
11-15	y	n	n	n	n	n
15-19	y	n	y	n	n	n
19-22	y	y	y	n	y	n
22-25	y	y	y	y	y	n
25-29	y	y	y	y	y	y

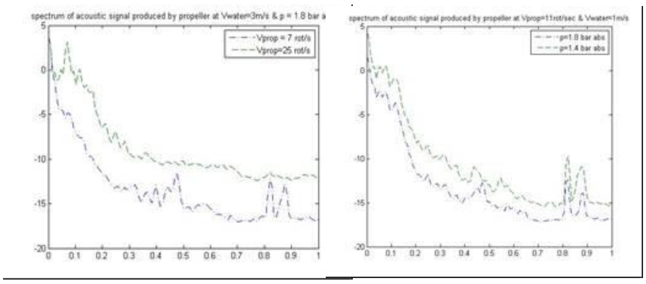

(a) (b)

Figure 6 Spectrum of the propeller noise at different conditions

Figure 6 (a) illustrates the spectrum of the signal where at the speed rotation of 7 rotation/sec doesn’t produce the cavitation and at 25 rotation/sec is with cavitation. Figure 6 (b) show that when the propeller rotates at the same speed in the sampe speed water flow. It is clear that the acoustic signal without cavitation is dominated by the acoustic signal caused by the fan and the impeller. The propeller cavitation can be visually observed in the photograph as shown in Figure 7 using the stroboscope. Hence, by observing both the measurement results and the video recordings of the phenomenon, it might be expected in-depth understanding of the physical mechanism and characteristics of noises generated by various types of propeller in various conditions.

Figure 7 Cavitation phenomena

4.2 Flow Noise

The water flow in the tunnel is then set to be run at different velocities and the pressure inside the tunnel is adjusted at different values as given in Table 2.

Table 2 Variables of measurement process

Speed variation (hPa)	3	12	25	43
Pressure variation (bar abs)				
1	x	x	x	x
1.3	x	x	x	x
1.6	x	x	x	x

Figure 8 (a) and (d) show the signal spectrum received by the hydrophone in the tunnel, where sampling frequency of the signal is 20 kHz. Figure 8 (a) illustrates the noise of the system when the water flows in the tunnel at the speed of 12 hPa. The spectrum of this signal experiences a few reflections caused by the walls of the tunnel where the frequency is mainly at 7 kHz and 19 kHz. These two frequency components always occur at any other measurement at different conditions. Figure 8 (b) and (c) compare two different spectrums where both signals are recorded at the water speed of 12 hPa and pressure at 1.6 and 1.3 bar abs, respectively. These figures show that at a pressure of 1.6 bar abs the signal with frequency of about 1 kHz occurs, which is not the case when the pressure is of 1.3 bar abs. It appears that a different situation takes place when two measurements are carried out in similar pressure with different water speeds. On the other hand, from two measurements which are made in similar water speed but with different pressures, then the spectrum of the signal will show as in Figure 8 (c) and (d). The frequency components below 7 kHz appearing in the two conditions are completely different.

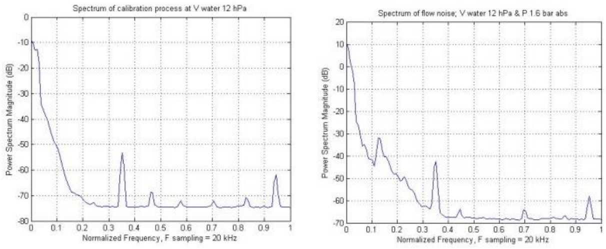

(a) during calibration process (b) Vwater = 12hPa & P = 1.6 bar abs

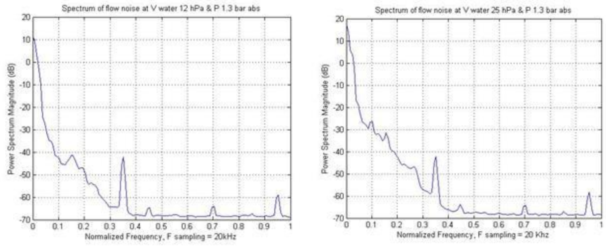

(c) Vwater = 12 hPa & P = 1.3 bar abs (d) Vwater = 25 hPa & P = 1.3 bar abs

Figure 8 Spectrum of the flow noise at different conditions

5 CONCLUSIONS

Using the cavitation tunnel facility, investigations of acoustic signals resulting from cavitation phenomenon and flow noise produced by an underwater object can be conducted. The propeller acoustic noise measurement system that makes use of the cavitation tunnel facility at IHL has been described and exemplified. It is observed that the occurrence of cavitation can be simulated for various values of water flow velocity, propeller rotation speed and water pressure. By synchronizing the acoustic signal measurement and video recording, the physical mechanism and characteristics of the measured acoustic signal can be studied in relation with the phenomenon that generates it as illustrated by the image or video recordings. Further investigation can be done using different kind of propellers.

Further, it has been demonstrated that using the cavitation tunnel facility, investigations of acoustic signals resulting from cavitation phenomenon produced by an underwater object such as a dummy model of submarine can be conducted. It is observed that the occurrence of acoustic signal can be simulated for various values of water flow velocity and water pressure.

Different spectra are expected to occur since different measurement conditions imply different frequency components occur at its spectrum. It proves that this preliminary study is a crucial step towards further investigations such as cavitation tunnel noise identification, reflection of flow noise, etc. The results of this study can be used to determine different kinds of signal processing tools to analyze the characteristics of the flow noise generated by the dummy model of submarine.

REFERENCES

Carlton, J. (2007). Marine Propellers and Propulsion. 2nd ed. Oxford, UK: Butterworth-Heinemann

Felli, M. (2011). ‘Noise measurements techniques and hydrodynamic aspects related to cavitation noise’, Project report 1 of Hydro Testing Alliance (HTA): An alliance to enhance the maritime testing infrastructure in the EU, [Online]. Available: Publication Management, http://puma.isti.cnr.it/publichtml/section_cnr_insean/cnr_insean_2011_PR_006.html,

Hodges, R. P. (2010). Underwater Acoustics: Analysis, Design and Performance of Sonar. John Wiley & Sons.

Howe, M. S. (2007). Hydrodynamics and Sound. Cambridge University Press The Edinburgh Building, Cambridge.

Park, C., Seol, H., Kim, K. & Seong, W. (2009).’A study on propeller noise source localization in a cavitation tunnel’, Ocean Engineering, 36, pp. 754 – 762.

Ross, D. (1987). Mechanics of Underwater Noise. New York: Pergamon Press.

Sharma, S. D., Mani, K. & Arakeni, V. H. (1990). ‘Cavitation noise studies on marine propellers’, Journal of Sound and Vibration, 138 (2), pp. 255-283.

Urick, R. J. (1983). Principles of Underwater Sound. McGraw-Hill, Inc.

Widjiati, E. Djatmiko, E. B., Wardhana, W & Wirawan (2012a), ‘Measurement of propeller-induced cavitation noise for ship identification’, Poster in ACOUSTIC 2012 Hong Kong, Hong Kong

Widjiati, E., Djatmiko, E. B., Wardhana, W & Wirawan (2012b). ‘Preliminary Study of the Flow Noise Measurement in the Cavitation Tunnel’. Presented in The Second International Conference on Port, Coastal, and Offshore Engineering (2nd ICPCO), Bandung, Indonesia

A. Yücel Odabaşı Colloquium Series
3rd International Meeting - Progress in Propeller Cavitation and its Consequences:
Experimental and Computational Methods for Predictions
15th – 16th November 2018, Istanbul, Turkey

Investigation into the Propulsive Efficiency Characteristics of a Ship with the GATE RUDDER® Propulsion System

Noriyuki Sasaki[1], Mehmet Atlar[1]
[1]Department of Naval Architecture, Ocean and Marine Engineering, University of Strathclyde, Glasgow G4 0LZ, UK

Abstract: Following the first successful application of the Gate Rudder® propulsion system on a 2500GT container ship (Lpp=102m) in Japan, excellent manoeuvring performance was reported with a significant fuel saving over her sister ship fitted with a conventional rudder propeller arrangement.

Based upon the investigations carried out by using model tests, CFD simulations and the full-scale data of two container vessels, this paper discusses the details of the propulsive efficiency characteristics of a vessel fitted with the GATE RUDDER® propulsion system in comparison those of the same vessel with the conventional rudder-propeller arrangement. In the paper the evolution history of the GATE RUDDER® concept is presented by tracing the development of the state-of-the-art energy saving devices (ESD) involving ducts since the GATE RUDDER® exploits the advantage of the duct effect. The components of the propulsive efficiency parameters, with an emphasis on the thrust deduction and effective wake parameters, are explored and discussed highlighting the differences for the hull with the GATE RUDDER® and the conventional rudder arrangements.

Keywords: Gate Rudder, Cavitation, Noise

1 INTRODUCTION

In order to improve the energy efficiency of ships, and hence to achieve targeted carbon emission (e.g. EEDI regulations by IMO), various technological and operational solutions have been studied by the maritime industry. These solutions recently include the developments of various novel Energy Saving Devices (ESD) applied on the underwater hull and renewable energy saving devices onboard, using alternative fuel sources and sophisticatedly designed optimal hull forms. Amongst these solutions, e.g. ESD's, still have their challenges to prove their effectiveness regarding performance and cost robustly on full-scale ships. Although many ESDs already exist, and some new types are still being introduced, their effectiveness need to be investigated and proven further by accurate voyage data especially after delivery.

GATE RUDDER ® system is a new and innovative ESD technology for ships to propel and steer them more efficiently compared to conventional rudder propeller as well as other ESDs. As opposed to a conventional single rudder system, which is usually located behind the propeller, the GATE RUDDER ® has two rudder blades with asymmetric sections, which are located aside the propeller, and each blade can be controlled independently. The two rudder blades, encircling the propeller at the top and sides, provide the vessel with a duct effect and hence produce additional thrust as opposed to the additional drag of the conventional rudder behind the propeller.

This paper presents the principles of the GATE RUDDER® concept by tracing evoluation of the state-of-the-art ESDs involving ducted propulsors. By using model tests, CFD simulations and the full-scale data of two container vessels, the paper explores the details of the propulsive efficiency parameters, with an emphasis on the thrust deduction and effective wake parameters, and discusses the differences for the hull fitted with the GATE RUDDER® and the conventional rudder arrangements.

2 GATE RUDDER CONCEPT

2.1 Evolution of Ducted Propellers

The rudder is one of the significant sources contributing to the ship resistance. The main purpose of the GATE RUDDER® propulsion system is, therefore, to replace this resistance source with the source of a thrust (i.e. similar to an accelerating duct) to improve the propulsor efficiency. With this idea, the replacement of the single rudder blade with a pair of blades and locating each blade aside the propeller can improve the propulsive efficiently significantly, like a ducted propeller, as an effective energy saving device as opposed to the rudder behind the propeller.
The performance of a ducted propeller system is usually evaluated based on their open water performance characteristics which are similar to that of a conventional screw propeller. However, the problems with the cavitation occurring at the inner surface and mainly near the impeller tip region of the ducts are a well-known, and unavoidable source of vibration and structural problems, especially for large vessels, such as VLCCs fitted with the ducted propellers. This has been the main reason why we are not able to see this first generation, conventional,

Corresponding author e-mail: Noriyuki.sasaki@strath.ac.uk accelerating type of ducted propeller on merchant's ships nowadays, while the small workboats, such as tugboats and fishing vessels can still take advantage of this type propulsor.

The second generation ducted propellers are the combination of a propeller, and the duct being placed in front of the propeller. This idea seems to be better than the first generation ducted propeller. However this idea also suffered from the risks for developing cracks in the connecting part between the duct and the hull plating at the aft end of a ship.

The latter part of the 20th century saw the third generation ducted propellers which appeared as their ducts having much smaller diameter than their propellers and installed slightly away from the propeller at the aft end of a ship. Within this generation, in 2005, NMRI invented their Weather Adopted Duct (WAD) system which was designed to take into account the performance improvement in actual sea conditions in-service. The WAD is to generate more thrust during rough sea conditions, where the ship requires more power to maintain the design speed, compared to the calm sea condition.

Through the above-summarised evolutionary history of the ducted propellers, we may notice the following important issues concerning their designs:

1) Ducted propellers are optimised based on their open water efficiency performance which does not necessarily display the maximum propulsive efficiency

2) The duct of a ducted propeller can be placed at any place if it works well

3) More efficient and critical part of a duct is always the upper half while the lower half of the duct is less efficient or may be considered useless from the propulsive efficiency point of view.

4) The smaller duct in front of the propeller could be one solution for better efficiency

One of the most recent successful ESDs introduced has been the Mewis Duct which was introduced in 2008 in Germany. Mewis described the roots of his novel ESD as shown in Figure 1 by claiming that his concept combines two ideas; one of which is the Sumitomo Integrated Lammern Duct (SILD) while other is the pre-swirl fins. However, the SILD had already integrated the pre-swirl fins in its arrangement.

Therefore, there is no significant difference in these concepts, while it is very obvious that the Mewis duct is a much-improved ESD compared to the SILD which was invented more than ten years before the Mewis Duct. It can be said that Mewis Duct will be the ultimate configuration for the ducted propellers which can be categorized as *Post-propeller* type ducted propulsors.

Figure 1 History of Mewis Duct presented by Mewis

2.2 GATE RUDDER® as a Ducted Propeller

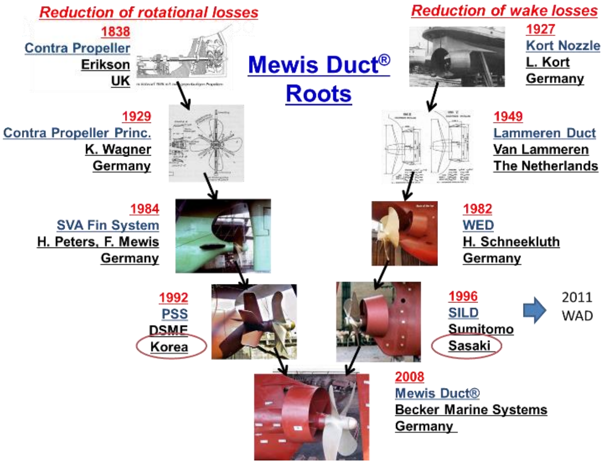

As stated earlier, the first generation conventional ducted propellers had minimal scope to be installed on the large commercial vessels due to the problems related cavitation and vibrations which have not been solved even now. However, we have seen through the evolution of the ducted propellers that the duct can be moved to anyplace if it will work well as in the case of many *Post-propeller* type ducted propellers. We are also aware of the fact that the lower part of the conventional duct may not be useful in the ship stern.

Inspired from the above-mentioned evolutionary observations and associated knowledge, the GATE RUDDER® propulsion system has been recently introduced based on the activities in Japan and UK. The major advantages of the GATE RUDDER® propulsion system compared with the *post-propeller* type ducted propellers can be claimed to be as follows Sasaki et al (2015), Sasaki et al (2018). :

1) The accelerating duct-like shape of the GATE RUDDER® with two separated sections (i.e. rudder blades) without their bottom parts, and placed aside the propeller, work as two efficient three-dimensional wings

2) The two separated rudder blades can be rotated independently from the upper parts, as a single rudder blade, to provide more efficient manoeuvring capability to the vessel.

3) The above-described arrangement accelerates the wake flow at the upper part of the propeller plane where the stagnated flow or higher wake shadow exists

4) The rudder blades produce 5-15% of the additional thrust of the propeller, like a duct, and this can reduce the high propeller loading

5) The replacement of a conventional rudder with the GATE RUDDER® system provides more attractive options for the aft end design arrangements.

As we can follow through the evolution of the *Post-propeller* type ducted propeller, the success of this type propulsor relies on the history of the “integration” of the propeller and duct. However, in the case of the GATE RUDDER®, the successful “integration” involves the propeller, hull and the rudder. Hence, more benefit from this integration can be expected as shown in Figure 2.

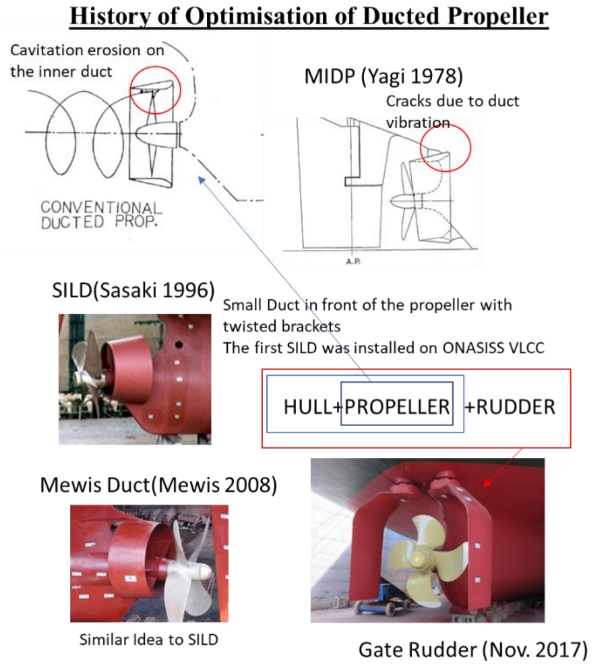

Figure 2 History of Ducted Propellers

2.3 Propulsive Efficiency with GATE RUDDER®

The GATE RUDDER® concept takes advantage of the rather complex integration of the hull, propeller and rudder flow in a unique propulsion system which is difficult to be described, and to be presented by any standard design and power prediction methodology.

If we consider the GATE RUDDER® is a propulsion system which consists of various sub-elements that can generate the required thrust, the propulsive efficiency of the GATE RUDDER® can be represented as the summation of the thrust to delivered power ratio due to the propeller and rudder blade elements as follows:

$$\eta_D = \frac{\sum_{i=1}^{3} T_i V}{\sum_{i=1}^{3} DHP_i} \qquad (1)$$

where, i= 1, 2, and 3 corresponds to the propeller, starboard rudder blade and port rudder blade, respectively. More

Using Equation (1) and assuming that the power is delivered only through the propeller, η_D can be written as follows:

$$\eta_D = \frac{(T_1+T_2+T_3)V}{DHP_1} \qquad (2)$$

Because propeller thrust T_1 and delivered power, D_1 can be represented by classical propeller-hull interaction coefficients, it follows:

$$\eta_{D1} = \frac{T_1 V}{DHP_1} = \frac{1-t_1}{1-w_1}\eta_O \eta_R \qquad (3)$$

Hence, Equation (1) can be modified as follows:

$$\eta_D = \frac{1-t_1}{1-w_1}\eta_O \eta_R + \frac{(T_2+T_3)V}{DHP_1} \qquad (4)$$

By using the simple momentum theory for the propeller efficiency,

$$\eta_D = \frac{1-t_1}{1-w_1}\frac{2\kappa}{[1+(1+C_T)^{0.5}]}\eta_R + \frac{(T_2+T_3)V}{DHP_1} \qquad (5)$$

where κthe is a correction factor from the ideal efficiency to actual propeller efficiency, and propeller thrust coefficient, C_T can be calculated by using Equation (6) as a function of water density ρ and propeller disc area S_P :

$$C_T = \frac{T_1}{0.5\rho[V(1-w_1)]^2 S_p} \qquad (6)$$

Based on these equations, it is obvious that the following next two characteristics of the GATE RUDDER® are very important for the evaluation of its performance:

1. Interaction between (T_2+T_3) and $(1-t_1)$
2. Interaction between (T_2+T_3) and $(1-w_1)$

Although η_R may have a small possibility of change by (T_2+T_3), this change can be neglected if we can avoid any error associated with the design or experimental in nature since the propeller design should be closely related to the change in the flow field. However, any large difference of η_R observed in the model test should be treated with care as the potential source of trouble.

Generally speaking, the above-highlighted interactions strongly depend on the axial distance between the ESD(s) and the aft end (stern post) of the vessel in front of the ESD. If the location of the ESD is far from the aft end, the interaction will be negligibly small. In contrast, if the location of ESD is very close to the aft end, as in the case of *the Post-propeller* type ducted propulsors, a strong interaction should be expected.

Figure 3 shows the efficiency gain in the ideal condition due to the assisting thrust (T_2+T_3) for the GATE RUDDER®. This means the presented values are based on the assumption that there is no interaction between (T_2+T_3) and neither ($1-t_1$) nor ($1-w_1$). In the figure, R and P is the hull resistance and required power, respectively.

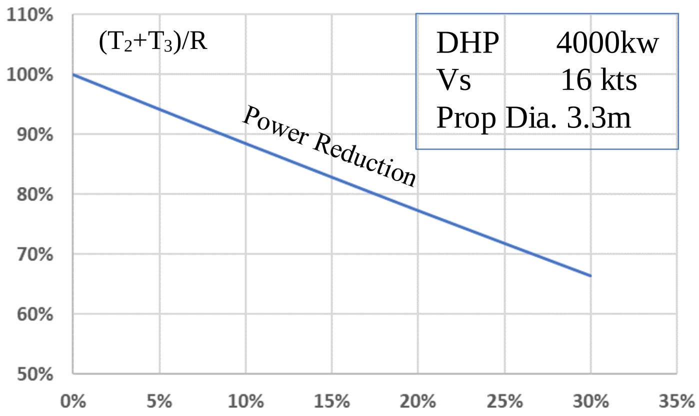

Figure 3 Ideal Power reduction by assisted thrust

Because the calculations in Figure 3 neglect the advantage of the propeller design conditions for lower thrust, the power reduction in this figure is slightly conservative, and further 2-3% can be considered by reflecting this advantage in the propeller design stage.

2.4 Interaction between GATE RUDDER® and Propulsive Coefficients

2.4.1 Thrust Deduction Factor

Thrust deduction factor originated from the hull is the reflection of the resistance increase on the hull due to the action of a propulsor. Because the propulsor creates a suction field at its upstream and hence accelerates the flow in front, this accelerated flow generates larger shear stress on the hull surface of the stern. These effects are the additional resistance source when the ship is propelled by the propulsor(s). To reduce this resistance increase, there are two practical design solutions. First one is to introduce a fine stern shape (with smaller half entry angles) in front of the propeller since the pressure is working on a normal direction to the hull surface. For this purpose, sometimes, cusp shapes are applied to the aft end lines of the ships. The second one is to place the propulsor relatively far from the aft end within the practical limits.

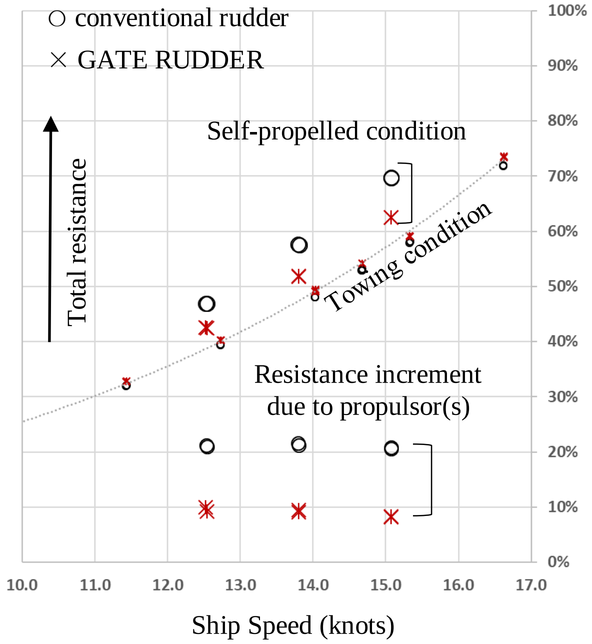

Figure 4 Comparison of total ship resistance between towing and self-propelled conditions for the models of 2500 GT container vessels with conventional and GATE RUDDER® systems

As can be seen in Figure 4, the resistance increment due to the propeller action for the GATE RUDDER® case is almost half that of the conventional rudder case. This is a general tendency which can be observed with all the model tests conducted with the GATE RUDDER®. These values are directly related to the thrust deduction factor of both rudders case. For example 20% of resistance increment of the conventional rudder case nearly equal to t = 0.2 while for the GATE RUDDER® t = 0.1, respectively.

Figure 5 shows the analysis arrangement of the thrust component from the rudder force measurements with the model of the same ship. This analysis is based the same way of an empirical prediction method for the lift and drag of a three-dimensional wing, and represented by the following formulation.

$$C_L = \varepsilon\kappa\alpha \tag{7}$$

$$C_D = \frac{F_Y' - \kappa\alpha}{\alpha} \tag{8}$$

$$\alpha = \frac{\sqrt{F_X'^2 + F_Y'^2 - C_D^2}}{\varepsilon\kappa} \tag{9}$$

$$F_X' = \frac{F_X}{0.5\rho V^2 S_R} \tag{10}$$

$$F_Y' = \frac{F_Y}{0.5\rho V^2 S_R} \tag{11}$$

where, C_L and C_D is the lift coefficient and drag coefficient of the rudder, respectively, while lift L is acting normal to the flow direction. F_X and F_Y are the measured rudder forces at the rudder fixed co-ordinate system as shown in Figure 5.

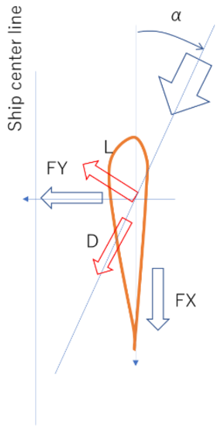

Figure 5 Coordinate system for rudder force measurement & analysis.

The measurements of F_X and F_Y allowed to evaluate C_L and C_D easily based on the assumption that that α is small. This measurement data was only available for the starboard side due to the limitation of the model deck space during the self-propulsion tests of the model presented in Figure 4.

Figure 6 presents the results of the angle of attack analyzed from the forces measured on the GATE RUDDER®. As expected the large lift produced on the GATE RUDDER® reflected on the measured angle of attack. This was due to the contraction of the wake flow which was brought about by not only from the hull geometry but also due to the suction effect of the propeller.

Another model test results, which provided further evidence on the interaction amongst the propeller, rudder blades and hull flow, more clearly, conducted at the Emerson Cavitation Tunnel using a dummy hull representing a large bulk carrier. As shown in Figure 7, this was a model with a segmented stern section, which is floated to measure the force acting on this section, under the action of the propeller and the model can be fitted with a conventional rudder and GATE RUDDER® for comparison.

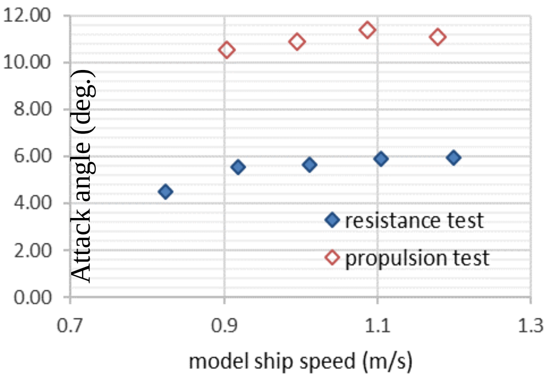

Figure 6 Attack angle α (deg.) analyzed from self-propulsion tests with a GATE RUDDER® model.

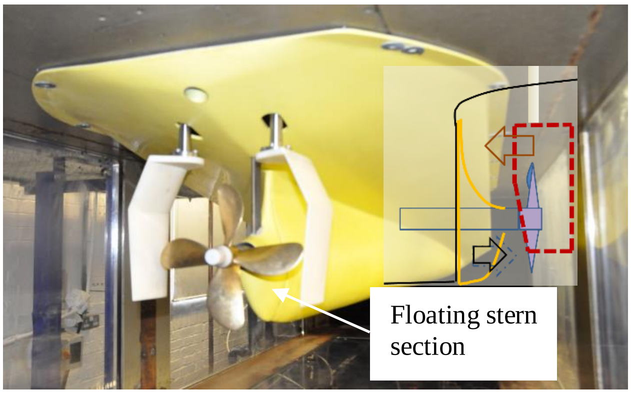

Figure 7 Dummy hull with a segmented and floating stern section with GATE RUDDER® in the Emerson Cavitation Tunnel.

Figure 8 shows the results of the measured forces on the GATE RUDDER® and the conventional rudder, in comparison. As it can be seen in this figure, the force acting on the GATE RUDDER® is in the same direction with the propeller thrust and with a magnitude of 4-5% of the propeller thrust. This value is slightly small compared with the figure obtained from the self-propulsion tests in the towing tank because of the exposure of the long and blunt rudder shafts required to measure the rudder blade forces outside the cavitation tunnel at the top. As shown in Figure 8, while the GATE RUDDER® displays increasing forward force (i.e. thrust) with increasing propeller thrust, the conventional rudder presents almost a constant resistance with increasing propeller thrust. increasing propeller loading generates

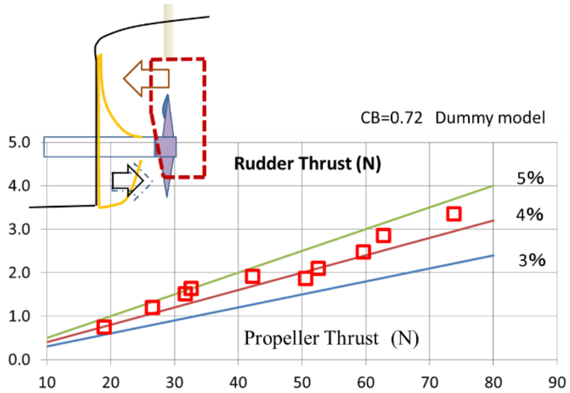

Figure 8 Rudder thrust generated by GATE RUDDER®

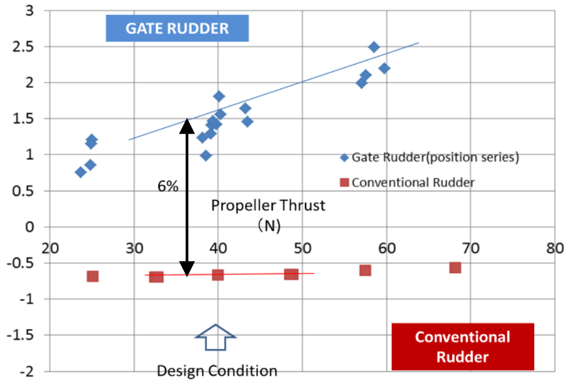

Figure 9 Comparison of rudder force on GATE RUDDER® and Conventional Rudder

Figure 10 shows the measured force acting on the floating stern section of the dummy hull model in the presence of the GATE RUDDER® and that of the conventional rudder in comparison. Apart from some scattered difference in resistance at low thrust (around 30N), both the GATE RUDDER® and conventional rudder arrangements induces similar drag forces on the stern part of the hull.

Figure 10 Force acting on the floating stern

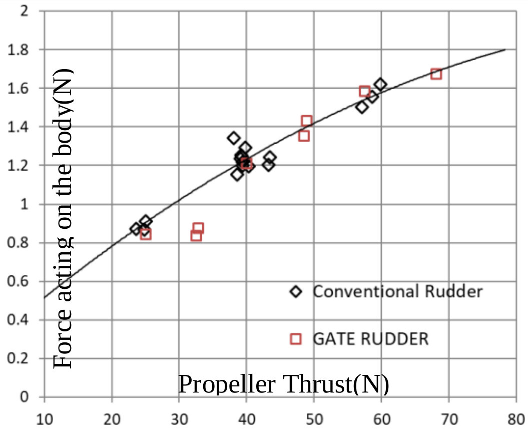

Unfortunately, we could not simulate this case by CFD to provide further insight into the interaction amongst the propeller, rudder and hull flow because of the complexity of test setting in the cavitation tunnel.

However, the CFD study conducted for the potential application of the GATE RUDDER® propulsion system on a RoRo vessel case provides some useful information on this complex interaction discussed in the following.

Figure 11 shows the comparison of the axial wake velocity ratio distributions at the aft end of a 6.75m RoRo model ship due to a conventional rudder and GATE RUDDER® system including the effect of the propeller's action. In complementing the velocity predictions, the comparative pressure predictions for the same vessel are also conducted for both rudder arrangements and shown in Figure 12.

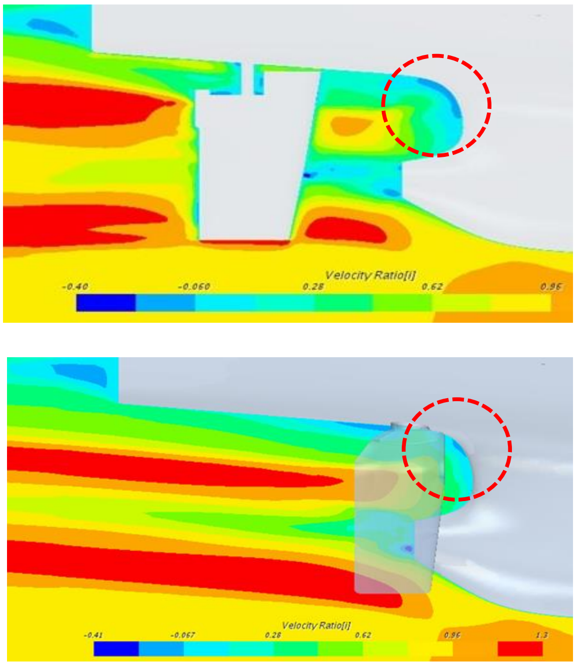

Figure 11 Comparison of axial flow velocity ratios for a RoRo vessel including the action of the propeller: Conventional rudder (top); GATE RUDDER® (bottom)

As shown in Figure 11 for the velocity distributions, it is obvious that the GATE RUDDER® does not affect the flow field around the ship stern so much in front of the propeller except the upper parts, which are indicated by dotted circles Figure 11, where the flow is always stagnating when we applied a conventional mariner stern. This will be favourable from not only the ship resistance point of view but also cavitation and noise aspects. The pressure distribution on both rudder surfaces are shown in Figure 12 and the figure show us that the blades of GATE RUDDER is working as wing of air plane which generates large lift force to one direction.

Based upon the above analysis the thrust deduction parameter appears to be not much affected in the case of GATE RUDDER® arrangement indicating that the resistance increment due to the action of the propeller is proportional to the propeller's thrust and not affected by the rudder thrust. In supporting this observation, the pressure distribution on the hull surface in front of the propeller is almost the same except the upper parts which may improve the thrust deduction factor with the GATE RUDDER®

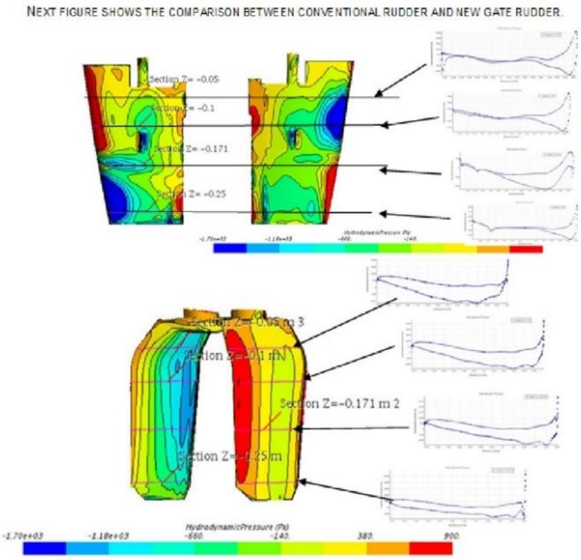

Figure 12 Pressure Distributions on the rudder Blade(s): Conventional rudder (top); GATE RUDDER® (bottom)

Therefore, we can conclude that thrust deduction of the ship with GATE RUDDER (t_G) can be represented by using the conventional rudder's thrust deduction (t_C) as follows:

$$t_G = t_C \times \frac{T_1}{T_1+T_2+T_3} - \delta t \quad (12)$$

where δt is associated with any contribution from improvement of flow as we saw this in front of the propeller in Figure 11 (dotted red circle)

Regarding to the scale effects of the rudder forces, and hence reflection on the thrust deduction, based on the analysis results of the full-scale data, it appears that the GATE RUDDER® forces experienced in the full-scale can be as high as 30% more compared to the predictions based on the model test measurements due to the low Reynolds number experienced in model scale. This also requires special attention in the power prediction and this is currently being investigated to be reported.

2.4.2 Effective wake

Although the description of the effective wake for a vessel with the GATE RUDDER® can be subjected to further discussion, by following the standard terminologies, it may be helpful if we can identify how the GATE RUDDER® should be regarded as: an appendage; or a propulsor. Within this context, by considering its overall functioning a whole system or unit, and the analysis and discussions conducted so far, it is more correct to regard as a propulsor. Having said that this treatment will have its own complexities, e.g. conducting an open water test with the GATE RUDDER® unit is not so easy with the two large surface piercing struts and the flat plate of the rudder top which may generate surface wave easily etc. However, these can be circumvented by some tailor made testing arrangements and analysis procedures, as we experienced with other special propulsors, e.g. ducted propulsors, pods, thrusters etc.

Regarding the effective wake description, which manifests itself in the propeller advance speed behind the hull mainly by the contraction effect of the viscous boundary layer due to the action of the propeller, it is best to evaluate at a location behind the hull where the induced velocities due to propeller is negligible. For this purpose a sketch which shows the representation of the effective wake due to the GATE RUDDER® and Conventional rudder is included in Figure 13. As it can be appreciated by sketches in this figure the GATE RUDDER® configuration will not be affecting the hull boundary layer structure and hence the resulting wake field compared to the that field with the conventional rudder arrangement will be similar or slightly slower.

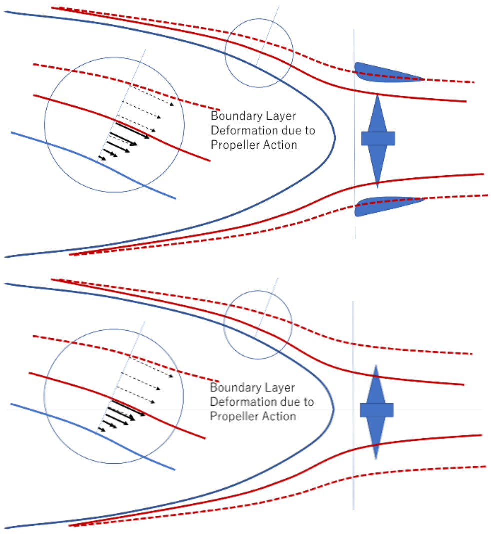

Figure 13 Schematic view of of effective wake resulting from: GATE RUDDER® (top sketch); and Conventional rudder (lower sketch) arrangements

In order to demonstrate the differences in the effective wake flow of the same hull fitted with the GATE RUDDER® and the Conventional rudder arrangement, CFD computations were conducted for the earlier mentioned RoRo vessel hull with the both rudder configurations and results are compared as shown in Figure 14.

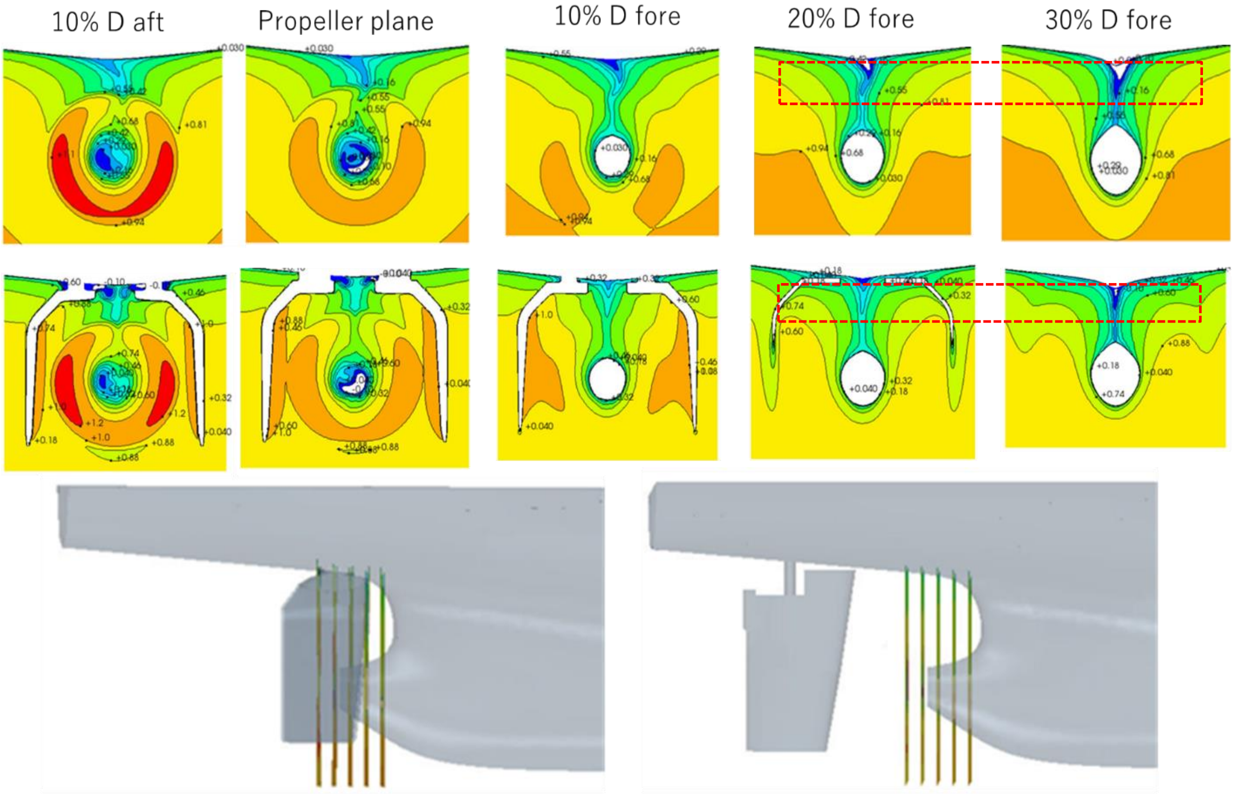

Figure 14 CFD predictions of effective wake and propeller induced velocities at the aft end of a RoRo vessel hull: with Conventional rudder-propeller arrangement (top figure); with GATE RUDDER® arrangement (bottom figure)

For the evaluation of the effective wake, it will be best to concentrate at the propeller upstream and near the stern region of the hull where the direct interference of the propeller-induced velocities are much reduced or negligible. It is therefore, the CFD simulations of the wake flows for the RoRo vessels are conducted more frequent at the propeller upstream (i.e. at three cross-sections: 0.1D; 0.2D; and 0.3D distances) locations between the propeller and the stern as well as the locations at the propeller plane and 0.1D downtream of the propeller, as shown in Figure 14. Amongst these presentations, perhaps, the first is to concentrate on the wake velocity at foremost location (i.e. 0.3D cross-section) where one may notice the larger region of the low velocity field of the GATE RUDDER® arrangement compared to the conventional rudder arrangement. This means the general tendency of the effective wake with the GATE RUDDER is larger than with the conventional rudder arrangement (i.e. $w_G > w_C$).

After this foremost section, if we move further close to the propeller plane and look into the flow velocity it is clear that the GATE RUDDER® induces the velocity change the in rudder blades as such the V-shaped wake pattern (green to blue) is changed to T-shaped wake pattern by the effect of the GATE RUDDER®. This may be more advantageous from the propeller cavitation and noise point of view as we can see the difference of the circumferential velocity distributions for both cases near the propeller plane (0.1D upstream) as shown in Figure 15.

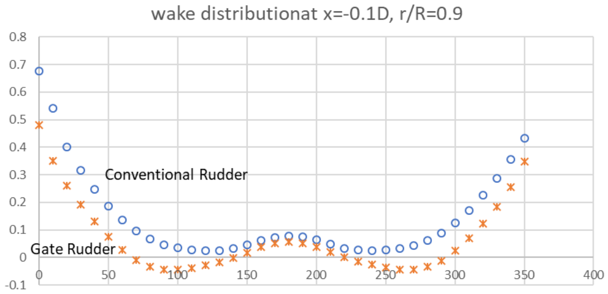

Figure 15 Wake distribution near the propeller plane for different rudder configurations.

5 CONCLUDING REMARKS

Based upon the analysis of the results obtained from the model tests, CFD simulations and the full-scale data of two container vessels, further investigation is conducted on the propulsive efficiency and the associated propeller-hull-rudder interaction parameters of a ship fitted with the GATE RUDDER® propulsion system in comparison with those of the conventional rudder propeller arrangement. The investigation indicated that:

1) Thrust deduction parameter of a hull with the GATE RUDDER® system can be represented by the following simple formula

$$t_G = t_C \times \frac{T_1}{T_1 + T_2 + T_3} - \delta t$$

where, T_1 is the propeller thrust, T2 and T3 is the thrust generated by each rudder blades of the GATE RUDDER® arrangement while δt is the contribution of regulated flow if exists.

2) Effective wake of a hull with the GATERUDDER® propulsion system is expected to be larger than that of a conventional rudder-propeller arrangement if the GATE RUDDER® is designed properly.
This, in turn, requires that the propeller efficiency should be calculated based on the correct effective wake which is different from that to be obtained by the thrust (K_T) identity method.

3) The wake distribution in the propeller plane can be improved by GATE RUDDER by changing the flow field at upper of stern in front of the propeller.
It seems that a simulated two dimensional wake screen is not enough to evaluate the cavitation and noise of GATE RUDDER system because of different trend of interaction among hull, propeller and rudder as shown in Figure 14 (red square part)

REFERENCES

Carlton J. (2012). Marine propeller and propulsion. 3rd Edition.

Sasaki, N., Atlar, M. and Kuribayashi, S. (2016). The new hull form with twin rudders utilizing duct effects, J Mar Sci Technology (2016) 21: 297.

Sasaki N., Atlar, M. and Kuribayshi, S. (2015). Advantage of twin rudder system with asymmetric wing section aside a propeller. Journal of Marine Science and Technology.

Turkmen, S., Carchen, A., Sasaki, N. and Atlar M. (2015). Anew energy saving twin ruder system, International Conference on Shipping in Changing Climates, Nov. 2015, Glasgow.

Sasaki N.,Kuribayshi, S.,Asaumi N. Fukazawa M.,Nonaka T., Turkmen S., Atlar M., Measuement and calculation of gate rudder performance, AMT'17, Glasgow, 2017.

A. Yücel Odabaşı Colloquium Series
3rd International Meeting - Progress in Propeller Cavitation and its Consequences:
Experimental and Computational Methods for Predictions
15th – 16th November 2018, Istanbul, Turkey

Parametric Study of a Pre-swirl Stator for a Tanker

Zeynep Tacar[1*], Emin Korkut[1]
[1]Istanbul Technical University, Faculty of Naval Architecture and Ocean Engineering, 34469 Maslak-Istanbul, Turkey

Abstract: Pre-swirl stators are one of the energy saving devices located before the propeller and used for giving a pre-rotation to the flow in order to provide more uniform flow to the propellers. Pre-swirl stators improve the propulsion efficiency not by generating additional thrust but changing the propeller blades loading favourably. Hence, it is very important to determine the optimum blade arrangement to have the optimum flow at the propeller plane and also experience the minimum added resistance by the stator blades.

In this study, a pre-swirl stator was designed and studied numerically for INSEAN 7000 DWT Tanker at a model scale of λ=16.5 by systematically varying some important parameters, such as the number of the blades, the angle of attack and angular position of the blades. The stators were located longitudinally 0.3D_p (propeller diameter) upstream of the propeller. The chord length of the blade section was chosen 0.25D_p. Reynolds Averaged Navier Stokes (RANS) method was used and SST k-ω was preferred as a turbulence model. The stator cases were analysed behind the hull condition at the service speed which corresponds to 1.773 m/s in model scale. The free surface effect was ignored to reduce the required analysis time so that, the analyses were performed with double body approach. In self-propulsion analyses, Virtual Disk method was used to simulate the propeller rotation. All cases were compared with the bare hull condition (without stator) and the optimum one was determined by comparing the propulsion efficiencies. This paper includes the details of the geometries and study and discusses further improvement of the methodology.

Keywords: Energy Saving Devices (ESD), Computational Fluid Dynamics (CFD), Pre-swirl Stator (PSS), Propulsion efficiency.

1 INTRODUCTION

Pre-swirl stators are the passive fin systems located before the propeller to generate a swirling flow opposite to the rotation direction of the propeller in order to reduce the rotational losses. This swirling flow generates an additional blade loading to the propeller blades and this more uniform loading increase the thrust, noting that the thrust of the stators is always negative but the swirling flow makes the improvement (Zondervan et al. 2011). Pre-swirl stators are used to change the wake field to enable the propeller to work more efficiently (Simonsen et al. 2012). Also the pre-swirl stators are called as poor man's contra-rotating propeller and the difference between pre-swirl stators and contra-rotating propeller is small. The stator blades are stationary, but in the contra-rotating propeller, both propellers rotate (Zondervan et al. 2011). A contra-rotating propeller can provide a 10-14% of the gain in efficiency (Celik and Güner 2007), the best among the ESDs in terms of gain in efficiency (Kim et al. 2004), but the PSS is simple and cheaper. Contra-rotating propellers have higher cost and a difficult shafting maintenance but pre-swirl stator systems have a simple shafting system, a less initial installation cost (Kim et al. 2004, Saettone et al. 2016) and more suitable for retrofitting. Also, it was reported that there were reliability problems in the contra-rotating propellers or vane wheel, which makes the ship owners not to prefer although the gain in the efficiency is 5% or more (Kim et al. 2004). On the contrary a PSS has a high reliability due to its fixed blades, size and simplistic design (Kim et al. 2004).

Studies have shown energy saving by the use of a pre-swirl stator system, such as a 4.5% saving of fuel (Zondervan et al. 2011), 5-8% gain in efficiency (Celik and Güner 2007), 3-8% gain in energy (Yong et al. 2015) and 3-6% reduction in the delivered power (Park et al. 2015). The gain can be explained by the increase of attack of inflow to the propeller, caused by an increased wake fraction and the swirling flow generated by the PSS (Kim et al. 2013).

A number of studies have been conducted on pre-swirl stators. A PSS were designed for a container ship and a twin-screw passenger vessel by using RANS and BEM methods (Zondervan et al. 2011). For the container ship 5, 6 and 7-bladed stators were designed. Stators were installed at the 0.15 D_p upstream of the propeller. 6-bladed stator was chosen as the best configuration and thrust was increased by 6.2%. Thickness of the stator blades was determined by cantilever beam theory. The diameter of the propeller was optimised and a propeller with a 0.3m less diameter was obtained as a result of the stator effect.

Zondervan et al. (2011) also investigated the effect of the PSS for a twin screw passenger vessel in addition to the

* *Corresponding author e-mail: ztacar@itu.edu.tr*

container ship case, and 5 and 6 bladed stators were studied. Two stator blades were designed as the shaft brackets, so they were given a special shape and twist to work both as stator blades and shaft brackets. 5-bladed stator was chosen as the best configuration and 4.7% of thrust gain was obtained.

The influence of the pre-swirl fins on propulsion was investigated by Simonsen et al. (2012). A 4-bladed PSS was designed for a bulk carrier ship. Three blades were installed on the port side while one blade was located on the starboard side. This asymmetric configuration was adopted for a wide range of vessels i.e. bulk carriers, container ships, bulk carriers etc. (Saettone et al. 2016). This configuration is related to the rotation direction of the propeller. It is aimed to reduce the upcoming flow on starboard side for a right handed propeller by deflecting the flow in upwards direction. Another important point on installing the blades on the hull is to locate the stator blades or fins to be angled based on the flow direction and prevent the blades having extreme angle of attack and flow separation on the blades. As a result, Saettone et al. (2016) found that pre-swirl fins enabled to reduce 1.8% of power requirement.

Lifting line method is one of the mostly used methods in stator design. Celik and Güner (2007) studied a downstream stator (post) by a lifting line code with different parameters, such as the axial distance between the propeller and the stator (AXD), number of the blades and the diameter of the stator; and obtained the optimum configuration with 9 blades. However their study was not practical, hence resulting in extra drag. Therefore it is important to optimize the number of the blades of the stators for practical use on ships.

The hydrodynamic design of a PSS with a variable pitch was investigated paired with a conventional propeller by (Saettone et al. 2016). A 4-bladed (3 of the blades on port side and 1 on the starboard side) PSS with a constant chord length was investigated. The PSS was located at the 0.5R upstream of the DTNSRDC 4381 propeller. The stator had a chord length of 1.5 m at the root and 0.9 m at the tip and the diameter of stator was equal to propeller diameter. All optimizations and analyses were performed in full scale and obtained 3.8% gain in efficiency.

Another asymmetric stator was studied for a container ship by Yong et al. (2015). In their study a 4 bladed stator was investigated: 3 of the blades were located on the port side (at 45°, 90°, 135°) and one blade was located on the starboard side (at 270°). The optimum pitch angles of the blades were as 14°, 19°, 12° and 2°, respectively. Model tests were performed for this initial design and the model test results indicated increase in resistance due to the excessive chord length of the stator and the pitch angle so, the stator was re-designed. The pitch angles of the blades were diminished to 8°, 14°, 9° and 1.5°, respectively. The initial design enabled to reduce the total resistance and the delivered power as 6.9% and 11%, respectively but the performance of the latest design has not been verified yet.

A patented PSS was designed by DSME, used a similar configuration that the blades having 17°, 19°, 23° and 22° pitch angles, respectively (Park et al. 2015), (Park and Oh 2014). The influence of the PSS was investigated both in model and full scale by a CFD method. In full scale, the effect of the PSS was increased due to the increasing relative boundary layer thickness (thickness/L_{pp}) in higher Re numbers. Increase in the thrust by the PSS was predicted 11% in full scale analyses.

An optimization study of a PSS was also conducted by Kim et al. (2013) as part of a European Union project VIRTUE. Both the lifting line and RANS methods were utilized in design and optimization of the stators. A base stator with 4 blades were generated and this configuration was used in the systematic variation study with 5 parameters: number of the stator blades, diameter of the stator (0.9 D_p-1.2 D_p), angular position, stator pitch angle and a twisted blade. The comparison of the stator configurations was made based on the value of Q_n (torque x rpm). In base PSS, one blade was installed on starboard side and 3 blades were located on the port side. The port side blades were located with 45° angular spacing. Average 4% power gain was achieved and 0.25 knots better performance was observed in sea trial tests (Kim et al. (2013).

Pre-swirl stators may also be utilized in hydrokinetic turbines. A numerical optimization study was held by (Gish et al. 2016). Number of the stator blades was determined by the following statement:

$$N_{stator}=2.Z_{turbine} \pm 1$$

where, N_{stator} and $Z_{turbine}$ were the number of the stator blades and number of the turbine blades, respectively. The turbine considered in their study had 3 blades so the number of the blades of the stator was determined as $N_{stator}=5$. The stator was located at the $0.25D_{turbine}$ upstream of the turbine and the chord length of the stator was $0.25D_{turbine}$.

Selection of the blade section is another important parameter since the shape of the section should be determined to minimize the drag and also avoid the flow separation due to stall. Three symmetric and three asymmetric NACA profiles were investigated by (Gish et al. 2016). The symmetrical profiles were NACA 0008, 0010 and 0012 and the asymmetric profiles were NACA 1412, 2412 and 4412. NACA 0012 and NACA 2412 were chosen as the best sections regarding the maximum stall angle and max C_l/C_d at the stall angle. Then two dimensional numerical simulations were performed in order to determine the angle of attack angles of the blades. Aiming to find the best angle, NACA 0012 and NACA 2412 sections were analysed ranging from 0° to the stall angle of the section with 1° increment. As a result, NACA 0012 section with 3° angle of attack was selected due its effect on the accelerated inflow velocity that was the highest among the configurations, expecting to have the maximum gain on the turbine efficiency.

Similarly, Amin and Xiao (2014) investigated to improve the efficiency of a horizontal axis tidal turbine by using the PSS. They obtained 7% increase in radial velocity with the PSS and the streamlines were deflected around the stator before entering to the turbine blades and this deflected flow enabled to increase the efficiency of the turbine. The turbine's overall efficiency was increased 13% with the use of PSS.

Another PSS design study was performed for the INSEAN 7000DWT Tanker as part of STREAMLINE Project by Bensow (2015). In this project a PSS with 3 blades were designed. All blades were installed on the port side and blade sections were generated based on symmetrical NACA 65 profile. The span of the blades was 0.55Dp and the stators were located at the 0.3 D_p upstream of the propeller. The blades were positioned at 40°, 90° and 140° and the angle of the attack of the blades were 5°. It was noted that the sharp velocity deficit due to the flow separation on the hull was not observed in the PSS case.

In this study pre-swirl stators located at 0.3 Dp upstream of the propeller plane were investigated for the INSEAN 7000 DWT Tanker in model scale of λ=16.5. Numerical analyses were performed at the service speed of 14 knot, which corresponds to 1.773 m/s in model scale. In the numerical analyses Star-CCM+ was used as the solver and SST k-ω model was used for RANS closure. NACA0012 section was used as the stator blade section. Diameter, axial location, blade section, section chord length of the stators were kept constant. The effects of the number of the stator blades, angular positions of the blades and blade pitch angles were investigated systematically.

The main objective of this study is to improve the flow characteristics at the propeller plane and increase the quasi propulsive coefficient, QPC by installing PSS. Another objective of the study is to compare relatively the effects of the parameters, number of the blades, angular positions of the blades, and the blade pitch angles, on the propulsive coefficients, and try to get some insight into the phenomenon.

This study is part of a Ph.D. study of the principal author and the paper presents the preliminary results of the parametric study for PSS. In the following sections of the paper the details of the ship and propeller geometry are given in Section 2, and the design parameters and the design matrix are given in Section 3. In Section 4 the numerical study is explained and the results are presented and discussed in Section 5. Finally the conclusions obtained from the study are given in Section 6.

2 GEOMETRY AND MAIN PARTICULARS OF THE HULL AND PROPELLER

In this study, a 7000 DWT chemical tanker model, designed for the EU-STREAMLINE Project, with the scale ratio of λ= 16.5 was used. The model had a bulbous bow and a skeg in the aft, a single screw 4-bladed propeller and a spade rudder. No full scale ship exists. The main particulars of the ship both in model and full scale are given in Table 1.

Table 11 Main particulars of the ship in full-scale and model-scale

Parameters	**Full-Scale**	**Model-Scale (λ= 16.5)**
Length between perpendicular, L_{PP} [m]	94.0	5.697
Length of waterline, L_{WL} [m]	96.753	5.864
Beam, overall, B_{OA} [m]	15.422	0.935
Max. moulded breadth at design waterline, B_{WL} [m]	15.414	0.934
Draft at forward perpendicular, T_F [m]	6.005	0.364
Draft at aft perpendicular, T_A [m]	6.005	0.364
Displacement, ∇ [m^3]	6820.6	1.518
Wetted Surface, S [m^2]	2269.25	8.335
Block coefficient, C_B	0.762	0.762
Propeller distance from aft perpendicular [m]	2.114	0.128
Propeller diameter, D_P [m]	3.850	0.233
Number of propellers	1	1
Service speed, V_S	14 knot	1.773 m/s
Froude Number	0.23	0.23
Reynolds Number	6.123×10^8	9.136×10^6

A fixed pitch, 4 bladed, right-handed INSEAN E1637 propeller was used. The main particulars of the propeller are given in Table 2 both in model and full scale.

Table 12 Main particulars of the propeller in full-scale and model-scale

Parameters	Full-Scale	Model-Scale
Diameter, D_P [m]	3.85	0.233
Number of Blades, Z	4	4
Nominal Pitch Ratio ($P/D_{P0.75R}$)	1.0	1.0
Skew Angle, θ_S [deg]	3.0	3.0
Expanded Area Ratio (EAR)	0.58	0.58
Boss Diameter Ratio (D_H/D_P)(at propeller disc)	0.168	0.168

3 PRE-SWIRL STATOR PARAMETERS AND DESIGN MATRIX

In this study, diameter, chord length, axial location, foil section of the pre-swirl stators were kept constant. Effects of the number of the blades, angular positions of the blades and blade pitch angles were investigated. Constant parameters of the PSS can be seen in Table 3.

Table 3 Constant parameters of the pre-swirl stators

Parameter	
Diameter	$0.9D_P$
Chord Length of the blade section	$0.25D_P$
X-Location	$0.3D_P$ upstream of the propeller plane
Blade Section	NACA 0012

The parametric study is summarized in Table 4. In Table 4 PU, PC, PL and SC represent the port upper, port central, port lower and starboard central blades, respectively. In this study the stator blades were installed at 4 different angular positions. The initial position (Position 1) was 315°-270°-225°-90°. The second (Position 2) and third (Position 3) angular position configurations were obtained by rotating the blades 15° clockwise. The fourth angular position configuration was generated by rotating the blades 15° counter clockwise. The angular positions of the blades can be seen in Figure 1.

Table 4 Design matrix

Case	Blade Pitch Angle (°)					
	PU	PC	PL	SC		Angular Position
1	0	0	0	0	all blades	POS 1
2	0	0	0	-	wo SC	
3	0	0	0	0	half SC	
4	-	0	0	0	wo PU	
5	0	0	0	-	wo SC	POS 2
6	0	0	0	-	wo SC	POS 3
7	0	0	0	-	wo SC	POS 4
8	4	0	0	-	wo SC	POS 2
9	-4	0	0	-	wo SC	
10	-8	0	0	-	wo SC	
11	-4	4	0	-	wo SC	
12	-4	-4	0	-	wo SC	
13	-4	-8	0	-	wo SC	
14	-4	-8	-4	-	wo SC	
15	-4	-8	-4	-	wo SC	
16	-4	-8	-8	-	wo SC	

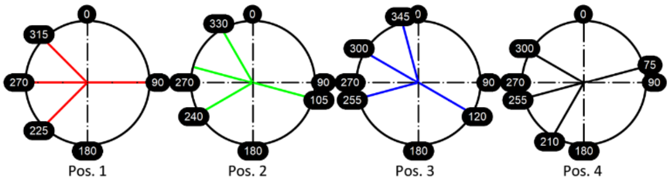

Figure 1 Blade angular positions

First of all, all blades (PU, PC, PL and SC) were located in the initial angular position (Pos.1); and SC and PU blades were removed in Case 2 and 4, respectively to study the influence of number of the stator blades. The effect of the size of SC blade was investigated in Case 3, then, the length of the SC blade was reduced to half size. Among these 4 cases, Case 2 (stator without SC blade) was determined to be the optimum. Then, the blades without the SC blade were located in the other angular blade positions and Position 1 and 2 gave similar results. So, the initial angular positions of the stator blades were kept constant for the rest of the study. The effect of the blade pitch angle was investigated on the PSS located in the 1st angular position and without the SC blade. In order to find the optimum blade pitch angles, blades were positioned for three different blade pitch angles: 4°, -4° and -8°. Firstly the blade pitch angle of PU blade was optimized. PC and

PL blades was kept at 0° pitch angle (initial configuration) and pitch angle of the PU blade was changed to 4°, -4° and -8°, respectively. -8° was chosen due to its effect on general propulsive efficiency, which indicated the maximum efficiency among the other pitch angles for the PU blades. -8° was kept fixed for the PU blade for the rest of the analyses. Then the same procedure was applied to PC and PL blades, respectively. The optimum blade pitch angles for PC and PL were determined as -8° for both blades. As a result of the blade pitch angle optimization study, -8° was determined as the optimum pitch angle for all blades.

4 COMPUTATIONAL STUDY

In the computational study RANS method was used with the double body approach, ignoring the effects of the free surface. SST k-ω model was used as the turbulence model. In this case density and kinematic viscosity values were ρ=998.962 m^3/s and ν =1.1121×10^{-6} m^2/s, respectively, which are obtained from recommended procedures of ITTC Fresh water and seawater properties (ITTC 2011) for 15.9°C in order to provide same conditions with the experiment.

Computational Domain and Boundary Conditions

A box-shaped domain with the dimensions -2L<x/L<3L; -2L<y/L<2L; -L<z/L<0 was used, where L is the length of the ship model. The boundary conditions for the inlet and outlet boundaries were defined as velocity inlet and pressure outlet, respectively. The top of the domain was defined as a symmetry plane as a requirement of double body method. Other boundaries were defined as slip wall except the hull surface. The hull was defined as no-slip wall.

Grid Generation

Cartesian cut cell method was used for the grid generation. y+ value was kept under 5 for all numerical analyses in order to avoid the buffer region which is between the range of 5-30. 8 prism layers with a 1.45 stretching ratio were generated to keep the y+ value less than 5.

4.1 Resistance Analyses of the Hull with and without stator blades

4.1.1 Resistance of the Bare Hull with Double Body Approach

Resistance analyses were performed for the bare hull in all speed range without the effect of the free surface. In numerical analyses STAR CCM+ was used. The same computational domain and grid were used for all analyses and the total thickness of the prism layers were varied slightly for each speed to keep the average y+ same for all speeds (1.140m/s - 2.026 m/s). Number of generated cells were in range of 1.805M-1.816M for the bare hull resistance analyses for all speed, and this difference was originated from the total prism layer thickness.

Computational results was compared with the experimental results which include both the viscous and residual resistance components. In order to compare the numerical and experimental results, viscous and residual components of the experimental total resistance were calculated by the following procedure.

a. Calculation of total resistance coefficient (C_{TM}):

$$C_{TM} = \frac{2R_{TM}}{\rho V S^2} \tag{1}$$

b. Calculation of the frictional resistance coefficient (C_{FM}):

The frictional resistance coefficient C_{FM} at model scale can be calculated based on ITTC 1957 formula given in Eq.1.

$$C_{FM} = \frac{0.075}{(\log \mathrm{Re} - 2)^2} \tag{2}$$

where, Re is the Reynolds number and given in Eq.3.

$$\mathrm{Re} = \frac{V L_{WL}}{\nu} \tag{3}$$

c. The calculation of the viscous resistance coefficient (C_{VM}):

$$C_{VM} = (1+k) C_{FM} \tag{4}$$

where (1+k) is the form factor and was computed as 1.18 for this model.

d. The calculation of residual coefficient (C_{RM}):

$$C_{RM} = C_{TM} - C_{VM} \tag{5}$$

e. The calculation of residual resistance (R_{RM}):

$$R_{RM} = \frac{1}{2} \rho C_R S V^2 \tag{6}$$

f. The calculation of viscous resistance (R_{VM}):

$$R_{VM} = R_{TM} - R_{RM} \tag{7}$$

In the service speed of 14 knot corresponding to the model speed of 1.773 m/s, the residual resistance coefficient, residual and viscous resistance were computed as:

$$C_R = 1.102 x 10^{-3}$$
$$R_R = 14.42 N$$
$$R_{VM} = 46.77 N$$

In Figure 2, the viscous resistance component obtained from the CFD study is given in comparison with the experimental results by above procedure. The maximum difference was obtained as 2.08% at the highest speed (V_m=2.026 m/s).

4.1.2 Resistance of the Hull with Stator Blades

The same computational domain and grid with the bare hull resistance analyses was used for the analyses with the stator blades, only the mesh region near to the stator blades was refined by using volumetric control blocks in order to capture the effects of the stator blades more accurately. An average 2.2M cells were used in the resistance analyses with the stator blades. Differences in cell quantity was arose from change in pitch angles and angular positions of the blades. A mesh scene from aft view with port side stator blades can be seen in Figure 3. 0.92-3.73% increment in towed resistance was experienced for the cases with PSS compared to bare hull condition.

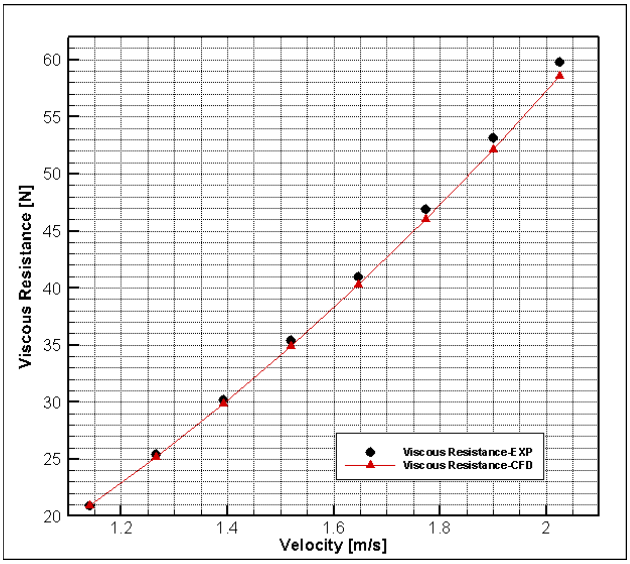

Figure 2 Comparison of CFD vs. EXP for viscous resistance component at model scale

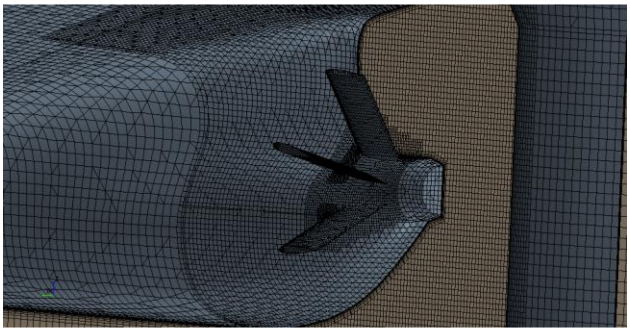

Figure 3 Mesh scene from aft view with the stator blades

4.2 Self-propulsion Analyses with Virtual Disk

There are several ways to simulate the rotation of the propeller in a self-propulsion analysis. Virtual disk model is one of these methods. In this method a momentum source in a cylindrical region represents the propeller thus, there is no need to use the real propeller geometry. This method enabled us to simulate the propulsion with less cell quantity and less computation time comparing with the Moving Reference Frame (MRF) or sliding mesh methods but also with less fidelity due to absence of the real propeller geometry. The value of the momentum source was estimated from the experimental open water curves.

In self-propulsion tests and analysis an external towing force (FD) should be applied in order to compensate Reynolds number difference in full-scale and model-scale, hence to achieve the demanded load of the propeller. This force derives from the difference of the model and full-scale skin friction coefficients so, named also as Skin Friction Correction (SFC). F_D or SFC can be calculated as given in the following (ITTC 2002):

$$F_D = \frac{1}{2}\rho S V^2 \left[(1+k)(C_{FM} - C_{FS}) - \Delta C_F\right] \tag{8}$$

where;

S: Wetted surface area of the model [m2]

V: Velocity of the model [m/s]

1+k: Form factor of the model (1+k=1.18 for this model)

ΔCF: Roughness allowance

$$\Delta C_F = \left[105\left(\frac{k_s}{L_{WLS}}\right)^{1/3} - 0.64\right]10^{-3} \tag{9}$$

k_s: Hull surface roughness [m]

$k_s = 150x10^{-6}\,[m]$

$\Delta C_F = 0.575x10^{-3}$

Three analyses were performed for the different rate of revolutions (n= 8, 8.2 and 8.4 rps) in order to determine the self-propulsion point. The rate of revolution, n value in the self-propulsion condition and the thrust value at the corresponding n was obtained by linear regression method.

The thrust identity method was used in order to obtain the propulsive factors. The advance coefficient J_{0T}, $10K_{QP}$ and η_{0T} were read from the open water diagram. The wake fraction, thrust deduction fraction, hull, relative-rotative and propulsive efficiencies were calculated as given in the following statements:

Thrust identity wake fraction:

$$t = \frac{T + F_D - R_T}{T} \tag{10}$$

Hull efficiency:

$$\eta_H = \frac{1-t}{1-w_{tT}} \tag{11}$$

Thrust identity relative-rotative efficiency:

$$\eta_R = \frac{K_{Q0T}}{K_{QP}} \tag{12}$$

Propulsive efficiency:

$$\eta_D = \eta_{0T} * \eta_H * \eta_R \tag{13}$$

In Figure 4, streamlines on the stator blades of the optimum case at self-propulsion point can be seen.

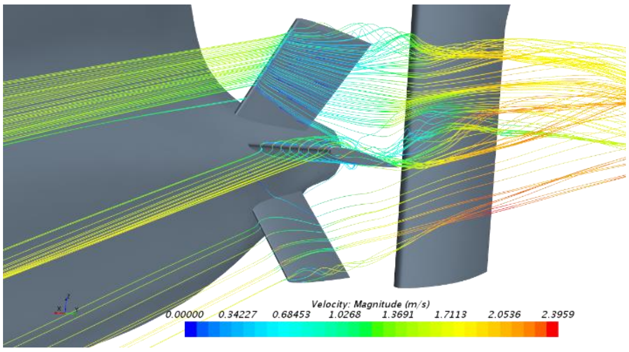

Figure 4 Streamlines on stator blades for the optimum configuration, Case 16

In Figure 5, velocity vectors were given at $0.06D_p$ upstream of the propeller plane. On the left hand side vectors of stator case 16 at the self-propulsion point were given. Stator blades caused an asymmetric inflow to the propeller in order to generate a pre-swirl counter direction of the propeller rotation. In Figure 6, velocity vectors were given at 0.06 D_p downstream of the propeller plane. Vectors of the stator and without stator case can be seen on the left and right hand side, respectively. Vector sizes of the stator case at downstream plane is smaller than the case without stator. This indicate that the stator reduce qualitatively the rotating flow downstream of the propeller, which enables to recover the energy loss due to the rotation.

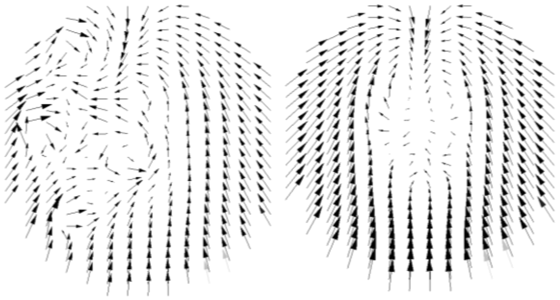

Figure 5 Velocity vectors at 0.06 D_p upstream of the propeller plane (left: with stator, right: without stator).

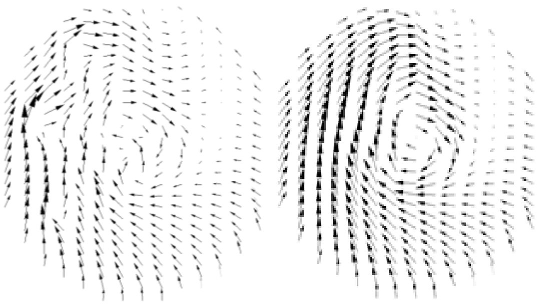

Figure 6 Velocity vectors at 0.06 D_p downstream of the propeller plane (left: with stator, right: without stator).

5 RESULTS AND DISCUSSION

Results of the study are summarized in Table 5, 6 and 7 to investigate the pre stator performance on the propulsive efficiency of the 7000 DWT chemical tanker model. As far as the relative-rotative efficiencies η_R are concerned, the predicted relative-rotative efficiencies are less than unity, which is not realistic. This lower relative-rotative efficiencies were originated as a result of the use of the double body method. In the double body method since only the viscous component of the resistance is taken into account the towed resistance of the model was obtained lower compared to the experimental results. This causes a difference in the rate of revolution between the real condition and the double body condition occurred, hence in the relative-rotative efficiency.

Table 5 Effect of the number of the blades on efficiencies in Position 1 (initial angular position)

Case	n [rps]	η_{0T}	w_{tT}	t
no PSS	8.245	0.650	0.206	0.181
1	8.241	0.649	0.209	0.174
2	8.209	0.649	0.212	0.174
3	8.214	0.649	0.211	0.174
4	8.247	0.650	0.207	0.174

Table 5 Effect of the number of the blades on efficiencies in Position 1(initial angular position) (cont.)

Case	η_H	η_R	η_D	$\%\eta_D$	
no PSS	1.031	0.9880	0.662		
1	1.045	0.9880	0.670	1.22	**all blades**
2	1.048	0.9880	0.672	1.59	**wo SC**
3	1.047	0.9880	0.672	1.48	**half SC**
4	1.042	0.9880	0.669	1.00	**wo PU**

In Table 5, the effects of the number of stator blades are summarized. In Case 1, all blades (PU, PC, PL and SC) were present, in Case 2, PU, PC and PL blades were present and in Case 3, three blades (PC, PL and SC) were present. In Case 4, all blades were present but the size of longitudinal blade SC was reduced to half. The results shown that Case 2 (wo SC case) gave the maximum increase in the propulsive efficiency among the other cases.

In Table 6, the effects of the blade angular positions on efficiencies are given. Since the initial studies on the effect of number stator blades indicated the Case 2 (wo SC case) was the optimum in terms of the propulsive efficiency, the Case 2 (wo SC case) was chosen only to investigate influence of different blade angular positions. As far as the results are concerned, the increase in the propulsive efficiency was similar for different positions. Then the blades were kept fixed in the initial position for the remainder of the study.

Table 6 Effects of the angular blade positions on efficiencies

Case	n [rps]	η_{0T}	w_{tT}	t
no PSS	8.245	0.650	0.206	0.181
2	8.209	0.649	0.212	0.174
5	8.209	0.650	0.211	0.174
6	8.210	0.650	0.211	0.174
7	8.213	0.649	0.211	0.173

Table 6 Effects of the angular blade positions on efficiencies (cont.)

Case	η_H	η_R	η_D	$\%\eta_D$	
no PSS	1.031	0.988	0.662		
2	1.048	0.988	0.672	1.59	**woSC POS1**
5	1.048	0.988	0.673	1.60	**woSC POS2**
6	1.046	0.988	0.671	1.45	**woSC POS3**
7	1.048	0.988	0.672	1.60	**woSC POS4**

In Table 7, the effects of pitch angles for each blade were investigated for Case 2 (wo SC case) in Position 1. Blades were installed at zero pitch angles initially. The pitch angles of the blades were varied at 4°,-4° and -8°, respectively. As the pitch angle increases in the counter clockwise direction, the propulsive efficiency also increases. Therefore the pitch angle of -8° was determined as the optimum pitch angle configuration for the stator study.

Table 7 Effects of the blade pitch angles on efficiencies

Case	n [rps]	η_{0T}	w_{tT}	t
no PSS	8.245	0.650	0.206	0.181
2	8.209	0.649	0.212	0.174
8	8.209	0.650	0.211	0.174
9	8.218	0.649	0.213	0.175
10	8.225	0.648	0.215	0.175
11	8.223	0.648	0.215	0.177
12	8.229	0.647	0.215	0.173
13	8.237	0.646	0.218	0.172
14	8.244	0.646	0.219	0.174
15	8.243	0.646	0.218	0.174
16	8.239	0.646	0.218	0.170

Table 7 Effects of the blade pitch angles on efficiencies (cont.)

Case	η_H	η_R	η_D	$\%\eta_D$	
no PSS	1.031	0.988	0.662		
2	1.048	0.988	0.672	1.59	**initial**
8	1.048	0.988	0.672	1.57	**PU4**
9	1.048	0.988	0.672	1.54	**PU-4**
10	1.051	0.989	0.673	1.69	**PU-8**
11	1.048	0.989	0.671	1.44	**PC4**
12	1.053	0.989	0.674	1.86	**PC-4**
13	1.060	0.989	0.678	2.36	**PC-8**
14	1.058	0.989	0.676	2.06	**PL4**
15	1.056	0.989	0.675	1.95	**PL-4**
16	1.061	0.990	0.678	2.50	**PL-8**

6 CONCLUSION

A numerical study has been carried out to investigate the effect of a pre-swirl stator on the propulsive efficiency for a 7000 DWT chemical tanker model, using RANS method with SST k-ω turbulence model. In order to investigate the effect of the number of the stator blades, angular blade positions and blade pitch angles, a parametric study was performed. A 4-bladed, two 3-bladed and a 4-bladed stator with one half-sized blade were analysed for the first angular position. Then the optimum configuration (a 3-bladed PSS without the SC blade) was analysed for the remainder angular positions. Optimization study was performed after determining the optimum angular blade position. The following conclusions were withdrawn from the study:

- The numerical method, RANS method with SST k-ω turbulence model applied here predicts well the resistance and propulsive factors with a reasonable accuracy.
- The optimum PSS was determined as the 3-bladed stator (without SC blade) located in Position 1 and with the blade pitch angle of -8°. The optimum PSS configuration indicates an increase in the propulsive efficiency, hence reduction in the fuel consumption of the ship.
- In order to obtain an increase in the propulsive efficiency parameter of the ship the PSS should be installed around $0.3D_p$ before the propeller plane with a diameter of $0.9\ D_p$ and 3 blades on port side with blade pitch angles of -8°.
- A further increase in the propulsive efficiency may be obtained by the combination of PSS with an energy saving duct, which requires a further study.
- A further study to include scale effect issues for the full-scale is recommended.

REFERENCES

Amin, I. and Q. Xiao (2014). "Numerical simulation of a horizontal axis tidal turbine with a pre-swirl stator." Developments in Maritime Transportation and Exploitation of Sea Resources: 863-869.

Bensow, R. E. (2015). Large Eddy Simulation of a Cavitating Propeller Operating in Behind Conditions with and without Pre-Swirl Stators. 4th International Symposium on Marine Propulsors, smp.

Celik, F. and M. Güner (2007). "Energy saving device of stator for marine propellers." Ocean engineering **34**(5): 850-855.

Gish, L., A. Carandang and G. Hawbaker (2016). Numerical optimization of pre-swirl stators for horizontal axis hydrokinetic turbines. OCEANS 2016 MTS/IEEE Monterey, IEEE.

ITTC (2002). "The Specialist Committee on Procedures for Resistance, Propulsion and POW Tests."

ITTC (2011). "ITTC Recommended Procedure of Fresh Water and Seawater Properties 7.5-02-01-03."

Kim, K., M. Leer-Andersen, S. Werner, M. Orych and Y. Choi (2013). "Hydrodynamic optimization of pre-swirl stator by CFD and model testing." International Shipbuilding Progress **60**(1-4).

Kim, M., H. Chun and Y. Kang (2004). "Design and experimental study on a new concept of preswirl stator as an efficient energy-saving device for slow speed full body ship." Transactions-Society of Naval Architects and Marine Engineers **112**: 111-121.

Park, S. and G. Oh (2014). Numerical Multi-scale Analysis of Turbulent Flow Around Low-speed Ship with Energy Saving Pre-swirl Stator. The Twenty-fourth International Ocean and Polar Engineering Conference, International Society of Offshore and Polar Engineers.

Park, S., G. Oh, S. Hyung Rhee, B.-Y. Koo and H. Lee (2015). "Full scale wake prediction of an energy saving device by using computational fluid dynamics." Ocean Engineering **101**: 254-263.

Saettone, S., P. B. Regener and P. Andersen (2016). "Pre-Swirl Stator and Propeller Design for Varying Operating Conditions." Proceedings of PRADS2016 **4**: 8th.

Simonsen, C. D., C. Nielsen, C. Klimt-Møllenbach, C. R. Holm and A. Minchev (2012). "CFD based investigation of potential power saving for different rudder types, positions and pre-swirl fins." Final report for DCMT fuel saving project, www. dcmt. dk.

Yong, J. S., C. K. Moon, J. L. Won, W. L. Kyoung and H. L. Joon (2015). Numerical and Experimental Investigation of Performance of the Asymmetric Pre-swirl Stator for Container Ship. Fourth International Symposium on Marine Propulsors, Austin, Texas, USA.

Zondervan, G.-J., J. Holtrop, J. Windt and T. Terwisga (2011). On the design and analysis of pre-swirl stators for single and twin screw ships. Second International Symposium on Marine Propulsors, Hamburg, Germany.

A. Yücel Odabaşı Colloquium Series
3rd International Meeting - Progress in Propeller Cavitation and its Consequences:
Experimental and Computational Methods for Predictions
15th – 16th November 2018, Istanbul, Turkey

The Effect of Extreme Trim Operation on Propeller Cavitation in Self-Propulsion Conditions

Matthias Maasch, Osman Turan and Sandy H. Day
Department of Naval Architecture and Marine Engineering, University of Strathclyde, 100 Montrose Street, Glasgow G4 0LZ, UK

Abstract: Experimental and numerical studies have shown that operating an LNG Carrier in extreme bow-up trim conditions can lead to substantial savings of over 25% in nominal ship resistance. The present study applies the Extreme Trim Concept to RANSE self-propulsion simulations including the prediction of propeller cavitation. It was investigated how the transient cavitation location and volume changed with varying ship displacements and trim angles over a range of ship speeds. Further, the effect of extreme trim and cavitation development on the ship delivered power was analyzed. Results have shown that by operating an LNG Carrier in extreme trim, power consumption and the extent of cavitation were reduced considerably. This study proved that the Extreme Trim Concept can be a valuable operating approach for reducing the environmental impact of LNG Carriers.

Keywords: Extreme Trim Concept, LNG Carrier, Self-propulsion simulation, Cavitation prediction.

1 INTRODUCTION

LNG Carriers operate a well-defined trading pattern in which a significant period of time is spent in unladen ballast conditions. During ballast voyage, in order to reach an operable ship draft, large amounts of ballast water are carried. Given that ballast water is unpaid load it is desirable to reduce the ballast loading while at the same time being operable on an efficient level. Therefore, the Extreme Trim Concept proposes to operate an LNG Carrier at extreme bow-up trim, thus realizing an operable draft at the aft, i.e. the propulsor is well submerged, with a minimum amount of ballast water carried. Previous experimental and numerical studies have shown that by applying extreme bow-up trim, over 25% reduction in nominal resistance compared to level trim operation is possible (Maasch et al., 2017).

Operating at an optimal trim at a constant displacement is thought to improve the flow field around the ship and hence decrease the wave making resistance. The impact on the frictional resistance component is marginal since, at a constant displacement, the hull wetted surface area does not change significantly. Another aspect of trim optimization is the influence on the propulsive performance, i.e. the inflow to the propeller and the propeller submergence. The latter often limits the range of bow-down trim angles to be tested since the propeller comes closer to the water surface with larger trim angles. (Reichel et al., 2014)

Experimental towing tank trim tests on the chosen LNG Carrier test case have shown that operating this ship at moderate trim angles either to stern or bow does not improve the ship's performance significantly (Day et al., 2010). The same trend was validated by numerical simulations. Hence, former results show that small changes to the ships trim do not have a positive effect on the wave making component of the total resistance or the propulsive performance, indicating that the hull is well designed for level trim operation at the tested loading condition. Mewis and Hollenbach outline that for each loading condition an ideal trim angle (including level trim) reduces the power consumption of a ship. In particular, modern cargo ships that feature a wide flat (submerged) transom and a pronounced bulbous bow do benefit from an optimized trim in off-loading conditions. (Mewis and Hollenbach, 2007)

Due to a small rotation of the hull (hydrostatic trim), a wet transom could emerge out of the water surface quite significantly, thus improving the wave making resistance. Also, a wide bulbous bow could be rotated to a more suitable water depth where its intended purpose of improving the bow free surface flow would be re-established. The LNG Carrier test case, however, operated in ballast loading conditions, features a dry and narrow flat transom and a relatively slender bulbous bow which could explain the hulls insensitivity to a standard trim optimization.

The Extreme Trim Concept, on the other hand, does not primarily aim to improve the wave making component but rather the frictional component of the total resistance, by reducing the ship's displacement and hence the wetted surface area. Similar to other large cargo ships, such as container carries, LNG Carrier have a high ballast water capacity to ensure safe and efficient operation in ballast loading conditions. Hollenbach et al outline that for those ship types ballast water can be used to influence a ship's trim (Hollenbach et al., 2007). Accordingly, instead of

* *Corresponding author e-mail: matthias.maasch@strath.ac.uk*

carrying large amounts of ballast water to operate at level trim conditions, the ballast water volume was reduced to a minimum in order to reach an extreme bow-up trim.

The present study extends the work published in (Maasch et al., 2017) by simulating the model scale LNG Carrier in four loading conditions over a speed range of 14-20 knots (full-scale) in self-propulsion conditions including propeller cavitation prediction.

2 NUMERICAL BACKGROUND

In order to investigate the effects of the Extreme Trim Concept on the propulsive performance of the LNG Carrier, numerical self-propulsion simulation at model scale were performed within this study.

This type of simulation, similar to self-propulsion towing tank experiments, is able to predict the performance of a vessel by simulating the hydrodynamic interaction of the hull, its propulsion system (in this CFD study the only relevant propulsion-system component was the propeller) and its rudder with each other and as a multi-component system with the environment, i.e. a domain of water and air. To solve the underlying flow physics, a state of the art commercial flow solver was used. In particular, the flow in the 3D dimensional numerical mesh was solved in time by an implicit unsteady flow scheme for the Reynolds-Averaged Navier-Stokes Equations (RANSE). In order to obtain a numerical solution for the flow field around a ship hull, the RANSE (see Eq. 1) solver allowed to divide the flow velocities and pressures into a time-averaged part (u, v, w, p) and a fluctuating part (u', v', w').

$$\begin{aligned}\rho(u_t + uu_x + vu_y + wu_z) &= \rho f_1 - p_x + \mu(u_{xx} + u_{yy} + u_{zz}) \\ &\quad - \rho((\overline{u'u'})_x + (\overline{u'v'})_y + (\overline{u'w'})_z) \\ \rho(v_t + uv_x + vv_y + wv_z) &= \rho f_2 - p_y + \mu(v_{xx} + v_{yy} + v_{zz}) \\ &\quad - \rho((\overline{u'v'})_x + (\overline{v'v'})_y + (\overline{v'w'})_z) \\ \rho(w_t + uw_x + vw_y + ww_z) &= \rho f_3 - p_z + \mu(w_{xx} + w_{yy} + w_{zz}) \\ &\quad - \rho((\overline{u'w'})_x + (\overline{v'w'})_y + (\overline{w'w'})_z)\end{aligned} \qquad (1)$$

Here, the Reynolds stresses contain the turbulent fluctuations (see Eq. 2) that required a turbulence model in order to find a numerical solution. (Bertram, 2000a)

$$\begin{matrix} -\rho\overline{u'u'} - \rho\overline{u'v'} - \rho\overline{u'w'} \\ -\rho\overline{u'v'} - \rho\overline{v'v'} - \rho\overline{v'w'} \\ -\rho\overline{u'w'} - \rho\overline{v'w'} - \rho\overline{w'w'} \end{matrix} \qquad (2)$$

The turbulent flow was computed by the k-Omega SST model which blends the k-Epsilon model with the k-Omega model depending on the distance to the wall (i.e. ship hull). (SIEMENS, 2017a)

The free surface was solved using a Volume of Fluid (VOF) model under the assumption that both phases, water and air, share velocity and pressure (SIEMENS, 2017b). To be able to predict the generation of cavitation for different simulated loading conditions at various ship speeds, the transient growth and collapse of vapor volume in the computational domain needed to be accounted for in the Volume of Fluid model by an additional source term. Since the standard formulation of the VOF method does not compute phase-transition, i.e. for a two-phase fluid including transition due to cavitation, a suitable cavitation model was added to the simulation setup (Schnerr and Sauer, 2001). The growth and collapse of vapor over time can be expressed by Eq. 3. For cavitation to occur, the vapor bubbles needed a surface on which to nucleate. Hence, a number (N) of uniformly distributed seeds which provide that surface were required to be present in the computational domain.

$$Q_V = N \cdot 4 \cdot \pi \cdot R^2 \cdot v_r \qquad (3)$$

Assuming a spherical vapor bubble with the radius R, the bubble growth velocity v_r remained as an unknown quantity in the physical setup. Further neglecting bubble-bubble interaction and bubble coalescence, the bubble growth velocity can be generally modelled by the Rayleigh-Plesset Cavitation Model (see Eq. 4).

$$R\frac{dv_r}{dt} + \frac{3}{2}v_r^2 = \frac{p_{Sat} - p}{\rho_l} - \frac{2 \cdot \sigma}{\rho_l \cdot R} - 4\frac{\mu_l}{\varphi_l \cdot R}v_r \qquad (4)$$

However, for a simulation case where the local pressure, e.g. at propeller blade depth, is sufficiently low and the pressure difference of local pressure and ambient pressure, e.g. at a larger distance to the propeller blade, is large, the reduced formulation of the Rayleigh-Plesset Cavitation Model, also called Schnerr-Sauer Cavitation Model can be applied to compute the bubble growth velocity. This simplified approach neglects the influence of bubble growth acceleration ($R \cdot dv_r/dt$), viscous effects ($4 \cdot \mu_l \cdot v_r/(\varphi_l \cdot R)$) and the surface tension effects ($2 \cdot \sigma/(\rho_l \cdot R)$), yielding Eq. 5. (SIEMENS, 2017c)

$$v_r^2 = \frac{2}{3}\left(\frac{p_{Sat} - p}{\rho_l}\right) \qquad (5)$$

The local pressure at the bubble boundary was represented by the saturation pressure p_{Sat}. With the above described setup, a number of self-propulsion simulation were performed to compute the required power delivered to the propeller and propeller cavitation.

3 SIMULATION SETUP

For setting up the self-propulsion simulations efficiently, repeatable steps in the pre-processing, the simulation run and the post-processing were automated. Therefore, a software chain was established as shown in Figure **1**1.

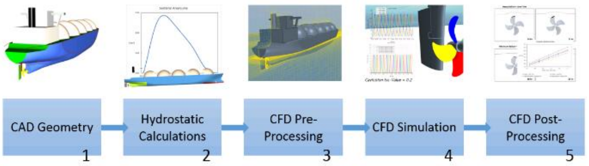

Figure 1 Automated Simulation Setup

The simulation pre-processing allowed to perform hydrostatic calculations and the generation of the numerical mesh in an automated manner. The hydrostatics of the LNG Carrier CAD model were calculated according to the draft at the aft perpendicular and the fore perpendicular where four sets of trim positions were considered as shown in Table **1**1.

Table 1 Loading Conditions, TL: Draft at fully laden conditions, TB: Draft at heavy ballast loading conditions

#	ID	Draft	
		Aft	**Fore**
1	Fully Laden – Level Trim	T_L	T_L
2	Heavy Ballast – Level Trim	T_B	T_B
3	Min. Ballast – Extreme Trim	T_B	0
4	Heavy Ballast – Extreme Trim	T_L	0

Along with setting the hydrostatic floating position of the LNG Carrier, the CAD model was automatically divided in geometric parts so that custom meshing settings could be applied while generating the numerical mesh. Further, mesh refinement volumes were generated that adapted its shape to the ship hull for each loading condition automatically. Thus, the total number of cells in the numerical mesh was kept small. Figure 2 illustrates the refinement volume generation for two different loading conditions for the bow and the stern region.

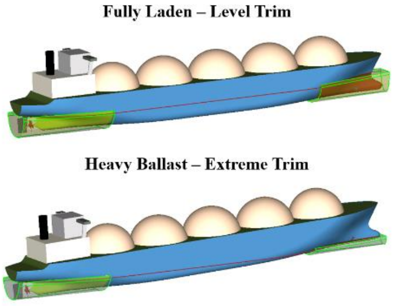

Figure 2 Numerical Mesh Pre-processing

In particular, the figure shows how the refinement volume around the bow (green transparent shape) of the LNG Carrier adapts its shape to cover the region near the hull surface only.

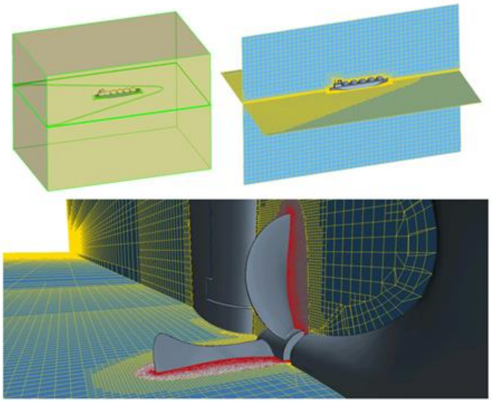

Figure 3 Global Numerical Mesh and Mesh Detail

In addition, global volumes for the numerical mesh control were prepared in the same manner. Refinement regions for the hull, the free surface, the rotating domain of the propeller and the ship wake were created automatically. Figure 3 shows the domain pre-processing in the top-left corner and the resulting numerical mesh from a global perspective in the top-right corner. A detailed view of the stern mesh and the rotating domain mesh is given as well. This approach allowed to produce a suitable numerical mesh of around 7 million cells, with approximately 4.3 million cells in the rotating domain, for each loading condition automatically.

For the domain setup to be suitable to work as a numerical towing tank, the box shaped tank volume was set up consisting of velocity inlets at the front (upstream), the bottom and the top, a pressure outlet at the back (downstream) and symmetry planes at the sides (port and starboard). Using a velocity inlet condition allowed to avoid a velocity gradient between the fluid (either water or air) and the domain boundaries. The ship hull and its appendages, to allow interaction of the structure and the fluid, were of type no-slip wall. In order to simulate the rotating propeller, a sliding mesh domain was created around it. Whereas the stationary domain was meshed using hexahedral cells, the rotating domain consisted of polyhedral cells. A hexahedral cell mesh is a typical choice for a simulation with a free surface, as it can be accurately aligned with the undisturbed free surface. For flow regions, where rotational or multi-directional flow dominates, polyhedral cells are the preferred choice. While hexahedral cells have three optimal flow directions (normal to each set of parallel faces), polyhedral cells with e.g. 10 or 12 faces have five or six optimal flow directions. In addition, polyhedral cells have a higher number of neighbor cells which allows for a better approximation of flow gradients. (Peric and Ferguson, 2005)

Another advantage may be that a mesh of polyhedral cells tolerates a fast growth in cell size. In the present case this allowed to produce very small cells on and near the propeller blades to capture cavitation while at the same time an appropriate cells size at the sliding mesh interface was reached to blend into the surrounding mesh (see Figure **4**4).

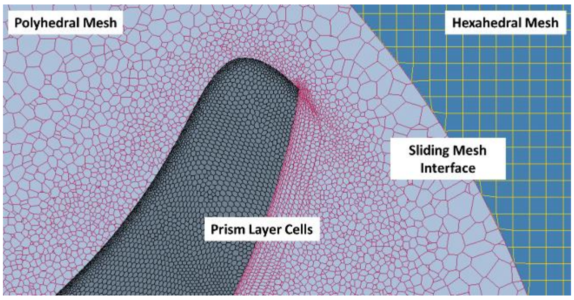

Figure 4 Numerical Mesh of Rotating and Stationary Domain

The fine cells at the propeller blade surface also allowed to resolve the boundary layer flow with a $Y_{+}\sim 1$, whereas the LNG Carrier hull boundary layer was modelled with a $Y_{+} \gg 30$.

The first objective of this study, the delivered power to the propeller, was computed from the propeller torque Q and the propeller rotation rate rps as shown in Eq. 6.

$$P_D = 2 \cdot \pi \cdot rps \cdot Q \tag{6}$$

By taking the Skin Friction Correction Force F_0 (see Eq. 7) into account, the LNG Carrier was operating at its full-scale self-propulsion point (ITTC, 2017a).

$$F_0 = [(1+k)(C_{FM} - C_{FS}) - \Delta C_F] 0.5 \cdot \rho_l \cdot S \cdot v^2 \tag{7}$$

with

$$\Delta C_F = 0.044 \left[\left(\frac{k_S}{L_{WL}} \right)^{\frac{1}{3}} - 10 Re^{-\frac{1}{3}} \right] + 1.25 \cdot 10^{-4} \tag{8}$$

and

$$k_S = 150 \cdot 10^{-6} \tag{9}$$

The form factor k for each operating condition was found by experimental Prohaska model tests prior to the self-propulsion simulations. The frictional force coefficients C_{FM} for model scale and C_{FS} full scale were calculated by the ITTC friction line (see Eq. 10) (ITTC, 2017b).

$$C_F = \frac{0.075}{(log_{10} Re - 2)^2} \tag{10}$$

To obtain the self-propulsion point within a reasonable time frame, the simulation was initialized with a high time step t_{SP} (see Eq. 11) as described in (ITTC, 2014) and the propeller rotation was smoothly ramped up from zero to its approximate final value.

$$t_{SP} = \frac{L_{PP}}{v_S \cdot 200} \tag{11}$$

After the flow field converged, the time step was reduced to a value t_{CAV} (see Eq. 12), suitable to predict the performance of marine propellers (ITTC, 2014) and to track the generation and the collapse of cavitation, which was the second objective of this study. This time step setting corresponded to approximately 1.8° propeller rotation per time step. Further, this time step allowed to realize a Courant number of $CFL < 1$ in all relevant regions near the hull.

$$t_{CAV} = \frac{1}{rps \cdot 200} \sim \frac{1.8°}{\Delta t} \tag{12}$$

After another short period of convergence time, the propeller rotation rate was adapted manually until the self-propulsion point was reached within a limit of 1% as shown in Eq. 13.

$$\left| \frac{T \cdot 100}{R_T - F_0} - 100 \right| < 1\% \tag{13}$$

Then, the domain reference pressure p_{Ref} was reduced from the initial atmospheric pressure (101325 Pa) to a reference pressure based on the local full scale cavitation number at the dimensionless propeller radius $r/R = 0.7$ to allow cavitation to develop. The local cavitation number was calculated according to Eq. 14.

$$\sigma_{0.7} = \frac{p_{0.7} - p_v}{0.5 \cdot \rho \cdot v_{a0.7}^2} \tag{14}$$

The local velocity in the propeller plane at the radius $r/R = 0.7$ was calculated according to Eq. 15.

$$v_{a0.7} = \sqrt{v_a^2 + (0.7 \cdot \pi \cdot D \cdot rps)^2} \tag{15}$$

The advance velocity v_a was calculated based on the nominal wake fraction computed by numerical towing tank simulation for the same loading conditions prior to this project and under the assumption of advance ratio (J) similarity of model to full scale. The local pressure $p_{0.7}$ was defined as shown in Eq. 16.

$$p_{0.7} = p_{Ref} - \rho \cdot g \cdot z_0 - \varphi \cdot g \cdot 0.7 \cdot R \tag{16}$$

To post-process the cavitation development, an average cavitation volume over one propeller rotation was calculated and plotted for comparison. In addition, the wake angle range over which cavitation appeared was computed along with the amount of sheet cavitation as percentage of propeller blade area. A visual comparison of propeller cavitation was also performed by extracting a front-view image of the propeller at an instance of maximum cavitation volume.

4 SIMULATION RESULTS

After the simulations converged at the full-scale self-propulsion point, relevant performance data was extracted from the running simulation automatically, post-processed and compared. This allowed to understand the influence of different loading conditions on the self-propulsion performance.

At the end of each simulation run, further data describing the cavitation pattern and volume were extracted automatically and again, post-processed and compared in order to evaluate the influence of extreme trim on propeller cavitation. In addition, the influence of cavitation on the propeller performance was assessed. Results will be presented in a comparative manner, labelling each loading conditions with #1 - #4 according to Table 1.

During each simulation run, the accuracy of the numerical solver was monitored by recording a time and cell value history of the Courant number (CFL) and the Y_+ on the hull and the propeller respectively. For further information about the theoretical background of both CFL and Y_+ the reader can refer to (ITTC, 2014).

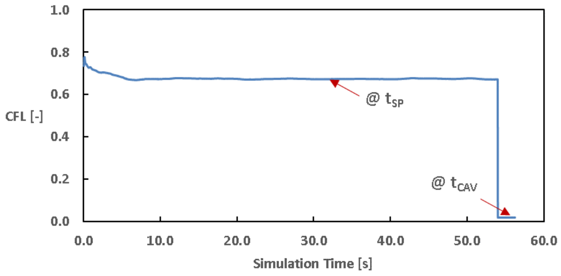

Figure 5 Time History of CFL Number on and near LNG Carrier Hull

Figure 5 shows the average Courant number in the cells on and near the LNG Carrier hull for fully laden conditions at 14 knots full-scale speed. For both, the large time step (see Eq. 11) and the small time step (see Eq. 12) a value of $CFL < 1$ was computed. Since the time step was coupled to the ship speed a similar CFL time history was recorded for each speed and loading condition. The same velocity-dependent approach was used for the generation of the near wall mesh which determined the Y_+ (see Figure **6**6).

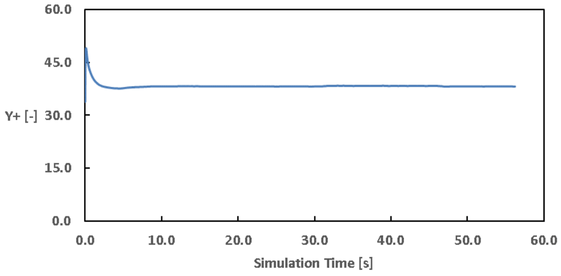

Figure 6 Average Y+ on the LNG Carrier Hull

For monitoring the CFL and the Y_+ on the propeller blades, a more detailed histogram plot was chosen to track the values per number of cells.

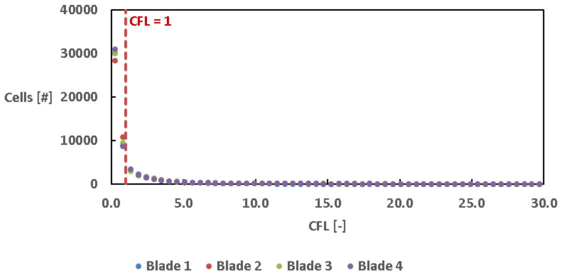

Figure 7 Histogram of Courant Number in Cells of Propeller Blades

Whereas the flow within the majority of cells, i.e. 80%, on the propeller blades was solved with a $CFL < 1$, 20% of the cells were solved with values of $1 < CFL < 30$. Those cells were mainly distributed along the blade leading edge where high flow velocities appeared.

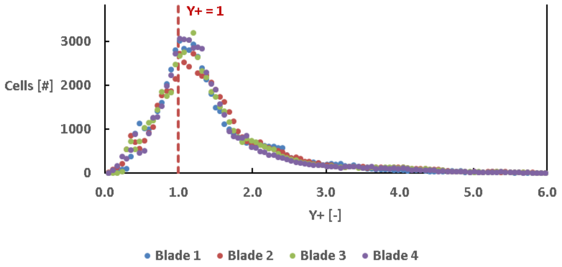

Figure 8 Histogram of Y+ in Cells of Propeller Blades

Approximately the same distribution of cells (80%/20%) was found for the $Y+ < 2$ and $2 < Y+ < 6$.

4.1 Performance at Self-Propulsion Point

In effective (self-propulsion) operating conditions, i.e. the propeller rotates behind the ship hull, in order to operate at the self-propulsion point, the generated thrust by the propeller is higher than the resistance of the bare ship hull in nominal conditions. The additional resistance induced by the propeller originates from an increase of flow velocities at the aftbody of the hull – resulting in an increase in frictional resistance, and a decrease of the pressure at the aftbody – resulting in an increase in inviscid resistance. This phenomena can be expressed by the thrust deduction factor, which relates the nominal resistance to the thrust created by the propeller in effective conditions. (Bertram, 2000b)

If results from nominal resistance simulations/tests and self-propulsion simulations/tests are available, as for the present study, the thrust deduction factor can be calculated as shown in Eq. 17 (Carlton, 2011).

$$t = \frac{T + F_0 - R_{T,nominal}}{T} \tag{17}$$

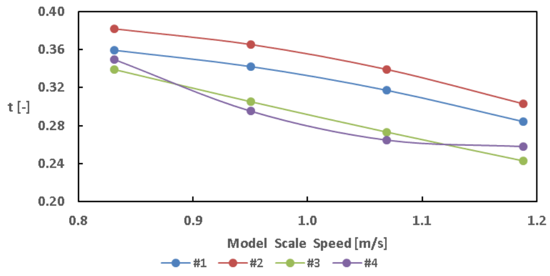

Figure 9 Thrust Deduction Fraction

Compared to values for thrust deduction factors that can be calculated from empirical equations for this type of single-screw ship (for empirical equations see (Carlton, 2011)), the above values are relatively high for lower ship speeds and reasonable for higher ship speeds. Overall, the interaction between propeller and ship hull improves at higher ship speeds. In particular, for the level trim conditions #1 and #2, the performance decreases at heavy ballast draft (#2) as the propeller operates close to the free surface. The extreme trim conditions #3 and #4 show a better performance compared to the level trim conditions. This can be explained by the much smaller imprint of the ship hull on the wake field (i.e. wake fraction), hence a more uniform propeller inflow (see reader may refer to (Maasch et al., 2017) for details). Since the ship power delivered to the propeller is calculated from propeller rps and torque, it is worthwhile to present those quantities in a comparative manner, too. Hence, Figure 10 and Figure 11 compare rps and torque for the calculated loading conditions. The propeller rps was mainly driven by the ship speed and displacement as for low speed and low displacement a low rps was computed. Consequently, the fully laden condition #1 showed the highest rps, followed by the heavy ballast loading level trim condition #2 and the heavy ballast extreme trim condition #3. For the minimum heavy ballast extreme trim condition #4 the propeller operated with the lowest rps due to largely reduced ship displacement.

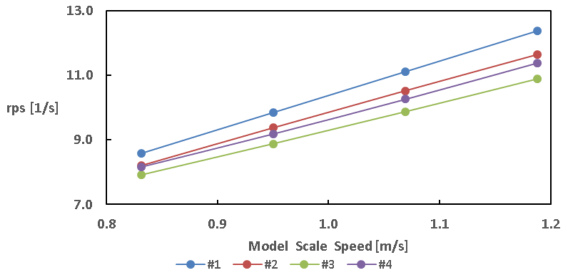

Figure 10 Propeller RPS

The propeller torque, shown below in Figure 11, reflects the quality of the operating conditions for the propeller at more detail and somewhat independent of small differences in ship displacement. It is evident that the load on the propeller largely reduces in extreme trim conditions. However, for both, the level trim conditions #1 and #2 and the extreme trim conditions #3 and #4, the torque values are close with almost no difference between #3 and #4. This demonstrates that the propeller works efficiently in extreme trim conditions.

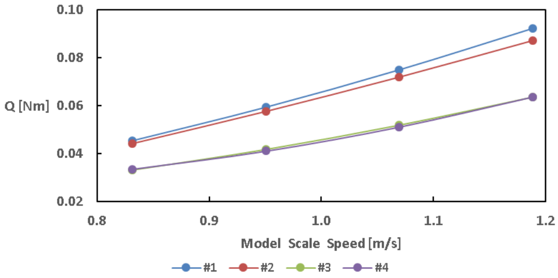

Figure 11 Propeller Torque

Following Eq. 6, both propeller rps and propeller torque yield the power delivered to the propeller. As presented in Figure 12, the required power is similar to the trend of the propeller torque. Since the propeller showed a good performance in heavy ballast extreme trim conditions #4, there is only a small difference to the minimum ballast extreme trim condition #3, despite the higher displacement.

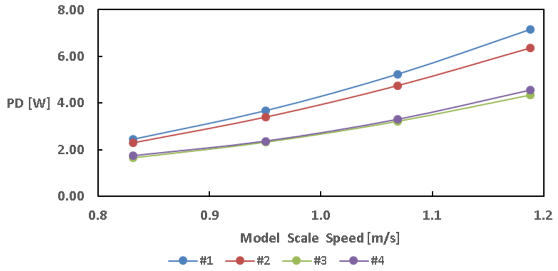

Figure 12 Power Delivered to the Propeller

This phenomena can be explained by the increased submergence of the aftship which allowed the propeller to work in a more favorable flow environment.

4.2 Propeller Cavitation

Once the full-scale self-propulsion point was reached for each simulation, the numerical cavitation model was activated. Cavitation occurs, when the local flow pressure falls below the vapor pressure. For the present simulations, this local pressure drop was caused by the propeller operating at a high rotation rate and close to the water surface. Figure shows the transient cavitation volume per one propeller rotation, i.e. a passage of 4 blades, in cubic millimeters. In comparison, Figure 14 illustrates the appearance of cavitation at a maximum volume for each speed and loading condition. In addition, the free surface along with the aftship overhang is shown (if the hull pierced the surface). For the lowest model-scale speed, corresponding to 14 knots full-scale, no cavitation occurred. The top chart in Figure 13 shows the transient cavitation volume for the laden level trim conditions (#1). Depending on the ship speed and the resulting propeller rps, a lower cavitation volume was computed at lower speeds. At heavy ballast level trim conditions (#2) the lower draft caused a slightly higher cavitation volume, despite the reduced propeller rps. For the minimum ballast extreme trim condition (#3), hardly any cavitation was detectable when checking the vapor volume visually during the simulation run. However, the solver computed cavitation volume, here presented as ten times as much (see 3rd chart in Figure 13) as actually recorded. For the heavy ballast extreme trim loading condition (#4), no cavitation was computed for the three lower speeds. Only at the speed corresponding to 20 knots full-scale, cavitation occurred.

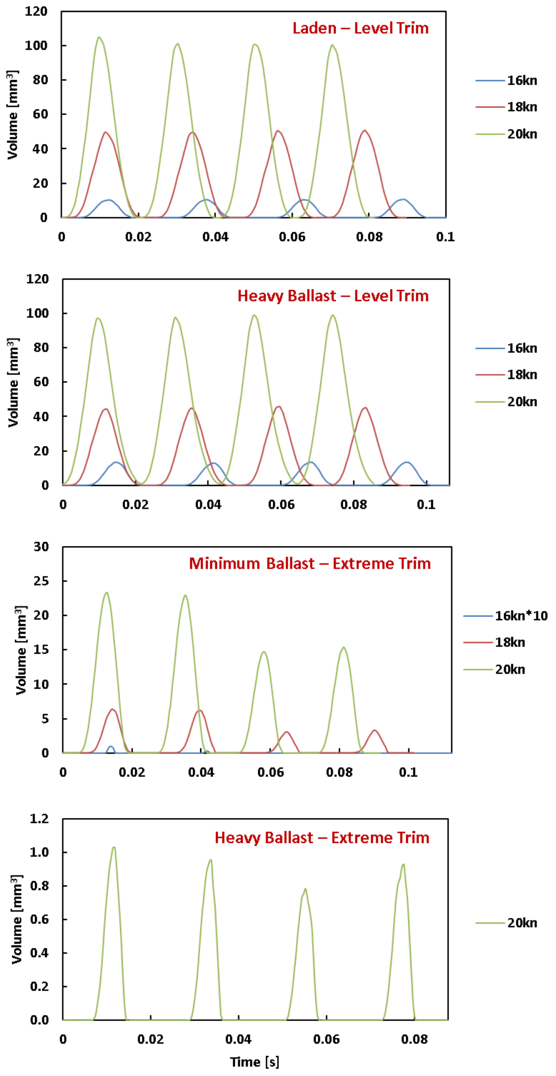

Figure 13 Transient Cavitation Volume per Propeller Rotation

From the transient recordings of the cavitation volume, an average was calculated, allowing to compare each speed and loading condition with less detail (see Figure).

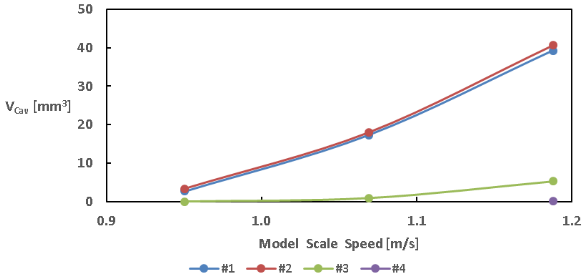

Figure 14 Average Cavitation Volume per Propeller Rotation

Due to the low draft at condition #2 the propeller operated very close to the water surface, hence producing a similar average cavitation volume as the LNG Carrier operating in fully laden conditions. This can also be seen in Figure 14. In extreme trim conditions at a minimum ballast, only little cavitation volume occurred.

Finally, the percentage of sheet cavitation on the propeller blade area was calculated as shown in Figure 15. Using this quantity, one can estimate if and by how much the thrust generated by the propeller breaks down due to cavitation. If the thrust breaks down due to cavitation, one would need to operate at higher propeller *rps* since the decreased thrust leads to a higher power consumption for a constant speed (Lewis, 1988).

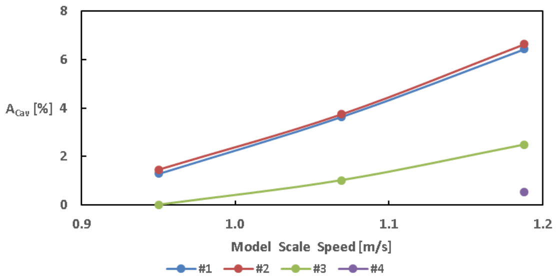

Figure 15 Area of Sheet Cavitation as Percentage of Propeller Blade Area

If less than 10% of the propeller blade area are covered by sheet cavitation, a thrust breakdown is usually highly unlikely. This is the case for all speeds and loading conditions. However, the level trim loading conditions showed values close to 10%, so that a thrust breakdown becomes likely for higher ship speed. For the extreme trim loading conditions, on the other hand, a thrust breakdown seems to be unlikely, even for higher speed than the ones already computed. To counter-check the above claim, after a stable cavitation pattern was reached, cavitation was switched off and the transient thrust and torque recordings were analyzed with the result that no change in performance could be detected.

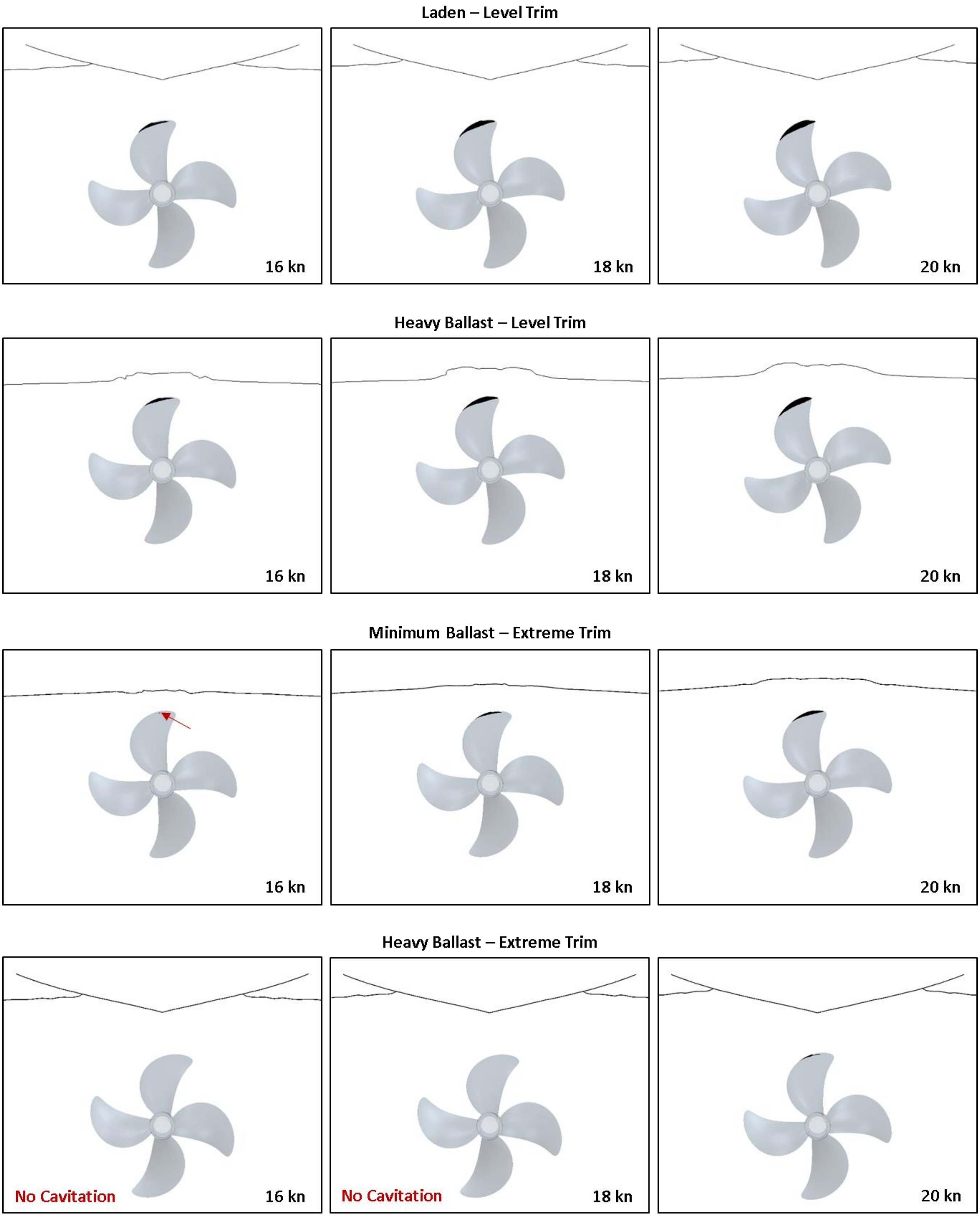

Figure 16 Cavitation Pattern for each speed and loading condition

5 CONCLUSION AND OUTLOOK

Within the presented study, numerical self-propulsion simulations including the prediction of propeller cavitation for an LNG Carrier geometry at model scale were performed. Four loading conditions were computed, two at level trim and two at an extreme bow-up trim angle. This was done to show how the self-propulsion performance of the ship improves when operated at an extreme trim angle.

The presented simulation setup, which was largely automated by coupling commercial software tools suitable to perform a marine CFD study, allowed to pre-process, run and post-process the simulations with only little interaction of the user compared to an approach where repeatable steps in the setup would have been executed manually. Thus, a set of 16 numerical simulations were prepared, executed and assessed in a short period of time.

Two objectives were investigated within this study, the effect of the Extreme Trim Concept on the power delivered to the propeller and on the propeller cavitation.

It was shown that by operating the LNG Carrier at an extreme bow up trim angle, the power consumption was reduced by around 25%. This substantial reduction was reached by reducing the ship displacement while at the same time keeping a favorable inflow to the operating propeller. Fortunately, the heavy ballast extreme trim loading condition showed similar improvements in the required power reduction as the extreme trim operation condition at minimum ballast. Thus, due to the higher displacement, it is likely that an improved ship stability would be reached when operating in waves.

Due to the propeller operating at lower rps in extreme trim conditions compared to level trim, the propeller cavitation was reduced substantially, too. At level trim conditions, the propeller cavitated at speeds corresponding to 16, 18 and 20 knots full-scale. At the most favorable loading condition (heavy ballast extreme trim), only at 20 knots cavitation was detectable. For all simulated cases the cavitation did not cause a thrust breakdown.

In order to extend the work done within this project, the LNG Carrier performance should be investigated at higher speeds with a more refined numerical mesh in order to capture more details of cavitation. In addition, the influence of the Extreme Trim Concept on both the seakeeping performance and the ship stability would need to be assessed, too.

ACKNOWLEDGEMENT

This research has been funded by the Engineering and Physical Research Council (EPSRC) through the project, “Shipping in Changing Climates. All supports are greatly appreciated. EPSRC grant no. EP/K039253/1.

Results were obtained using the EPSRC funded ARCHIE-WeSt High Performance Computer (www.archie-west.ac.uk). EPSRC grant no. EP/K000586/1. The authors would like to further acknowledge Lloyds Register and SHELL as sponsors of this study.

REFERENCES

BERTRAM, V. 2000a. Practical Ship Hydrodynamics. 1.4 Numerical approaches (computational fluid dynamics) Butterworth-Heinemann.

BERTRAM, V. 2000b. Practical Ship Hydrodynamics. 3.1 Resistance and propulsion concepts. Butterworth-Heinemann.

CARLTON, J. S. 2011. Marine Propellers and Propulsion. Chapter 12 - Ship Resistance and Propulsion. Butterworth-Heinemann.

DAY, S., CLELLAND, D. & TURAN, O. 2010. Tests of LNG Carrier in Calm Water and Waves - Summary of Results. University of Strathclyde.

HOLLENBACH, U., KLUG, H. & MEWIS, F. 2007. Container Vessels – Potential for Improvements in Hydrodynamic Performance. 10th International Symposium on Practical Design of Ships and Other Floating Structures. Design of Ships and Other Floating Structures: American Buero of Shipping.

ITTC 2014. ITTC – Recommended Procedures and Guidelines. 7.5-03-02-03 Practical Guidelines for Ship CFD Applications.

ITTC 2017a. ITTC – Recommended Procedures and Guidelines. 7.5-02-03-01.1 Propulsion/Bollard Pull Test.

ITTC 2017b. ITTC – Recommended Procedures and Guidelines. 7.5-02-02-01 Resistance Test.

LEWIS, E. W. 1988. Principles of Naval Architecture Second Revision. In: LEWIS, E. W. (ed.) Volume II - Resistance, Propulsion and Vibration. The Society of Naval Architects and Marine Engineers.

MAASCH, M., TURAN, O., KHORASANCHI, M. & FANG, I. 2017. Calm water resistance and self propulsion simulations including cavitation for an LNG carrier in extreme trim conditions. Shipping in Changing Climates SCC 2017. London.

MEWIS, F. & HOLLENBACH, U. 2007. Hydrodynamic Measures for Reducing Energy Consumption during Ship Operation. STG Sprechtag „Möglichkeiten der Energieeinsparung im Schiffsbetrieb“. Hamburg.

PERIC, M. & FERGUSON, S. 2005. The advantage of polyhedral meshes. Available: https://pdfs.semanticscholar.org/51ae/90047ab44f538491 96878bfec4232b291d1c.pdf.

REICHEL, M., MINCHEV, A. & LARSEN, N. L. 2014. Trim Optimisation - Theory and Practice. 20th International Conference on Hydrodynamics in Ship Design and Operation. Wrocław: FORCE Technology.

SCHNERR, G. H. & SAUER, J. 2001. Physical and Numerical Modeling of Unsteady Cavitation Dynamics. ICMF-2001, 4th International Conference on Multiphase Flow. New Orleans, USA.

SIEMENS 2017a. STAR-CCM+ Documentation. K-Omega Turbulence.

SIEMENS 2017b. STAR-CCM+ Documentation. Using the Volume Of Fluid (VOF) Multiphase Model.

SIEMENS 2017c. STAR-CCM+ Documentation. Cavitation and Gas Dissolution.

A. Yücel Odabaşı Colloquium Series
3rd International Meeting - Progress in Propeller Cavitation and its Consequences:
Experimental and Computational Methods for Predictions
15th – 16th November 2018, Istanbul, Turkey

Investigation of Cavitating Marine Propeller Performance Using Blade Element Momentum Theory

Mehmet Salih Karaalioğlu[1, 2*], Sakir Bal[1]
[1]Istanbul Technical University, Faculty of Naval Architecture and Ocean Engineering, 34469 Maslak-Istanbul, Turkey
[2]Faculty of Marine Sciences, Ordu University, Fatsa-Ordu, Turkey

Abstract: In this study, effect of cavitation on marine propeller has been investigated by momentum blade element momentum theory combined with boundary element theory and corrections for tip-hub losses and section curvature are also implemented to improve the accuracy of the method. Momentum Blade Element Theory (MBET) is a powerful propeller analysis tool to predict the performance of propeller. MBET (strip theory) is composed of momentum theory and blade element theory. Momentum theory refers to analysis of loading on the blades by application of conservation of linear and angular momentum theories. Blade element theory on the other hand, refers to an analysis of forces and torques for a section of blade. The results of MBET are extremely dependent on accuracy of lift and drag coefficient of sections. In order to include the effects of cavitation, cavitating blade section coefficients are computed from potential based panel method. This panel method discretizes the exact surface of blade sections into panels. A database of lift and drag coefficients is generated before MBEM application. Tip and hub losses corrections have also been included in the calculations. Benchmark model propeller DTMB 4119 has been selected. The numerical results have been discussed and compared with experimental results.

Keywords: DTMB4119, marine propeller, cavitation, strip theory, panel method

1 INTRODUCTION

In the past, several theoretical methods were developed for marine propeller design and analysis. These methods differ from computation time, complexity, and accuracy of model. One of the most comprehensive methods is CFD (computational fluid dynamic) analysis. Capabilities of CFD is growing rapidly during last decades. Unfortunately, CFD needs high computer resources. Due to developments of hardware and codes, nowadays a marine propeller in uniform flow can be resolved, using full RANS simulation, within hours of CPU time on a modern personal computer, Yet, this is too expensive and time consuming for many applications such as design optimization or real time simulation. Therefore, low-order engineering codes like blade element momentum theory are still popular tools especially for concept and preliminary design and analysis stages, due to fast and low computational costs.

The method of using actuator disc to represent a rotor was introduced by Rankine. Froude later explained the physical mechanism for actuator disk theory. Blade element momentum theory is based on the concept of dividing rotor blade into separate elements (Sun, Chen, Shen, & Zhu, 2016). This concept was proposed originally by Drzewiecki in 1892. In this study, Drzewiecki drew the velocity triangle for each element without including velocity induction (Okulov, Sørensen, & Wood, 2015). The concept of optimum rotor was established with the development of vortex theory. The amount of energy that can be extracted from the flow has a theoretical upper limit. It is called Betz-Joukowsky limit. Later Prandtl and Glauert found out the classical blade element momentum theory (Glauert, 1935).

(Benini, 2004) implemented a combined momentum blade element theory for light and moderately loaded marine propellers and compared his results with those of fully three-dimensional Navier-Stokes calculations. Wageningen B series was selected for propeller geometry. The classical blade element momentum theory assumes a small local angle of attack at all sections along the blade and that local induced drag negligibly reduces the local propeller thrust coefficient. (Whitmore & Merrill, 2012) proposed a nonlinear correction for classical blade element momentum theory. These nonlinear corrections had better represent the measured propeller performance.

(Bal, 2011) applied practical design method to obtain optimum cavitating ship propellers by combining a vortex lattice lifting line method and a lifting surface method. DTMB 4119 and DTMB 4381 propellers have been adopted for calculations. Agreement between the results of this practical technique and the experimental measurements was good for practical purposes. Also practical technique is modelled to improve the open water propeller performance by using a vortex lattice lifting line method together with a lifting surface method (Bal, 2011)

(Siddappaji & Turner, 2015) implemented blade element momentum theory to optimize and analyze the counter rotating propellers. Section lift and drag properties are

* *Corresponding author e-mail: karaalioglum@itu.edu.tr*

obtained XFOIL.(Leone, Testa, Greco, & Salvatore, 2013) investigate the capabilities and drawback of blade element momentum theory for self-pitching propellers analysis. Self-pitching propellers are unconventional propeller typrs where blades automatically adjust their pitch to suit the applied load, according to the prevailing working conditions. Agreement between numerical and experimental result is satisfactory.

In addition; some coupled RANS and blade element momentum theory numerical models are proposed to investigate ship wake field (Badoe, Phillips, & Turnock, n.d.; Winden, Badoe, Turnock, Phillips, & Hudson, 2013).

(Ülgen, 2017) implemented blade element momentum theory and RANS approach for DTMB 4119 , the standard test propeller, to calculate propeller hydrodynamic performance and compared their results. The comparision indicated that the blade element momentum theory has sufficient level of accuracy. The closed form of the nonlinear Blade Element Momentum Theory equation is presented by McCormick (Whitmore & Merrill, 2012). McCormick assumed a small local angle of attack at all sections along the blade (McCormick, 1994). He also assumed that the local induced drag only negligibly reduces the local propeller thrust coefficient. (Soydan, 2018) implemented blade element momentum theory without these assumption to calculate open water performance of DTMB 4119. The experimental data matches the nonlinear blade element momentum model with reasonable accuracy.

In this study, the performance of benchmark model propeller DTMB 4119 has been investigated by using MBEM. MBEM with hub, tip and camber correction models have been applied and the results compared with each other in terms of thrust and torque coefficients under cavitating and non-cavitating conditions. For cavitating case, MBEM has been applied for two different advance ratios. Lift and drag coefficient of propeller sections under cavitating condition is computed to be used with MBEM analyses. Thus, effect of cavitation is included in the MBEM analysis. The effects of cavitation on the results have been discussed.

2 MATHEMATICAL FORMULATION

Blade element momentum theory rely on blade element theory and momentum theory. In this method, blade is divided into several elements. These elements are called strips. It is assumed that there are no hydrodynamic relations among the elements. The equations can be derived from combining two methods and these equations can be solved iteratively. A brief summary of the formulation is given for the completeness of the study in the following sub-section.

2.1 Momentum Theory

It is assumed that fluid is 2D, homogenous, incompressible, steady, uniform and purely axial with no rotational motion. Propeller is replaced by an actuator disk that has zero thickness as shown in Figure 1. Across the disk, pressure changes discontinuously, but the velocity varies in a continuous manner. Momentum is calculated for downstream and upstream of actuator disk. Then force acting on disk is obtained from rate of change momentum (Hansen, 2010).

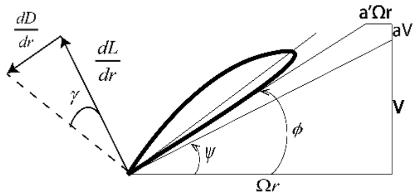

Blade Element T.

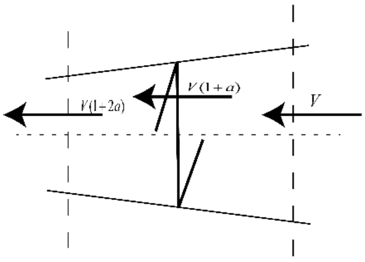

Momentum T.

Figure 1 Blade element and momentum representations of propeller action

Axial induction factor and circumferential factor are defined as;

$$a=\frac{V_2-V_1}{V_1} \qquad a'=\frac{\omega_1}{\Omega} \tag{1}$$

Thrust is equal to axial rate of momentum change, as follows;

$$\delta T = 2\pi r \delta r \rho V(1+a)(V_2-V) = 2\pi r \delta r \rho V^2(1+a)2a \tag{2}$$

Torque is defined as angular rate of momentum change, as folows;

$$\delta Q = 2\pi r \delta r \rho V(1+a) r^2 \omega_2 = 2\pi r \delta r \rho V(1+a) r^2 2a'\Omega \tag{3}$$

Thrust and torque are non-dimensional with respect to per unit span on the propeller;

$$\frac{dT}{dr} = 4\pi\rho r V^2 a(1+a) \tag{4}$$

$$\frac{dQ}{dr} = 4\pi\rho r^3 \Omega V a'(1+a) \tag{5}$$

Non-dimensional equation can be rewritten as follows;

$$r = xR,\ \Omega = 2\pi n,\ \text{n=rps},\ KT = \frac{T}{\rho n^2 D^4},\ KQ = \frac{Q}{\rho n^2 D^5} \tag{6}$$

Combining Equation 6 with Equations 4-5 gives;

$$\frac{dK_T}{dx} = \pi J^2 x K a(1+a) \qquad (7)$$

$$\frac{dK_Q}{dx} = \frac{1}{2}\pi^2 x^3 J K a'(1+a) \qquad (8)$$

$$K = \frac{2}{\pi}\cos^{-1}\left(\frac{\cosh(xF)}{\cosh(F)}\right) \quad \text{where } F = \frac{Z}{2x\tan\phi} - \frac{1}{2} \qquad (9)$$

In Equations 7-8 κ is called Goldstein factor (Tibery & Wrench J W, 1964). Lifting line theory can be used to calculate κ factors and the computed chart is given in Figure 2 for a three bladed propeller. ?

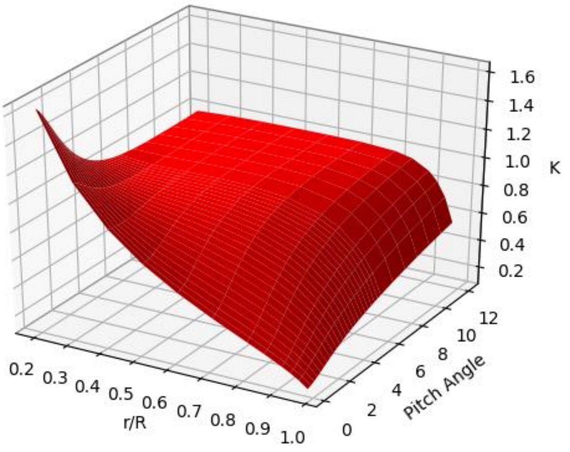

Figure 2 Goldstein factors

2.2 Blade Element Theory

It is assumed that blade can be divided into multiple elements. Every element operates independently under different flow conditions; rotational speed, chord length, twist angle. Forces on every strip are calculated individually and integrated from hub of the blade to the tip. Thus overall performance characteristic of blade can be determined by numerical integration. Generally, twenty elements are sufficient for convergence. Blade element theory is based on some assumptions. One of the assumptions is that there is no hydrodynamic interaction between strips. Another assumption is that the forces on blade depend on only the lift and drag coefficients of blade shape and angle of attack. Accuracy of MBEM theory depend on lift and drag coefficients. If the lift and drag coefficients of cavitating sections are used for iterative process, cavitation phenomenon is included in the MBEM analysis.

The iterative process of blade element momentum theory is presented in Figure 3.

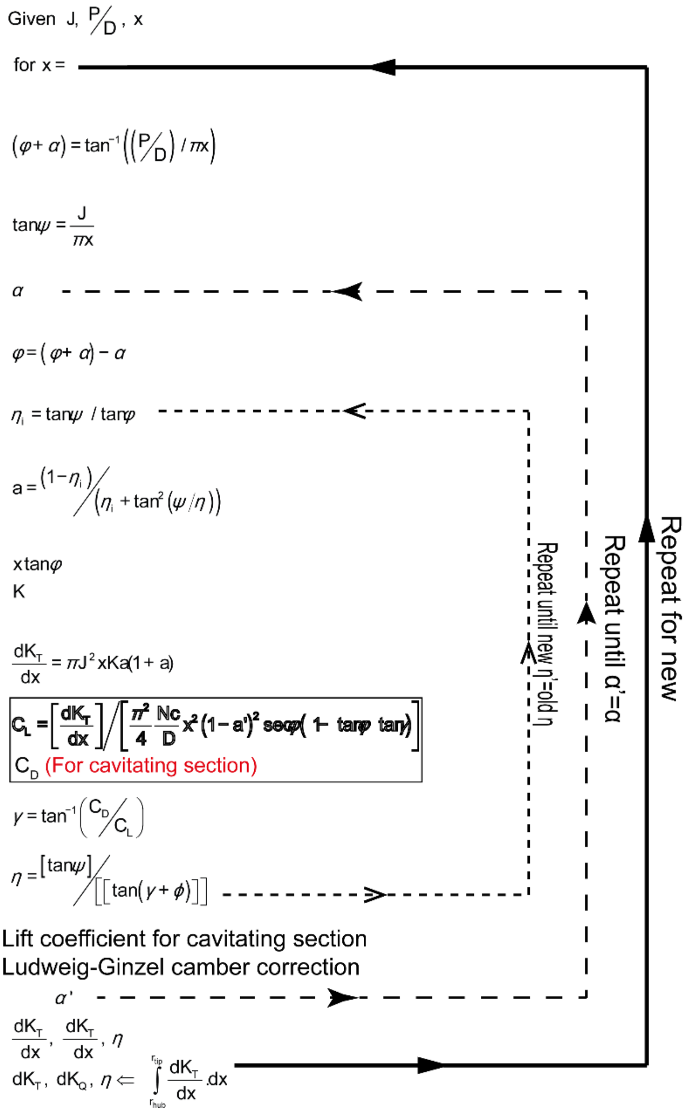

Figure 3 Flow algorithm for blade element momentum theory (Molland, Turnock, & Hudson, 2011)

The force normal to and tangent to flow are required for blade element theory, If the lift and drag coefficients are known, lift and drag force can be calculated by using Equations 10-11.

$$\frac{dL}{dr} = \frac{1}{2}\rho Z c U^2 C_L(\alpha) \qquad (10)$$

$$\frac{dD}{dr} = \frac{1}{2}\rho Z c U^2 C_D(\alpha) \qquad (11)$$

From Figure 1, it is possible to derive the following relationships;

$$\tan\psi = \frac{V}{\Omega r} = \frac{J}{\pi x}; \quad J = \frac{V}{nD} \qquad (12)$$

$$\tan\phi = \frac{V(1+a)}{\Omega r(1-a')} = \frac{(1+a)}{(1-a')}.\tan\psi \qquad (13)$$

$$\tan(\phi+\alpha) = \frac{P}{2\pi r} = \left(\frac{P/D}{\pi x}\right) \qquad (14)$$

Combining Equations 12-14 with Equations 10-11 yield;

$$\frac{dT}{dr}=\frac{dL}{dr}.\cos\phi-\frac{dD}{dr}.\sin\phi=\frac{dL}{dr}.\cos\phi\left(1-\tan\phi\tan\gamma\right) \tag{15}$$

$$\frac{dQ}{dr}=r\left(\frac{dL}{dr}.\sin\phi+\frac{dD}{dr}.\cos\phi\right)=r\frac{dL}{dr}\cos\phi\left(\tan\phi+\tan\gamma\right) \tag{16}$$

By making non-dimensionize the Eq. 15 and Eq. 16, Eq.17 and Eq. 18 can be derived as follows,

$$\frac{dK_T}{dx}=\frac{\pi^2}{4}\left(\frac{Zc}{D}\right).C_L.x^2(1-a')^2\sec\phi(1-\tan\phi.\tan\gamma) \tag{17}$$

$$\frac{dK_Q}{dx}=\frac{\pi^2}{8}\left(\frac{Zc}{D}\right).C_L.x^3(1-a')^2\sec\phi(\tan\phi+\tan\gamma) \tag{18}$$

3 NUMERICAL RESULTS

First the pressure distribution of NACA 66 (thickness form) with a=0.8 camber is computed by using panel method for 60, 80,100 and 120 panels and the results are compared with experiments (Erney, 2008). Here PCPAN program has been used (Kinnas & Fine, 2006). In this case, angle of attack is 6° and cavitation number is 1.25. As shown in Figure 4, 100 panel is sufficient for converged solution. After this convergence study, for all panel simulations,100 panel is used.

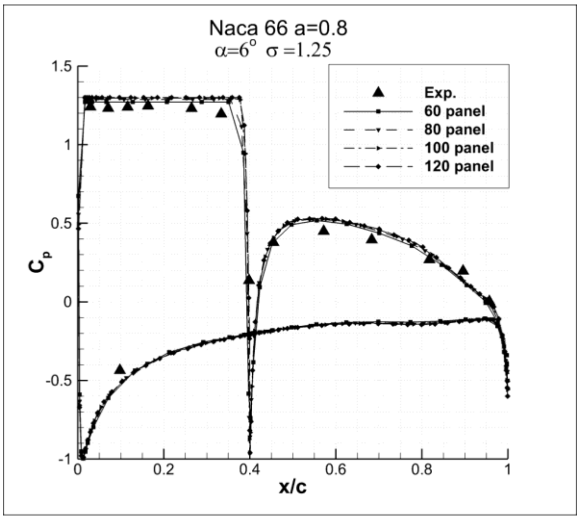

Figure 4 Pressure distribution of Naca 66 a=0.8 (α=6 σ=1.25)

Second, MBEM with tip-hub correction and Ludweig and Ginzel camber corrections have been applied to non-cavitating DTMB 4119 propeller for 20 strips (Ginzel, 1955). 20 strips were found to have a sufficient level of accuracy after a systematic convergence studies. For all MBEM, 20 strip is used. Numerical results are compared with experiments as shown in Figure 5. As seen Figure 5, the agreement between the results of MBEM and experimental results is satisfactory good. Corrections increased the agreement of the MBEM results with experiments much better.

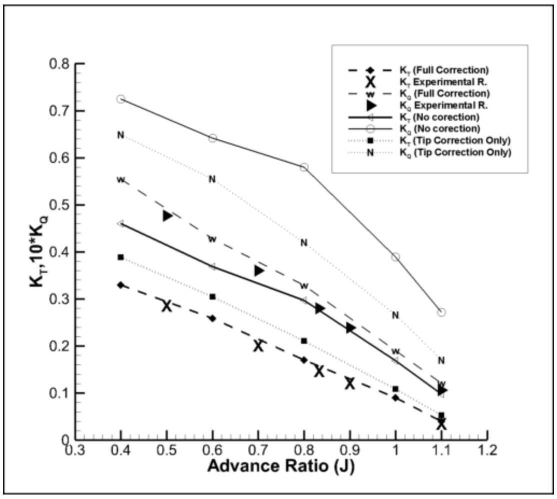

Figure 5 K_T and K_Q for DTMB 4119 (Non-cavitating condition)

Under cavitating condition, the lift and drag coefficients of avitating sections are used for momentum blade element method iterative process. First, cavitating section and the ratio of cavity length to chord length are determined via a lifting surface method. Then the lift and drag coefficients of these sections are obtained by using the panel method. MBEM analyses with cavitation are applied for one advance ratio J=2.3. Cavitation distribution on propeller blade for σ=3.3 and σ=3.7 are shown in Figure 6. σ is cavitation number defined as (Carlton, 2012);

$$\sigma=\frac{p-p_\infty}{0.5\rho nD^2} \tag{19}$$

Cavitation pattern is obtained by using the lifting surface method given in Ref (Bal, 2011).

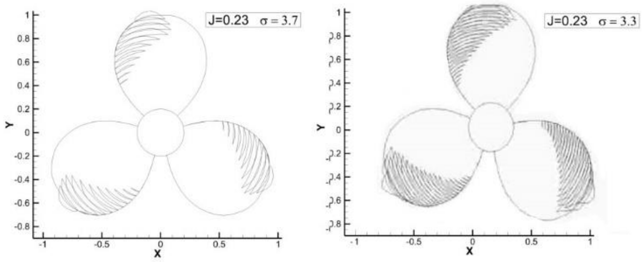

Figure 6 Cavitation pattern of DTMB 4119 for two advance ratio σ=3.3 and σ=3.7

Under cavitating condition, there is a satisfactory agreement for practical purposes between both results as given in Table 1.

Table. 1 K_T K_Q for two advance ratio (Cavitating case)

	K_T (Bal, 2011)	K_Q (Bal, 2011)	K_T (MBEM)	K_Q (MBEM)
J=0.23 σ=3.3	0.304	0.540	0.378	0.637
J=0.23 σ=3.7	0.337	0.536	0.392	0.617

4 CONCLUSION

In this study, for the hydrodynamic performance of DTMB 4119 standard test propeller, an MBEM has been described under non-cavitating and cavitating conditions. MBEM with corrections (hub, tip and camber) generated satisfactorily good results under non-cavitating conditions. Note also that MBEM is also fast and simple. Under cavitating condition, calculation has been performed for two different advance ratios and cavitation numbers, J=0.23, σ=3.3 and , J=0.23, σ=3.3. Results show that there is a good agreement for cavitating conditions between numerical and experimental results.

The next step is to define the cavitation number at each strip on the propeller and to find the cavity shape and lift and drag coefficients of the sections. Then these 2-D cavitating section data are given as an input for the MBEM. This will be a future study.

Here the blade element model makes small angle assumption, which are known to be inaccurate for higher advance ratio. It is expected that the MBEM model without these assumptions will have more accurate results. A nonlinear MBEM will also be applied in a future study.

Nomenclature

a	Axial inflow factor
a'	Circumferential inflow factor
ϕ,γ,ψ	Advance angle
α	Angle of attack
ψ	Angle
C_D	Drag coefficient
C_L	Lift coefficient
κ	Goldstein Factor
ω,Ω	Angular velocity
c	Blade chord length
Z	Number of blade
D	Diameter
n	Revolution per second
J	Advance ratio
σ	Cavitation number
ρ	Density
dD	Drag
dL	Lift
V_∞,V	Freestream velocity
x	Nondimensional radial location
P	Pitch
K_T	Thrust coefficient
K_Q	Torque coefficient
T	Thrust
Q	Torque

REFERENCES

Badoe, C., Phillips, A., & Turnock, S. R. (n.d.). *Ship wake field analysis using a coupled BEMt-RANS approach*. Retrieved from https://eprints.soton.ac.uk/368985/1/Badoe_Nutts2014.pdf

Bal, S. (2011). A practical technique for improvement of open water propeller performance. In *Proceedings of the Institution of Mechanical Engineers Part M: Journal of Engineering for the Maritime Environment* (Vol. 225, pp. 375–386). https://doi.org/10.1177/1475090211413957

Benini, E. (2004). Significance of blade element theory in performance prediction of marine propellers. *Ocean Engineering*, *31*(8–9), 957–974. https://doi.org/10.1016/j.oceaneng.2003.12.001

Carlton, J. (2012). *Marine Propellers and Propulsion*. *Marine Propellers and Propulsion*. https://doi.org/10.1016/C2010-0-68327-1

Erney, R. W. (2008). Verification and Validation of Single Phase and Cavitating Flows Using an Open Source Cfd Tool. *Thesis.*

Ginzel, G. 1. (1955). *Theory of the Broad-Bladed Propeller*. London. Retrieved from http://naca.central.cranfield.ac.uk/reports/arc/cp/0208.pdf

Glauert, H. (1935). Airplane Propellers. In *Aerodynamic Theory* (pp. 169–360). Berlin, Heidelberg: Springer Berlin Heidelberg. https://doi.org/10.1007/978-3-642-91487-4_3

Hansen, M. O. L. (2010). Aerodynamics of Wind Turbines. In *Wind Energy Explained* (pp. 91–155). https://doi.org/10.1002/9781119994367.ch3

Kinnas, S. A., & Fine, N. E. (2006). A numerical nonlinear analysis of the flow around two- and three-dimensional partially cavitating hydrofoils. *Journal of Fluid Mechanics*, *254*(1), 151. https://doi.org/10.1017/S0022112093002071

Leone, S., Testa, C., Greco, L., & Salvatore, F. (2013). Computational analysis of self-pitching propellers performance in open water. *Ocean Engineering*, *64*, 122–134. https://doi.org/10.1016/j.oceaneng.2013.02.012

McCormick, B. W. (1994). Aerodynamics, aeronautics and flight mechanics. Wiley. Retrieved from http://as.wiley.com/WileyCDA/WileyTitle/productCd-0471575062.html

Molland, A. F., Turnock, S. R., & Hudson, D. A. (2011). *Ship resistance and propulsion: Practical estimation of ship propulsive power*. *Ship Resistance and Propulsion: Practical Estimation of Ship Propulsive Power* (Vol. 9780521760). https://doi.org/10.1017/CBO9780511974113

Okulov, V. L., Sørensen, J. N., & Wood, D. H. (2015). The rotor theories by Professor Joukowsky: Vortex theories. *Progress in Aerospace Sciences*, *73*, 19–46. https://doi.org/10.1016/J.PAEROSCI.2014.10.002

Siddappaji, K., & Turner, M. G. (2015). Counterrotating Propeller Design Using Blade Element Momentum Theory. *Isabe-2015-20196*, (October), 4–6. https://doi.org/10.13140/RG.2.1.5089.9925

Soydan, A. (2018). *Gemi Pervanesi Performans Karakteristiklerinin Lineer Olmayan Kanat Elemani Momentum Teorisi Ve Hesaplamali Akişkanlar Dinamiği Yöntemleriyle İncelenmesi*. Master Thesis, Istanbul Technical University, Istanbul, Turkey.

Sun, Z., Chen, J., Shen, W. Z., & Zhu, W. J. (2016). Improved blade element momentum theory for wind turbine aerodynamic computations. *Renewable Energy*, *96*, 824–831. https://doi.org/10.1016/J.RENENE.2016.05.035

Tibery, C. L., & Wrench J W, J. (1964). *Tables of the Goldstein factor*. *David Taylor Model Basin, Report 1524, Applied Mathematics Laboratory, Washington, DC.*

Ülgen, K. (2017). *Comparison between blade element momentum theory and computational fluid dynamics methods for performance prediction of marine propellers*. Master Thesis, Istanbul Technical University, Istanbul, Turkey.

Whitmore, S. A., & Merrill, R. S. (2012). Nonlinear Large Angle Solutions of the Blade Element Momentum Theory Propeller Equations. *Journal of Aircraft*, *49*(4), 1126–1134. https://doi.org/10.2514/1.C031645

Winden, B., Badoe, C., Turnock, S. R., Phillips, A. B., & Hudson, D. A. (2013). Self propulsion in waves using a coupled RANS-BEMt model and active RPM control. Retrieved from https://eprints.soton.ac.uk/358865/